Experimental Investigation and Numerical Modeling of Deep Penetration Laser and GTA Welding Processes

Yadaiah Nirsanametla

Department of Mechanical Engineering

INDIAN INSTITUTE OF TECHNOLOGY GUWAHATI

2015

Experimental Investigation and Numerical Modeling of Deep Penetration Laser and GTA Welding Processes

submitted in partial fulfillment of the requirements

for the degree of

Doctor of Philosophy

by

Yadaiah Nirsanametla
(10610322)

Supervisor:

Dr. Swarup Bag

Department of Mechanical Engineering

INDIAN INSTITUTE OF TECHNOLOGY GUWAHATI

2015

Dedicated to

My parents, teachers and my wife Rupa

CERTIFICATE

This is to certify that the thesis entitled **Experimental investigation and numerical modeling of deep penetration laser and GTA welding processes,** submitted by **Mr. Yadaiah Nirsanametla** to Department of Mechanical Engineering, Indian Institute of Technology Guwahati, is a record of original research work under my supervision and is worthy of consideration for the award of the degree of Doctor of Philosophy of the Institute.

Date: 21st July, 2015.

Dr. Swarup Bag

Department of Mechanical Engineering,
Indian Institute of Technology Guwahati,
Guwahati, Assam 781039, India

Declaration

I declare that the present written submission is my thoughts in my own words. I have adequately been cited and referenced the original sources, where others' ideas have been involved. I also declare that I have followed to all principles of academic morality and honesty and have not neither fabricated nor falsified any idea/data in the present thesis. I realize that any defilement of the above will be cause for disciplinary action by the Institute and can also induce disciplinary action from the sources which have thus not been properly cited.

(**N. Yadaiah**)

Date: 21st July, 2015 Roll No: 10610322

Abstract

Fusion welding process is complex in nature since it involves several interactive physical phenomena. An accurate knowledge of weld induced distortions and residual stress, final microstructure and mechanical properties of weld joint are greatly influenced by thermal history, cooling rate and consequently the weld dimensions. Real-time measurement of the transient growth of temperature and material flow field during welding is extremely difficult and there is uncertainty to accurately measure the residual stress of weld joint. Alternatively, the computational model of increasing complexity based on scientific principle alone is an effective route to analyze the differential influence of process parameters during fusion welding process. The major difficulty of conduction heat transfer based modeling approach is *a-priori* definition of several heat source parameters which are limited by the definition of weld dimensions only from experimental measurement. The formation of keyhole in laser welding produces deep penetration weld joint whereas proper choice of surface active elements at optimum quantity promotes high penetration weld joint in gas tungsten arc (GTA) welding process. The mechanism of material flow by surface tension gradient prevails in GTA welding process. However, the interfacial phenomena like evaporation, homogeneous boiling, and multiple reflections in laser welding brings the complexity in formation of keyhole. Moreover, the absorptivity of laser and weld joint quality is greatly affected by presence of shielding gas.

Present thesis is primarily motivated in this direction. At first, major efforts are put forward to analyze the effect of controlled atmosphere during fiber laser welding of austenitic stainless steel (SS304 and SS316) through a series of experiments. The formation of keyhole in deep penetration fiber laser welding is analyzed through semi-analytical modeling approach. Secondly, a three dimensional finite element based conduction heat transfer model is developed using novel concept of egg-configuration volumetric heat source. The proposed heat source model and the proposed methodology using double-ellipsoidal heat source model aims to reduce the heat source model parameters. Noting that conduction only heat transfer model may not sufficient in a special situation. Thus, a full-fledged heat transfer and fluid flow model is used to analyze the effect of surface active elements in GTA welding process. Thirdly, the numerical process model is integrated with optimization algorithm such as Differential Evolution (DE) in an organized way so that the same can identify the uncertain model parameters using sensitivity analysis of the uncertain parameters. Finally, a

sequentially coupled thermo-mechanical model is developed to estimate the distortion of welded joint in deep penetration fiber laser welding and the same is validated with experimentally measured results.

The significant research work towards fusion welding process intensive to GTA, conduction mode and keyhole mode laser welding process are outlined by means of experiments as well as numerical simulation in Chapter 1. The analysis is focused on heat transfer using novel concept of egg-configuration heat source model, material flow in presence of surface active elements and distortion analysis for deep penetration fiber laser welding process. The key literature review on thermal and mechanical modelling of GTA and laser welding processes along with the influence of the welding atmosphere are presented in Chapter 2. The theoretical background of thermal and mechanical analysis using finite element method is presented in Chapter 3. The development of egg-configuration volumetric heat source model and implementation of the same in finite element based heat transfer model is described in this chapter. The semi-analytical modeling of keyhole geometry in fiber laser welding process is illustrated in this chapter. In Chapter 4, an experimental investigation of fiber laser welding under both controlled atmosphere of argon and open atmospheric conditions are presented in terms of weld bead profile and top surface appearance. The effect of heat source model parameters in thermo-mechanical analysis of linear GTA welding process is presented in Chapter 5. The concept of integrated modeling approach using GA based optimization technique is utilized in this effect. Chapter 5 also demonstrates the validation of the calculated results with experimentally evaluated weld dimensions and distortions for laser welding process. This chapter also shows that the presence of surface active elements such as sulphur and oxygen alter the weld pool shape and size in GTA welding process. It has been emphasized that only conduction mode heat transfer analysis is not sufficient to predict the weld pool dimension with varying percentage of surface active elements; it requires a fluid flow analysis within the weld pool. This chapter is also enriched with distortion and residual stress analysis in deep penetration fiber laser welding process. The conclusions and possible directions of future work are outlined in Chapter 6.

Keywords: fusion welding, finite element method (FEM), fiber laser, gas tungsten arc (GTA) welding, surface active elements, distortion, optimization, material flow, egg-configuration heat source, fluid flow, volumetric heat source, heat transfer

CONTENTS

List of Figures

List of Tables

Nomenclature

Symbol	Description	Unit
a_f, a_r, b, c	Semi-axes length of double ellipsoidal heat source model	mm
a_j	The activity of element 'j'	-
A	Constant	-
B	The magnetic flux induced in the work piece due to arc current	-
C_1, C_2, C_3	Concentration coefficients	-
C_p	Specific heat	J kg^{-1} K^{-1}
[C]	Specific heat capacity matrix	-
$[\bar{C}]$	Velocity dependent convective transport	-
$[c^{\theta}]$	Specific heat matrix at time t+θΔt	-
$[D^e]$	Depict the elasticity matrix	-
Δd_n	Minimum distance between nodes	mm
E	Young's modulus	Pa
E_T	Local slope between stress and plastic strain of specified material.	-
E_w	The non-dimensional predictable errors	-
f_r, f_f	Fraction of heat deposited in rear and front parts of double ellipsoidal heat source model	-
F_{em}^x, F_{em}^y and F_{em}^z	The components of electromagnetic forces respectively in the x-, y- and z- directions	J/C
$\mathbf{F}'$	Electromagnetic body force	J/C
F	The body force vector per unit volume	N m^{-3}
f_L	Volume fraction of liquid metal along the weld pool top surface	-
g	Acceleration due to gravity	m s^{-2}
G	Shear modulus	Pa

Symbol	Description	Unit
h	Convection heat transfer coefficient	$W\ m^{-2}\ K^{-1}$
h_{eff}	Lumped heat transfer coefficient	$W\ m^{-2}\ K^{-1}$
ΔH_j	Heat of evaporation of element 'j'	-
I	Welding current	A
I	Identity matrix	-
I_{na}	Locally absorbed beam energy	J
I_{nc}	Radial heat flux conducted into the keyhole wall	$W\ m^{-2}$
I_{nv}	Evaporative heat flux on the keyhole wall	$W\ m^{-2}$
I_o	Local incident beam intensity	$W\ m^{-2}$
J	The current density due to arc current.	A
J_j	Evaporation flux of element 'j'	-
k	Thermal conductivity	$W\ m^{-1}\ K^{-1}$
k_n	Thermal conductivity normal to the surface	$W\ m^{-1}\ K^{-1}$
$K_o(zr)$	The solution of second kind and zero-order modified Bessel function	-
[K]	Thermal conductivity matrix	-
$[K^{\theta}]$	Thermal conductivity matrix at time $t+\theta\Delta t$	-
$[\bar{K}]$	The modified form of conductivity and specific heat capacity matrix at current time step	-
$[\hat{K}]$	Penalty matrix	-
k^*	Non-dimensional thermal conductivity	-
L	Latent heat of fusion	$J\ kg^{-1}$
l	Average path of the laser beam in plasma before it reaches the keyhole wall	-
m	A constant, intuitively decide the shape of egg	-
M_j	Molecular weight of element 'j'	$G\ mol^{-1}$
[M]	Mass matrix	-
N_{HI}	Non-dimensional heat input index	-

Symbol	Description	Unit
N_r, N_f	Fraction of heat deposited in rear and front parts of egg-configuration heat source model	-
N_i	Shape functions of i^{th} node	-
O(f)	Objective function of 'f'	-
P	Laser power	W
P''	Power per unit depth	W m^{-1}
Pe	Peclet number	-
P_j^o	Equilibrium vapor pressure of element 'j' over pure liquid at the boiling point (T_b)	Pa
P_{Fe}^o, P_{Mn}^o, P_{Cr}^o, P_{Ni}^o	Equilibrium vapor pressures of the Fe, Mn, Cr, Ni	Pa
P	Pressure	Pa
Q	Heat input	W
Q_{LB}	Actual heat input	W
$\dot{Q}$	Volumetric heat source	W m^{-3}
q	Heat flux on to the surface	W m^{-2}
q_f	Power density distribution for front	W m^{-3}
q_r	Power density distribution for rear	W m^{-3}
q_s	Surface heat flux	J m^{-2}
q_v	Heat intensity in conical heat source model	W m^{-3}
$Q_{max.}$	Maximum value of the heat intensity	W m^{-3}
$\{\overline{Q}\}$	The modified form of load vector at current time step	-
r	The radial coordinate	-
r_e and r_i	The top and bottom radii	m
r_{eff}:	Effective radius of laser beam/arc	m
r_o	Distribution coefficient	-
R_s	Overall reliability	-
{Q}	Heat flow vector	-
{R}	Residual vector for all nodes	-
T	Temperature	K

Symbol	Description	Unit
t	Time variable	s
Δt	Time increment	s
Δt_c	Critical time step	-
T_b	Boiling point temperature	K
T_L	Liquidus temperature	K
T_m	Melting point of the material	K
T_O	Ambient temperature	K
T_S	Solidus Temperature	K
$\dot{T}$	First order temperature derivative with respect to time	-
{T}	Temperature vector	-
$\frac{dT}{dy}$	Average temperature gradient	K m^{-1}
V	Welding voltage	V
v	Welding velocity	m s^{-1}
u, v and w	Displacements in x, y, z directions respectively	m
U_s	Characteristic surface velocity	m s^{-1}
W_{ij}^c	Computed values of weld width (j=1) and the penetration (j=2)	mm
W_{ij}^e	Measured values at the same welding conditions (i^{th}) in a series of 'm' number of total sample welds	mm
z_e and z_i	The top and bottom surface z-coordinates	-
(x, y, z)	Cartesian coordinate system	-
r, z	Cylindrical coordinates in radial and axial direction	-
(x, ζ, z)	Moving coordinate system	-
CR	Cooling rate	K s^{-1}
θ	Average angle between keyhole wall and initial incident beam axis	degree
$\nabla = \{\frac{\partial}{\partial x} \ \frac{\partial}{\partial y} \ \frac{\partial}{\partial z}\}^T$	Gradient operator	-
Greek		
ŋ	Absorption coefficient	-

Symbol	Description	Unit
ε	Emissivity	-
δ_v	Boundary layer thickness	mm
$\{d\epsilon\}$	Total strain	-
$\{d\varepsilon^p\}$,$\{d\epsilon^t\}$ and $\{d\epsilon^e\}$	The incremental plastic strain, incremental thermal strain and incremental elastic strain	-
ε_x, ε_y and ε_z	Normal strains in x, y and z directions respectively	-
μ	Poisson's ratio	-
μ_m	Magnetic permeability	N A-2
σ	Stefan-Boltzmann constant	ND
$\sigma_1, \sigma_2, \sigma_3$	Principal stresses	N m^{-2}
σ_{av}	The average one dimensional stress	N m^{-2}
ρ	Density	Kg m^{-3}
β	Inverse Bremsstrahlung absorption coefficient of plasma	-
λ	Penalty parameter	-
χ	design variable	-
χ^L and χ^U	The lower and upper bounds of design variable	-
γ	Surface tension coefficient (N/m)	N m^{-1}
γ_{xy}, γ_{yz} and γ_{zx}	Shear strains in xy, yz and zx planes respectively.	-
τ	Shear stress	N m^{-2}
$\frac{d\gamma}{dT}$	Temperature coefficient of surface tension (N/m K)	N m^{-1} K^{-1}

Chapter - 1

Introduction

1.0 General Background

In fusion welding, two separate pieces of metals or non-metals are fused together to form a continuous metallic bond. The fusion welding processes are extensively used in an industry for joining of wide range of engineering materials from smaller to larger dimensional components [1, 2]. This has been the foremost driving factor for increasing research efforts in fusion welding processes. Moreover, laser welding and gas tungsten arc (GTA) welding with activating flux offer the deep penetration weld joint with high depth-to-width ratio. These types of welding processes are suitable to achieve successful joint for thick plates in a single pass. Furthermore, in high power density fiber laser welding, the focused beam leads to formation of a keyhole due to capillary action in the melt. The keyhole facilitates the beam to enter deep into the work piece and significantly increases depth of penetration with no considerable enlargement of bead width [3-6].

In a typical fusion welding process of metals and alloys, a heat source is applied locally to the interfaces of the materials to be joined so that they will be bridged by the molten liquid metal and be joined together as a weld after the solidification of liquid metal. The interaction between the base material and the welding heat source leads to a series of physical and chemical processes, such as rapid heating, melting and vigorous circulation of the molten metal driven by buoyancy, surface tension, impingement or friction, and, when electric current is used, electromagnetic forces [1, 7-10]. The result of the interaction between heat source and base material culminate the mechanical properties of the final weld joint, composition and geometry. Moreover, the resulting heat transfer and fluid flow affect the cooling rate, the size and shape of the weld pool, and the kinetics and extent of various solid-state transformations in the fusion zone and heat-affected zone [1, 7-10]. The weld geometry is influenced by the dendrite and grain growth selection processes. Both the partitioning of nitrogen, oxygen, and hydrogen between the weld pool and its surroundings, and the vaporization of alloying elements from the weld-pool surface significantly influence the composition, the resulting microstructure and properties of the weld joint [1, 7-10].

Due to highly localized transient heat input, the welding object causes thermal expansions and contractions which vary with time and location. The stresses that appear in hot regions near the weld are restrained by cooler regions further away. As a resulting effect, the plastic deformation occurs and leads to residual stresses and distortions in weld joint even after reaching to ambient temperature. Thus, the performance of the welding process in fabrication or repair introduces residual stresses and weld induced distortions in the structure. Welding distortion jeopardizes the shape and dimensional tolerance of the joint whereas residual stress reduces fatigue strength, corrosion resistance and stability limit [11-13]. Therefore, an accurate knowledge of the magnitude and distribution of residual stress and distortion is useful when assessing the fitness of the weldment in the industry. Since the composition, geometry, structure and properties of the welded joints are affected by the aforementioned physical and chemical processes, an understanding these constituent processes has been an important goal in the contemporary welding research. Hence, the primary goal and major thrust in the present work is the understanding of physical phenomena in fusion welding processes through the scientific principles and employment of the same to improve a reliable process model that can help in welding process design.

Accurate information of the resulting temperature distribution in fusion zone (FZ), heat affected zone (HAZ), and fluid flow field in FZ are prerequisites for the estimation of

weld thermal cycle, weld bead dimensions, and welding induced distortion and residual stress field. Precise experimental measurement of the temperature distribution and the velocity field in weld pool is proved to be extremely difficult or even impossible because of the complexity of the process, the small size of welds, the extreme peak temperature and temperature gradients in weld pool, and the difficulty of repeating welding conditions [14-23]. However, the temperature measurements in the solid regions which, usually involve the placement of thermocouples, are cumbersome and expensive [24-27]. Alternatively, the temperature field in fusion welding process is estimated either by solving heat conduction equation [24, 28-44] or through transport phenomena based heat transfer and fluid flow analysis [45-56]. This approach needs the mathematical structure of the heat source model, should at least approximately represent the phenomena of real heat source. The key issues to define a decent volumetric heat source are the geometric shape and size, non-symmetric heat density distribution due to moving arc or laser beam.

In the present work, the egg-configuration volumetric heat source model is proposed to address these issues. The proposed heat source model which is derived from ellipsoid shape provides the non-symmetry heat energy distribution with less number of model parameters and conserves the continuity in profile during moving heat source problem. The general equation of egg-configuration heat source provides the basis of Gaussian distributed disc, hemispherical, and semi-ellipsoidal volumetric heat source models which can be considered as the special cases of proposed heat source model. In fusion welding process, only the surface heat flux fails to realize enhanced heat transfer due to predominant effect of momentum transport of the material within molten pool. The convection in the weld pool can be substituted by apparent volumetric heat source which is unrealistic to define outside the molten pool volume. Moreover, to realize the actual dynamics of the weld pool, the transport phenomena based heat transfer and fluid flow analysis is essential. As a part of this research work, the suitability and possible areas of applications of process models based on conduction heat transfer alone and the transport phenomena based weld pool models are investigated. Furthermore, a coupled thermo-mechanical analysis is performed to estimate the welding induced distortion and residual stress.

It is anticipated fact that the conduction mode laser welding is different from keyhole mode fiber laser welding by the process of vapour-plasma welding plume formation and the absorption of laser radiation by this plume [57]. With a wavelength of 1.064 micrometers, fiber laser produces an extremely small focal diameter; as a result their intensity is up to 100

times higher than that of CO_2 lasers with the same emitted average power [58]. Hence the fiber laser produces deep penetration by forming a keyhole that entrains the energy over the depth without appreciable enlargement of weld width. A theoretical investigation is carried out to estimate the keyhole profile of deep penetration fiber laser welding by tracking the liquid/vapour interface over time considering the effect of interfacial phenomena like evaporation, homogeneous boiling, and multiple reflections within keyhole wall.

The welding process model requires several model parameters. Some of these parameters can easily be specified with a reasonable degree of certainty. In contrast, some process parameters such as arc efficiency, arc radius, the effective thermal conductivity and the effective viscosity of the liquid metal in weld pool cannot be specified accurately beforehand. Most of these variables depend on the actual welding conditions and hence their values cannot be ascertained with confidence except for certain narrow window of welding conditions [50, 53-55, 59-62]. The identification of uncertain model parameters from a few set of experimental results to predict the weld dimensions for a wide range of process conditions illustrates the specific direction of integrated model. However, it is comprehended that the optimization algorithm, although an important tool for the construction and organization of the integrated modeling approach, is the actual strength that lie in the quality, totality and robustness of the numerical process model. Two stochastic optimization modules such as parent centric recombination (PCX) operated generalized generation gap (G3) model [63-65] and differential evolution (DE) [66-68] are interfaced with numerical model to identify the unknown and uncertain process model parameters.

The justification of calculated results from the integrated phenomenological model for wide range process variables during GTA and laser welding processes is an important issue to endorse the level of efforts towards the improvement of such intricate mathematical model of increasing complexity. An experimental work is performed for both GTA and laser welding processes at varying process variables on stainless steel plates of two different thicknesses. The experimentally measured weld bead dimensions and welding induced angular distortions are employed next to validate the corresponding computed results. Moreover, the fiber laser experiments are undertaken at two different ambient atmospheres with similar process variable to examine the influence of welding ambient atmosphere. Furthermore, the GTA welding experiments are performed using a thin layer of three kinds oxide fluxes SiO_2, TiO_2, Al_2O_3 and mixture of them to investigate the effect of surface active elements.

In summary, the development of new egg-configuration volumetric heat source in conduction mode heat transfer analysis for numerical simulation of fusion welding process is the major thrust of present work. The identification of unknown parameters in double-ellipsoidal heat source model shows promising direction of research work. Thereafter, an experimental effort to investigate the influence of ambient atmosphere in fiber laser welding process and the formation of keyhole by mathematical model is conceived as a novel contribution of the present work. The effect of surface active elements in GTA welding process and analysis of the same using a thermo-fluid model towards the development of deep penetration welding process is also envisage as a major contribution of present work. The subsequent attempt to identify the uncertain model parameters using inverse approach shows promising direction of integrated process model. It is also realized that distortion of deep penetration laser welding using sequentially coupled thermo-mechanical analysis enhances the scope of utilizing the process model for practicing engineers in actual industrial problems.

1.1 Research Objectives

The overall objective of the present work is the quantitative understanding of deep penetration laser and GTA welding process based on fundamental theory and integration of these phenomenological facts to develop more application oriented process modeling approach. In this effect, the thermo-fluid and thermo-mechanical analyses are performed for fiber laser and GTA welding processes using activated flux. Also, the influence of welding atmosphere in fiber laser welding of stainless steel is secondary objective of present work. To achieve research objectives, following modules are accomplished either simultaneously or sequentially which are developed over the whole duration of research work.

- Development of a conduction heat transfer model based on finite element method using temperature dependent material properties, latent heat of fusion and solidification and Gaussian distributed volumetric heat source to compute temperature distribution. Using this model, the author has investigated the influence of front and rare part ratio of double ellipsoidal heat source model as a function of welding velocity. In effect, this approach reduces the *a-priori* definition of heat source parameters.
- Development of a new heat source model i.e. egg-configuration volumetric heat source model for conduction mode linear welding process to reduce the pre-defined model

parameters of a distributed heat source. The egg-shape heat source model is presented in more generalized form that aids to extract other heat source models.

- Estimation of the keyhole profile for deep penetration fiber laser welding process from a semi-analytical mathematical model which is based on point-by-point energy balance on the keyhole wall.
- Investigation on the effect of surface active elements in linear GTA welding process using transport phenomena based heat transfer and fluid flow model.
- Integration of numerical process model with optimization module to identify the unknown model parameters that are essential for modeling calculations and are not easily available from experiments.
- Development of sequentially coupled thermo-mechanical numerical process model using finite element method to compute the residual stresses and weld induced distortions. The material response is assumed as thermo-elasto-plastic along with temperature dependent physical properties.
- Experimental investigation of fiber laser welding under two different ambient atmospheres. The influence of welding atmosphere on weld bead shape and size, joint surface quality and welding induced distortions are investigated for austenitic stainless steel.
- Influence of surface active elements during autogenous GTA welding of austenitic stainless steel. The experiments are conducted using a thin layer of oxide fluxes for probable formation of deep penetration GTA welding. The microstructure of welded zone and heat affected zone of austenitic stainless steel is also analyzed by metallography.
- Validation of numerical model results of weld pool dimensions and distortions with the experimentally measured results for deep penetration fiber laser and GTA welding processes.

1.2 Layout of Thesis

The thesis is organized into six chapters to elaborate all the aspects that are aimed at research objectives. In **Chapter-1**, a brief introduction and general background of research work are presented. The objectives of research work, brief methodology and layout of the thesis are also described in this chapter.

Chapter-2 presents a critical literature review on existing work of fusion welding process in five significant directions. Firstly, the basic experimental effort on fusion welding process is described. The experimental work on the influence of fusion welding process variables and welding ambient atmosphere are presented. Furthermore, the influence of different oxide fluxes during GTA welding is described. Next, the significant effort on transport phenomena based heat transfer and fluid flow analysis in fusion welding process are described. The influence of temperature dependent material properties, computational issues in numerical and analytical models are critically reviewed. Subsequently, the literature on numerical modeling of welding induced distortions and welding residual stresses are presented. The formation of keyhole in laser welding and the modeling approach of keyhole profile are illustrated. The heat source model is more important for accurate prediction of welding thermal cycles and hence the prediction of welding induced distortions and residual stresses. A noteworthy effort on the development of various heat source models and their advantages and limitations are described. Lastly, the efforts on application of different optimization algorithms for prediction of uncertain model parameters are presented.

In **Chapter-3**, the mathematical background for the development of conduction heat transfer, fluid flow and stress analyses are described. The symmetric nature of solution domain and the heat source is taken into consideration. Once the weld bead shapes and dimensions are realized from experimental investigation, the Gaussian distributed volumetric heat source models such as double ellipsoidal and conical heat source models are applied to account for enhanced heat transfer in the growing melt pool. A comprehensive description of egg-configuration volumetric heat source model in the frame conduction mode heat transfer is illustrated. Next, the theoretical background of thermo-mechanical analysis for predicting the welding induced distortions and residual stresses by considering the material behavior as elastoplastic is presented. The plasticity is assumed as rate independent and is modeled by assuming bi-linear isotropic hardening behavior along with associated flow rule. Finally, the mathematical background to estimate the keyhole profile for deep penetration fiber laser welding is described. Chapter-3 furthermore illustrates the theoretical basis for the optimization algorithms that are used to identify suitable values of unknown or uncertain model parameters for an integrated modeling approach. The algorithm of optimization process such as parent-centric recombination operated generalized generation gap (PCX-G3) and Differential evolution (DE) are illustrated here. The integrated modeling approach where the optimization algorithm is used to drive the numerical model for identifying the uncertain

model variables such as arc efficiency, effective arc radius, and effective values of material properties at high temperature shows a promising direction of research work.

Chapter-4 presents the detailed experimental methodology performed on fiber laser welding and gas tungsten arc (GTA) welding processes. The fiber laser welding was performed in two different welding ambient atmospheres i.e. open atmosphere and self-protective atmosphere of argon with similar processing variables to estimate the characteristic difference between them. The GTA welding was performed using a thin layer of three kinds oxide fluxes SiO_2, TiO_2, Al_2O_3 and mixture of them to investigate the effect of activated flux in GTA welding process. The metallographic analysis, weld pool dimensions, weld induced distortions and the characteristic difference between the open and self-protective atmosphere of argon welds are presented in this chapter.

In **Chapter-5,** the results from numerical model are validated with experimentally measured values. The influence of heat source model parameters are illustrated for double-ellipsoidal and newly developed egg-configuration heat source models in the frame of conduction mode heat transfer analysis. The egg-configuration heat source model is approximately represent the phenomena of real heat source with less number of model parameters as compared to existing heat source models in the literature. Therefore, the developed heat source model is calibrated for GTA and laser welding processes. Theoretical estimation of keyhole profile of fiber laser welding is also analyzed in this chapter. The comprehensive model which improves the reliability of heat transfer and fluid flow calculations has been developed by integrating the optimization algorithm. The optimization modules estimated the uncertain model parameters from a limited volume of experimental data. The influence of surface active elements on stainless steel is illustrated in this chapter using the transport phenomenon based 3D heat transfer and fluid flow model. Furthermore, this chapter presents the esteemed results of distortion and residual stress in fiber laser welding from thermo-elasto-plastic model based on finite element method.

The conclusions of present research work are described in **Chapter 6**. The present work is a contribution towards the growing quantitative knowledge-base in GTA and laser welding processes and most intricate phenomena in welding science called ‘heat source model’. The recommendations for future work are also indicated in this chapter.

Chapter – 2

Literature Survey

2.0 General background

In a typical fusion welding process, the application of an intense heat source melt the localized region along with the interface of two or more metallic plates. Subsequent solidification of the molten region produces the intended weld joint. Complex phenomena due to heating, melting, cooling and solidification inside the weld pool are involved in fusion welding process. If it is not controlled appropriately, these may lead to adverse effect on the properties of the weld and degrade the material properties in the heat affected zone. The weld thermal cycles and molten weld pool behavior have decisive influences on the weld quality. Therefore, an accurate analysis of the time-temperature cycles and weld pool behaviors is of critical importance for deep insight into weld metallurgy, induced residual stress, distortion of the weldment and the process control parameters.

The objective of the present work is to understand heat transfer, material flow and final distortion in fusion welded structure. To develop physics based model in deep penetration GTA and laser welding processes, the analyses of thermo-fluid and thermo-mechanical behavior are necessary. Present work is dealt with the influence of welding ambient atmosphere during fiber laser welding and influence of oxide flux coating during GTA welding process. In deep penetration laser welding, the mechanism of heat transport is different from conduction mode laser welding process. The presence of keyhole entrains the energy transport to form high penetration welding. Hence the estimation of keyhole profile from physical mechanism enhances the scope of utilization of heat transfer based numerical model. In particular, the research work pursues to quantitatively predict the thermal cycles, temperature distribution in the weldment, liquid convection in the weld pool, weld bead shape and size, keyhole profile, welding induced distortions and residual stresses. Since the subject of heat transfer, fluid flow and mechanical analysis covers a wide range of topics, it is not viable to review all the topics in this chapter. Hence, key problems and issues pertinent to the subject of this study are selected for review. The aim of this chapter is to look into certain extent the experimental investigations on GTA and laser welding processes and the issues related to numerical modeling approaches for heat transfer, fluid flow and mechanical analysis in fusion welding processes.

2.1 Laser and GTA welding processes

Laser welding is a high energy beam process that continues to expand into modern industries and new applications because of its many advantages. The laser welding produces deep penetration and high aspect ratio (depth-to-width ratio) weld, and a small heat affected zone (HAZ) that cools very rapidly and produces very small amount of distortion. The most significant difference between traditional electric arc welding and laser beam welding processes is in the mode of energy transfer. Unlike electric arc energy transfer, laser energy absorption by a material is affected by many factors like the type of the laser, the incident power density, and the base metal's surface condition. Laser beam welding with its precision, low heat effected zone and high speed has gained increasing acceptance in the industry. This joining process is well suited for high volume automated manufacturing processes.

Laser welding is a non-contact process that requires an access to the weld zone from one side of the parts being welded. The weld is formed as the intense laser light rapidly heats the material typically calculated in milliseconds. The flexibility of the laser offers mainly two

types of welds: conduction mode and keyhole mode. Figure 2.1 describes the conduction, conduction/penetration and keyhole mode laser welds. The main difference between these two modes of laser welding process is that the surface of the weld pool remains unbroken during conduction mode laser welding and opens up to allow the laser beam to enter the melt pool in keyhole mode welding. The transition from the conduction mode to keyhole mode depends on the peak laser intensity. Normally if the laser intensity is greater than 10^6 W.cm^{-2} keyhole forms in laser welding. When the laser intensity is less than 10^6 W.cm^{-2}, it is called conduction mode laser welding process [69]. Typical input-response model of laser welding process is represented schematically by Fig. 2.1.

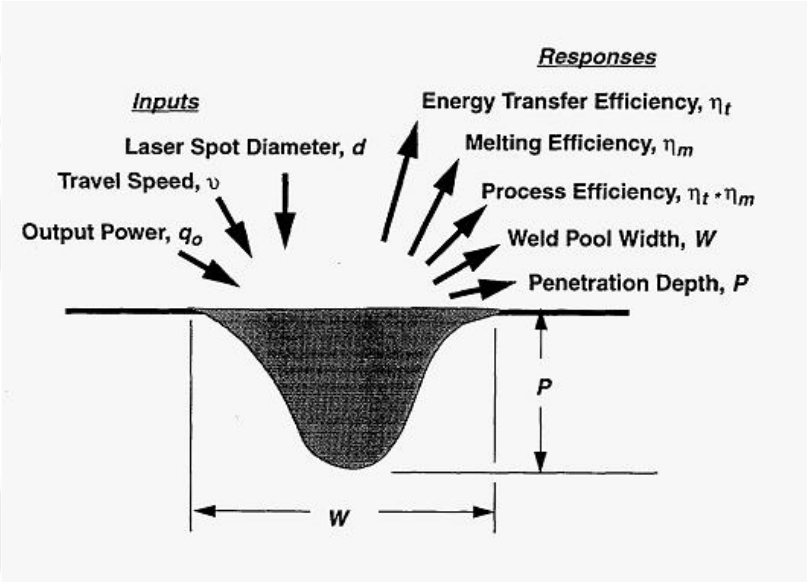

Figure 2.1: Schematic representation of typical input-response model for laser welding process [70].

There are several laser sources used for welding purpose. Each type of laser has its own advantages and disadvantages and is suited for various applications. CO_2 laser is gas laser that is based on a carbon dioxide gas mixture with a wavelength of 10.6 micrometers [71, 72]. Fiber laser belongs to the solid state laser group. They generate a laser beam which is amplified in specially designed glass fiber. With a wavelength of 1.064 micrometers, fiber laser produces an extremely small focal diameter and the intensity is up to 100 times higher than that of CO_2 laser [58, 73, 74]. There are significant differences between Fiber laser and Nd:YAG laser (lamp-pumped and diode-pumped) although both operate at approximately similar wavelength. Ytterbium Fiber laser uses a telecommunications grade diode to pump an optical fiber. It has superior beam quality, stability and higher electrical wall plug energy efficiency. Fiber laser is virtually maintenance free, extremely compact and the technology

makes it invulnerable to the common misalignment and adjustment problems inherent with YAG lasers [58, 73, 74]. Since Nd:YAG laser operates on a wavelength almost ten times less than CO_2 laser, the absorption coefficient for most of the steels is essentially higher for the Nd:YAG laser due to shorter wavelength. Excimer gas laser operates in the UV region which produce short pulses (tens of nanoseconds duration) and very high peak powers. Diode laser operates on a wavelength in the near infra-red region of the spectrum which is an advantage as compared to CO_2 or Nd:YAG lasers [14, 16, 17, 19, 21, 22, 73, 74].

GTA welding uses a permanent, non-consumable tungsten electrode to create an arc to the work piece. To prevent electrode degradation, it is shielded by an inert gas. The GTA welding process can be done with or without filler material. Figure 2.2 illustrates the typical GTA welding process. When thin sheets are welded to close tolerances, filler metal is usually not added. When a filler metal is used, it is deposited to the weld pool from a separate rod or wire. The term TIG welding (tungsten inert gas welding) is often applied to this process. GTA welding is applicable to nearly all metals in a wide range of stock thickness. It can also be used for joining various combinations of dissimilar metals. The GTA welding process can be operated in various current modes such as direct current (DC) with electrode negative (EN) or positive (EP) and alternating current (AC). These different current modes result in various arc and hence different weldment characteristics.

2.1.1 Experimental investigation

Several researchers have investigated different aspects of the fusion welding processes by experiments. The influence of the welding process variables such as welding current and voltage; laser power and welding speed have been studied by researchers [58, 59, 73-83]. The investigators [84-88] have studied the effect of the surface active elements in the formation of weld bead dimensions and behavior of the molten weld pool. It is evident that the type of weld pool protection and the shielding media plays an important role in the weld joint quality. Very few researchers have studied the influence of the welding ambient atmosphere [71, 89-92] on weld pool formation and the effect of different shielding media [93-106] on molten pool formation. El-Batahgy [75] has conducted a series of experiments to investigate the influence of the process variables on different types of austenitic stainless steels during a carbon dioxide laser welding process. The microstructure for all laser welds was always austenite with very less percentage of ferrite. The lower the laser power and/or the higher the welding speed lead to the finer solidification structure due to low heat input. The

presence of keyhole formation alters the weld pool characteristics in high power laser welding process. Figure 2.3 illustrates the formation of molten weld pool in conduction mode and keyhole mode laser welding processes. In-process formation of molten weld pool had captured by using high speed charge coupled device (CCD) camera. The significant literatures on the influence of welding ambient atmosphere under different shielding media and the effect of surface active elements on the formation of weld pool are described in the subsequent sections.

2.1.2 Influence of ambient atmosphere on welding

Due to high temperature gradient during fusion welding processes, there is the possibility of reactions between weld pool and surrounding atmosphere. The expected instability in most of the metals in their elemental form occurs during welding since high temperature causes them to react with oxygen and nitrogen in air. These elements may dissolve in the molten weld pool, becomes part of final weld joint, and initiate the weld defects.

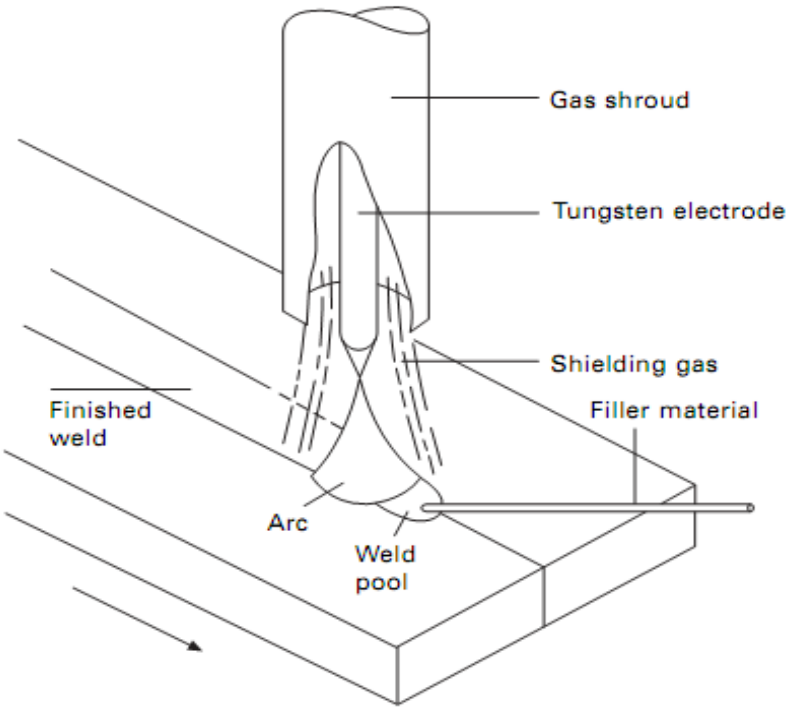

Figure 2.2: Schematic representation of gas tungsten arc welding process [69].

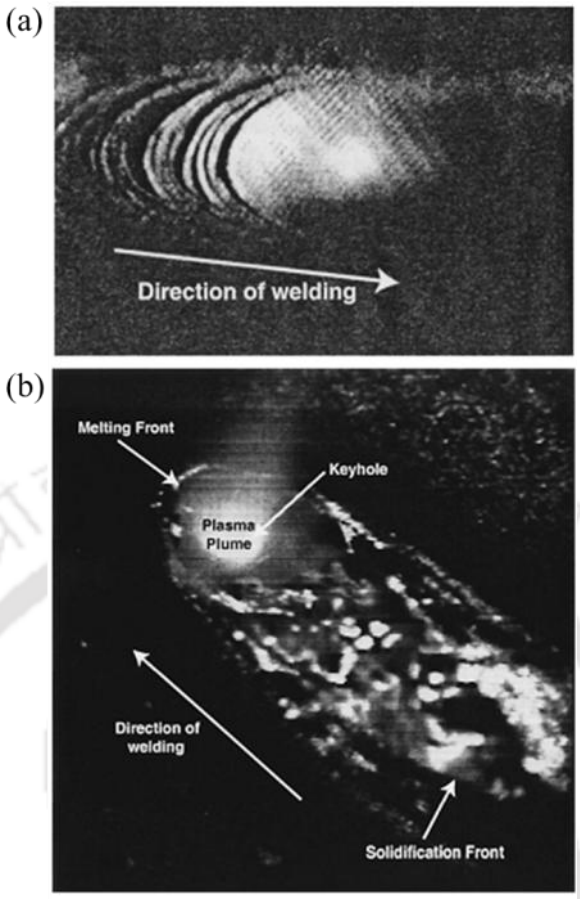

Figure 2.3: High speed charge coupled device (CCD) camera pictures of molten weld pools, (a) Conduction-mode laser welding and (b) Keyhole-mode laser welding [107].

Therefore, most of the welding techniques involve shielding usually in the form of gas or flux to eliminate the contact of air with molten weld pool. Several protection techniques such as gas, slag, gas and slag, vacuum and self-protection offer different degree of protection for molten weld pool from the surrounding atmosphere [10, 96]. Ramazan and Koray [89] studied the influence of the welding atmosphere during gas metal arc welding (GMAW) of low carbon steel. Figure 2.4 describes microstructure of both classical GMAW and controlled atmosphere GMAW weldment [89]. From this figure it can be observed that the microstructure of base metal consists of ferrite and pearlite phases. Some deformation bands were also detected in the microstructure. It is obvious that columnar grains are formed in weld metals and these grains are decorated by grain boundary allotriomorphs. In this study, the authors found that in controlled atmosphere of argon toughness of the weld metal is higher and mechanical properties of the weldment are better due to less porosity as compared to classical GMAW process.

Bayram et al. [90] have studied the effect of the welding atmosphere and heat input during resistance spot welding of 316L austenitic stainless steel. Tensile shear load bearing capacity increases when heat input increases due to the enlargement of the nugget size. The occurrence is slightly higher in nitrogen atmosphere as compared to open atmospheric condition. Dursun [91] investigated the influence of welding current and the weld atmosphere during resistance spot welding of 304L austenitic stainless steel. The author concluded that an optimum weld quality was obtained by using 9 kA peak weld current in nitrogen atmosphere. Ramirez et al. [94] investigated the influence of welding variable on solidification substructure to cause weld metal porosity. The amount of porosity increases with increase of nitrogen gas introduced in argon shielding gas atmosphere. Few researchers have also explored the influence of the alternate shielding and mixture of them on weld joint quality [71, 95, 101, 108]. Kang et al. [101] have conducted the experiments on the effect of argon, helium, mixture of argon and helium, and alternate supply of pure argon and helium alternatively during GMA welding process. Figure 2.5 demonstrates the weld macroscopic views of the cross-section corresponding to the different types of shielding gases and with various kinds of gas supply under similar welding conditions [101]. As compared to conventional supply of Ar, the case of supplying Ar + 67% He mixture by conventional method and supplying alternately Ar and He shows deeper and broader weld penetration. Moreover, this study also confirmed that under the similar welding conditions, an alternative supply of shielding gas provides lowest degree of weld induced distortion.

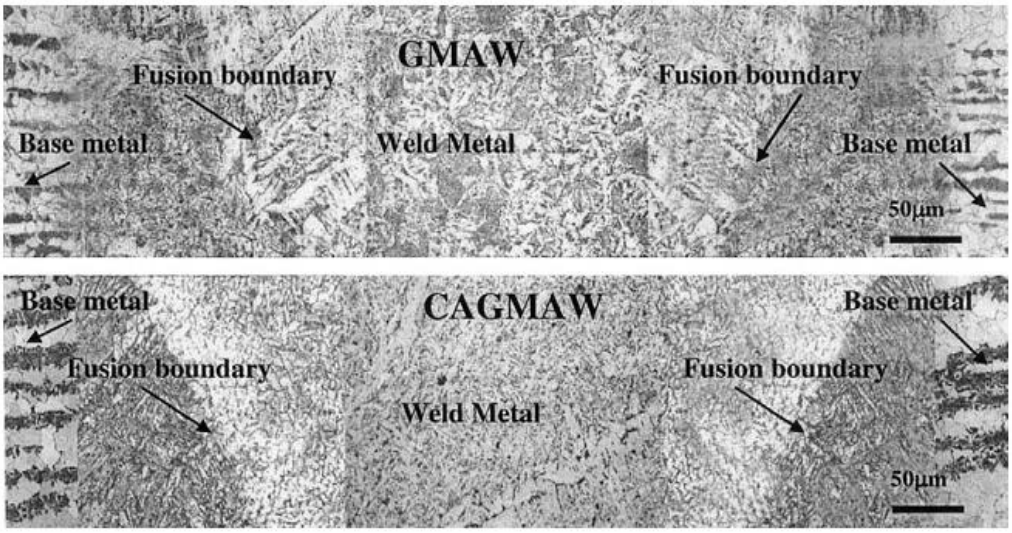

Figure 2.4: Microstructure profile of classical GMAW and controlled atmosphere GMAW weldment [89].

Dong et al. [71, 108] investigated the nitrogen absorption and desorption during CO_2 laser welding of stainless steel in controlled atmosphere of Ar-N_2 mixed gas. The nitrogen desorption in the Ar atmosphere was less than arc welding. Figure 2.6 describes the experimental weld macrographs of GTA and laser welding process at two different welding atmospheres [108]. This figure shows that no porosity has been observed in CO_2 laser weld metals in nitrogen atmosphere as compared to GTA welding at 40% Ar and 60% N_2 atmosphere. This is because of the existence of monatomic nitrogen in the arc. Ostsemin [92] investigated the temperature measurement of the electrode-metal drop during carbon dioxide controlled atmosphere of arc welding. It is thus obvious that the shielding media plays a significant role in the weld joint quality. However, the degree of protection of weld pool can be increased by avoiding poor technique of shielding gas supply. Self-protective atmosphere or controlled atmosphere of argon avoids the weld pool reaction with oxygen, nitrogen etc. during welding process. This leads to less degree of weld defects such as gas porosity.

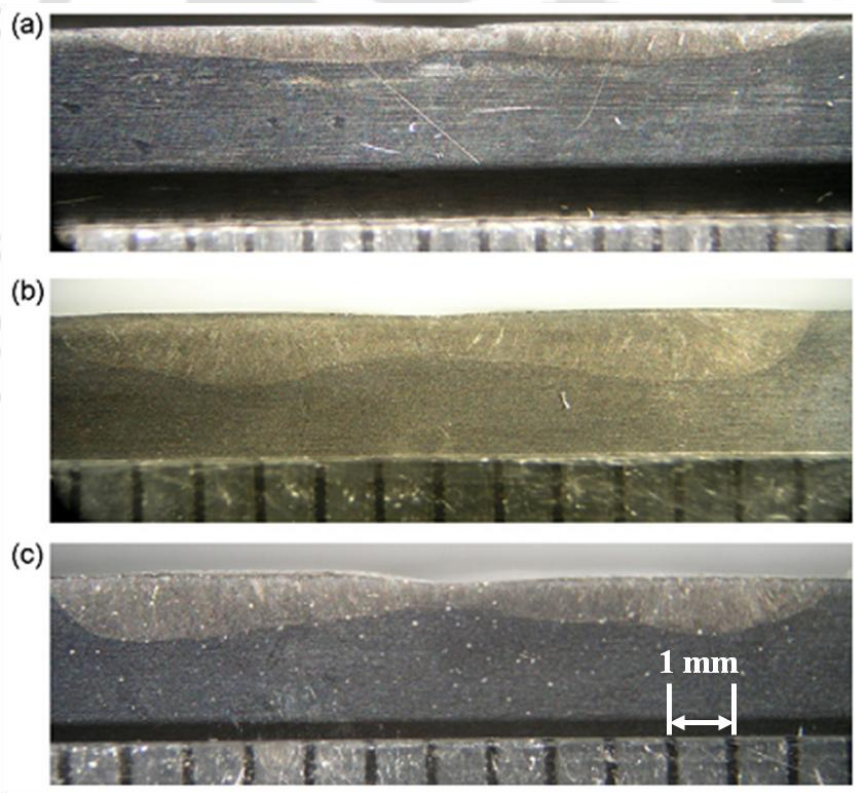

Figure 2.5: Weld macrographs variation with type of shielding gas supply and different types of gases, (a) Argon supply, (b) Ar+67% of He and (c) Alternative supply of Ar and He [101].

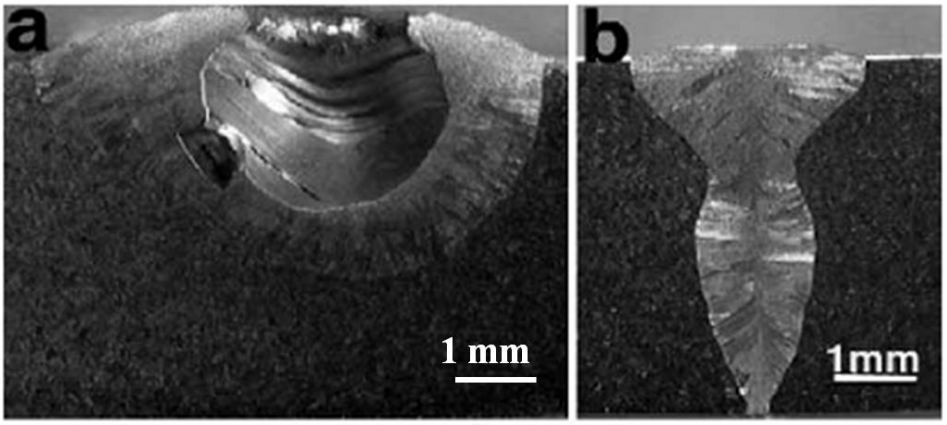

Figure 2.6: Weld bead cross section of high-Nitrogen steel (0.32 pct. N), (a) GTA welding in 40% Ar and 60% N_2 atmosphere and (b) CO_2 laser welding in pure N_2 atmosphere [108].

Gas atoms in laser beam path are ionized and formed weld plasma that consists of neutral, excited, and ionized atoms of base metal and shielding gas. Plasma plume absorbs some portion of laser beam energy and causes refraction and defocusing of laser beam [107]. The shape and size of the keyhole is affected by the presence of shielding gas due to change of surface tension of the weld pool, reaction energy by the gas with hot metal and modification in plasma-plume formation [109]. In general, Helium is most suitable shielding gas for CO_2 laser whereas Argon or Nitrogen is appropriate for Nd:YAG laser since high ionization potential of He aids to control plasma formation in CO_2 laser welding. Argon generally favours less plasma formation during welding. However, at high power laser, the shielding becomes more critical and affects significantly the weld penetration. Therefore, pure argon may be an optimal shielding gas for fiber laser welding since the wave length of fiber laser is close to Nd:YAG laser [110, 111]. Hence, present work is motivated to use argon not in the form of shielding gas rather to use this gas in a controlled chamber that is called protective atmosphere of argon. There is limited study observed in the literature on the effect of shielding gas for fiber, disk and diode lasers.

2.1.3 Influence of surface active elements

The heat and fluid flow in molten weld pool can significantly affect temperature gradients, cooling rates and solidification structure. The conventional heat transfer and fluid flow pattern in fusion welding control the shape of weld pool and depth of penetration. Often, the critical variable that controls the molten pool variation is the amount of surface active elements present in the weld material. The presence of main minor elements of group VIIB

(oxygen, sulfur, selenium and bismuth) may change the weld pool shape and size during gas tungsten arc (GTA) welding. The effect of minor elements on weld pool formation is generally experimented by three different variants of GTA welding processes [93, 97, 112-113]. One of the methods is analyzing or varying the chemical components of work piece materials. Other promising practices are smearing the oxides and halides on work piece surface or using active elements through addition with shielding gas. The weld pool shape and size changes significantly by adding these active elements to the material and this can be used in a beneficial way to get high penetration welding. In 1980s, Heiple et al. [93, 114-117] was first examined systematically the influence of surface active in the formation of weld pool. Their study showed that the presence of active elements such as Se, O and S in the weld pool altered the surface tension coefficient from negative to positive. Therefore, the direction of Maragoni convection reverses from outward to inward and as a result the weld penetration increases intensely.

Pitscheneder et al. [86] studied the role of sulfur and influence of process variables on the temporal evolution of weld pool geometry during multi-kilowatt laser beam welding of steels. Though the presence of sulfur can improve weld penetration in many cases, its presence in the weld metal does not always result in high aspect ratio. Figure 2.7 shows the surface tension and temperature coefficient of surface tension as a function of temperature and activity of sulfur for the steel samples containing 20, 40 and 150 ppm sulfur [86]. This figure shows that the surface tension of the alloy and temperature coefficient of surface tension are strong function of temperature and the sulfur activity.

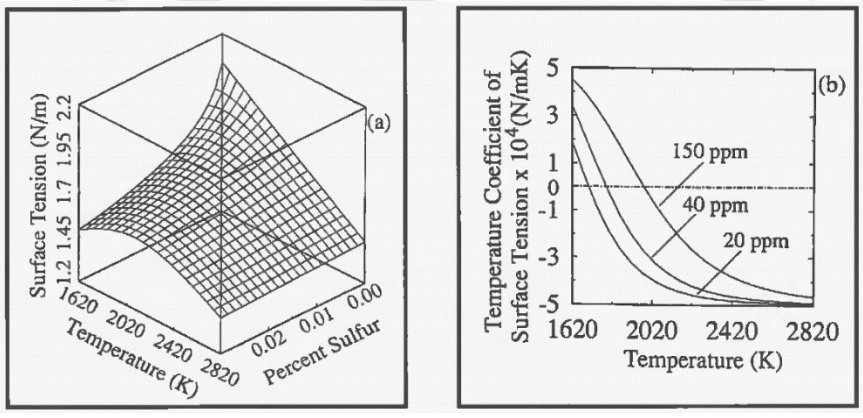

Figure 2.7: Variation of surface tension of (a) FE-S as a function of sulfur activity and temperature and (b) temperature coefficient of surface tension of Fe-S as a function of temperature for samples containing 20, 40 and 150 ppm sulfur [86].

Lu et al. [99] studied the weld pool formation at different welding speeds and welding currents under the Ar-0.1%CO_2 and Ar-0.3%CO_2 shielding gases. Figure 2.8 describes the weld bead shapes at different welding speeds and welding currents [99]. All the weld bead shapes under the Ar-0.1%CO_2 are wide and shallow whereas the weld shapes are narrow and deep under the Ar-0.3%CO_2 since the convection pattern in molten weld pool are different under Ar-0.1%CO_2 and the Ar-0.3%CO_2 shielding gases.

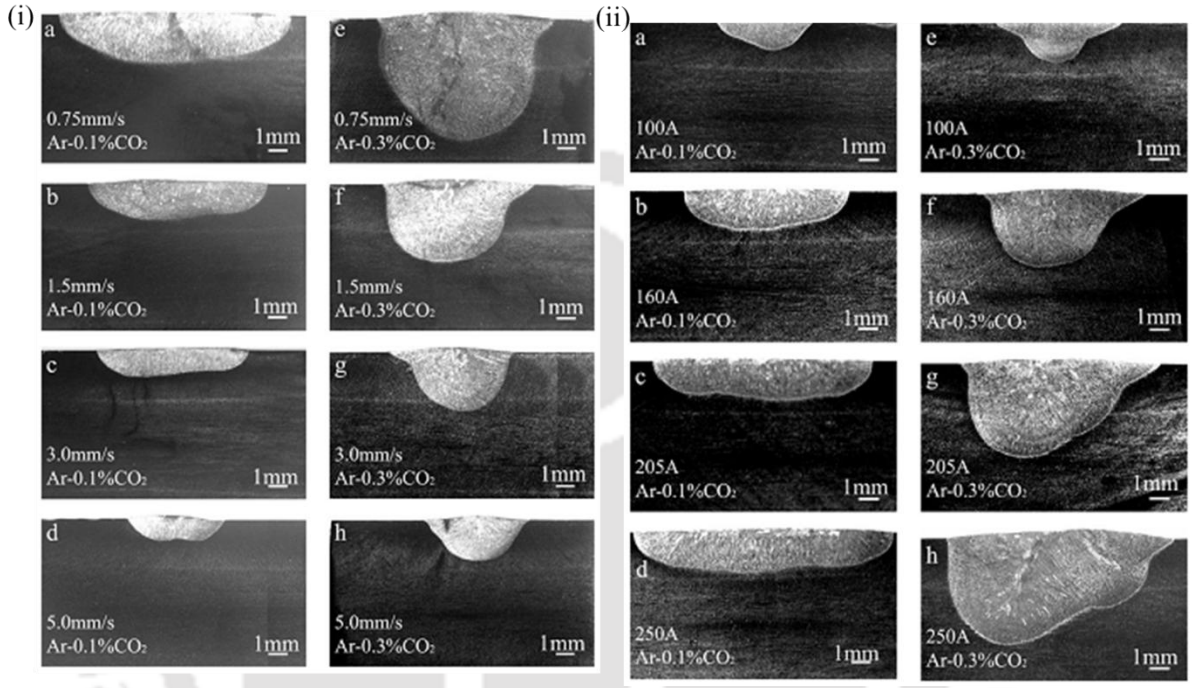

Figure 2.8: Weld bead shapes under Ar-0.1%CO_2 and Ar-0.3%CO_2, at different (i) welding speeds and (ii) welding currents [99].

Zhao et al. [118] studied the influence of surface active element (sulfur) on flow pattern in molten pool using a numerical model. Figure 2.9 illustrates the variation of aspect ratio (D/W) with sulfur concentration and maximum surface tension temperature at different sulfur concentrations. It is obvious from this figure that initially the aspect ratio increases sharply and then remains nearly constant. It is also observed from this Fig. 2.9 (b) that as sulfur concentration increases, the maximum surface tension temperature increases. The maximum surface temperature in the weld increases with sulfur content reaches to a maximum value and decreases thereafter.

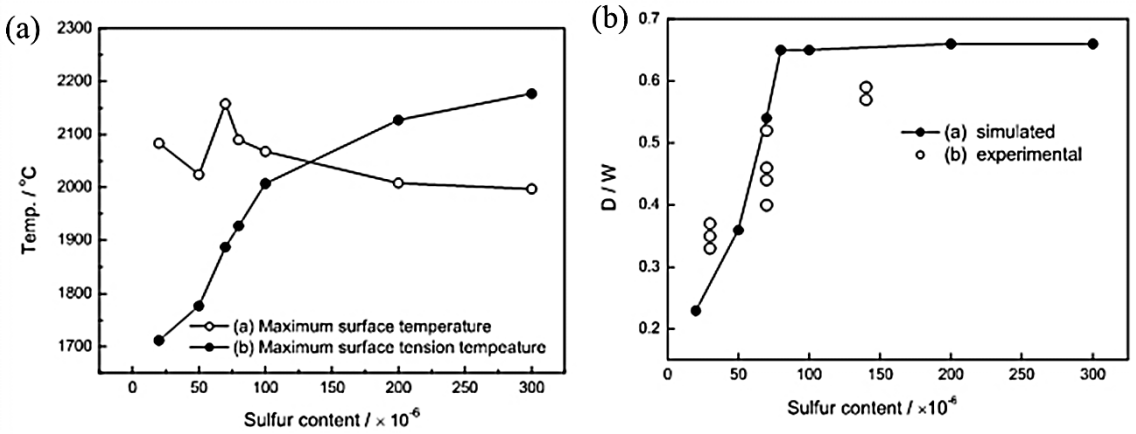

Figure 2.9: (a) Temperature variation with sulfur content in weld metal and (b) influence of sulfur content on aspect ratio (D/W) [118].

In weld pool modeling of the fusion welding process, the fluid flow analysis is significant along with the conductive heat transfer analysis when material contains surface active elements [86, 87, 119]. Sahoo et al. [85] investigated the influence of the surface active elements such as oxygen and sulfur in blocking vaporization sites on weld pool surface. The presence of oxygen and sulfur in metal leads to increase in metal vaporization rate. This phenomenological analysis is not possible within the frame of only heat conduction analysis and without consideration of flow dynamics of molten material. Experimental evidence of the effects of surface active elements is obvious and this analysis is significant to design the process parameters for high penetration GTA welding process [99, 120].

In recent time, the numerical simulation of the fluid flow and heat transfer analysis using different shielding gases were studied by several researchers [102-104, 121-124] by interacting welding arc model to the work piece surface. This approach essentially eliminates the need of heat source model since the temperature distribution of arc can be used to estimate heat flux on work piece surface. The arc model might be adjustable with different shielding gas environment, welding current, and electrode gap. However, the interface between anode and arc column is most important issue to calculate the heat flux [104]. The sensitivity of arc model to the change of volume percentage of mixed shielding gas is still unclear. Moreover, the interaction of the arc with deformable work piece geometry is another important issue in terms of reliable modelling approach and hence a free surface modeling of work piece surface under the pressure of arc plasma is necessary. There is a lack of enough research in this direction. Alternatively, a straight-forward surface heat flux following Gaussian distribution may act as representation of heat source without much error in calculations [37, 39, 42, 125-

126]. The effective radius of arc is defined by the actual radius on the work-piece surface assuming 95 % of heat flux falls within the effective radius.

It is thus obvious from literature review that a dedicated surface tension model is necessary to take into account the effect of surface active elements for the analysis of flow dynamics. Lu et al. [121] and Dong et al. [103, 124] were studied the effect of surface active element such as oxygen through the development of sophisticate finite volume based numerical model using FLUENT software. The model considers constant material properties and the solution domain for fluid flow is considered as whole geometry. It is expected that the viscosity is kept very high outside the flow domain to satisfy near solid medium. The effect of surface active elements has been incorporated in this model through a surface tension model [84] that is a function of solute concentration (i.e. oxygen here) and temperature. However, the coefficient of surface tension may go through an inflection point somewhere on the surface if the weld pool contains fairly high oxygen concentration. In this situation, the fluid flow in weld pool is likely to have more complicated shape as compared to simple recirculation [84].

2.1.4 Keyhole formation in laser welding

In high power density welding processes such as laser and electron beam welding, the focused beam leads to formation of a keyhole due to capillary action in the melt. The keyhole facilitates the beam to enter deep into the work piece and significantly increases the depth of penetration with no considerable enlargement of bead width [127]. Hence the keyhole formation influences the weld joint quality in a high power density laser welding to extent the limit of scanning speed of laser source. The formation of keyhole involves several simultaneous physical processes and brings the complexity in physics based numerical model. A number of previous works has been performed to understand the physical process involved in the formation of keyhole [3-6, 128-131]. Some of the significant literatures are presented in this section.

Andrews [3] derived the keyhole profile by considering the whole of the laser energy is used in vaporization of the metal. Kross et al. [4] developed a keyhole model in which non-equilibrium evaporation from the keyhole surface is considered. Kaplan [5] has estimated the keyhole profile using a point-by-point determination of the energy balance at the keyhole wall. DebRoy and his co-workers analytically estimated the keyhole profile of different

materials during laser welding process [6, 128]. Zhao and DebRoy estimated the keyhole profile of laser weldment of aluminium alloy 5182 [6]. From this work it is observed that the beam axis intersects the front keyhole wall and the front keyhole wall has a larger angle with the beam axis than the rear keyhole wall. Due to the temperature gradient difference near the rear and front walls the keyhole shapes becomes asymmetry with respect to beam axis. Figure 2.10 describes a typical estimated keyhole profile and three-dimensional temperature field for high power laser welding process [6]. Cheng et al. [110] considered both the effect of Fresnel absorption and inverse bremsstrahlung absorption of plasma on the laser power distribution. Laser intensity absorbed on the keyhole wall through Fresnel absorption is hardly uniform and distributes mainly on the front wall and the bottom of keyhole wall. Inverse bremsstrahlung absorption of keyhole plasma plays a dominant role in absorbing laser power compared with Fresnel absorption. Jin et al. [129-130] have measured the actual keyhole size using a high speed camera. Eriksson et al. [109] performed experimental measurements of the molten metal flow on the keyhole front wall. The flow is highest at the centre of the keyhole front. Jandaghi et al. [131] have studied the vaporization rates during pulsed Nd:YAG laser welding via the mathematical model of keyhole profile.

The keyhole dynamics is complex in nature and is very much unlikely to predict the stability of keyhole even for stationary laser welding condition [111]. Generally two approaches are followed by researchers to analyze the formation of keyhole in laser welding process. One approach is the data from experimental measurement confirms the geometric shape of the keyhole. Other approach is the prediction of keyhole geometry by physical model of energy balance. However, the formation of keyhole profile depends a lot on the equilibrium between the pressure induced by surface tension and recoil pressure, fluctuations of the surface tension and recoil pressure due to the uneven distribution.

2.2 Conduction mode heat transfer analysis

With the application of intense heat on the surface of the work piece the molten zone is created and the welding is performed by alloying solidification. Figure 2.11 illustrates the schematic representation of the fusion welding process. There exist three distinct regions in the weldment, namely, the fusion zone (FZ), the heat affected zone (HAZ) and the base material. In fusion welding process, the interaction of the heat source with the base material leads to a series of complex physical processes.

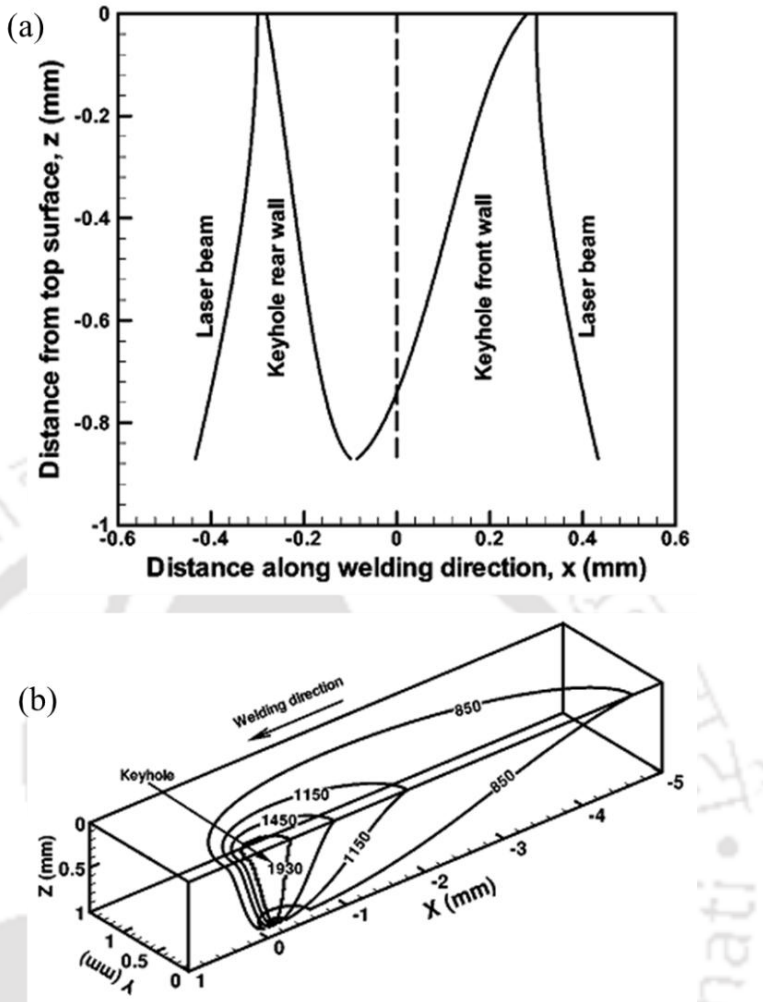

Figure 2.10: During laser welding of aluminium alloy 5182 of laser power, 2500 W and speed, 106 mm s^{-1}, (a) estimated keyhole profile along the symmetry plane and (b) three-dimensional temperature field along with keyhole profile, the temperatures values are in K [6].

The FZ undergoes melting and solidification. In the molten pool, the liquid metal circulates vigorously driven by electromagnetic, surface tension gradient and buoyancy forces. It is well known fact that the convective heat flow affects the FZ geometry and the temperature distribution in the HAZ. The HAZ, which experiences significant temperature changes, may undergo various solid-state transformations. The material region which is not affected by welding process is the base material. During fusion welding, the complex physical processes take place in a small area, usually of the order of few millimeters. The spatial variation of temperature in the weldment is quite high, generally up to several hundreds to thousands of degrees. The small welded area where various physical processes occur and the high spatial temperature gradients are two characteristics of the welding process.

The most instinct phenomenon in conduction mode heat transfer analysis is the modeling of heat source. Over the decades, several researchers have proposed various heat source models that vary from point, line to distribute over surface or volume. The representation of heat source is analogous to type of welding process and final weld pool shape and size. Henceforth, this section is focused on various approaches to model heat source in weld pool simulation.

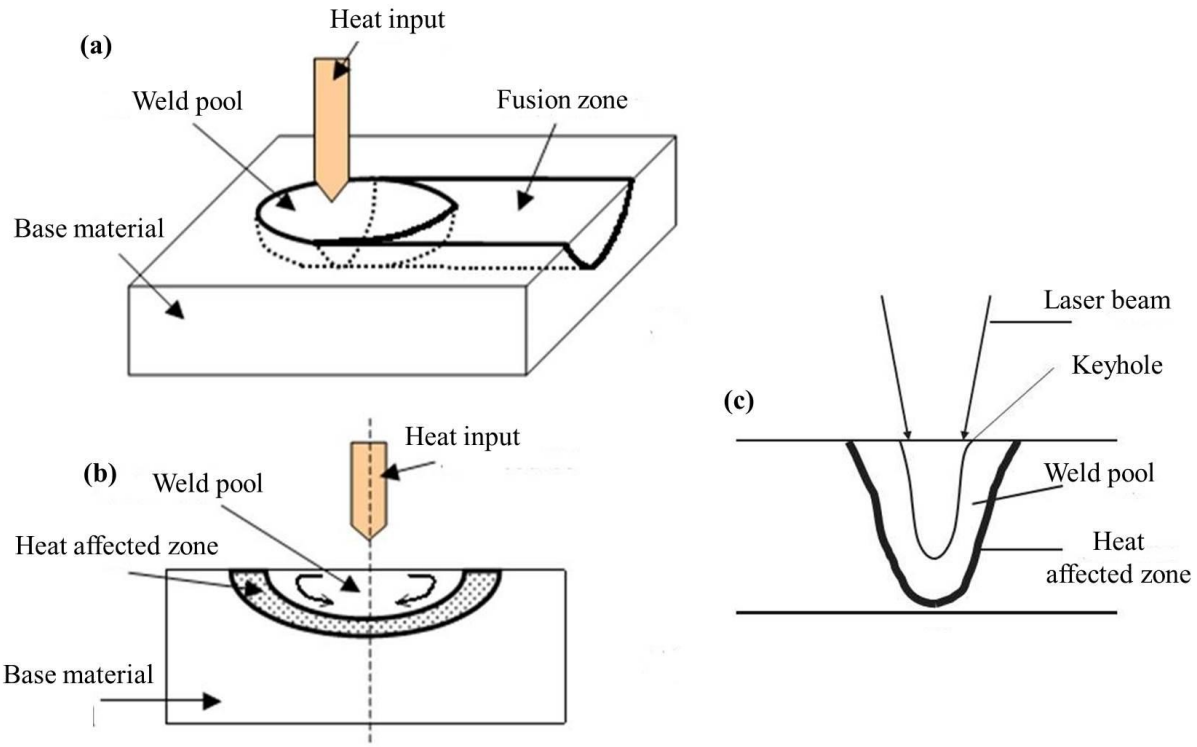

Figure 2.11: Schematic representation of conduction mode fusion welding process and keyhole mode laser welding process: (a) interaction between the heat source and the base material, (b) the transverse section and (c) the transverse section portion of keyhole mode laser welding process [10].

2.2.1 Heat source models

The basic idea of the heat source model is the replacement of the physical process with an appropriate surface heat flux or volumetric heat generation. In the early 1940s, Rosenthal [28, 29] first attempted to estimate thermal history both for stationary and continuous arc welding processes analytically. Based on conduction heat transfer and considering temperature independent material properties, Rosenthal presented the temperature distribution as

$$T - T_O = \frac{Q}{4\pi kr} \times \left[- \left[\frac{\rho C_P V_w \xi}{2 \times k} + \frac{\rho C_P V_w r}{2 \times k} \right] \right] \quad (2.1)$$

where T is the temperature variable, T_0 is the ambient temperature, Q is the heat input, k is the thermal conductivity, r is the radial distance from the heat source, ρ is the density, C_P is the specific heat, V_w is the velocity of the welding heat source and ξ is the moving coordinate in the Y-direction. For the linear welding process with moving heat source, the moving coordinate (ξ) can be represented as

$$\xi = Y - V_w t \quad (2.2)$$

where‘t’ is the time variable. However, the author neglected the latent heat of fusion and considered the welding heat source as point heat source. The analytical solutions are restricted to several number of simplified assumptions, even though, these served as basic reference for the estimation of thermal cycles and cooling rates in fusion welding processes. Grong [7] transformed the Rosenthal [28, 29] and Rykalin [132] formulae into a dimensionless version. Over a wide range of materials and heat input, Christensen *et al.* [133] confirmed that the Rosenthal model are in good agreement with experimental results in dimensionless form. However, Eager and Tsai and several other researchers [7, 134] showed that the Rosenthal model is not suitable to estimate the temperature in and around the weld joint since these models assume that the temperature at the heat source is infinity and material properties are insensitive to temperature. However, these analytical models are proved that the predicted temperatures away from the center of heat source are in fair agreement with experimental results.

Jeong *et al.* [33] presented an analytical solution to calculate the transient temperature distribution in fillet arc welds using a bivariate Gaussian distributed heat source model along with convective boundary conditions. In this work, the authors transformed the solution of the temperature field for a plate of finite thickness to the fillet welds by means of the conformal mapping technique. The analytical solution was verified by comparing the predicted results with the experimentally measured isotherms of GTA and flux cored arc (FCA) fillet welds. The comparative results showed satisfactory accuracy. Kang and Cho [35] also presented an analytical solution to predict the transient temperature distribution in fillet arc welding. However, the authors included the influence of the molten metal produced from the electrode with different arc efficiencies and Gaussian distribution parameters. Figure 2.12 describes the variation of isotherms with different process variables, arc efficiencies and distribution parameters along with experimental isotherms [35].

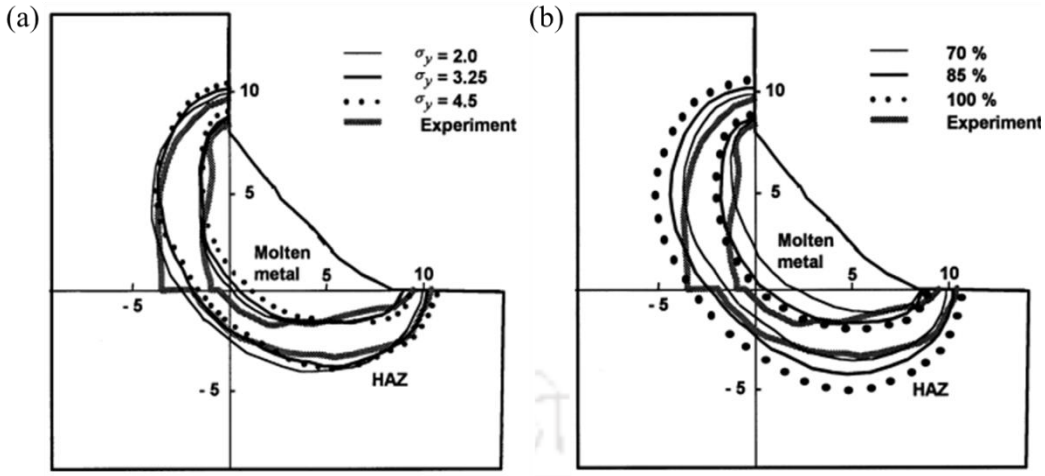

Figure 2.12: Temperature distribution corresponding to parameters, (a) arc efficiency=78%, current=240 A, voltage=30 V, welding speed=5 mm/s and distance from arc start point=35 mm and (b) distribution parameter=3.25 mm, current=240 A, voltage=30 V, welding speed=5 mm/s and distance from arc start point=35mm [35].

Nguyen et al. [36, 135] have developed a closed form analytical solution for a 3-D semi-ellipsoid and double ellipsoidal heat source models in a semi-infinite body. The authors utilized them for predicting the weld bead geometry and calculation of residual stresses for bead-on-plate weld. Kasuya and Shimoda [34] made an effort to estimate the temperature distribution with and without considering the latent heat of fusion. It was observed that the difference in cooling rates was substantial for an initial time of about 0.15 s. The peak temperature was condensed to 1273 K and the estimated cooling rate by both the models (with and without latent heat) was almost alike. Guo et al. developed an analytical solution for quasi-steady state conduction mode laser welding of thin sheets assuming the work piece as a semi-infinite body and constant thermo-physical properties [41]. The phase change influence was taken into account in this model with Stefan condition. Karkhin et al. [43] studied the influence of latent heat on weld bead dimensions during laser welding of thin sheets of aluminum alloys. Kar and Mazumder described a three dimensional heat conduction model to analyze laser seam welding of SS304 sheets using analytical model [32].

It is obvious that analytical model cannot consider the sensitivity of the material properties with temperature and comply with several other assumptions. Since the Rosenthal-Rykalin formulae cannot produce satisfactory results for temperature distributions in and near the weld pool, several researchers have attempted to modify the analytical solutions and tried to improve the prediction accuracy. After Pavelic's attempt in 1969 [24], several researchers

started considering the distributed heat source models in heat transfer analysis of fusion welding processes.

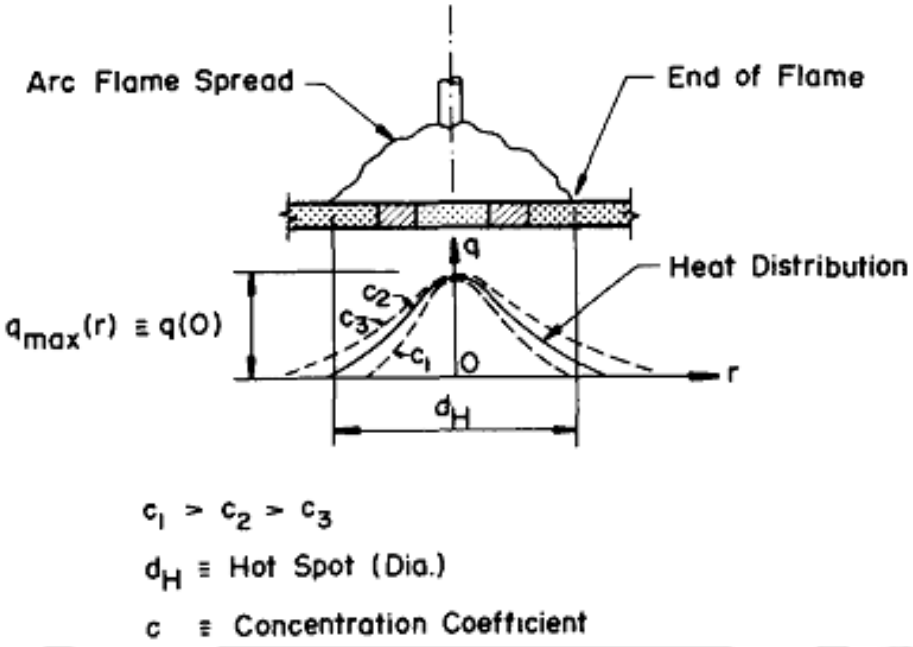

Figure 2.13: Schematic representation of Gaussian distributed 'disc' heat source model [24].

The most instinct phenomena for numerical solution of temperature distribution and velocity field in fusion welding process are the requirement of suitable heat source. The input energy to the solution domain is decided by the nature and distribution of heat source model. In analytical solution, the researchers have assumed that the welding arc or laser beam can be represented as a point, plane or line heat source depending on the dimensionality of the problem. But, the actual welding arc or a laser beam is distributed over a finite area rather than at a single point or line. Pavelic *et al.* [24] introduced a distributed heat source i.e. 'disc' heat source model. This model overcomes the limitations of the analytical methods by considers the distributions of the heat energy over a surface area and is more practical approach as compared to Rosenthal's point, line, and plane heat source models. However, the disc heat source model does not account the digging action of the welding arc or laser beam. This type of surface heat source models fails to predict the depth of penetration. Figure 2.13 represents the Gaussian distributed disc heat source model with different concentration coefficients [24]. This distributed heat source model is explored by several researchers [136-138]. Friedman [136] and Krutz et al. [137] implemented 'disc' model in a finite element

based heat transfer analysis and achieved considerably better temperature distributions in the fusion and heat affected zones than computed with the Rosenthal model. Anderson [138] developed a two dimensional finite element model using distributed heat source for the prediction of thermal stress in submerged arc welding including the phenomenon of phase transformation.

The 'disc' heat source model does not account the digging action of the arc which is essential for deep penetration welding processes such as electron beam and laser beam processes. To overcome these limitations, Hibbert and Paley [139] used a constant heat density distribution over the fusion zone with a finite difference based heat transfer analysis. But, the boundary of heat density distribution was not well defined. The researchers articulated the volumetric heat source models for fusion welding processes by mapping with various geometric shapes. In 1984, Goldak *et al*. [30] developed distributed heat source such as semi- and double ellipsoidal heat source models with Gaussian distribution to account the digging action i.e. volumetric heat distribution of the welding arc. Semi-ellipsoidal heat source model is suitable when the welding arc is stationary i.e. in case of spot welding process. When the welding arc moves with certain velocity the double ellipsoidal heat source model fits suitable since the temperature gradient in front and at the trailing edge of the molten pool are not similar. Figure 2.14 describes the Gaussian distributed double-ellipsoidal heat source model. Wu et al. [140] have developed an efficient heat source model for the simulation of keyhole plasma arc welding process by considering the effect of decay of heat intensity distribution of the plasma arc along the direction of the work piece thickness to configure the keyhole formation. Figure 2.15 (a) and (b) show the conical heat source model and modified conical heat source model developed by Wu et al. [140].

Recent literature indicates that the researchers have tried to modify the various types of heat source models, identification of model parameters and development of composite heat source models combining the existed heat source models for various fusion welding processes. Wu et al. [142] have implemented a combined heat source model for the simulation of keyhole plasma arc welding process. In this model the authors combined the double ellipsoidal and cylindrical heat source models to account the configuration of keyhole mode plasma arc welding shape. The heat source parameters are estimated through optimization techniques using the geometric features of weld. Luo et al. [143] investigated the thermal effects of AZ61 magnesium alloy during vacuum electron beam welding using a combined heat source model, Gaussian distributed heat flux on top surface and volumetric conical heat

source model through thickness of the plate. Li et al. [144] have developed combined heat source model during simulation of tandem submerged arc welding (T-SAW) process. In T-SAW the arc is deflected by the magnetic force in the plane having arc movement and plate thickness direction. The proposed heat source model is a combined effect of Gaussian distributed surface and double ellipsoidal heat source models taking into account the reflection angle.

Li et al. [145] investigated the heat transfer and fluid flow analysis of plasma arc welding process by using a modified heat source model which is composed of a double-ellipsoidal volumetric heat source at the upper part and a conical volumetric heat source at the lower part of the work piece surface by considering the actual configuration of plasma arc welds and the key-hole effect of plasma arc welding process. Overall, the recent heat source models in fusion welding simulation are the analytically estimated various geometric shapes that follow Gaussian distribution. The distributed heat source models are mapped with regular geometric shapes like disc, conical, spherical, semi-ellipse, double ellipsoidal, or combinations of these configurations. However, the shape and size of volumetric heat source is based on the experimentally measured weld dimensions. The unknown parameters of heat source are estimated by using experimental data and multivariate optimization [141].

Present work motivates to develop such a volumetric heat source that minimize the model parameters, more generalized form in nature and without violating the non-symmetry heat density distribution for linear welding process. Presently, different heat source models for calculating the temperature fields including weld pool and heat affected zone dimensions are widely used under conduction regime. The temperature profile of the weldment is of interest if the residual stress and distribution or the structure and properties of welded joint are calculated. In that respect, there may be the paramount interest on the development of a decent volumetric heat source model that should involve less number of parameters and more general in nature. In the present work, an egg-configuration volumetric heat source model is proposed to simulate temperature distribution, time temperature history, and cooling rate during autogenous fusion welding process. It has been shown that Pavelic et al. [24] ‘disc’ heat source, Hibbert and Paley [139] volumetric heat source, Westby's [146] heat source, Goldak et al. [30] ellipsoidal heat source models are the special cases of the proposed heat source model.

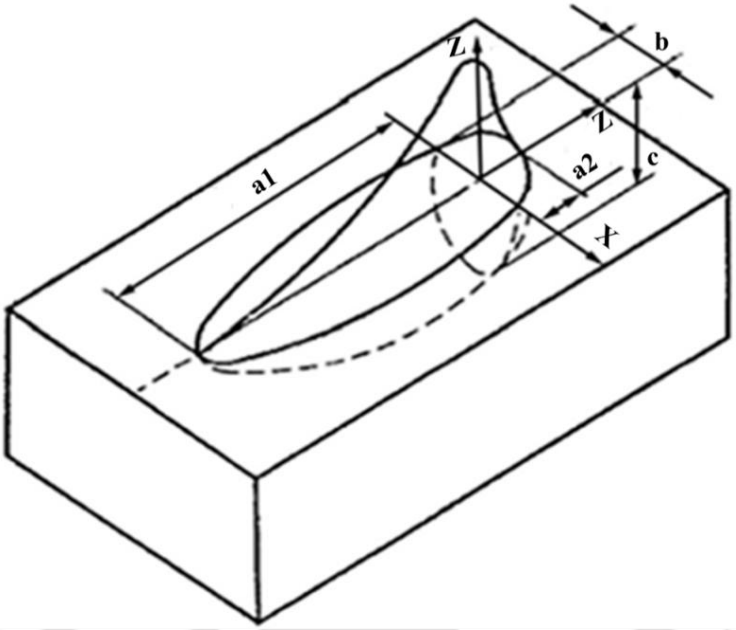

Figure 2.14: Schematic illustration of double ellipsoidal heat source model [30].

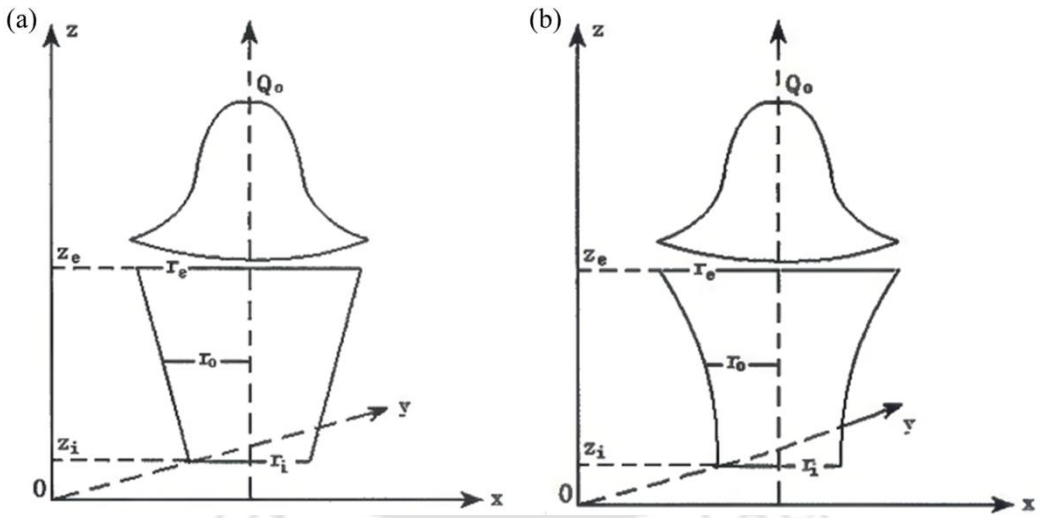

Figure 2.15: Schematic representation of (a) conical heat source model and (b) modified conical heat source model by Wu et al. [140].

2.2.2 Numerical heat transfer model

The main disadvantage of the analytical modeling approach of fusion welding process is the representation of welding arc or laser beam as a point heat source (concentrated) and the assumption of temperature independent material properties. Moreover, the analytical models could infrequently consider the influence of latent heat of fusion. Furthermore, a semi-infinite work piece is necessary to estimate the temperature for the analytical model. In the real

condition, the substrates to be welded are always of finite size. One of the initial numerical models of laser welding is introduced by Mazumder et al. [147]. Chande et al. enhanced the aforementioned model by incorporating the temperature dependent material properties and latent heat of fusion via an increased specific heat over temperature range of melting and solidification [148]. Several researchers have investigated the quantitative study on deep penetration laser welding process by using different heat source models. Frewin and Scott presented a three dimensional heat transfer analysis based on finite element method during pulsed laser beam welding [37]. The temperature distribution is quite sensitive to the power density distribution and absorption coefficient of the laser beam. Zacharia et al. [149] investigated the experimental and numerical modelling of Nd:YAG pulsed laser welding process of austenitic stainless steel by taking into account the fluid flow in the weld pool and the model was used to simulate the cooling rates and thermal cycles. Sudnik et al. [150] studied the numerical investigation of the laser beam welding process to measure the weld pool geometry. A linear correlation was found between the length and depth of the weld pool with varying laser power and constant welding speed assuming a conduction mode process. However, the surface of the weld pool remains unbroken during conduction mode laser welding and opens up to allow the laser beam to enter the melt pool in keyhole mode welding. Jin et al. [151] developed a 3D finite element based thermal model for deep penetration laser welding process based on an actual keyhole size. De et al [42] reported a two dimensional axisymmetric finite element based heat transfer model during conduction mode laser spot welding process. Bag et al. [126] developed a conduction mode heat transfer model during laser spot welding using an adaptive volumetric heat source model to predict the weld pool dimensions.

Researchers explored the numerical and experimental investigation on shallow penetration gas tungsten arc welding (GTAW) process by utilizing several numerical methods. Kim and Na [152] investigated the numerical modelling of heat transfer and fluid flow in pulsed current GTA weld pool. Kim and Basu [153] developed an unsteady two dimensional axisymmetric model to predict weld bead geometry and velocity profile during gas metal arc welding process (GMAW). Fan et al [154] numerically analyzed thermal and fluid flow combining buoyancy force, electromagnetic force, surface tension gradient and arc drag force for a partially and fully penetrated weld pool in stationary GTAW. Lu et al. [122] established an integrated mathematical model to investigate heat transfer and fluid flow in

GTAW. Bag et al. [125] developed a 3D quasi-steady state thermal model based on finite element method to investigate the weld pool dimensions and thermal cycles.

The conduction based numerical model attempts to consider Gaussian distributed surface heat flux or volumetric heat source. It is realized that the surface heat flux may not be sufficient for deep penetration laser welding process. In that case, the volumetric heat source is more appropriate and *a-priori* knowledge of solidified weld dimensions from experiment is required. It was conceived that the consideration of a volumetric heat source with less number of parameters will be effective in conduction mode heat transfer analysis. However, the enhanced heat transfer due to convective flow of material is accounted inherently in transport phenomena based heat transfer model. The effort made towards modeling of convective transport of heat in fusion welding process is discussed in subsequent sections.

2.2.3 Cooling rate

The final weldment quality (mechanical properties and microstructure) in and around the fusion zone significantly depend on the time-temperature history, in particular, the cooling rate. The finite element based heat transfer and fluid flow process models can be utilized further to calculate the cooling rate from the computed transient temperature field in and around the fusion zone. Mazumder and Steen have developed a three-dimensional heat transfer model for calculating the time-temperature history for a laser seam welding process of titanium [147]. In this work, the authors have predicted the cooling rate at three different locations: on the weld pool surface, at the bottom surface and at a point 0.275 mm below the top surface. The calculated results showed that a rapid initial heating takes place till a peak temperature was reached, followed by a rapid cooling (Fig. 2.16). The cooling rate at the bottom surface is very low as compared to the same on top surface.

Paul and DebRoy experimentally measured the dendrite arm spacing in the final weld microstructure and correlated to the calculated cooling rates [51]. Cool and Bhadeshia have been studied the effect of various alloying elements on the evolution of its microstructure in steel as a function of cooling rate [155]. De et al. examined the effect of laser spot welding process variables such as laser power and on time, on the time-temperature history, microstructure and hardness of low alloy steel weldment [55]. He et al. examined the cooling rates during fusion welding of SS 304 sheets using a transient heat transfer and fluid flow model based on the solution of the equations of conservation of mass, momentum and energy in the weld pool [53]. In this work, the authors reported the calculated thermal cycles at three

different monitoring places located in radial (0°), axial (90°) and at a specified angular (45°) direction from the weld center. Thermal cycles showed rapid heating till the peak temperature was reached, followed by fast cooling as the laser power was switched off. To emphasis the severity of cooling rate in laser welding, the same was compared with the cooling rates typically observed in conventional GTA welding process. The authors testified the difference of cooling rates between laser and GTA welding process and reported as 41,380 K/s for laser welding and a value of 250 K/s for GTA welding.

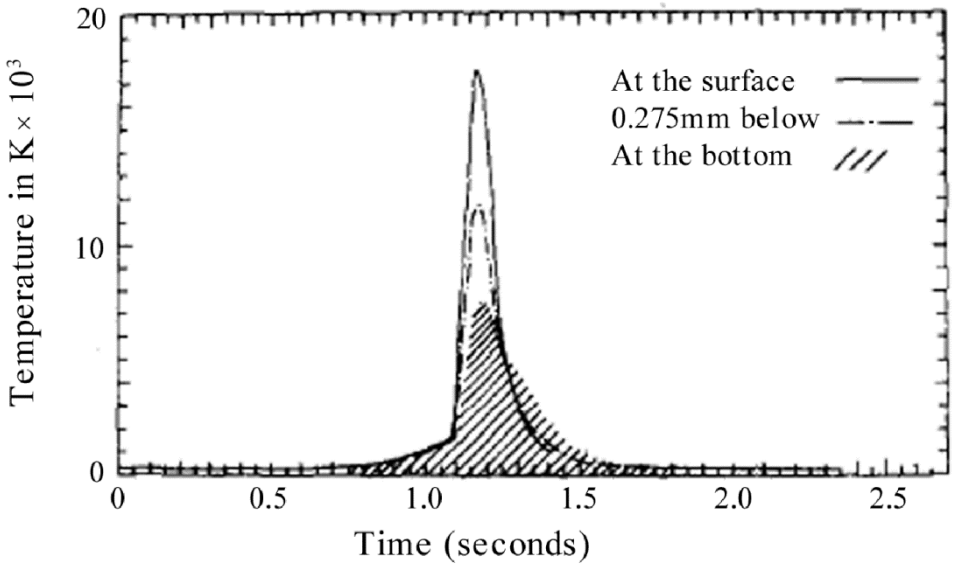

Figure 2.16: The time-temperature history for the welding conditions, laser power is 1.5 kW and welding speed is 7.5 mm/s of 2 mm thick titanium alloy [147].

2.3 Transport phenomena in fusion welding

The fusion welding process is complex in nature and intricate several physical phenomena such as heat transfer, mass transfer, fluid flow, chemical reaction, and phase transformation occur simultaneously during the process. The interaction of various phenomena as well as a large number of process variables possibly incites to find desired weld features by empirical correlations. This approach demands large volume of experimental data and might not perform in the finest way when a new set of design variables is of interest. Moreover, this approach may not produce all weld attributes influenced by scientific principle alone. Quantitative calculation of various aspects in weldment structure is necessary to have better understanding of the differential influence of process parameters through fundamental study of heat transfer and fluid flow in the fusion welding process. The application of

transport theory provides beneficial knowledge about various characteristics of a welded structure as well as produces quantitative information of weld pool dimensions and mushy zone, temperature and velocity field, and microstructural properties.

A number of thermal, microstructural, and mechanical models of the fusion welding process have been developed by several researchers from a simplified to more complex nature using various numerical methods [2, 30, 37, 140, 156]. DebRoy et al. reported an extensive review of the physical processes prevalent in fusion weld pool [1]. In the view of authors, the convective flow in molten weld pool would be driven by surface tension, buoyancy and electro-magnetic force when electric current is used. Aerodynamic drag forces of the plasma jet might be contributed to the convective flow in the weld pool. Buoyancy effects originated from the spatial variation of the liquid-metal density mainly because of temperature variation and, to a lesser extent, from local composition variations influence the material flow. Electromagnetic force in arc welding is a consequence of the interaction between the divergent current path in the molten pool and the magnetic field that it generates. In arc welding, a high velocity plasma stream imposes on the molten pool. The spatial gradient of surface tension acts as a driving force (called Marangoni stress) along the top surface of the molten pool.

The nature of liquid convection in molten weld pool and the shape of the weld pool owing to various driving forces are schematically shown in Fig. 2.17 [7-10, 157]. Because of the variations of temperature and composition, the temperature coefficient of surface tension may be positive or negative and the shape of the molten weld pool is influenced by the nature of surface tension force (Fig. 2. 17 (b) and (c)). The measurement of liquid flow velocities in the small and intensely heated molten weld pool is more difficult than that of temperatures. Henceforth, a practical recourse is to use quantitative calculations to gain understanding of the phenomena of heat transfer and fluid flow during fusion welding process.

2.3.1 Experimental measurement

A number of investigators worked on establishment of the empirical correlations based on experimental results to understand the feasible fusion welding process parameters by using sensors data during online monitoring of the process [15, 17, 20, 22-23, 158-161]. In fusion welding process, the most comprehensive output is the weld bead dimensions along with thermal history that define the mechanical properties of the weld joint. Jou carried out a

series of experiments to investigate the interaction and correlations of welding current, voltage, welding speed and arc length affecting the formation of weld pool in GTA welding process [20]. The author also studied the influence of arc length on arc efficiency and heat distribution parameter or effective arc radius which is defined by the radial distance from the center of electrode within which 95% of energy is transferred. The heat distribution parameter has significant effect on both the shape and the size of molten weld pools. Starling et al. utilized a linear regression model to establish a relationship between welding parameters and weld dimensions in narrow gap-GTA welding process with magnetic arc oscillation [15].

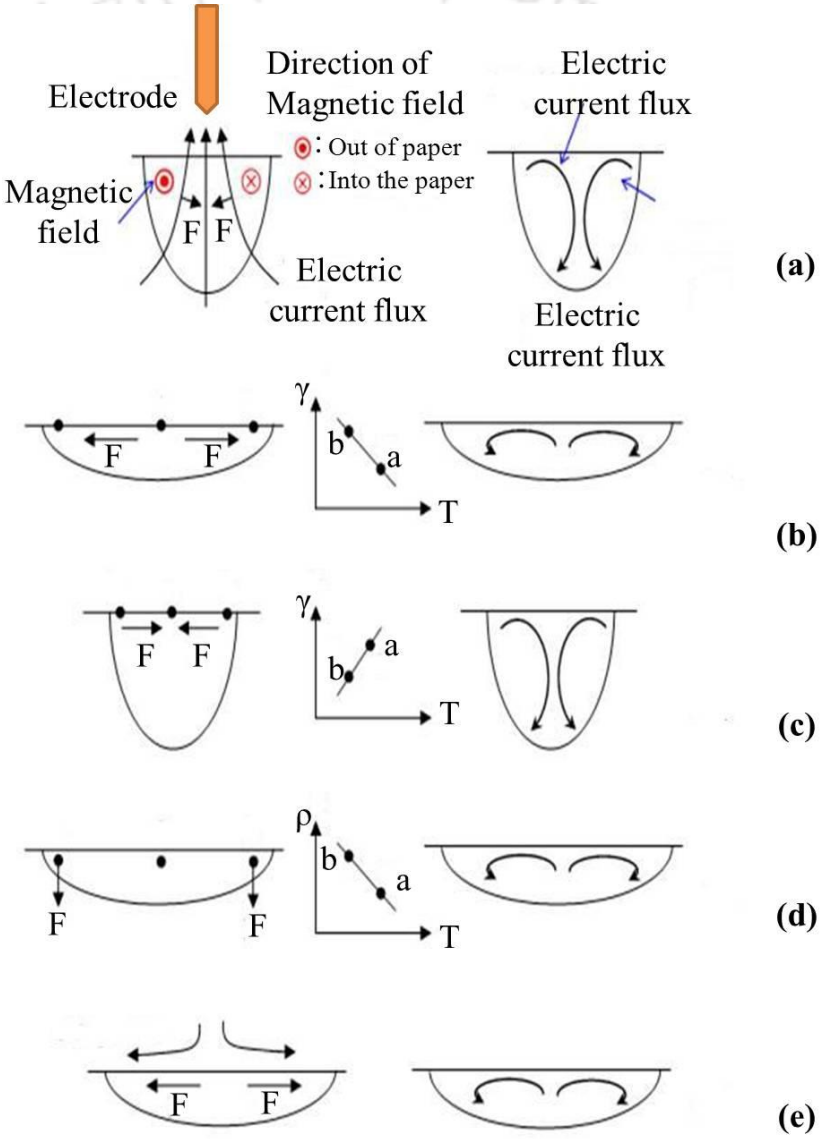

Figure 2.17: Various driving forces in molten weld pool and resulted molten material convection: (a) electromagnetic force, (b) and (c) surface tension force, (d) buoyancy force and (e) arc plasma force [157].

Deutsch et al. investigated the effects of weld speed and focal position on weld bead dimensions in laser seam welding of 1.6 mm thick AA5182 aluminum alloy [22]. The authors indicated that the changes in the focal positions from the positive to the negative values for a constant weld speed could considerably affect the weld bead dimensions. Benyounis et al. have studied the combined influence of laser power, welding speed and focal position on weld bead dimension of CO_2 laser welding of medium carbon steel [23]. The authors showed that the laser power and weld speed had greater influence on weld bead width as against the focal distance. Tzeng carried out the experiments on pulsed laser seam welding of 0.7 mm galvanized steel sheets [17]. In this work, the author specified that the weld speed between 0.9 to 1.5 mm/s and the mean pulse power in the region of 330 to 390 W could lead to sound welds with least amount of porosities.

Zhang et al. utilized a non-contract seam tracking technology in GMA and GTA welding processes [158]. This technology is based on high frequency, high resolution ultrasound to achieve high accuracy in weld seam identification. Zhao et al. succeeded an automatic control of pulsed GTA welding process with wire filler by recording the image of the molten weld pool with an optical sensing method and estimated three-dimensional shape parameters of weld pool surface with an image processing algorithm [159]. Ancona et al. reported the utilization of an optical inspection system for monitoring manual GTA welding process of steel pipes [160]. Weglowski et al. endeavored to monitor weld quality in GTA welding using arc light as a signal [161]. Kovacevic et al. monitored the surface weld pool geometry by using high shutter speed camera combined with structured light for the laser seam weld [162].

In the case of laser spot welding, the temporal evolution of temperature field on the weld pool surface was studied by Pitscheneder [163] using a high speed thermo-camera. The measurement of transient velocity field in molten weld pool was attempted by Matsunawa et al. [164] using high speed CCD camera. Dutta et al. followed a combined experimental and computational method for the calculation of arc efficiency in GTA welding [165]. Giedt et al. reported an average arc efficiency of 80% for welding of 304L stainless steel [166]. Christensen et al. [133] also reported arc efficiencies of GTA welding in the range of 21–48%. Figure 2.18 describe the welding heat source efficiency for various welding processes [10]. A significant amount of research efforts were centered on the finding of values of actual absorption coefficient or arc efficiency. However, the reliable value of absorption coefficient

is possibly too difficult to obtain in a confident for fusion welding processes. Furthermore, the experimental investigations for finding these values are expensive and time-consuming. Therefore, a number of researchers have tried to realize the same through analytical and numerical process models by integrating with optimization modules.

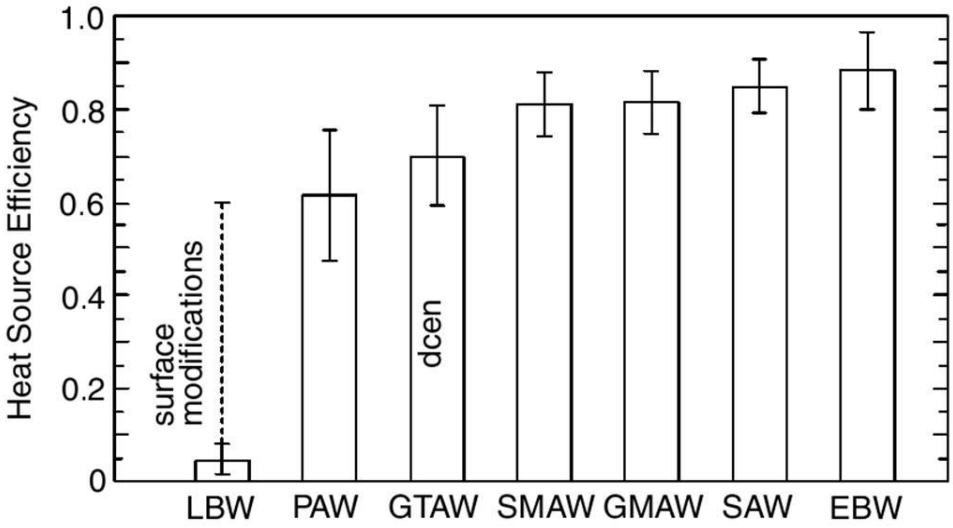

Figure 2.18: Heat source efficiencies for various welding processes [10].

2.3.2 Convective heat transfer in weld pool

The temperature distribution and molten material flow in weld pool cannot be estimated by conduction heat transfer analysis alone. This is performed by using the transport phenomena based heat transfer and fluid flow analysis. However, the physics based process models need some model parameters which are uncertain. The evolution of very simplified to more sophisticated model is made including the effect of material flow in the process. The conduction mode heat transfer analysis is often performed using a dedicated heat source model to compensate the effect of actual fluid flow within the weld pool [37, 39, 42, 125, 126, 167]. This approach primarily helps to reduce the computational time and is important in real industrial process design. Additionally, the conduction-based model is also significant in calculation of distortion and residual stress where overall temperature distribution in the whole geometry is of greater importance than local variation in the weld pool [167-171]. It is noteworthy that the heat source model employed for the keyhole mode welding process such as high power laser and electron beam welding is different from the conduction mode welding process [140].

The volumetric heat source model is often replaced by real surface heat flux to include the effect of dynamics of the molten material during the fusion welding process [49, 52-54, 56, 60]. However, the flow dynamics play a significant role in quantitative study of weld pool shape and size. The material flow is assumed either laminar or turbulent in nature. The flow pattern is also influenced by the involved process parameters and subjective to the interactions of various physical and metallurgical phenomena occurring during the welding process. Till date, there has been no correct systematic specification of welding process parameters to decide the nature of flow owing to limitation of experimental measurement. The effect of convection within the molten pool and its influence on heat transport are often performed by artificially increasing the thermal conductivity and viscosity of molten material. This approach has received wide acceptance in the recent past. However, these augmented material properties are based on an overall kernel of optimization module to achieve the desired experimental results in an inverse manner [53, 54, 60]. Strategically, this approach considers the uniform turbulence effect within the weld pool by increasing the value of material properties at the melting temperature of an arbitrary fold. This approach eliminates the uncertainty in defining the material properties at very high temperature.

Alternately, few researchers accomplish material flow considering the effect of turbulence and using kinetic energy-based turbulence models. These models are used to simulate convective flow of liquid material as well as species concentration distribution within the weld pool [49, 52, 56, 103, 121]. However, the k-ε turbulence model increases the computational time owing to the solution of additional equations. Moreover, the empirical constants involved in k-ε turbulence model are not well defined for liquid material. In weld pool modeling of the fusion welding process, the fluid flow analysis is significant along with the conductive heat transfer analysis when the material contains surface-active elements [86-87, 172]. The presence of main minor elements of group VIIB (oxygen, sulfur, selenium, and bismuth) may change the weld pool shape and size during gas tungsten arc (GTA) welding. The weld pool shape and size change significantly by adding these active elements to the material, and this can be used in a beneficial way to get high penetration welding. This phenomenological analysis is not possible within the frame of only heat conduction analysis and without consideration of flow dynamics of molten material. In recent times, the numerical simulation of the fluid flow and heat transfer analysis using different shielding gases have been studied by several researchers [102-104, 121-124] by interacting welding arc model to the work piece surface. This approach essentially eliminates the need of the heat source model

since the temperature distribution of the arc can be used to estimate heat flux on the work piece surface. However, the interface between the anode and arc column is the most important issue to calculate the heat flux [104]. The sensitivity of the arc model to the change of volume percentage of mixed shielding gas is still unclear. Moreover, the interaction of the arc with deformable work piece geometry is another important issue in terms of reliable modeling approach, and hence a free surface modeling of the work piece surface under the pressure of arc plasma is necessary.

There is a lack of enough research in this direction. Alternatively, a straightforward surface heat flux following Gaussian distribution may act as representation of heat source without much error in calculations [37, 39, 42, 125, 126]. It is thus obvious from the literature review that a dedicated surface tension model is necessary to take into account the effect of surface-active elements that directly influence the flow dynamics. Lu et al. [121] and Dong et al. [103, 124] studied the effect of surface-active elements such as oxygen through the development of a sophisticated finite volume-based numerical model using FLUENT software. The model considers constant material properties, and the solution domain for fluid flow is considered as whole geometry. It is expected that the viscosity is kept very high outside the flow domain to satisfy near solid medium. The effect of surface-active elements has been incorporated in this model through a surface tension model [84] that is a function of solute concentration (i.e., oxygen here) and temperature. However, the coefficient of surface tension may go through an inflection point somewhere on the surface if the weld pool contains fairly high oxygen contents. In this situation, the fluid flow in the weld pool is likely to have a more complicated shape as compared to a simple recirculation [84].

In present work, the attention has been focused on numerical simulation of heat and fluid flow considering the effect of surface-active elements. Assuming the laminar flow of liquid metal, a 3D finite element-based heat transfer and fluid flow model is developed using temperature- and composition dependent surface tension coefficients and considering the latent heat of melting and solidification along with other temperature-dependent material properties. The analysis has been performed using the in-house developed FORTRAN code. To estimate the uncertain model parameters such as arc efficiency, effective arc radius, and the enhanced material properties at high temperature, an inverse approach is followed by integrating differential evolution (DE)-based optimization algorithm with the numerical model.

2.4 Influence of temperature dependent material properties

The thermal and mechanical properties of a specific material are greatly sensitive to temperature. Most of the analytical models and some of the earlier numerical models also neglect the effect of temperature on material properties. Some researchers have investigated the influence of the temperature dependent material properties [25, 84, 85, 173-177] in thermal and mechanical analysis of fusion welding process. The details on the influence of various temperature dependent material properties such as thermal conductivity, density, specific heat, yield strength, elastic modulus etc., are reported in the present section. It is worth mentioning that the coefficient of surface tension that affects the convective transport of heat in molten weld pool depends on temperature along with the properties such as thermal conductivity, emissivity and specific heat which influences the temperature distribution of solution domain. Sahoo et al. reported an elaborate analysis on fluid flow in molten weld pool in the presence of surface active elements by considering the variation of surface tension gradient [84, 85]. The authors showed that the surface tension decreased linearly with temperature when the sulfur content in the weld pool was negligible. Also it is observed that surface tension first increases and then decreases with increase in temperature and likely to isolate at higher temperature when the sulfur content in the weld pool is significant.

Zacharia et al. [25, 173] have studied the influence of temperature dependent material properties in the modeling of fusion welding processes (laser and GAT welding processes). The calculated depth of penetration had the tendency of deeper when the temperature independent surface tension gradient was used [25]. The authors further studied the influence of temperature dependent materials properties in modeling of GTA welding process of 304 stainless steel [173]. In both the cases, the calculated results are compared with the experimental results and found the better agreement have been achieved when the temperature dependent material properties are used in modeling. Mundra et al. [174] examined the influence of the thermo-physical properties such as the viscosity, thermal diffusivities of both the solid and liquid, the temperature coefficient of surface tension and energy absorption coefficient on the results of heat transfer and fluid flow calculations (depth of penetration and diameter of the weld bead, and the weld pool surface velocities and temperature distribution) in fusion welding simulation. Figure 2.19 describes the influence of k/C_P of solid on weld bead dimensions, peak temperature, maximum surface velocity and the Peclet number. In this study, the authors found that both the weld width and penetration decreases by increase in the

k/Cp value. Moreover, the increase of k/Cp value leads to low peak temperature on the surface of the molten weld pool. This is due to the total enthalpy of the pool decreases. Nevertheless, the maximum velocity at the weld pool surface is not considerably affected because the decreased temperature is convoyed by lower weld bead width, and subsequently, the temperature gradient induced Marangoni stress does not change considerably.

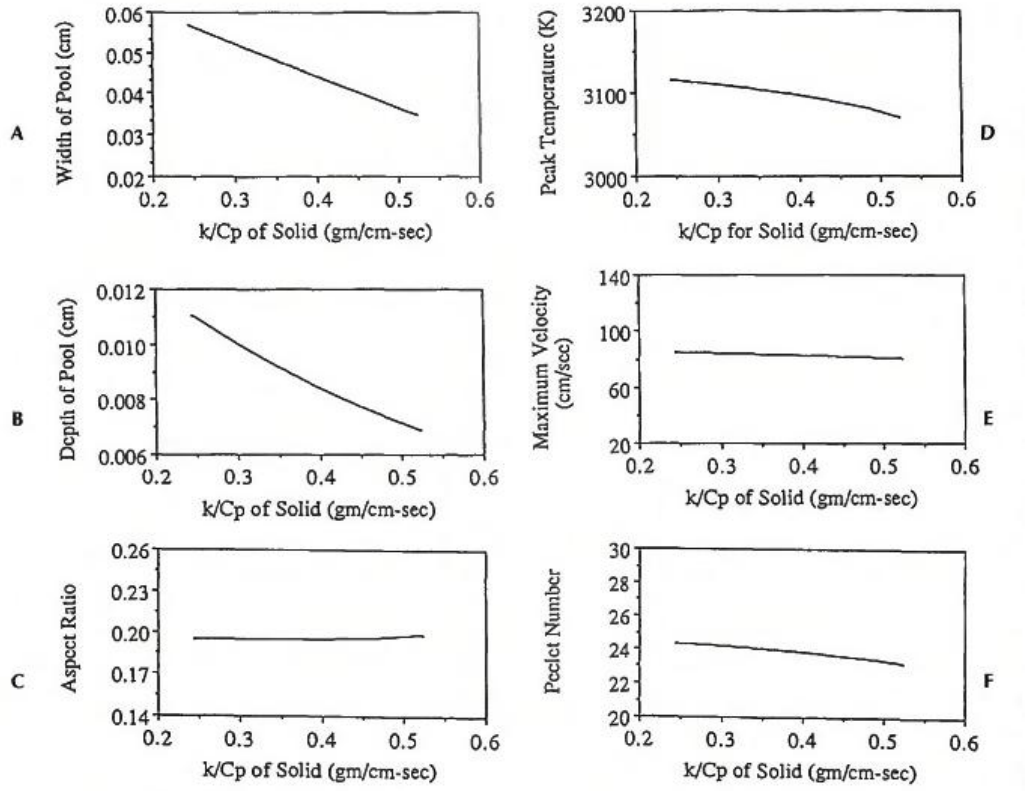

Figure 2.19: Effects of k/Cp of solid on: A—diameter; B—depth; C—aspect ratio of the weld pool; D—the peak temperature; E—maximum surface velocity; F—the Peclet number for heat transfer [174].

Little and Kamtekar [175] studied the influence of different thermal conductivity values on the computed time-temperature history in the fusion welding of steel. The authors found that the transient temperature distribution during fusion welding process significantly affects the value of thermal conductivity chosen. A higher value of thermal conductivity leads to a lower peak temperature near the welding line. Higher peak temperature achieves in the regions away from the weld. It is also showed that a higher value of thermal conductivity leads to a more rapid fall in temperature along the weld line. The authors specified that the heat exchange between the plate surfaces and the surroundings would have insignificant influence on the calculated transient temperatures. Zhu et al. [176] have examined the

influence of temperature-dependent material property on the transient temperature during simulation of fusion welding of an aluminum plate using three different sets of material properties (temperature dependent, at room temperature, and at average values over the entire temperature history). The authors found in their work that the temperature dependent thermal conductivity has certain effect in thermal simulation, but specific heat and density have negligible effect. However, the thermal history is better predictable when the average thermal properties are considered. The yield has rich effect whereas thermal expansion coefficient and Young's modulus have little effect on the distortions and residual stresses calculation.

The aforementioned studies manifest the necessity of amalgamation of temperature dependent material properties and it is obvious that the correct representation of material properties with temperature sensitivity can significantly influence the worth of the calculated results.

2.5 Thermo-mechanical analysis

In fusion welding, due to highly localized transient heat input, the welding work piece causes thermal expansions and contractions to occur that vary with time and location. The stress that appears in hot region near the weld is restrained by cooler region further away. As a result, the plastic deformation occurs and leads to residual stress and distortion in the weldment that remains after the temperature has returned to ambient level. Welding induced distortion can lead to misalignment of structural elements, inability to fit one welded subassembly into another, and loss of aesthetics. Thus, distortion can cause serious effects on the performance and service of the welded structure. Therefore, the assessment of these weld induced distortions and residual stresses have great significance in welding industry. Some of the common types of distortions occurred in weld joints are listed in Fig. 2.20 [178]. Changes of welding induced residual stress during fusion welding process are the result of welding heat source acting on the welded structure. Figure 2.21 describes the changes of temperature and resulting stress that occurs during fusion welding process [179]. It is presumed that the welding is performed along the X-axis and the moving welding heat source is situated at a point O. The stresses and temperature changes are demonstrated at different cross-sections. At the cross-section A-A, the thermal stresses are almost zero. Due to existence of molten weld pool at cross-section B-B, the stress near the welding heat source is equal to zero. Stresses in short distance from fusion welding heat source are compressive, since the expansion of these areas is controlled by the surrounding metal where the temperature is lower. As the

temperature of these areas is high and the yield strength of the material is low, stresses in these areas are as high as the yield strength of the material at corresponding temperature. Stress in the area away from the welding line is tensile and is balanced with compressive stresses in regions near the welding line. At cross-section C-C, the weld metal and base metal areas near the welding line have cooled, they contract and cause tensile stresses in areas near to the welding line. As the distance from the welding line increases, the stresses vary to compressive and subsequently become tensile in nature. At cross-section D-D, high tensile stresses are formed in areas near the welding line whereas compressive stresses are created in areas away from the welding line. This is the typical distribution of welding induced residual stresses that remain after welding is finished. Present section demonstrates some of the significant works on experimental measurement of residual stresses and welding induced distortions along with numerical models for stress analysis.

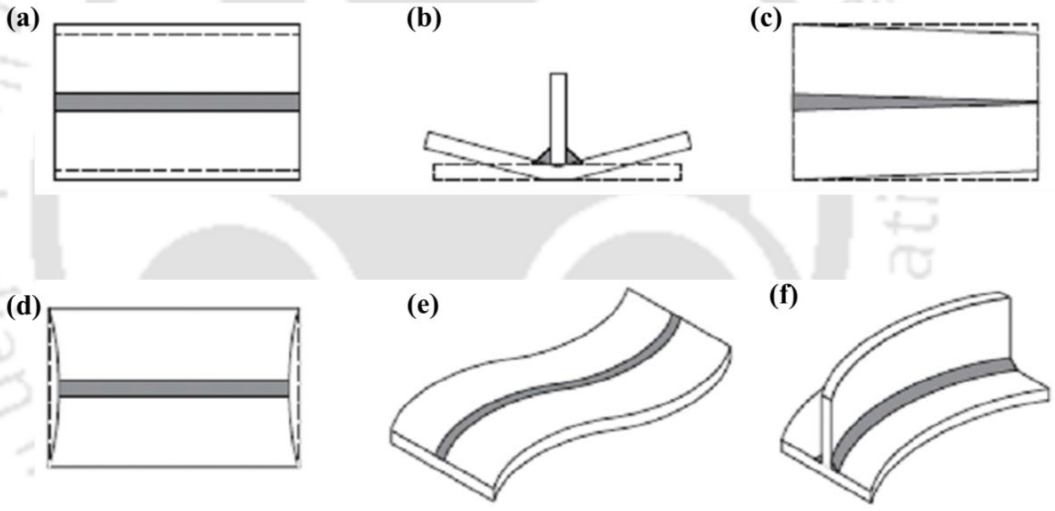

Figure 2.20: Types of welding distortions, (a) Transverse shrinkage, (b) Angular distortion, (c) Rotational distortion, (d) Longitudinal shrinkage, (e) Buckling distortion and (f) Longitudinal bending distortion [178].

2.5.1 Experimental measurement of welding induced distortions

In fusion welding, plastic thermal strain develops near the weld area owing to heating, melting and cooling of the weldment. The plastic strain leads to permanent deformation of the welded structure. Measurement of welding-induced distortion is normally accomplished during or after the welding and in some cases the actual data are used to predict the accuracy of the mathematical model or to establish empirical correlations. In principle, any dimensional

measuring instrument can be utilized for measuring the welding induced distortion [180]. For example, the angular distortion of a T-joint can be measured easily by a ruler as the welded plate is situated on a flat reference plane as shown in Fig. 2.22 (a). In Fig. 2.22 (b) a mechanical dial gauge is utilized to quantify the bending distortion continuously as it moves across the welded beam. As given in Fig. 2. 22(c), a ruler can also be used to measure the continuous angular shrinkage of a panel welded with stiffeners. This type of measurement provides the shape of the structure after welding relative to a reference plane.

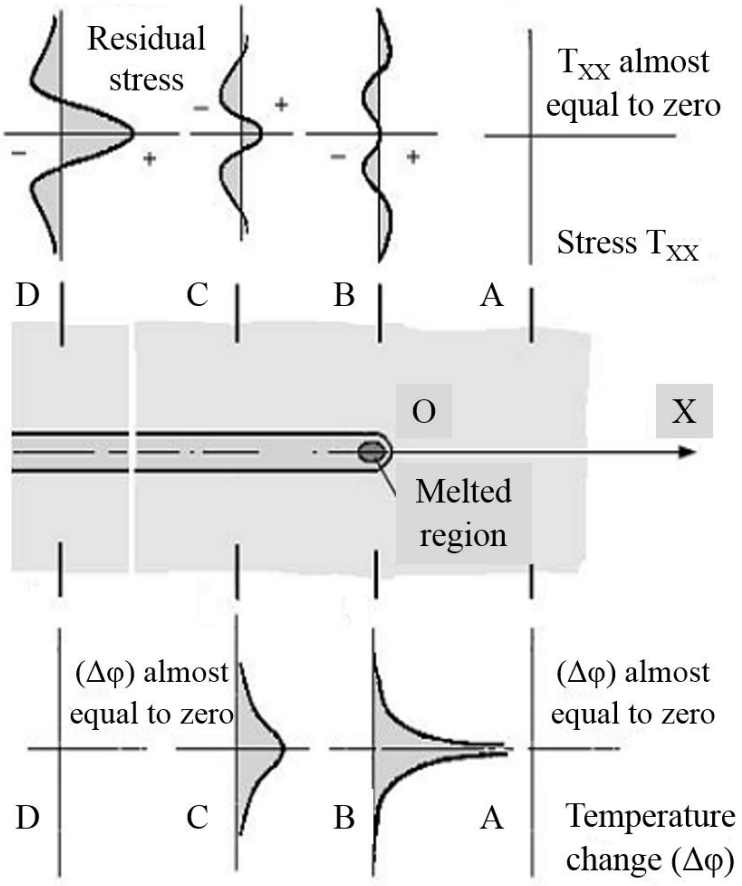

Figure 2.21: Changes of temperature and stresses during fusion welding [179].

2.5.2 Numerical modeling of welding induced distortions and residual stresses

The analytical model to predict weld distortion and residual stresses are based on some of the relevant physical processes and primarily suffer severe limitations in handling many of the real time features. The analytical model usually assumes constant material

properties for computing both temperature and the displacement fields. It is also difficult to consider complex geometry and restraints in standard analytical models.

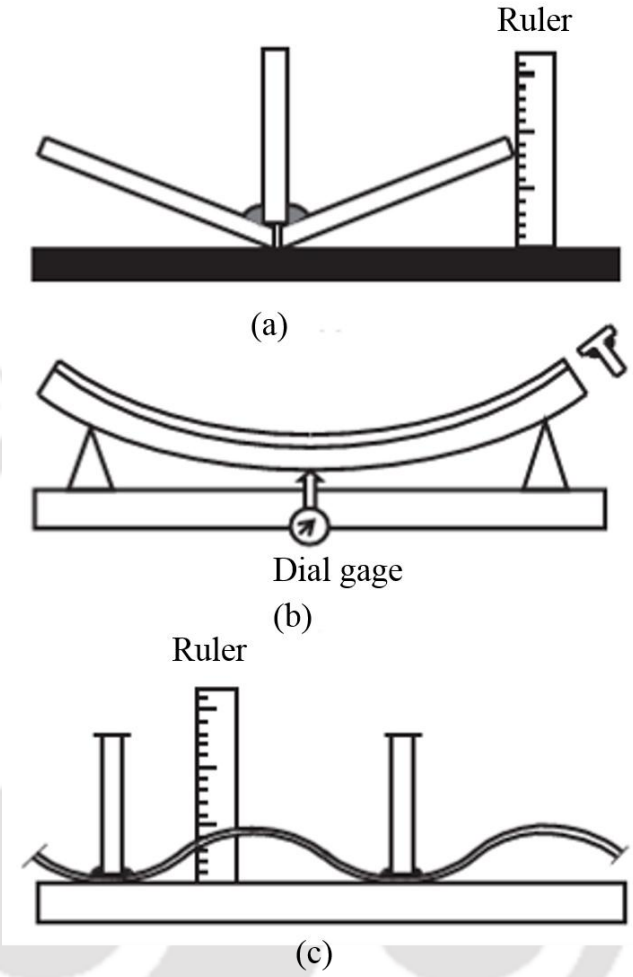

Figure 2.22: Distortion measurement in the post-weld cooled state: (a) angular distortion; (b) bending distortion; (c) angular shrinkage of panels welded with stiffeners [180].

Papazoglou et al. considered the effect of phase transformation in computing residual stresses of a typical butt-joint geometry [181]. Based on the calculated temperature history and the continuous cooling diagram of material, the authors firstly predicted the expected phases in the weld microstructure, and next, attained the phase transformation induced strain that also contributed to the total strain. Rybicki et al. suggested a set of empirical formulae to calculate the transverse distortion of square box beams in automotive structure [182]. The authors proposed from a large volume of experimental measurements that the distortion to be a function of the cross-sectional geometry of the beams and heat input. These empirical relations are still remaining specific to the type of joints, work piece materials and geometry,

and other associated conditions that are embodied in the experimental database. Shiva Prasad et al. presented a sequential thermal and mechanical analysis based on FE method during fusion welding process by considering the material properties as a function of temperature [183]. The authors show that the calculated values of longitudinal and transverse residual stresses were tensile near the weld and compressive away from the original weld interface.

Carmignani et al. [184] have studied the generation of the residual stresses during the deep penetration laser welding of the rectangular AISI 304 thick steel sheet which is used in ship building industry by using finite element method. Bang et al. reported a three dimensional thermal-elastic-plastic stress analysis to calculate welding induced distortion and residual stresses in resistance multi-spot welding using temperature dependent mechanical properties [185]. In this work, the authors presented both the longitudinal and the transverse residual stresses as tensile and was maximum in HAZ. Tsirkas et al. [171] developed a finite element model to predict the laser welded panel distortions. This work was achieved by performing a nonlinear heat transfer analysis using conical heat source model. The coupled thermo-mechanical analysis was performed considering the metallurgical transformations and using continuous cooling transformation (CCT) diagram.

Jung et al. proposed plasticity based distortion analysis (PDA) and established a relationship between the plastic strain and angular distortion [186]. In this method, the authors first carried out a thermal-elastic-plastic analysis to calculate temperature distribution and subsequently the temperature induced plastic strains distribution. The calculated plastic strain distribution was mapped into a thermo-elastic analysis by means of the equivalent incompatible thermal strains. Six components of cumulative plastic strains were mapped one by one into six elastic models by using corresponding temperature fields and six individual distortions were determined from the six elastic analyses. Finally, the authors calculated the total welding induced distortion by adding individual distortions induced by each cumulative plastic strain component. Deng and Murakawa [187] presented a computational procedure to calculate the temperature distribution and the residual stresses in multi-pass welds for SUS304 stainless steel pipe. In this analysis, the authors developed a finite element based uncoupled three dimensional (3D) and two dimensional (2D) axisymmetric thermo-mechanical models. Based on calculated results the authors recommended that temperature distribution and residual stresses of a 2D axisymmetric model are effective to predict the transient temperature field and residual stresses, and also the computational time is less for a 2D axisymmetric model as compared to 3D models.

Trivedi et al. [167] performed a transient heat conduction and thermo-mechanical analysis using an adaptive heat source for laser spot welding process. In this analysis, weld pool dimensions are calculated numerically using an adaptive heat source model considering the temperature dependent material properties and latent heat which is influenced during melting and solidification of the metal. Spina et al. [188] investigated the efficiency of the numerical analysis to predict the temperature profile, mechanical responses induced by the laser welding of AA5083 sheets. To investigate this work a three dimensional finite element model was developed to predict the temperature distribution and final distortions, and was compared with experimentally tested results. In thin plate welded structures, the welding distortion occurs due to relatively low stiffness. Deng et al. [189, 190] predicted the welding residual stresses and weld distortions in a low carbon steel butt welded joint of 1 mm thick plate by using a three dimensional thermo-elastic-plastic finite element based model. The experimental results were compared with simulated results.

Ermantani et al. [177] studied the effect of the thermal conductivity and weld efficiency on residual stresses. The longitudinal tensile residual stresses were large at weld bead and when the magnitude of the conductivity increased from 30 to 75 W. $(mK)^{-1}$ there was a reduction of stress by 15%. Deng [168] reported a reasonable better prediction technique for calculating the welding induced distortion and residual stresses of carbon steel including the effect of phase transformation. Ullah et al. [191] presented an analysis of the weld-induced residual stresses and distortions in thin-walled cylinders. In this study the weld-induced residual stresses and distortions were analyzed by a finite element based sequentially coupled thermal and mechanical model and calibrated the developed model with experimentally evaluated temperature distribution, residual stresses and distortions.

Asadi et al. [194] analyzed and predicted the residual stresses developed in GMA welding by using regression model and compared with experimental results for low carbon steel. Andrea et al. [192] presented a three dimensional model using ANSYS for thermo-mechanical analysis of laser and GTA welding processes. Ameen et al. [193] investigated the influence of the butt joint design on thermal stresses in GTA welding process for carbon steel. In this work, the butt welding was performed by different V-groove angles and suggested that the specimen with less than 6 mm thickness can be welded without edge angle preparation. Due to increase the thermal stresses in presence of edge angle, the higher thermal stresses distribution was at edge angle 60° and lowest thermal stresses distribution was at 90°. Lacki

and Adamus [195] estimated weld pool geometry, transient temperature field, residual stresses and distortions in electron beam welding process of 30HGSA steel tube.

It is thus clear that a rigorous thermo-mechanically analysis will be of significant help in understanding the welding induced distortion and residual stresses. The above discussion reveals the fact that the initial attempts were empirical and analytical which had significant limitations in terms of general use and reliability. The numerical models for calculating the welding induced distortion and residual stresses have shown a promise to be able to undertake most of realities that are present in real weld design. Two-dimensional numerical models have generally assumed plane-strain condition to calculate weld induced distortion and residual stresses that may not be appropriate for actual weld joint geometries. An accurate full scale three-dimensional thermal-elastic-plastic analysis is of great interest even till date.

2.6 Parametric optimization in fusion welding

One of the key problems of numerical modeling is to define the precise values of input parameters such as arc efficiency, effective arc radius, effective thermal conductivity, and viscosity. These input parameters are typically decided through huge volume of numerical trial-and-error exercises. These input parameters are not only temperature dependent but also system dependent due to the existence of high fluctuating velocities in small molten weld pool. Therefore, the exact value of these input parameters is difficult to ascribe through scientific principle alone. To overcome this problem, several researchers make an effort to identify the suitable time-averaged value of these uncertain input parameters through inverse approach [62, 196-198]. The inverse approach involves the integration of optimization algorithms with numerical process models (either transport phenomena based heat transfer and fluid flow model or conduction heat transfer analysis alone) to calculate the uncertain input parameters using the known experimental data. An initial attempt in this direction was reported in 1984 by Katz and Rubinsky [199]. They made an effort to find the transient position of the solid-liquid interface during stationary arc welding through a finite element based inverse modeling approach. In this effort, the authors utilized the measured temperature data from two thermocouples embedded in the solid region at different distances from the origin. At each time-step, the error between the calculated and the corresponding experimentally measured temperature data were realized and the solid-liquid interface was adjusted accordingly to diminish the prediction error.

De et al. [60, 62, 200] estimated the uncertain input parameters utilizing the experimentally measured weld pool dimensions using the inverse approach. They integrated an optimization module with numerical transport phenomena based heat transfer and fluid flow model to estimate the unknown parameters in an iterative manner starting from an initial guessed values. De and DebRoy [62, 196] evaluated optimized values of uncertain parameters such as effective viscosity, thermal conductivity, and absorptivity from a limited volume of experimental data during conduction mode laser welding process by utilizing an gradient based optimization scheme and a numerical heat transfer and fluid flow model. Bag et al. [197] calculated a set of uncertain model parameters for laser spot welding using a gradient based optimization algorithm. Trivedi et al. [198] reported an inverse approach to estimate laser absorptivity value using few experimentally measured weld pool dimensions.

Evolutionary optimization techniques such as genetic algorithm (GA) are proficient for finding the global minima by avoiding the local minima. Several researchers successfully utilized GA based optimization tools in manufacturing processes, in particular to estimate the uncertainty in numerical modeling of welding process. The key elements of GA are shown in Fig. 2.23. A GA typically operates through a simple cycle of four stages iteratively, (i) creation of a population of strings; (ii) evaluation of each string; (iii) selection of the best strings, and (iv) genetic manipulation to create a new population of strings. In recent past, the binary string form is further replaced by real number and a wide application of real number coded GA are observed in literatures. A brief description of three significant approaches in GA and their corresponding applications in enhancing reliability in numerical process models of fusion welding process are presented in subsequent sections. Deb et al. reported a review on real parameter based genetic algorithms which are usually described by an efficient recombination operator to create an offspring [65].

Ono et al. presented a mean centric unimodal normal distribution crossover (UNDX) operator that utilizes multiple parents and creates offspring around the center of mass of these parents [201]. Figure 2.24 (a) schematically represents three parents and a few offspring created by the UNDX operator. Higuchi et al. proposed the mean-centric simplex crossover (SPX) operator that allots a uniform probability distribution for generating offspring in a bordered search space around the area marked by the parents [202].

```
begin (1)
    t = 0;
    initialize P(t)
    evaluate P(t)
    While (Not termination-condition) do
    begin (2)
        t = t+1;
        select P(t) from P(t-1);
        recombine P(t)
        evaluate P(t)
  end (2)
end (1)
```

Figure 2.23: Key element of genetic algorithm.

A distinctive feature of the SPX operator as compared to the UNDX operator is that the SPX assigns a uniform probability distribution for generating any solution in a restricted region. Figure 2.24 (b) shows the density of solutions with three parents for the SPX operator. The SPX operator is computationally faster than the UNDX operator. Deb et al. further developed a parent-centric simulated binary crossover (SBX) operator that assigns a higher probability for an offspring and is closer to the parents. Afterwards, a parent-centric recombination (PCX) operator was proposed by using this parent-centric concept and modifying the UNDX operator [65]. Figure 2.24 (c) schematically represents the distribution of offspring solutions with three parents using PCX operator.

In addition to the recombination operator, the researchers have also realized the requirement of a population alteration model for real parameter optimization algorithm [63, 202-203]. Generally a minimum generation gap (MGG) has driven well for a host of GA schemes [65, 203]. In order to make the MGG model computationally faster, Deb et al. further improved a model, a generalized generation gap (G3) model, which substitutes the roulette-wheel selection operator of the MGG model with a block selection operator [65]. For the real parameter optimization through a number of analytical functions, the G3 model which is proposed by Deb and his coworkers is shown to be elite-preserving, a steady-state and computationally faster algorithm [65]. The G3 model with the PCX operator has performed better than the UNDX operator. The PCX operated G3 algorithm has been utilized for

estimating the uncertain parameters in modeling of several fusion welding processes [204-208]. Mishra et al. presented that multiple sets of process parameters can be realized for a target weld geometry by following the similar optimization procedure [204-206].

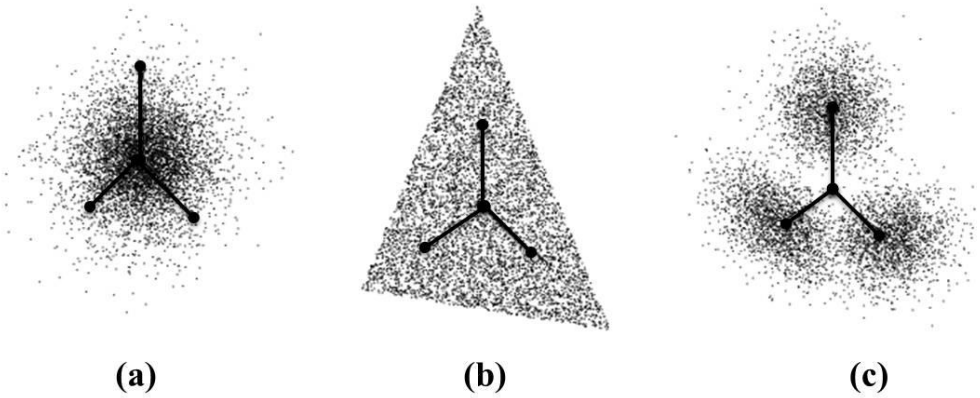

Figure 2.24: Recombination operators, (a) UNDX, (b) SPX and (c) PCX [65].

Differential evolution (DE) is also one of the most significant population based algorithm like GA and similar operators such as crossover, mutation and selection are used. The DE is proposed by Storn in 1997 [209-210] and the critical idea behind DE is a scheme for generating trial vectors. The basic difference between GA and DE is the fact that while DE relies on the mutation, GA relies on the crossover operation. The DE algorithm utilizes mutation operation as a search mechanism and the selection operation as direct search to the prospective regions in the search space. DE creates new vectors by adding the weighted difference between two population members to a third member. If the ensuing vector yields a lower objective functional value than a predetermined population member, the newly generated vector replaces the vector with which it has been compared. The comparison vector may or may not be part of the generation process. Moreover, the best parameter vector is estimated for each and every generation with the aim of keep track of the progress that is made during the minimization process. DE is useful to many engineering problems in different areas including welding process models [66-68, 210-211]. Nandan et al. utilized DE optimization tool to estimate the uncertain parameters during modeling of friction stir welding process by integrating FE model with optimization tool [68].

In numerical modeling of fusion welding process, the input model parameters such as arc efficiency, effective thermal conductivity, arc radius and effective viscosity cannot be assigned with confidence based on scientific principle alone. But, the parameters like welding power, welding speed etc. can be correctly specified. To estimate the correct values of

uncertain model parameters, an effort towards integration of suitable optimization tool with numerical model is required. Some of the important efforts by several researchers have been outlined in this section along with a brief description of the optimization tool. In the present work, the author also estimated the uncertain model parameters by integrating the transport phenomena based heat transfer and fluid flow model with suitable optimization tool.

2.7 Summary

This chapter provides significant efforts towards understanding the effect of ambient atmosphere and keyhole formation during fusion welding processes, specifically laser and GTA welding processes. The understanding of phenomenological mechanism of heat transfer and fluid flow analysis in fusion welding process with an aim to accurately estimate the time-temperature history and influence of surface active elements during fusion welding processes are illustrated in this chapter. The thermo-mechanical modeling of fusion welding process along with optimization of uncertain input parameters for the development of reliable numerical model are covered here. The literature review on the subject acts as a platform to decide the scope of present work.

2.8 Scope of Present Work

Based on the survey of existing work in literatures, the objective of the present work is outlined as follows.

- The initial aim of the present work is the development of a conduction mode heat transfer model in autogeneous fusion welding process. The most instinct phenomenon of conduction mode heat transfer analysis is the model of the heat source. Present work introduces a novel concept of ‘egg’ configuration heat source model for simulation of fusion welding process. It is proved that the use of such egg-configuration volumetric heat source term will enhance the scope of utilization of the conduction heat transfer based analysis in fusion welding process. The formation of keyhole is often neglected in conduction mode heat transfer analysis for high power density laser welding process. There is a scope to estimate the keyhole profile using a mathematical model for deep penetration fiber laser welding process.
- However, only heat conduction analysis might not be sufficient to consider the effect of surface-active elements. In the liquid metal flow, the most significant driving force is the

surface tension force and it is incorporated through temperature- and concentration-dependent coefficients of surface tension. It is, therefore, significant to examine the effect of oxygen as a surface-active element on the development of weld pool during autogenous GTA welding process. In this effect, three dimensional heat transfer and fluid flow model is necessary to analyze the effect of flow dynamics during formation of weld pool.

- The numerical heat transfer and fluid flow model (or only the conduction heat transfer models) in fusion welding process often fails to offer the reliable predictions due to uncertainty of input variables that are necessary to define preciously for modeling calculation. In general, the values of such input parameters are obtained either from past experience or through a huge volume of numerical experiments. Such input parameters can be realized by integrating the numerical process model within the kernel of optimization algorithm. The present work is aimed at finding the input model parameters which is necessary in transport phenomena based heat transfer and fluid flow model by integrating the numerical model with GA based optimization module.
- During fusion welding process, thermo-chemical reactions occur between weld pool and working atmosphere that severely affects the weld metal properties and weld joint quality. Therefore, the welding atmosphere influences notably on the quality of the weld joint. In present work, the welding of austenitic stainless steel using a 2 kW ytterbium fiber laser under controlled atmosphere of argon as well as in open atmospheric condition are investigated. The characteristic difference in terms of weld pool shape and size, and quality of joint at various process parameters under controlled atmosphere of argon is being compared with that of open atmospheric condition. Also, there is a scope to enhance the penetration depth for GTA welding process and the same is achieved by investigating the influence of different activating flux during formation of the weld pool.
- Most of the mechanical models used to calculate distortion and residual stress that relied on conduction heat transfer analysis and such analysis are performed with temperature independent material properties and practically for bead-on-plate welding. The reliability of the calculation of temperature field is the primary motivation of the present work that can be used to calculate the distortion and residual stress in fusion welding process in accurate manner. Present work is aimed at the prediction of weld induced distortion of fiber laser welding process in butt joint configuration.

Chapter – 3

Theoretical Background

3.0 Introduction

The fusion welding process involves complex physical phenomena that include heat transfer, material flow and distortion in welded structure after solidification. The theoretical basis of heat transfer, fluid flow, distortion and residual stress in deep penetration fusion welding processes are illustrated in this chapter. A comprehensive numerical heat transfer model is developed based on finite element method using Gaussian distributed volumetric heat source. One of the most intricate phenomena in the welding science is the model of 'heat source'. By addressing the shortcomings and deficiencies of the previous heat source models, a new heat source model is developed to simulate temperature distribution in autogenous fusion welding process. However, the mechanism of keyhole formation is different from conduction mode laser welding and GTA welding processes. Hence a semi-analytical model is developed to estimate the keyhole shape and size in deep penetration fiber laser welding

process. A well tested thermo-fluid model is also utilized to investigate the influence of surface active elements in GTA welding process. Afterwards, a coupled thermo-mechanical analysis is performed to estimate the distortion and residual stress of a welded joint.

One of the sensitive parts of weld pool simulation is to identify the definite set of input parameters that can be defined in confidence. In addition to the welding process variables, work-piece geometry and material properties, the heat transfer and fluid flow calculations require an additional set of model parameters as input which cannot be stated with confidence based on the scientific principle alone. The most appropriate values of some of these significant uncertain parameters are estimated by integrating a GA (genetic algorithm) based global optimization module with the numerical model. A real parameter based genetic algorithm, PCX operated G3 model and DE (differential evolution) are used here that minimizes the sensitivity of the error in the prediction of weld bead dimensions. These are obtained from a few known set of welding experiments and are identified their suitable values. The optimized values of these unknown parameters are then used with more reliably for the conduction heat transfer and fluid flow calculations at similar welding conditions.

3.1 Conduction mode heat transfer analysis

The conduction mode heat transfer analysis is often preferred due to reduced amount of computational time, ease of modeling and ease of coupling with stress analysis model. To approximate the influence of convective heat transport within weld pool, the volumetric heat is often used in conduction based heat transfer model. The thermal conductivity of the molten material is increased artificially in several folds to account the enhanced heat transfer due to high convective flow of liquid molten metal within the weld pool [167, 212-213].

In the present work, the conduction heat transfer, convective heat transfer and thermo-mechanical models are developed in three-dimensional Cartesian coordinate system. The integrated heat transfer and fluid flow process model is developed to investigate the influence of surface active elements in linear GTA welding process. Moreover, conduction heat transfer based thermo-mechanical model is used to analyze the thermal and mechanical behaviour of linear GTA and laser welding processes. It can further be pointed out that a pseudo-steady state heat transfer analysis is required for linear welding processes where the heat source moves at constant velocity with respect to the work-piece. The mathematical background and theoretical formulation to develop both the transient and steady-state heat transfer analysis

using volumetric heat source is presented in the following sections. The corresponding formulation for the transport phenomena based convective heat transport analysis and thermo-mechanical analysis are presented subsequently.

The governing equation and the boundary conditions that are followed for 3D transient conduction heat transfer analysis and their discretization using finite element method are presented in this chapter. The following assumptions are made for the development of a numerical heat transfer model:

- Due to symmetric nature of the problem, only one-half of the solution geometry is considered in present work that effectively reduces the computational time. However, in some cases the full plate is considered for thermo-mechanical analysis.
- The heat input is considered as Gaussian distributed over the double ellipsoidal and conical shape. In addition, a new heat source model is developed for the simulation of conduction mode fusion welding process and same is used for transient heat transfer analysis.
- Temperature dependent thermal conductivity and specific heat, constant density and emissivity are considered for simulation.
- The initial temperature of the work piece is assumed as 300 K.
- The convection and radiation heat losses from the surfaces of work piece are taken into account by considering 'lumped' heat transfer coefficient [30, 37].
- To avoid computation complexity for free surface modeling, the top surface of the welded sample is considered as flat.

If Y-axis is considered the moving coordinate axis of laser beam or gas tungsten arc with velocity 'v', the heat conduction equation can be stated in a Cartesian coordinate system as:

$$k_m\left(\frac{\partial^2 \mathrm{T}}{\partial \mathrm{x}^2}+\frac{\partial^2 \mathrm{T}}{\partial \mathrm{y}^2}+\frac{\partial^2 \mathrm{T}}{\partial \mathrm{z}^2}\right)+\dot{\mathrm{Q}}=\rho \mathrm{C_p}\left(\frac{\partial \mathrm{T}}{\partial \mathrm{t}}-\mathrm{v}\frac{\partial \mathrm{T}}{\partial \mathrm{y}}\right) \tag{3.1}$$

where (x, y, z) is coordinate system attached to the heat source, k_m is the thermal conductivity of the material (W m^{-1} K^{-1}) and is given by the following equation to compensate the fluid flow of the molten material as

$$k_m=\begin{cases} k_o & T<T_m \\ k_o+k' & T\geq T_m \end{cases} \tag{3.2}$$

where k_o is the thermal conductivity of the material used; k' is the additional value by which the convection heat transfer capability is equally considered in the thermal model; T_m is the

melting point of the material used. T is the temperature variable (K), $\dot{Q}$ is the rate of heat generation per unit volume (W m^{-3}), ρ is the density of the material (Kg m^{-3}), C_p is the specific heat capacity of the material (J kg^{-1} K^{-1}), t is time variable (s) and v is the welding velocity (m s^{-1}). The first three terms on the left side of equation (3.1) refer to the conductive heat transfer in x, y and z direction, respectively. The term on the right side of equation (3.1) depicts the transient nature of the heat transfer process.

Figure 3.1 schematically refers to the solution domain and applied boundary conditions on a transverse cross-section of the welding plate. The temperature gradient normal to the weld interface is zero. The top surface of the plate is subjected to heat flux which is due to welding heat source (laser beam or gas tungsten arc) and rest of the surfaces are subjected to convection and radiation heat losses other than weld interface or symmetric surface. The natural boundary condition can be represented mathematically as:

$$k_n \frac{\partial T}{\partial n} - q + h(T - T_0) + \sigma\varepsilon(T^4 - T_0^4) = 0 \quad (3.3)$$

where σ, ε, k_n, q, h, and T_o illustrates Stefan-Boltzmann constant, emissivity, thermal conductivity normal to the surface, imposed heat flux onto the surface, convection heat transfer coefficient, and ambient temperature respectively. To avoid non-linearity in radiation term, a lumped heat transfer coefficient which accommodates both convection and radiation heat losses is considered in present work. The lumped heat transfer coefficient is expressed as [30, 37]

$$h_{eff} = 2.4 \times 10^{-3} \times \varepsilon \times T^{1.61} \quad (3.4)$$

where T is temperature (K), h_{eff} is lumped heat transfer coefficient and ε is emissivity. Therefore, equation (3.3) is modified as

$$k_n \frac{\partial T}{\partial n} - q + h_{eff}(T - T_o) = 0 \quad (3.5)$$

The initial condition for the transient heat transfer analysis of welding process is stated at time t = 0

$$T(x, y, z, 0) = T_o \quad (3.6)$$

where T_o is the initial temperature of the work piece.

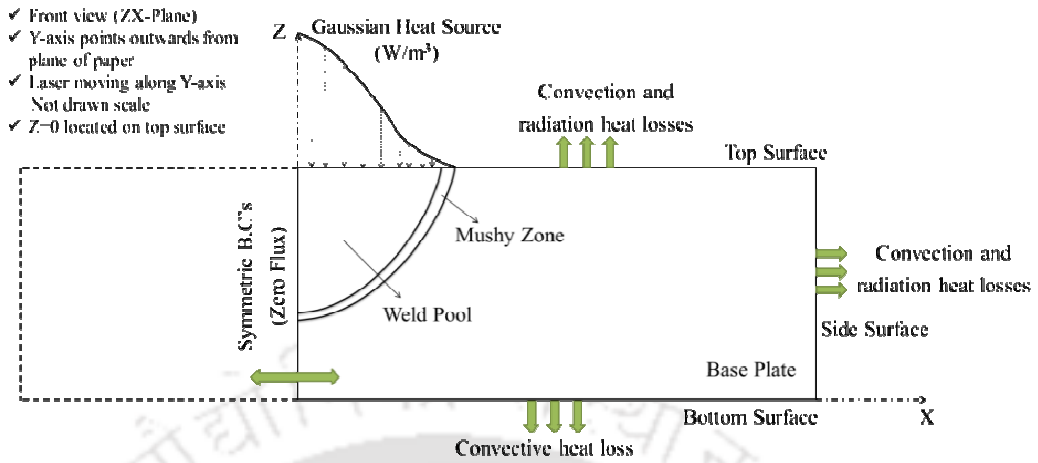

Figure 3.1: Schematic representation of solution domain along with applied boundary conditions.

3.1.1 Heat source in fusion welding

The distribution of heat flux at the work piece surface exposed to a real source can be described by Gaussian or normal distribution [24]. However the heat transport by convection may play a significant role for the distribution of energy within the weld pool volume. It is a common practice to define a volumetric energy distribution that acts as a heat source to solve only the heat conduction equation by eliminating the effect of more comprehensive fluid flow phenomena [30, 214]. Several developments have been achieved to design appropriate heat source model from case-to-case basis and type of fusion welding processes. The Gaussian distribution of power density is good approximation for most of the fusion welding processes. The amount of heat deposition depends on the overall shape and dimensions of the defined volume of heat source. Also the defined volume decides the symmetric or non-symmetric nature of heat energy with respect to the center of heat source.

A Gaussian distributed double ellipsoidal heat source has been implemented in numerical model [30]. Figure 3.2 (a) schematically illustrates the double ellipsoidal volumetric heat source. The volumetric heat source actually compensates the effect of liquid metal flow within the weld pool [30, 140]. It is obvious from Figure 3.2 (a) that the rear half of the source is a quadrant of one ellipsoid whereas the front half is a quadrant of another ellipsoid. The four parameters, a_r, a_f, b, c define this heat source model. Physically, these heat source model parameters correspond to weld bead dimensions that can be determined by knowing the weld dimensions from experimental observation [30]. When the laser beam

and/or arc moves along Y-direction, the power density distribution for front and rear portions can be represented as

$$q_f(x,y,z,t) = \frac{6\times(3)^{1/2}\times Q\times f_f}{a_f\times b\times c\times(\pi)^{3/2}} \times e^{-3x^2/a_f^2}.e^{-3(y)^2/b^2}.e^{-3z^2/c^2} \quad (3.7)$$

$$\text{and } q_r(x,y,z,t) = \frac{6\times(3)^{1/2}\times Q\times f_r}{a_r\times b\times c\times(\pi)^{3/2}} \times e^{-3x^2/a_r^2}.e^{-3(y)^2/b^2}.e^{-3z^2/c^2} \quad (3.8)$$

where f_f, f_r are the fractions of the heat deposited in front and rear parts of the double ellipsoid. a_r, a_f, b, and c are double ellipsoidal heat source parameters. The actual heat input which causes heating and melting of the work piece is expressed as

$$Q = \eta \times P \quad \text{or} \quad Q = \eta \times V \times I \quad (3.9)$$

where P, η, V and I depict the laser power, laser absorption coefficient or efficiency, welding voltage and current respectively. The sum of the fraction of heat deposition parameter (front and rear) satisfies the following equation.

$$f_f + f_r = 2 \quad (3.10)$$

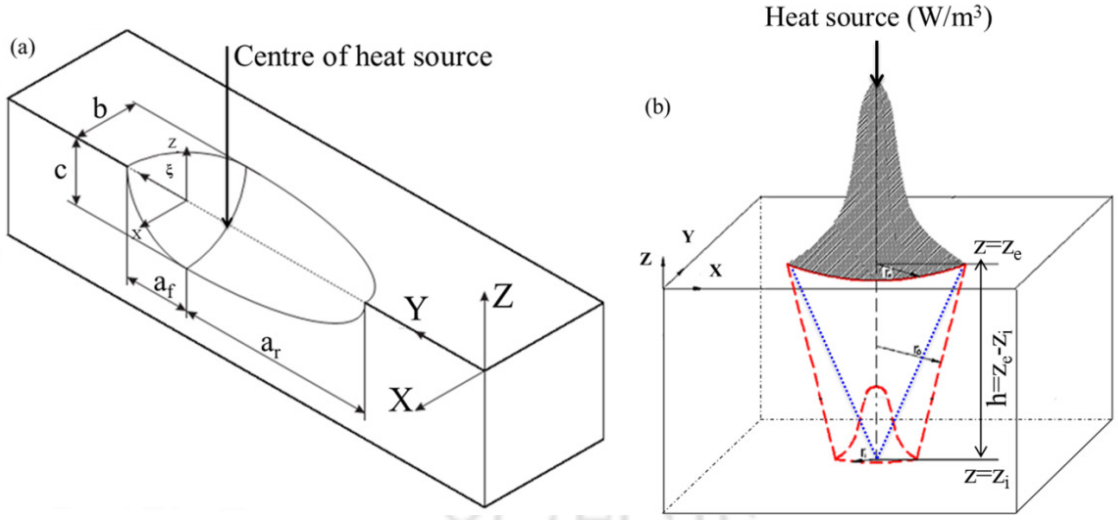

Figure 3.2: Representation of heat source model: (a) double ellipsoid and (b) conical heat source.

In case of controlled atmosphere of argon laser welding simulation, the heat density distribution is assumed Gaussian in radial direction and a linear distribution along one axis over the volumetric shape of truncated cone. Figure 3.2 (b) represents the conical heat source model. In this heat source model, the volumetric heat source exerted along the plate thickness depends on two assumptions: the heat intensity deposited region is minimum at the bottom

surface and maximum at the top surface of the work piece and the diameter of the heat density distribution region is linearly decreased along the thickness direction. At any plane perpendicular to the central axis is kept constant. So, this heat source model is the repeated addition of a series of Gaussian heat sources with various distribution coefficients and the same central maximum values of heat density along thickness of work piece. The heat flux distribution at any plane perpendicular to the z-axis can be written as

$$q_v(r,z) = q_{max}\exp\left[-\frac{3\times r^2}{r_o^2(z)}\right] \tag{3.11}$$

where q_{max} is the maximum value of the heat intensity, r_o is the distribution coefficient and r is the radial coordinate. The height of the conical heat source is h is equal to z_e- z_i; here z_e and z_i are the top and bottom surface z-coordinates respectively. The distribution coefficient r_o can be expressed as:

$$r_o(z) = r_e - (r_e - r_i) \times \frac{z_e - z}{z_e - z_i} \tag{3.12}$$

When r_i is zero, equation (3.12) become as

$$r_o(z) = r_e - r_e \times \frac{z_e - z}{z_e - z_i} \tag{3.13}$$

The heat intensity in conical heat source model takes the form

$$q_v(r,z) = \frac{9\times P\times \eta\times e^3}{\pi\times(e^3-1)} \times \frac{1}{(z_e-z_i)\times(r_e^2+r_e r_i+r_i^2)} \times \exp\left(-\frac{3\times r^2}{r_o^2}\right) \tag{3.14}$$

Similarly, when r_i is zero, Eq. (3.14) become as given below

$$q_v(r,z) = \frac{9\times P\times \eta\times e^3}{\pi\times(e^3-1)} \times \frac{1}{(z_e-z_i)\times(r_e^2)} \times \exp\left(-\frac{3\times r^2}{r_o^2}\right) \tag{3.15}$$

where P is the laser power (W) and ŋ is the laser absorption coefficient.

3.1.2 Development of 'new heat source' model

The proposed heat source model in this investigation is an egg-like configuration which can be obtained from the modification of ellipsoid shape. In order to present the current heat source model, the detailed description of the Pavelic's [24] and of the Friedman's [136] model are required and explained in *Appendix I*.

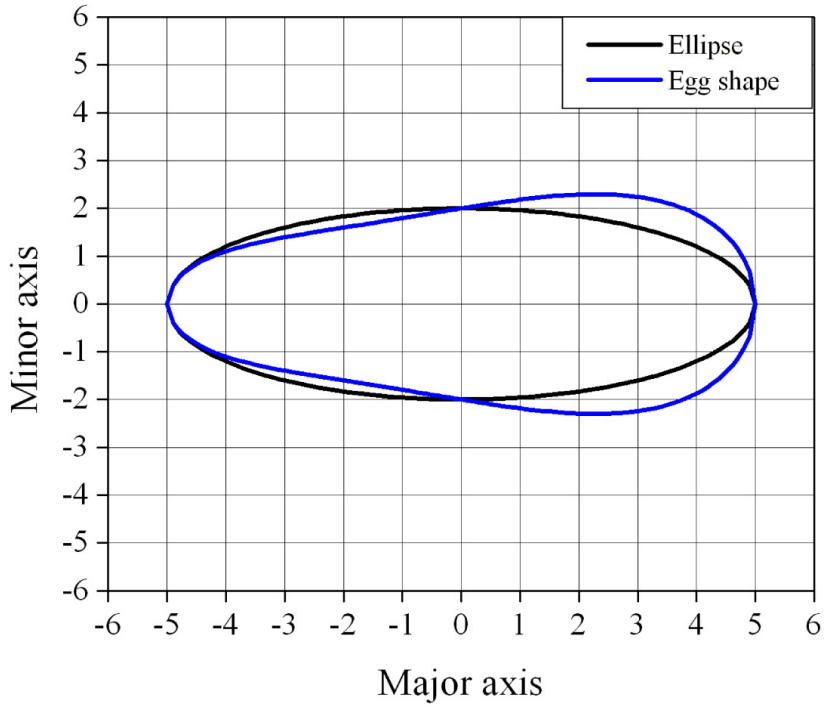

Figure 3.3: Comparison of 2D egg shape and ellipse with same semi-axes: ellipse and egg shape with m = 0.2.

The egg-like shape is generally represented by modifying the basic shape of ellipsoid through demolition of symmetric profile. This modification is incorporated by using several types of equations i.e. linear, quadratic, exponential etc. over basic shape of ellipsoid. Usual properties of an egg configuration are symmetry about one axis, smaller at one end, convex nature, and have a positive curvature [215, 216]. The three dimensional egg-shape in Cartesian coordinate system is defined by modifying the ellipsoidal as

$$\frac{y^2}{b^2} + \left\{\frac{x^2}{a^2} + \frac{z^2}{c^2}\right\} \times \{t(y)\} = 1 \qquad (3.16)$$

where (x, y, z) is a local coordinate system which moves with the heat source along direction 'y'. The semi-axes lengths of ellipsoid are a, b, c and the function t(y) decides the shape and degree of asymmetry of an egg-curve when the velocity vector of heat source is along 'y' direction. The definition of equation (3.16) is limited that the heat source moves along a fixed direction (here, Y –direction). If the heat source moves along 'x' direction, the definition of heat source need to be changed according to local coordinate system and the functional form of t(y) needs to be changed to t(x). It is noteworthy that several functional form of t(y) is also possible [216]. The temperature distribution or fusion zone shape for a moving heat source is symmetric with respect to the axis along which the welding torch (normal to work-piece

surface) moves with constant velocity. Figure 3.3 depicts the 2D ellipse and egg shape curves and comparison between them with same semi axes lengths. It is obvious that the profile of egg-curve is non-symmetrical as compared to ellipse and it can be used advantageously for a moving heat source case. The Gaussian distribution of the power density in a proposed egg shape configuration heat source model with the center at (0, 0, 0) and semi-axes a, b, c parallel to coordinate axes x, y, z can be stated as

$$q(x,y,z) = q_m e^{-[By^2+(Ax^2+Cz^2)t(y)]} \quad (3.17)$$

where q_m is the maximum value of the power density at the center of a proposed egg shape and A, B, C are the distribution parameters. The parameter t(y) decides the geometric shape of egg-like heat source and this function is included within the equations (3.16) and (3.17) since the arc or laser moves linearly along Y- direction. Moreover, t(y) actually modifies the distribution of volumetric heat flux density. Presently, the functional form is considered as

$$t(y) = \frac{1}{my+m^2y^2+1} \quad (3.18)$$

where the term 'm' intuitively decide the shape of egg. It is true that several form of shape factor t(y) is possible such as linear, quadratic, exponential etc. The choice of specific functional form t(y) is arbitrary that makes easy to apply improper integral for this specific problem. The introduction of the term "m" actually generalizes the equation (3.18) rather than fixing a numerical value.

Figure 3.4 describes the sensitivity of the shape of egg with change of "m" value and semi-axis length. This sensitivity analysis actually helps to identify the proper value of "m" for a specific shape of weld pool. Moreover, the linear term in eq. (3.18) "my" brings the non-uniformity in power density distribution and dissimilar geometric shape along positive and negative y axis.

Figure 3.4 shows that there is change of egg shape with different values of 'm' with similar semi-axis length. At m = 0, the equation (3.16) reduces to an ellipse which is a special case for stationary hear source. In this study the 'm' is considered as constant for all welding conditions. The choice of 'm' intuitively depends on the best mapping of weld pool shape for all experimental conditions. Figures 3.5 (a) and (b) show the shape and size of egg-configuration heat source model for different experimental conditions depicted in Table 4.15 (c) corresponding to constant 'm' value of 0.2.

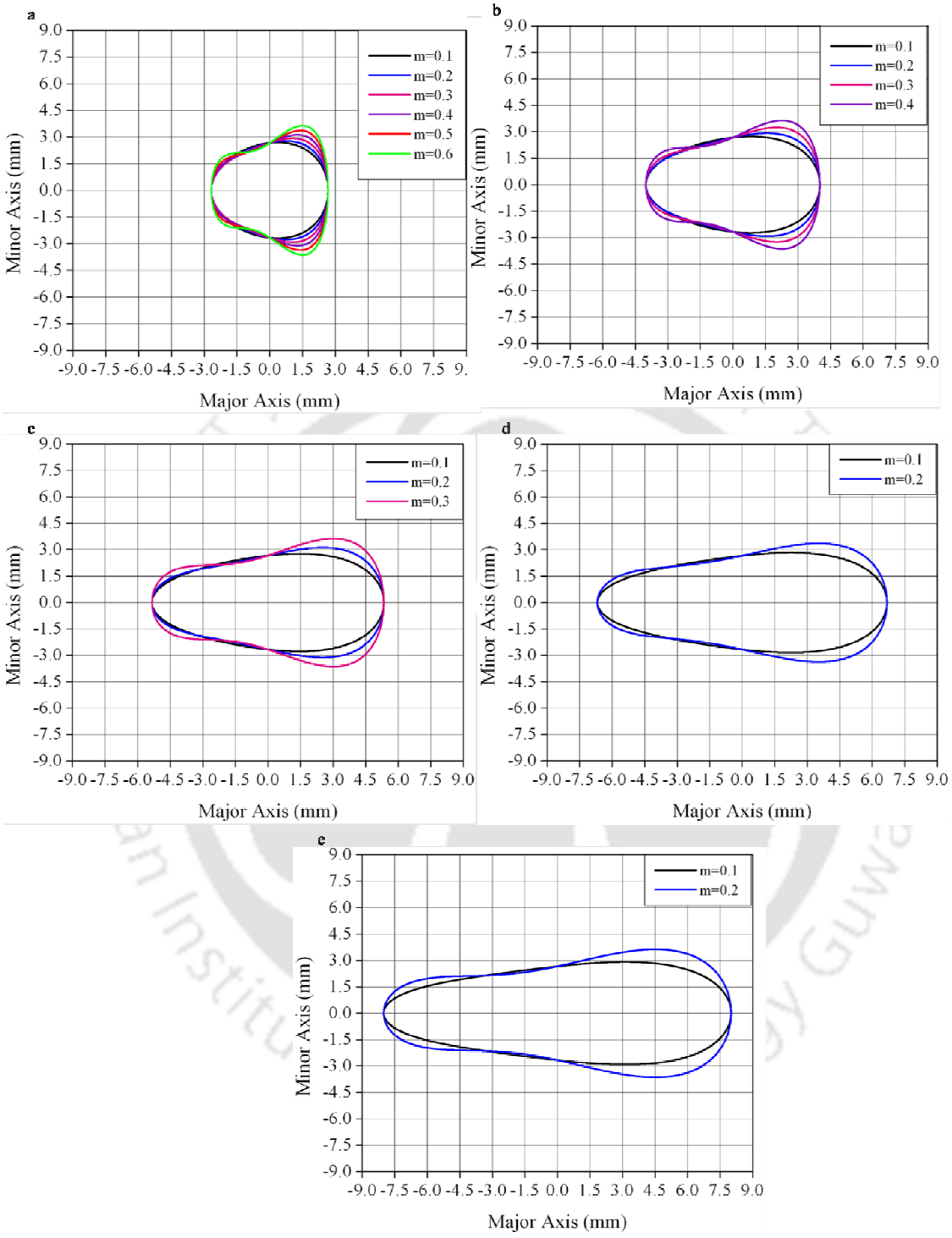

Figure 3.4: Egg configuration at different values of m and ratio between major and minor axis length: (a) ratio = 1, (b) ratio = 1.5, (c) ratio = 2.0, (d) ratio = 2.5 and (e) ratio = 3.0.

It is noteworthy that the mapping of the weld pool shape and size are performed on the basis of two experimentally measured parameters i.e. width (along X axis) and depth (along Z

axis) without much information about the length (along Y-axis) since it is difficult to measure experimentally after welding is done. However, the choice of 'm' is quite arbitrary which is best suited on the basis of sensitivity analysis of 'm' on egg-shape (Fig. 3.4) for all welding conditions used in present simulation.

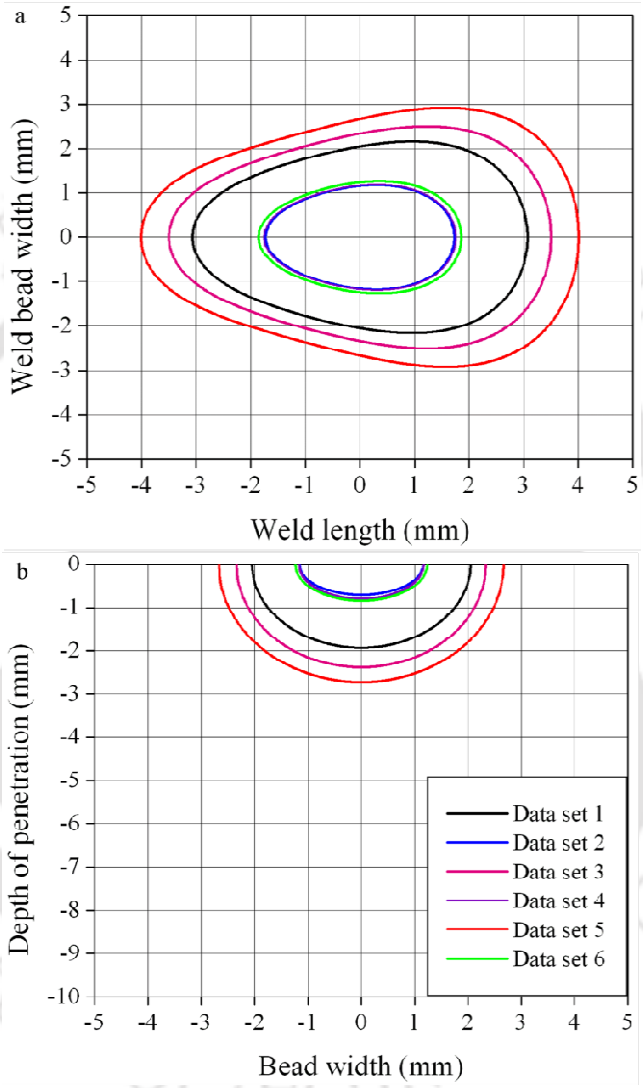

Figure 3.5: 2D Egg configuration for m = 0.2 and ratio = 1.5 (b:a) corresponding to experimental data set of Table 4.15 (c): (a) XY- plane and (b) YZ plane.

The maximum heat flux density at the center (q_m) is calculated from the conservation of energy over the half volume of egg which is symmetric with respect to x-y plane. Therefore, total volumetric energy distributed over the half of egg is expressed as

$$2Q = \int_{-\infty}^{\infty}\int_{-\infty}^{\infty}\int_{-\infty}^{\infty} q(x,y,z)\,dx\,dy\,dz \qquad (3.19)$$

where Q is the net heat input to the solution domain. It is noteworthy that the heat source is unbounded in this case and the distribution of heat density dies out from the boundary of geometric shape. By integrating equation (3.19), the maximum power density is expressed as

$$q_m = \frac{4BQ\times\sqrt{ABC}}{\pi\sqrt{\pi}(2B+m^2)} \tag{3.20}$$

The total heat input into the system is expressed as

$$Q = \eta VI \quad \text{or } Q = \eta P \tag{3.21}$$

where η is the arc efficiency or laser absorption coefficient. To estimate A, B, C, the semi-axes of a proposed egg-shape a, b, c in the x, y, z directions respectively, are defined such that the heat density falls to $0.05q_m$ at the surface of the egg-shape. The distribution parameters are estimated as (refer *appendix I*)

$$A \approx \frac{3}{a^2}\ ;\ B \approx \frac{3}{b^2};\ C \approx \frac{3}{c^2} \tag{3.22}$$

Therefore q_m can be expressed in terms of a, b, and c as given below

$$q_m = \frac{36\sqrt{3}Q}{\pi\sqrt{\pi}\times abc(6+m^2b^2)} \tag{3.23}$$

The volumetric distribution of heat intensity in moving coordinate system (x, y, z) within the egg-shape is expressed as

$$q(x,y,z) = \frac{36\sqrt{3}Q}{\pi\sqrt{\pi}\times abc(6+m^2b^2)} \times e^{-\left[\frac{3y^2}{b^2}+\left(\frac{3x^2}{a^2}+\frac{3z^2}{c^2}\right)\times\left(\frac{1}{my+m^2y^2+1}\right)\right]} \tag{3.24}$$

Physically the heat deposition in front and rear part of the egg-shape should not be the same due to welding speed in one specific direction. It is also evident from the shape of egg that heat deposition in front and rear are different. To take into the effect of uneven heat distribution, the heat density distribution inside the front section can be expressed as

$$q_f(x,y,z) = \frac{36\sqrt{3}QN_f}{\pi\sqrt{\pi}\times abc(6+m^2b^2)} \times e^{-\left[\frac{3y^2}{b^2}+\left(\frac{3x^2}{a^2}+\frac{3z^2}{c^2}\right)\times\left(\frac{1}{my+m^2y^2+1}\right)\right]} \tag{3.25}$$

where N_f is the fraction that accounts the amount of heat deposited in front portion. In similar way N_r accounts the heat deposition in rear part of the arc or laser beam. Therefore, the total energy is expressed as

$$Q = \eta VI = \frac{1}{2}(N_fQ) + \frac{1}{2}(N_rQ) \tag{3.26}$$

$$\text{i.e. } N_r + N_f = 2 \tag{3.27}$$

However, the deterministic value of N_r and N_f can be expressed in terms of model parameters (m and b) and is shown in Appendix I. Since the model parameter 'b' changes according to the welding conditions, the values of N_f and N_r changes accordingly and always satisfy the relation of equation (3.27). It is noteworthy if 'm' value is equal to zero then the power density becomes equal to power density of semi-ellipsoidal heat source model. However, the semi-ellipsoidal heat source model is generally used for stationary arc or laser where symmetrical heat source profile is important with respect to the centre of heat source [30, 42, 126]. The heat intensity distribution is non-symmetrical with respect to the centre of heat source in egg-like shape since the total heat energy (Q) for rear or front part is not symmetrical. This is due to fact that the volumetric shape and size with respect to centre of heat source is not symmetrical and in this way it is different from semi-ellipsoidal heat source model. This fact also provokes to define the fraction of heat deposited in front and rear (N_f and N_r) which are considered in equation (3.25). Figure 3.6 describes three dimensional asymmetric power density distribution over egg configuration on half of the welding plate.

It is obvious that all other different heat source models such as disc and ellipsoidal [24, 30, 139, 146] are the subsets of proposed egg-shape heat source model. When the heat source moves along the y-axis then the heat density distribution inside the front part of the proposed egg-shape configuration in a fixed coordinate can be expressed as

$$q_f(x,y,z,t) = \frac{36\times\mathrm{sqrt}(3)\times Q\times N_f}{\pi\times abc\times\mathrm{sqrt}(\pi)\times[6+b^2m^2]} \times e^{-\left[\frac{3(y+v(\tau-t))^2}{b^2}+\left(\frac{3x^2}{a^2}+\frac{3z^2}{c^2}\right)\times\left(\frac{1}{m(y+v(\tau-t))+m^2(y+v(\tau-t))^2+1}\right)\right]} \quad (3.28)$$

where v, and τ depict the welding speed, and a lag factor. The lag factor τ is used to define the position of heat source at time t = 0 on fixed coordinate system (x, y, z).

3.1.3 Keyhole mode laser welding

In this section, the mathematical background of keyhole model in laser welding is presented. The keyhole profile can be estimated using a mathematical model that contemplates energy balance on liquid-vapor interface where the following assumptions are considered:

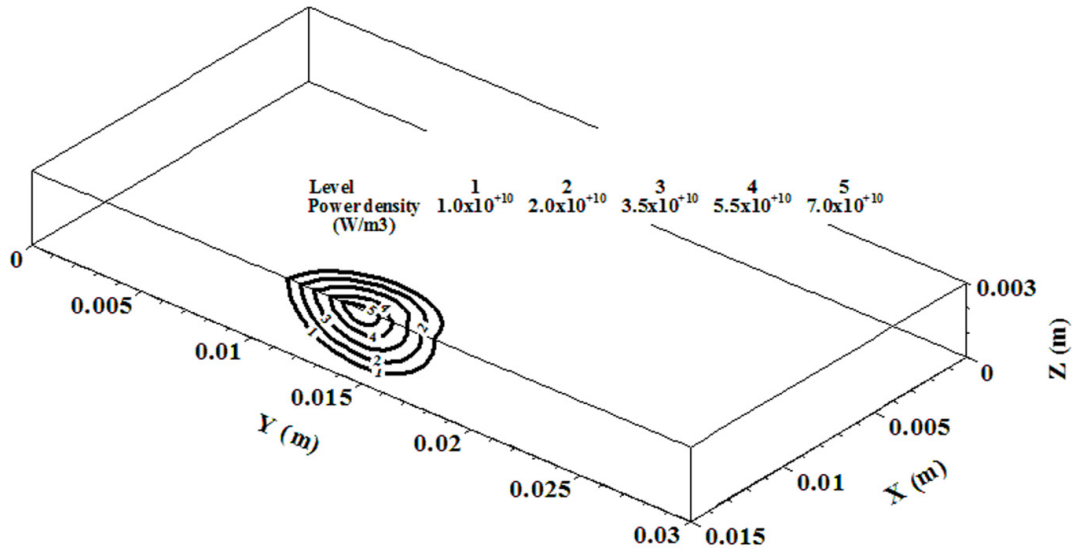

Figure 3.6: Schematic representation of 3D power density distribution over egg shape configuration in solution domain.

- It is assumed that the boiling point of the alloy is equal to the temperature on the keyhole wall. Since the keyhole is open to the atmosphere, at this temperature, the summation of the equilibrium pressures of all alloying elements is 1 atm.
- In the direction at right angles to the fiber laser beam axis along horizontal plane, heat transfer rate is much larger than those parallel to the laser beam axis. The heat is transported mostly along the horizontal plane because the surface temperature on keyhole wall is the boiling point of the alloy and the keyhole is oriented almost vertically.
- The keyhole surface is assumed to be free of oxides and Fresnel absorption coefficient is considered to be constant at all locations on the surface.

For estimating the keyhole geometry, four different groups of input data are required such as geometrical parameters, welding process variables, alloying material properties and computational model parameters. The output of the model contains the geometry of the keyhole profile if a stable keyhole is formed and the profile of keyhole is estimated based on point-by-point energy balance on the keyhole wall [5, 6].

3.1.3.1 The energy balance on keyhole wall

Figure 3.7 describes schematically the energy balance at keyhole walls of an infinitely small thick zone. A relationship exists between the net absorbed energy flux, I_{na}-I_{nv}, and the

heat flux conducted into the metal, I_{nc}. The local keyhole wall angle 'θ' is calculated by the heat balance on keyhole wall as given below

$$(I_{na} - I_{nv}) \times \sin\theta = I_{nc} \times \cos\theta \quad (3.29)$$

Hence the local keyhole wall is estimated as

$$\tan\theta = \frac{I_{nc}}{I_{na} - I_{nv}} \quad (3.30)$$

where I_{na}, I_{nc} and I_{nv} depict locally absorbed beam energy, radial heat flux conducted into the keyhole wall and evaporative heat flux on the keyhole wall respectively.

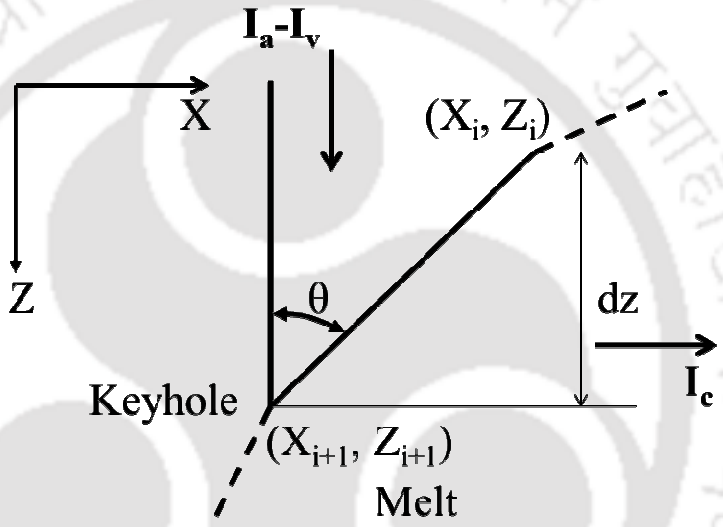

Figure 3.7: Schematic representation of energy balance at keyhole walls and the relationship between the net absorbed energy flux, I_a-I_v, and the heat flux conducted into the metal, I_c [6].

3.1.3.2 Estimation of I_{na}, I_{nv}, and I_{nc}

I_{nc} can be calculated from a two-dimensional temperature field in an infinite plate with reference to a linear welding heat source and is given as follows

$$I_{nc}(r, \emptyset) = -\mathcal{K}_n \frac{\partial T(r,\emptyset)}{\partial r} \quad (3.31)$$

where$(r, \emptyset)$, $\mathcal{K}_n$ and T represents location in the plate with line source as the origin, thermal conductivity and temperature variable respectively. Two dimensional temperature field can be

estimated by considering the conduction of heat from the keyhole wall into the infinite plate as [29]

$$T(r,\emptyset) = T_a + \frac{P''}{2\pi K_n} K_o(\wr r) e^{-\wr r \emptyset} \quad (3.32)$$

where T_a is ambient temperature, P'' is power per unit depth, $K_o(\wr r)$ is the solution of second kind and zero-order modified Bessel function, and $\wr = v/(2k)$; here v is welding speed and k is thermal diffusivity. I_{na} accounts absorption during multiple reflections and plasma can be calculated from following equation

$$I_{na} = e^{-\beta l}(1 - (1 - \eta)^{\pi/(4\theta)}) I_o \quad (3.33)$$

where β, l, η, θ and I_o represents inverse Bremsstrahlung absorption coefficient of plasma, average path of the laser beam in plasma before it reaches the keyhole wall, absorption coefficient of work piece, average angle between keyhole wall and initial incident beam axis, and local incident beam intensity respectively. I_{nv} on the keyhole wall is represented as

$$I_{nv} = \sum_{j=1}^{m} J_j \Delta H_j \quad (3.34)$$

where m, ΔH_j and J_j depict total number of alloying elements in alloy, heat of evaporation of element 'j' and evaporation flux of element 'j' respectively. J_j is given by modified Langmuir equation as

$$J_j = \frac{44.34}{7.5} a_j P_j^o \sqrt{\frac{M_j}{T_b}} \quad (3.35)$$

where a_j, P_j^o, M_j and T_b represents the activity of element 'j', equilibrium vapor pressure of element 'j' over pure liquid at the boiling point (T_b), molecular weight of element 'j' and boiling point temperature respectively. Moreover, the equilibrium vapor pressures of the various vaporizing species over pure liquid were calculated using relations given below [217-220]

$$\log(760 \times P_{Fe}^O) = 11.5549 - 1.99538 \times 10^4 \times \frac{1}{T_b} - 0.62549 \times \log(T_b) - 2.7182 \times 10^{-9} \times T_b + 1.9086 \times 10^{-13} \times T_b^2 \quad (3.36)$$

$$\log(1.013 \times 10^5 \times P_{Mn}^O) = -5.58 \times 10^{-4} \times T_b - 1.503 \times 10^{-4} \times \frac{1}{T_b} + 12.609 \quad (3.37)$$

$$\log(1.013 \times 10^5 \times P_{Cr}^O) = -13.505 \times 10^3 \times \frac{1}{T_b} + 33.658 \times \log(T_b) - 9.29 \times 10^{-3} \times T_b + 8.381 \times 10^{-7} \times T_b^2 - 87.077 \quad (3.38)$$

$$\log\left(P_{Ni}^{O}\right) = 6.666 - 20765 \times \frac{1}{T_b} \quad (3.39)$$

where P_{Fe}^{O}, P_{Mn}^{O}, P_{Cr}^{O}, P_{Ni}^{O} and T_b depict equilibrium vapor pressures of the Fe, Mn, Cr, Ni and boiling point of respective various vaporizing species over pure liquid respectively.

3.1.4 Finite element discretization

Eight-noded brick element is used to discretize the solution domain. In the finite element model, the boundary conditions are implemented by specifying the value of coefficient of heat transfer and the surrounding temperature at the nodes. Assuming the Galerkin method of weighted residue technique, the governing equation and the boundary conditions are stated as

$$[c]\{\dot{T}\} + [K]\{T\} = \{Q\} \quad (3.40)$$

The above equation (3.40) can be written as

$$\{R\} = \{Q\} - [c]\{\dot{T}\} - [K]\{T\} = 0 \quad (3.41)$$

where {R} is the residual vector for all nodes, [K] and [C] are the thermal conductivity matrix and the specific heat capacity matrix. $\dot{T}$ is first order temperature derivative with respect to time, {T} is the temperature vector and {Q} is the heat flow vector including laser power and heat exchange on the boundary.

The equation (41) is to be solved by an iterative method at each time step for non-linear analysis and is expressed as below

$$\left(\frac{[c^{\theta}]}{\Delta t} + \theta\,[K^{\theta}]\right)\{T\}^{(t+\Delta t)} = \left(\frac{[c^{\theta}]}{\Delta t} - (1-\theta)[K^{\theta}]\right)\{T\}^{(t)} + \theta\,\{Q\}^{(t-\Delta t)} + (1-\theta)\,\{Q\}^{(t)} \quad (3.42)$$

where $[K^{\theta}]$ and $[c^{\theta}]$ are the thermal conductivity matrix and specific heat matrix at time t+θΔt, Δt is the time increment and θ is the weight coefficient (=2/3 in the Galerkin method). Thus, equation (3.42) has been reduced to linear form of algebraic equation. Henceforth, it can be solved by an iteration method to calculate the temperature at each time step. The above equation can be reduced for a specific time step as given below

$$[\bar{K}]\{T\} = \{\bar{Q}\} \quad (3.43)$$

where $[\bar{K}]$ is the modified form of conductivity and specific heat capacity matrix at current time step and $\{\bar{Q}\}$ is the modified form of load vector at current time step.

3.1.5 Solution strategy

Figure 3.8 outlines the overall solution procedure of the conduction heat transfer model of fusion welding process considering volumetric heat source. Few of the significant steps as are described as follows

- The CAD model of solution domain is created first and is discretized into a finite number of elements (SOLID 70) in such a manner that a very fine mesh near to the heat source and coarser away from the same are followed. Moreover, the meshing is considered in simulations that the elements through thickness direction are minimum of 6.
- All the process parameters (laser power, welding speed, etc.,) and model parameters (temperature dependent and independent material properties, initial and boundary conditions along with volumetric heat source model, etc.,) are defined next.
- In transient analysis, the total weld time (welding plate length/welding speed) is divided into small time steps, and then the heat transfer analysis is implemented for each time step explicitly.
- The output of the model is the thermal cycle and cooling rate. From this results it can be estimated the weld bead shape and dimensions.

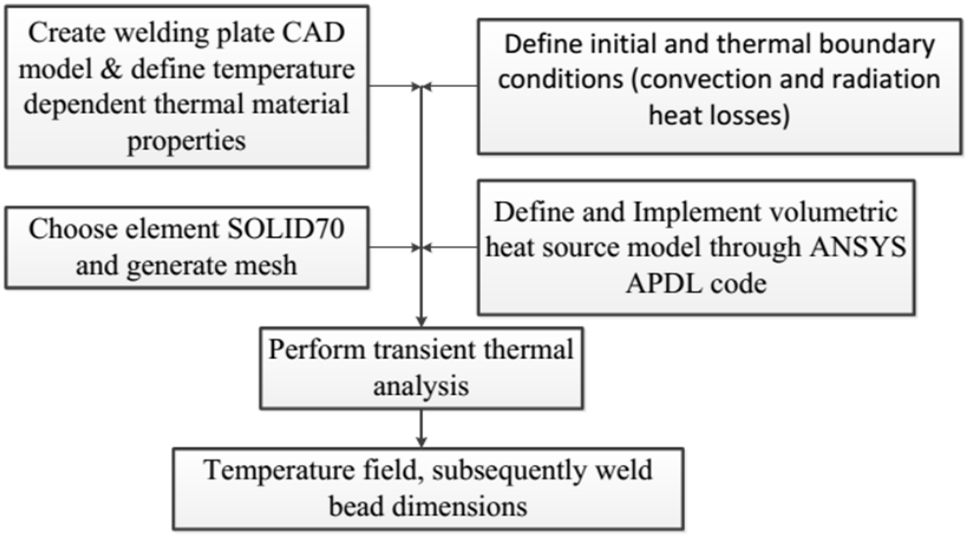

Figure 3.8: Overall procedure followed in conduction mode heat transfer analysis.

3.2 Transport phenomena based heat transfer and fluid flow

Transport phenomena based heat transfer and fluid flow models in fusion welding process are always more realistic than conduction mode heat transfer analysis. Such convective transport of heat in molten weld pool is driven by the temperature gradient of surface tension acting on the top surface of the melt pool, the electromagnetic force and the buoyancy force present in the weld pool. Moreover, the weld pool is not symmetric in the direction of the movement of the welding heat source in the case of linear welding processes. Furthermore, only heat conduction analysis might not be sufficient to consider the effect of surface-active elements. In the liquid metal flow, the most significant driving force is the surface tension force and it is incorporated through temperature- and concentration-dependent coefficients of surface tension. In view of these aspects, a 3D numerical heat transfer model is enhanced further combining the convective transport of heat that require the solution of the conservation of mass, momentum and energy within the solution domain simultaneously. An effort to accomplish the same is aimed at in the present work to examine the influence of surface active elements for linear GTA welding process. The corresponding theoretical background for a comprehensive 3D transient heat transfer and fluid flow analysis is presented in the subsequent sections.

3.2.1 Governing equations and boundary conditions

In thermal modelling of the welding process, the principle of conservation of energy is maintained. Under a moving coordinate system (assume x, y, z), the general governing equation for heat conduction is stated as follows

$$\nabla \cdot (k \cdot \nabla T) + \dot{Q} = \rho C_p \left(\frac{\partial T}{\partial t} + \mathbf{U} \cdot \nabla T - \mathbf{V} \cdot \nabla T \right) \qquad (3.44)$$

where $\nabla = \{\frac{\partial}{\partial x} \ \frac{\partial}{\partial y} \ \frac{\partial}{\partial z}\}^T$ represents the gradient operator, $\mathbf{U} = \{u \ v \ w\}^T$, ρ is the density in kg m^{-3}, C_p is the specific heat in J kg^{-1} K^{-1}, **V** is the welding velocity vector, k is the thermal conductivity in W m^{-1} K^{-1}, t is the time in s, T is the temperature in K, and $\dot{Q}$ is the rate of internal heat generation in W m^{-3} s^{-1}. The term corresponding to **U** in right side of equation (3.44) accounts the convective flow of liquid metal. The internal heat generation term is neglected here.

The heat flux is applied on the top of work piece surface while rest of the surfaces is subjected to heat loss owing to convection and radiation. The boundary conditions for energy transport in an integrated form is represented as follows

$$k_n \frac{\partial T}{\partial n} - q_s + h(T - T_o) + \sigma\varepsilon(T^4 - T_o^4) = 0 \quad (3.45)$$

where n, k_n, q_s, h, ε, T_o and σ indicates the direction normal to the surface, thermal conductivity normal to the surface, imposed heat flux onto the surface as a result of external heat source, convective heat transfer coefficient, emissivity, ambient temperature and Stefan-Boltzmann constant, respectively. The first term on the left hand side of equation (3.45) represents heat conduction normal to the boundary surface, the second term, q_s stands for imposed heat flux onto the surface, and the third and fourth terms, respectively, refer to convection and radiation heat loss from the surface. To avoid nonlinearity arises due to radiation heat loss term (fourth power of temperature), 'a lumped heat transfer coefficient' is used. It combines the radiation and convective heat losses together and is expressed as

$$h_{eff} = 2.4 \times 10^{-3} \times \varepsilon \times T^{1.61} \quad (3.46)$$

where h_{eff} is the effective heat transfer coefficient in W m^{-2} K^{-1} and T is the temperature in K. Therefore, equation (3.45) is modified as

$$K_n \frac{\partial T}{\partial n} - q + h_{eff}(T - T_o) = 0 \quad (3.47)$$

The heat energy is assumed to be distributed in a Gaussian manner. On the symmetric surface, the temperature gradient normal to the surface is zero. The rest of the work piece surfaces are subjected to convection and radiation heat losses. The dragging force exerted on the top surface of the weld pool by the arc plasma is usually much smaller in comparison to the surface tension driven forces and hence, neglected. The distribution of heat flux on the top surface considering Gaussian distribution is mathematically expressed as

$$q_s = \frac{P_w \eta_{gau} d}{\pi r_{eff}^2} \times \exp\left(-\frac{d.x^2}{r_{eff}^2} - \frac{d.y^2}{r_{eff}^2}\right) \quad (3.48)$$

where P_w refers to the power of heat source, η_{gau} is arc efficiency, r_{eff} is the effective radius of the heat source, and d is the power density distribution factor of heat source. It is noteworthy that the measurement of arc efficiency and effective arc radius is difficult and hence assumed as uncertain model parameters.

The conservation of momentum and mass are expressed mathematically as [221]

$$\rho\left(\frac{\partial \mathbf{U}}{\partial t} + \mathbf{U}.\nabla\mathbf{U}\right) = \nabla.\sigma_s + \mathbf{F} \quad (3.49)$$

$$\nabla.\mathbf{U} = 0 \quad (3.50)$$

where σ_s is the total stress tensor, ρ is the density of the material, $\mathbf{F}$ corresponds to the body force vector per unit volume and t is the time variable. The total stress tensor in equation (3.51) is expressed using Stoke's law as [221]

$$\sigma_s = \mu[(\nabla\mathbf{U}) + (\nabla\mathbf{U})^T] - P\mathbf{I} \quad (3.51)$$

where P is the pressure, μ is the viscosity of the molten metal and $\mathbf{I}$ is the identity matrix. From equations (3.49) and (3.51) along with suitable modification due to welding torch movement, the momentum conservation equation is modified as

$$\rho\left(\frac{\partial \mathbf{U}}{\partial t} + \mathbf{U}.\nabla\mathbf{U}\right) = -\nabla P + \mu\nabla.[(\nabla\mathbf{U}) + (\nabla\mathbf{U})^T] + \rho\mathbf{V}.(\nabla\mathbf{U}) + \mathbf{F}' + \rho\mathbf{g}\beta(T - T_o) \quad (3.52)$$

where P depicts the pressure, μ represents the viscosity of the molten metal, $\mathbf{g}$ is acceleration due to gravity, β is the coefficient of thermal expansion, T_0 is the reference temperature and $\mathbf{F}'$ represents the electromagnetic body force. The last term of equation (3.52) indicates the buoyancy force (Boussinesq approximation) distributed over the volume.

Figure 3.9 schematically presents the boundary conditions applied for the heat transfer and fluid flow analysis. Since, the deformation of free surface is small and it requires extra computational cost, the free surface of weld pool is assumed as flat. A bead-on-plate joining configuration is assumed for numerical simulation. Since the actual solution domain is symmetric in nature, half of the domain is considered for analysis to save computational time. The heat flux as well as momentum flux normal to symmetric surface is zero. During welding, the liquid metal is assumed as isotropic, Newtonian, viscous, and incompressible fluid. The flow of liquid metal within the weld pool is assumed as laminar. The solution boundaries for both mass and momentum equations are defined by the solid-liquid interface and the free surface of the weld pool. It is noteworthy that the solution domain for fluid flow analysis is separated from whole geometry which considerably saves computational time since fluid flow domain is generally less as compared to whole geometry for thermal analysis. In fusion welding process, the body forces are the buoyancy force and electromagnetic force. The electromagnetic force is calculated using the following expression

$$\mathbf{F}' = \mathbf{J} \times \mathbf{B} \quad (3.53)$$

where **J** is the current density and **B** is the magnetic flux induced in the work piece due to arc current. In present work, the electromagnetic force is included explicitly through the body force term defined in momentum equations. Hence it is not necessary to solve electromagnetic force equations implicitly with specified boundary conditions. The components of electromagnetic force are estimated using a set of analytical expressions for simplicity as [46]

$$F_{em}^{x} = -\frac{\mu_m I^2}{4\pi^2 r_{eff}^2 r}\exp\left(-\frac{r^2}{2r_{eff}^2}\right)\times\left[1-\exp\left(-\frac{r^2}{2r_{eff}^2}\right)\right]\left(1-\frac{z}{t_{sh}}\right)^2\frac{x}{r} \tag{3.54}$$

$$F_{em}^{y} = -\frac{\mu_m I^2}{4\pi^2 r_{eff}^2 r}\exp\left(-\frac{r^2}{2r_{eff}^2}\right)\times\left[1-\exp\left(-\frac{r^2}{2r_{eff}^2}\right)\right]\left(1-\frac{z}{t_{sh}}\right)^2\frac{y}{r} \tag{3.55}$$

$$F_{em}^{z} = -\frac{\mu_m I^2}{4\pi^2 r^2 c}\left[1-\exp\left(-\frac{r^2}{2r_{eff}^2}\right)\right]^2\left(1-\frac{z}{t_{sh}}\right) \tag{3.56}$$

where, x, y and z are the distances of any point within the weld pool from the center of the welding arc in the respective directions; r is the radial distance of any point within the weld pool from the center of the arc; F_{em}^{x}, F_{em}^{y} and F_{em}^{z} are the components of electromagnetic forces respectively in the x-, y- and z- directions; I is the RMS value of the applied welding current; r_{eff} is the effective radius of the welding arc, t_{sh} is the thickness of the work piece being welded and μ_m is the magnetic permeability of work piece material.

A no-slip boundary condition for laminar flow at the solid-liquid interface is expressed as

$$u = 0; v = 0 \text{ and } w = 0 \tag{3.57}$$

A slip boundary condition on the symmetric plane is expressed as

$$u = 0; \frac{\partial v}{\partial x} = 0 \text{ and } \frac{\partial w}{\partial x} = 0 \tag{3.58}$$

The weld pool top surface can be considered as flat with the following boundary conditions

$$\mu\frac{\partial u}{\partial w} = f_L\frac{\partial \gamma}{\partial T}\frac{\partial T}{\partial x}; \qquad \mu\frac{\partial v}{\partial w} = f_L\frac{\partial \gamma}{\partial T}\frac{\partial T}{\partial y} \quad \text{and} \quad w = 0 \tag{3.59}$$

where γ is the temperature-dependent surface tension coefficient and f_L is the volume fraction of liquid metal along the weld pool top surface.

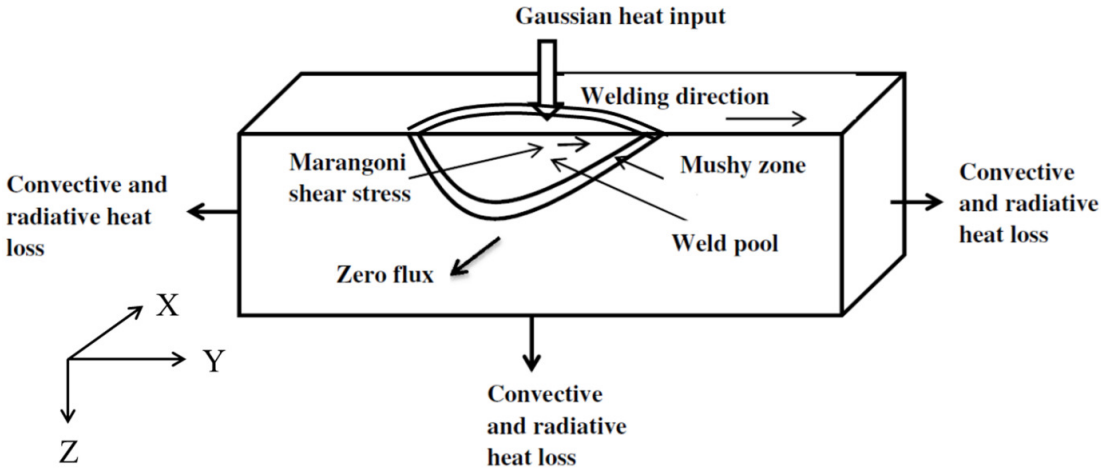

Figure 3.9: Three dimensional solution geometry with applied boundary conditions.

3.2.2 Finite element discretization

The mass, momentum and energy equations along with boundary conditions are discretized following Galerkin's method of weighted residue technique [214, 221, 222] and using eight nodded isoparametric brick element. The solution procedure confirms to the reduced integration penalty method. In this method the continuity equation is dismissed from the solution method by associating the constraint with pressure. This association is accomplished by replacing P as follows

$$P = -\lambda(\nabla . \mathbf{U}) \tag{3.60}$$

where λ is the penalty parameter and is assumed a large number so that it can fascinate the continuity equation. Considering the linear elemental interpolation function, the unknown variables (velocity and temperature) within the element is expressed in terms of the corresponding nodal variables as

$$u=\sum_{i=1}^{8}[N_i]\{u_i\};\ v=\sum_{i=1}^{8}[N_i]\{v_i\};\ w=\sum_{i=1}^{8}[N_i]\{w_i\};\ T=\sum_{i=1}^{8}[N_i]\{T_i\} \tag{3.61-3.64}$$

Performing mathematical treatments, the momentum equations is written in a matrix form as

$$\left[\bar{\bar{K}}\right]\{U\} = \{F\} \qquad \text{where } \left[\bar{\bar{K}}\right] = [M] + [\bar{C}] + \left[\hat{K}\right] + [K] \tag{3.65}$$

[M],$[\bar{C}]$, [K], and $\left[\hat{K}\right]$ refer to mass, velocity dependent convective transport, viscous diffusion and penalty matrix, respectively. The energy equation is similarly represented in matrix form as

$$\left[\bar{\bar{H}}\right]\{T\} = \{f\} \tag{3.66}$$

where $\left[\bar{\bar{H}}\right] = [\bar{H}] + [H] + [C] + [S]$ and $\{f\} = \{f_q\} + \{f_h\}$

[H], $[\bar{H}]$, [C] and [S] refer to conductivity, convective, velocity dependent energy transport and velocity matrix, respectively. It is noteworthy that the numerical integration of penalty matrix in equation (3.65) is performed by reduced integration method (2x2x2 points Gauss quadrature method) to avoid over-constraint due to penalty term whereas other terms followed 3x3x3 points Gauss quadrature method. A frontal solver has been developed to solve the linear system of equations.

3.2.3 Overall flow chart

Figure 3.10 illustrates the step by step procedure followed in a coupled heat transfer and fluid flow analysis.

- The model starts with the solution of the conservation of energy equation to find the temperature field in the work piece by assuming the initial fluid velocity as zero.
- Define the locality of the solid-liquid interface point by dint of tracing the liquidus temperature isotherm.
- When the weld pool raises in size, solve the conservation of momentum equation to calculate the velocity field of molten weld metal. In the conservation of momentum equations, the existence of 'velocity' in convective term makes the equations solve iteratively to find a converged velocity field in successive iteration until it converges.
- Subsequently solve the conservation of energy equation again, after getting the converge solution of velocity field.
- The solution of the conservation of energy equation by considering the obtained velocity field modifies the temperature field.
- The modified temperature field is compared with the previously calculated temperature field. Once discrepancies between these two temperatures are within a specified error limit, go to the next time step or load step.

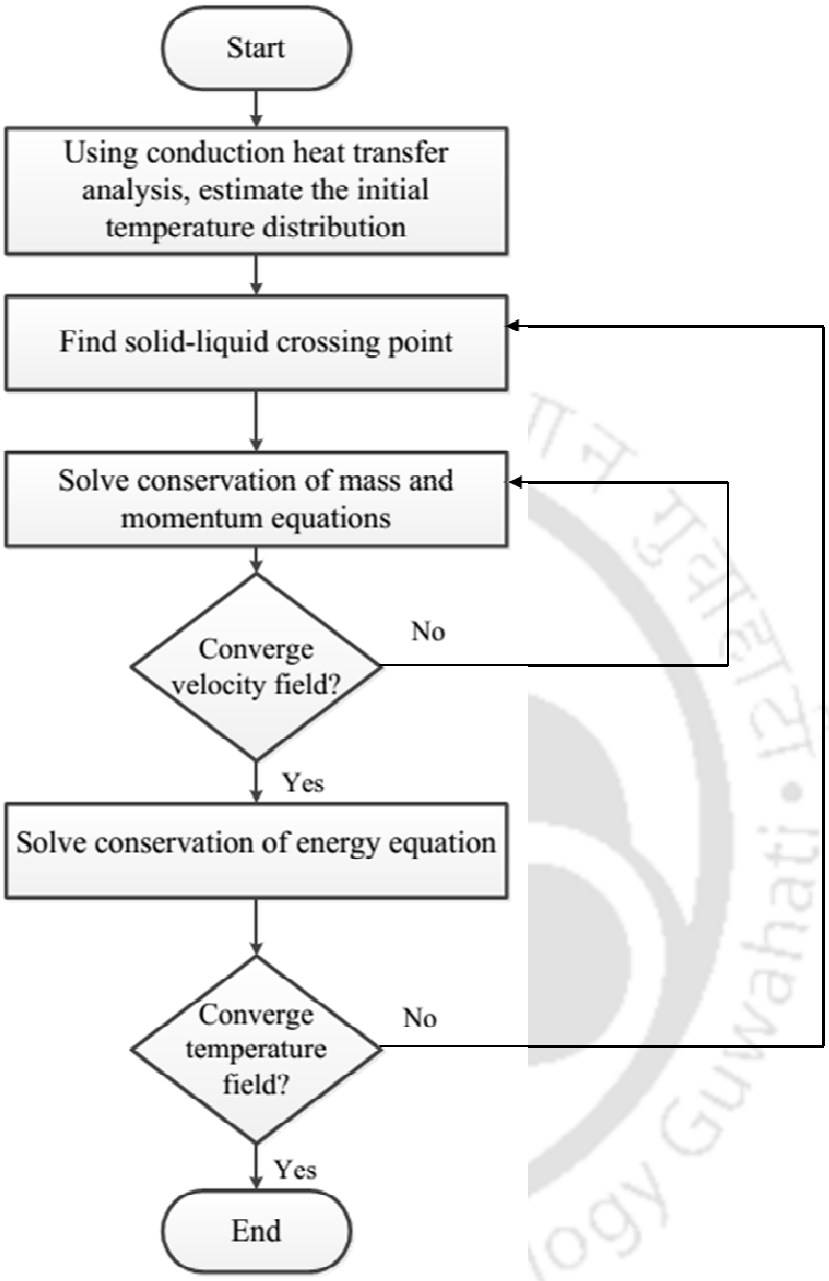

Figure 3.10: Transport phenomena based heat transfer and fluid flow analysis flow chart.

3.3 Thermo-mechanical analysis

In the present work, a thermo-mechanical analysis is also carried out to calculate the welding induced distortions and residual stresses of laser butt joint. The present section describes the theoretical background of mechanical analysis. It includes the mechanical

boundary conditions along with material model. The nodal temperature values are estimated from the conduction heat transfer analysis are integrated as a predefined field. The material was assumed to follow an elasto-plastic law with isotropic hardening behaviour (von Mises plasticity model). The detailed mathematical background of mechanical analysis is given in the subsequent sections. Figure 3.11 shows the elements used in thermal and mechanical analysis in the present work.

3.3.1 Governing equations and boundary conditions

In the present work, the material response is assumed as thermo-elasto-plastic along with temperature dependent mechanical properties. The elasto-plastic analysis is generally performed by incremental mode of stress and strain. Rate independent plasticity is considered followed by von-Mises criterion, the associated flow rule and bilinear isotropic hardening behaviour. In Cartesian coordinate system, the strain-displacement relation can be written as [185, 222]

$$\epsilon_x = \frac{\partial u}{\partial x}\ ;\ \epsilon_y = \frac{\partial v}{\partial y}\ ;\ \epsilon_z = \frac{\partial w}{\partial z} \tag{3.67}$$

$$\gamma_{xy} = \frac{\partial u}{\partial y} + \frac{\partial v}{\partial x};\ \gamma_{yz} = \frac{\partial v}{\partial z} + \frac{\partial w}{\partial y}\ ;\ \gamma_{xy} = \frac{\partial w}{\partial x} + \frac{\partial u}{\partial z} \tag{3.68}$$

where u, v and w represents displacements in x, y, z directions respectively; ε_x, ε_y and ε_z refer to the normal strains in x, y and z directions respectively; and γ_{xy}, γ_{yz} and γ_{zx} represents shear strains in xy, yz and zx planes respectively. Assuming the isotropic material, the thermal strain remains same in three directions and the increment of the total strain is sum of the incremental plastic strain, incremental thermal strain and incremental elastic strain, represented as

$$\{d\epsilon\} = \{d\epsilon^t\} + \{d\varepsilon^p\} + \{d\epsilon^e\} \tag{3.69}$$

Following Prandtl-Reuss flow rule and von-Mise'syield criteria, the incremental stress can be represented as

$$\{d\sigma\} = \left[D_{ep}\right]\{d\epsilon\} - [D^e]\{\alpha\}(\Delta T) \tag{3.70}$$

$$\text{where } \left[D_{ep}\right] = \left([D^e] - [D^e]\left\{\frac{\partial f}{\partial \sigma}\right\}\left\{\frac{\partial f}{\partial \sigma}\right\}^T [D^e]\frac{1}{3G+E_T}\right) \tag{3.71}$$

where $[D^e]$ depict the elasticity matrix which consists of mechanical properties like Young's modulus, E and Poisson's ratio μ, G is shear modulus and E_T is local slope between stress and

plastic strain of specified material. The last term of equation (3.70) represents the thermal strain which may vary depending upon the special temperature distribution. [D_{ep}] is some sort of elasto-plastic matrix where the first term in equation (3.71) is due to elastic response of material or recovery of elastic response when the material is in plastic zone. The second term of the equation (3.71) is due to plastic flow of material which is zero when the material is elastic zone only. The evolution of the yield surface are governed by the hardening rule. In present case, von-Mises yield surface is considered and bilinear isotropic hardening rule is assumed that may be appropriate for the selected material.

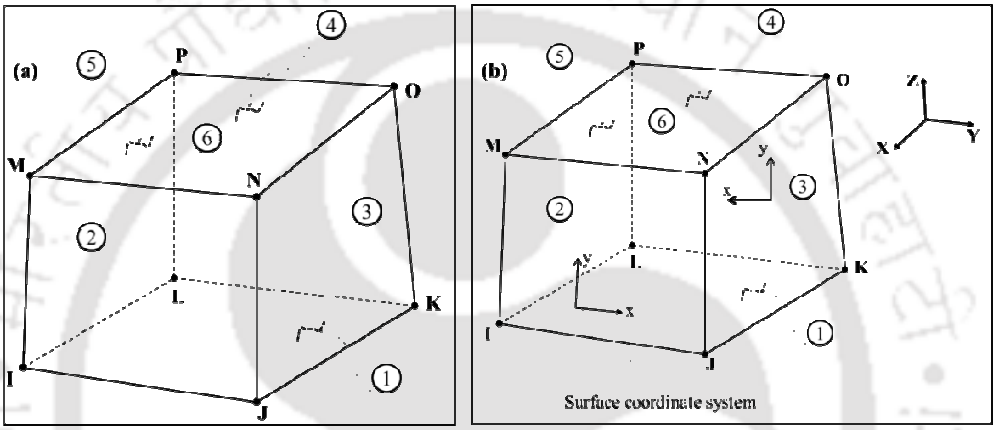

Figure 3.11: (a) Solid 70 for thermal analysis and (b) Solid 45 for mechanical analysis [223].

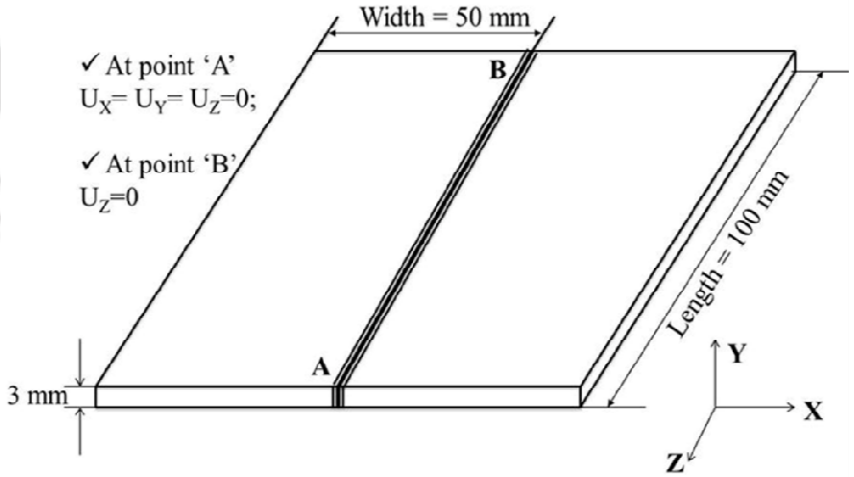

Figure 3.12: Applied mechanical boundary conditions considered in the present work.

The boundary conditions for the mechanical analysis are depicted in Fig. 3.12 corresponding to full geometry.

3.3.2 Material model

In the present work, the numerical analysis is performed by considering the temperature dependent thermal and mechanical properties. An elastic-plastic material model is used in the mechanical analysis module. The isotropic hardening rule is selected to consider the plasticity in the ANSYS APDL code [223]. The elasticity is defined by Young's modulus and Poisson's ratio, and the plasticity is defined by yield stress and the elastic-plastic tangent modulus. Moreover, the von Mises stress is used to predict yielding of the welded joint.

3.3.3 Computational aspects

In the present work, the temperature dependent thermal and mechanical properties are used for thermo-mechanical analysis. Thermal properties such as specific heat and thermal conductivity are considered temperature dependent and other properties are assumed as temperature independent. The latent heat of fusion is considered for the simulation through an artificial increase or decrease in the specific heat of the material [167]. After discretization of the governing equation along with boundary conditions for heat conduction, the linear system of equations for an element is written as

$$[\mathrm{C(T)}]\{\mathrm{T}\} + [\mathrm{K(T)}]\{\mathrm{T}\} + [\mathrm{V(T)}]\{\mathrm{T}\} = \{\mathrm{Q(T)}\} \tag{3.72}$$

where [K] refers to the conductivity matrix, [C] is the capacitance or specific heat matrix, {T} is nodal temperatures vector, [V] is the velocity matrix due to moving arc and {Q} is the nodal heat flow vector. It is noteworthy that the system of equations depicted in equation (3.72) is non-linear due to temperature dependent of material properties.

The material behavior is considered as elasto-plastic in nature. In the present work, the influence of micro-structural changes, creep and transformation induced plasticity are not considered. The plasticity is assumed as rate independent and is modelled by assuming bi-linear isotropic hardening behaviour along with associated flow rule. The von-Mises yield criteria is followed as

$$\sigma_{av} = \sqrt{\frac{1}{2}[(\sigma_1 - \sigma_2)^2 + (\sigma_2 - \sigma_3)^2 + (\sigma_3 - \sigma_1)^2]} \tag{3.73}$$

where, $\sigma_1, \sigma_2, \sigma_3$are principal stresses and σ_{av} is the average one dimensional stress. During both i.e. thermal and structural analysis a full "Newton-Raphson" iterative solution technique is used for obtaining the solution.

The simulations (conduction heat transfer and thermos-mechanical analyses) are carried out using FE based ANSYS 14.0 software (user defined APDL code). The estimated data in the form of nodal temperature are utilized to measure weld bead dimensions. The thermal modeling was carried out using Gaussian distributed volumetric heat source models (given in section 3.1.1).

3.3.4 Flow chart for mechanical analysis

Figure 3.13 shows the step by step procedure (flow chart) followed in a thermo-mechanical analysis based on finite element method using FE software ANSYS 14.0. Few important steps are delineated below.

- In mechanical analysis, the similar FE model used in thermal analysis is considered other than type of element. SOLID 45 element is used which is defined by eight nodes having three degrees of freedom at each node, translation in the nodal X, Y, and Z directions.
- Next, the temperature dependent material properties are defined.
- The reading of nodal temperatures is considered for overall thermal analysis at different time steps. Impose the mechanical boundary conditions.
- Perform structural analysis and estimate the welding induced distortion and residual stresses at different sections of welded geometry.

3.4 Optimization of unknown model parameters

The essential requirement for the optimization module is to enhance the reliability and robustness of the numerical model. In the present work, the optimization modules are utilized to estimate the model uncertain parameters such as efficiency and thermal conductivity at high temperature. Two different optimization modules such as GA based PCX operated G3 model and differential evolution are utilized for two different tasks.

It is worth mentioning that the GA based PCX-G3 is integrated with the numerical heat transfer model to optimize the front and rear length ratio of double-ellipsoidal volumetric heat source model. Subsequently, the work has been conducted to optimize the model uncertain parameters such as arc efficiency or absorption coefficient, thermal conductivity at high temperatures, viscosity etc., by integrating the DE module with numerical conduction and convective heat transfer model. Within various schemes of GA, the author has been chosen for a real number based GA of PCX-G3 algorithm and differential evolution.

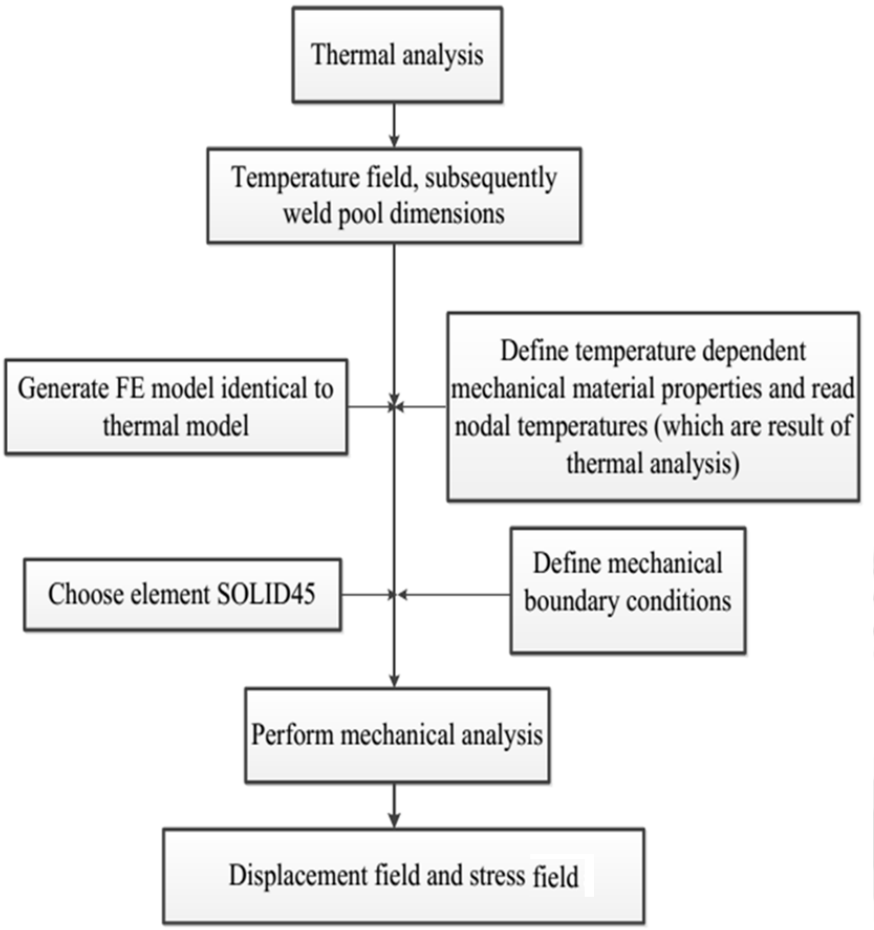

Figure 3.13: Overall procedure followed in thermo-mechanical analyses.

There is no definite scientific cause for the choice of these two particular GA based optimization modules in the present work. The author's selection is motivated by the view of several past researchers such that these techniques in GA generally needs lesser number of iterations to reach an optimum solution as compared to other real number based evolutionary algorithms. The basic theoretical background of two optimization modules and their integration process with numerical model is presented briefly in the following sections.

In the convective heat transfer analysis, the most important uncertain model parameters such as arc efficiency, effective arc radius, enhanced thermal conductivity and viscosity are considered. It is obvious that there is a need to use an appropriate value of effective radius in the numerical model to estimate the actual heat input into the work-piece from the welding heat source. Moreover, the effective radius value is easy to estimate with confidence in the case of laser welding whereas it is extremely difficult for arc welding. The optimization procedure starts with the formation of an objective function. In the present work,

the objective function defines the error between the calculated and the corresponding experimental values of one or more dependent variables attained from few numbers of observations.

3.4.1 Optimization using GA based PCX-G3 model

GA is a random search technique that can find optimum values of a set of unknown variables from a large volume of discrete data sets through making a suitable fitness function. This fitness function is sensitive to the values of unknown variables. These discrete data sets can be binary strings or real numbers, and are mentioned as population. The generation of the individual data set (initial population) is done randomly and each data set signifies a potential solution.

The estimation of the ratio of rear and front length of a double ellipsoidal volumetric heat source ($\chi = \frac{a_r}{a_f}$) model is performed using real number based PCX-G3 GA as optimization tool[34]. The objective function is defined by the squared error term between experimental and calculated weld pool dimensions. It is expressed as

$$\min : F_o(\chi) = \sum_{i=1}^{m}\sum_{j=1}^{2}\left[\frac{W_{ij}^c - W_{ij}^e}{W_{ij}^e}\right]^2 = \sum_{i=1}^{m}\sum_{j=1}^{2}\left[W_{ij}^* - 1\right]^2 \qquad (3.74)$$

$$s.t. \qquad \chi^L \le \chi \le \chi^U$$

where W_{ij}^c refer to the computed values of weld width (j = 1) and the penetration (j = 2), and W_{ij}^e the corresponding measured values at the same welding conditions (i^{th}) in a series of 'm' number of total sample welds, χ^L and χ^U are the lower and upper bounds of design variable χ. The ratio χ is assumed as a polynomial function of weld velocity and is expressed as

$$\chi = A_0 + \sum_{i=1}^{n} A_i v^i \qquad (3.75)$$

where A is constant, "v" the weld velocity, and n is the degree of polynomial. Here, the uncertain parameter χ is variable in nature and is computed in each sample point of m number of total sample welds. Therefore, the coefficients of polynomial are uncertain parameters indirectly, if we presume the degree of polynomial. The overall algorithm of PCX

operated G3 model to calculate the polynomial coefficients are described briefly step by step as follows.

- Step 1: The initial population is generated randomly for a parent, consists of a set of unknown variables, in the present problem, A_1, A_2 and A_3. Here a parent denotes to an individual in the current population. The best parent is the individual that has the best fitness and provides the minimum value of the objective function (equation 3.74) in the total population.
- Step 2: The best parent is selected from the entire population and two more parents randomly selected from the current population.
- Step 3: Two new individuals or offspring are generated using a recombination scheme (PCX-based G3 model) from above three selected parents. A recombination scheme is a technique for generating new offspring from the parents.
- Step 4: Select the two more new parents randomly from the current population.
- Step 5: A combined subpopulation is formed with offspring of step 3 and the two randomly chosen parents (step 4).
- Step 6: The objective function for all the observations using newly generated offspring (step 5) are evaluated and four individuals are ranked based on the decreasing order of their respective objective function values. Then, the last two individuals in the rank are used to replace the parents selected in step (2). This replacement confirms that the solution will never diverge and it holds the best individual in any generation or iteration. In this step, two offspring are also added in the initial population created in step (1) through replacing two existing individuals in a random manner. In this manner the initial population is enriched with good individuals.
- Step 7: Steps 2 to 6 are repeated till the required minimum value of objective function is achieved or till the convergence criteria is achieved. The steps described above corresponding to PCX operated G3 model is shown in Fig. 3.14.

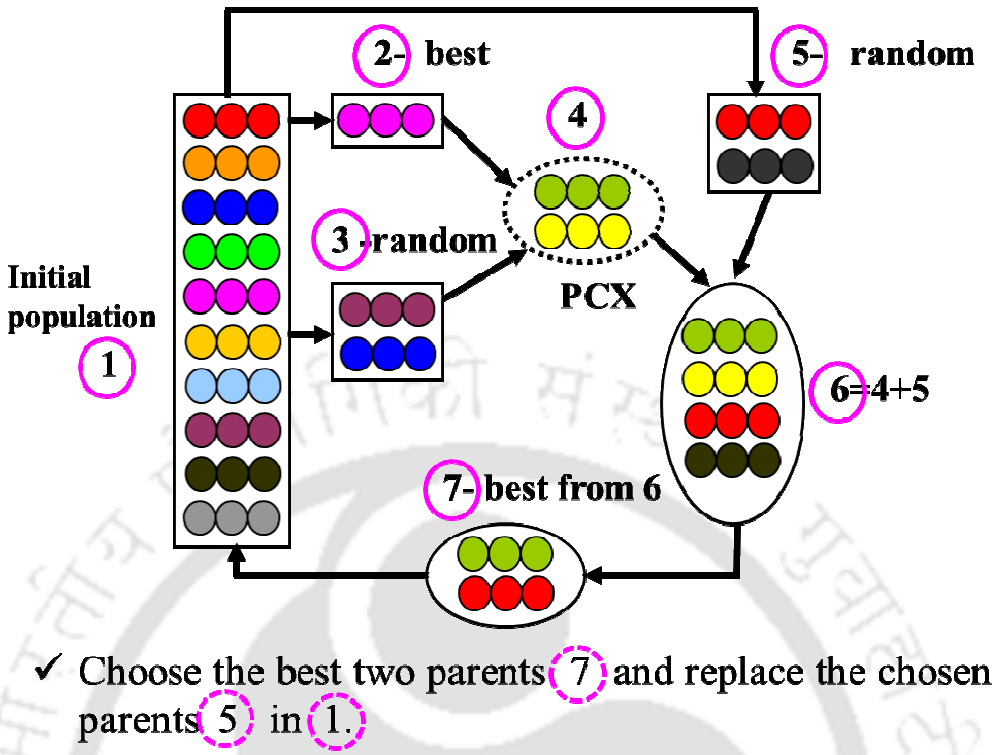

Figure 3.14: Working principle of PCX operated G3 model.

3.4.2 Optimization using Differential Evolution

The DE algorithm which is one of the most prominent new generation evolutionary algorithms, proposed by Storn and Price [209, 210] is used to estimate the uncertain parameters associated with a reliable heat transfer and fluid flow model. DE is a fast and robust stochastic search algorithm capable of handling non-differentiable, nonlinear and multimodal objective functions.

The material properties are enhanced several times to take into effect of uniform turbulence within weld pool [214]. The uncertain parameter set (**P**) is represented as

$$\mathbf{P} = \{\eta \quad r \quad k \quad \mu\}; \quad \mathbf{P}^* = \{\eta^* \quad r^* \quad k^* \quad \mu^*\} \tag{3.76}$$

where * indicates the non-dimensional form of the parameters with respect to chosen reference value. The objective function, $O(\mathbf{P})$, for the optimization process is defined by the error between the computed and corresponding measured values of weld dimensions in non-dimensional form as

$$O(\mathbf{P}) = \sum_{i=1}^{m}\left[\left(\frac{W_i^c - W_i^c}{W_i^e}\right)^2 + \left(\frac{D_i^c - D_i^c}{D_i^e}\right)^2\right] = \sum_{i=1}^{m}[(W_i^* - 1)^2 + (D_i^* - 1)^2] \tag{3.77}$$

where 'W' refers weld width and 'D' refers weld penetration, 'c' corresponds to computed value from numerical model and 'e' refers to experimentally measured value at similar welding conditions (i^{th}) in a series of 'm' number of welds.

DE is a population based algorithm like genetic algorithm (GA) that uses similar kind of operators; crossover, mutation and selection. The main difference between GA and DE is the mutation scheme that makes DE self-adaptive in nature [210]. The general problem formulation using DE [224] in the context of present optimization problem is as follows. The algorithm starts with a population of size 'n' in 4- dimensional parameter vectors. At a generation of 'G', each individual (at fixed i) is encoded by real number as

$$\mathbf{P}_{i,G} = \{P^1_{i,G} \;\; P^2_{i,G} \;\; P^3_{i,G} \;\; P^4_{i,G}\} \tag{3.78}$$

where $i = 1\ldots..n$ and P^1, P^2, P^3, P^4 corresponds to η^*, r^*, k^*, μ^* respectively. The initial population covers the full search space as much as possible by uniformly randomizing individuals inside the search space defined by maximum and minimum limit of parameters

$$\mathbf{P}_{min} = \{P^1_{min} \;\; P^2_{min} \;\; P^3_{min} \;\; P^4_{min}\}; \quad \mathbf{P}_{max} = \{P^1_{max} \;\; P^2_{max} \;\; P^3_{max} \;\; P^4_{max}\} \tag{3.79}$$

The initial value of the l^{th} parameter in the j^{th} individual at the generation G = 0 is generated by

$$P^l_{j,o} = P^l_{min} + rad(0,1).\{P^l_{max} - P^l_{min}\} \tag{3.80}$$

where l = 1, 2, 3, 4 and rad (0, 1) symbolizes a uniformly distributed random variable inside the range [0, 1]. After the initialization phase, DE performs the mutation operation to produce a mutant vector corresponding to each individual in the current population. For every target vector $\mathbf{P}_{i,\,G}$ at the generation G, its affiliated mutant vector is generated as $\mathbf{Q}_{i,G} = \{Q^1_{i,G} \; Q^2_{i,G} \; Q^3_{i,G} \; Q^4_{i,G}\}$. This mutant vector can be developed according to

$$\mathbf{Q}_{i,G+1} = \mathbf{P}_{r1,G} + \chi.\{\mathbf{P}_{r2,G} - \mathbf{P}_{r3,G}\} \tag{3.81}$$

with random indexes r1, r2, r3 ∈ {1, 2, ……..., n} which are mutually different. χ is a real and constant factor ∈ [0, 2] which controls the amplification of the differential variation $\{\mathbf{P}_{r2,G} - \mathbf{P}_{r3,G}\}$. Mutant vector obtained in the previous step and target vector under consideration are subjected to crossover, to generate trial vector as

$$\mathbf{R}_{i,G+1} = \{R_{1i,G+1} \;\; R_{2i,G+1} \;\; R_{3i,G+1} \;\; R_{4i,G+1}\} \tag{3.82}$$

where

$$R_{ji,G+1} = Q_{ji,G+1} \quad \text{if } (r(j) \le CR \text{ or } j = rn(i))$$
$$= P_{ji,G} \quad \text{if } (r(j) > CR \ \ or \ j \ne rn(i)) \qquad j = 1, 2, 3, 4. \qquad (3.83)$$

CR corresponds to the crossover constant with $\in$ [0, 1]; r(j) is the j^{th} evaluation of a uniform random number generator with outcome $\in$ [0, 1]; rn(i) is a randomly chosen index and is a subset of {1, 2, 3, 4} that make sure, $R_{i,G+1}$ gets at least one parameter from $Q_{i,G+1}$. In selection operation, the objective function value of each trail vector is compared with the corresponding target vector in the current population. The selection operation can be performed as follows

$$\mathbf{P}_{i,G} = \mathbf{R}_{i,G} \quad \text{if } (O(\mathbf{R}_{i,G}) \le O(\mathbf{P}_{i,G}))$$
$$= \mathbf{P}_{i,G} \quad \text{otherwise} \qquad (3.84)$$

These three operations (mutation, crossover and selection) were repeated until meeting the termination criteria. The details of DE for optimization of uncertain model parameters presented above are shown in Fig. 3.15.

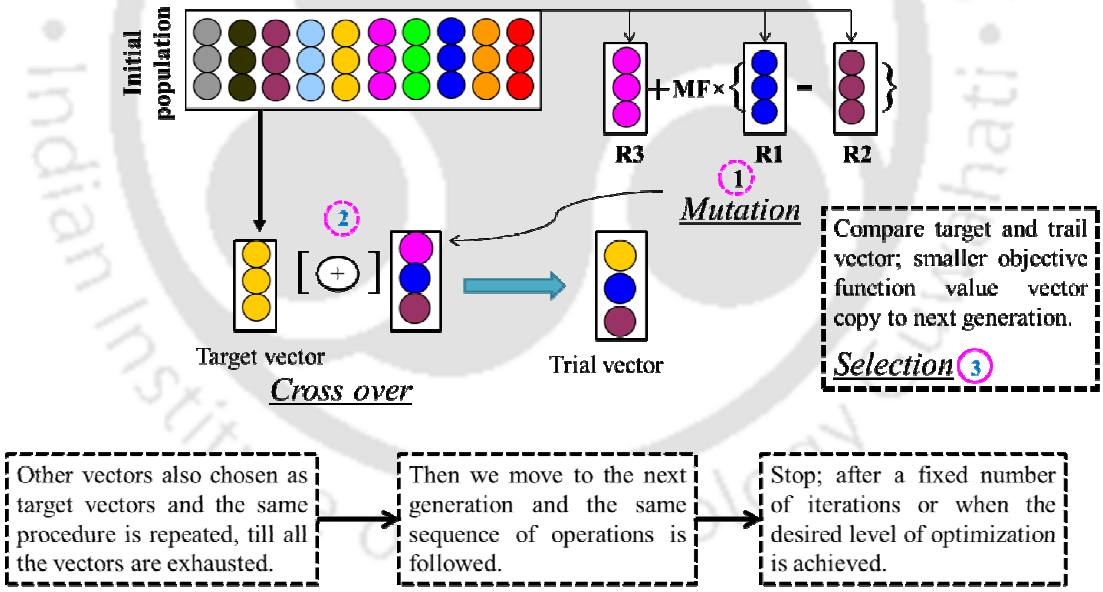

Figure 3.15: Working principle of Differential Evolution (DE) used for optimizing the uncertain model parameters.

3.4.3 Integrated model

The GA based algorithm involving PCX-G3 model and DE are integrated with the numerical models to produce a reliable and robust calculation methodology. The integrated

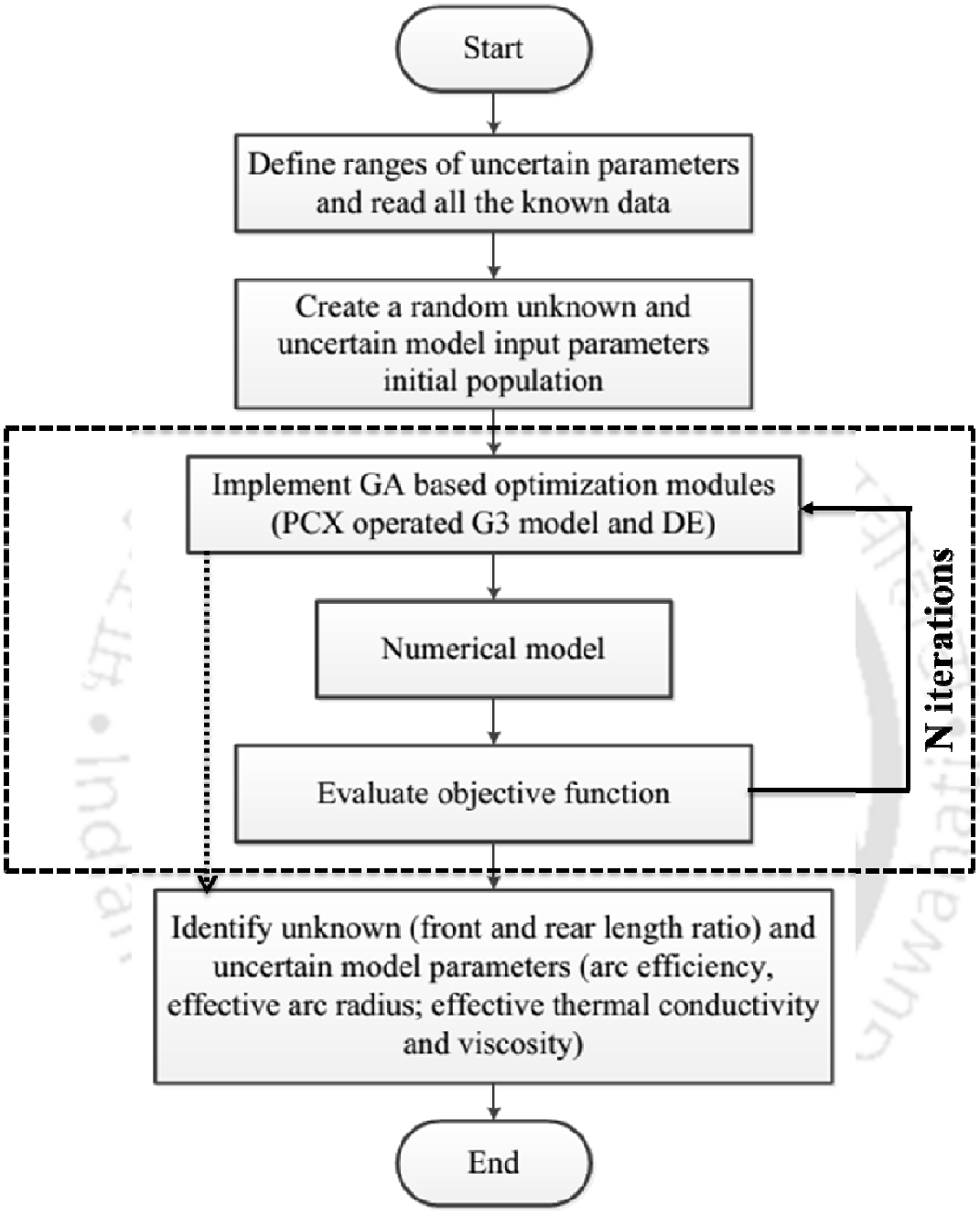

Figure 3.16: Overall flow chart of integration of optimization modules.

models are successfully used in the present work to realize two different aspects. Firstly, an appropriate relation between welding velocity and front and rear length ratio of volumetric heat source is found out. Secondly, the suitable values of a set of uncertain model input parameters (arc efficiency, effective arc radius, effective thermal conductivity and viscosity) are estimated that are important for reliable numerical modeling approach. The overall

procedure of integration of the optimization modules with process model is shown in Fig. 3.16.

The integrated model starts with defining the ranges of uncertain model parameters and defining all the known required data. Then, randomly generated initial population is created within the feasible range of uncertain model parameters. Next, the GA based optimization modules (PCX operated G3 model and DE) are used for estimating the uncertain model parameters. Finally, the optimum values of uncertain model parameters are selected based on minimum objective functional values.

3.5 Summary

In the present chapter, the theoretical background of all the aspects of conduction and convective heat transfer analysis in GTA and laser welding processes are presented. This consist of three dimensional transient state heat transfer analysis using volumetric heat source (double ellipsoid, newly developed egg-configuration and conical) models. It also includes the transport phenomena based heat transfer and fluid flow analysis of GTA welding process and the GA based optimization algorithms (PCX operated G3 model and DE) to estimate the optimum values of the uncertain or unknown input model parameters. Moreover, this chapter also includes the mathematical background and modeling aspects of thermo-mechanical analysis to predict the welding induced distortions and residual stresses of fusion welding process.

Chapter – 4

Experimental Investigation

4.0 Introduction

A comprehensive experimental study is carried out in the present work to produce a reliable database for the elaborate and extensive validations of the computed results from the numerical heat transfer, fluid flow and thermo-mechanical models. Subsequently, the welding experiments are conducted to investigate the influence of welding atmosphere in deep penetration fiber laser welding and the effect of the activating flux in linear GTA welding process. Controlled atmosphere of argon and open atmospheric condition are two variants of welding atmosphere that are considered for linear fiber laser welding process. The differential influence of ambient atmosphere on two grades of stainless steel at two different thicknesses values is studied in present work. In linear GTA welding process, the experiments are carried out using a thin layer of different activating fluxes to investigate the effect of surface active elements aiming to produce deep penetration welded joint. In laser welding process, the initial

set of experiments is conducted on SS304 and SS316 to validate the finite element simulation of temperature profiles. No additional filler wires are used in either case and hence, they are carried out in autogenous mode. However, some of the experimental results are considered from independent literatures for validation of computed results of GTA and laser welding processes. The fiber laser welding experiments were conducted at Laser Material Processing Division, Raja Ramanna Centre for Advanced Technologies (RRCAT), Indore, India. An indigenous experimental set up is also developed in the central workshop, Indian Institute of Technology Guwahati, India to conduct GTA welding experiments using DCEN mode (Pi 400 Plasma from ***Migatronic*** that can be used for both plasma arc and GTA welding processes). In this chapter, a brief outline of all the experimental procedures and detailed outcomes of experimental investigations are presented.

4.1 Fiber laser welding

The laser welding experiments are carried out using a continuous wave (CW) 2.0 kW fiber laser based welding system. The bead-on-plate fiber laser welding was performed to examine the influence of welding ambient atmosphere on SS304 and SS316 of 3 mm and 5 mm thickness plates. The chemical composition of SS 304 and SS 316 used in the experiments is described in Tables 4.1 and 4.2 respectively. A mixed mode fiber laser beam power which is the mixture of two fundamental modes i.e. 60% of TEM01, and 40 % of TEM00 provides a near flat top beam profile is considered as shown in Fig. 4.1 [225-226]. The combined intensity profile for a mixed mode laser beam is expressed by the following equation

$$I_{fl}(r) = \frac{2P_{fl}}{\pi r_{ofl}^2}[a_y + (1 - a_y)\frac{2r^2}{r_{ofl}^2}]\exp\left[-\frac{2r^2}{r_{ofl}^2}\right] \quad (4.1)$$

where P_{fl}, r_{ofl}, a_y and r depict the fiber laser power on the substrate (W), radius of the Gaussian (TEM00) beam component (m), fraction of the lower mode (TEM00) in mixed mode laser beam and the distance from the center of the laser beam (m) respectively. The laser welding workstation is also equipped with gas on/off mode and laser power on/off mode. Table 4.3 describes the fiber laser setup characteristics to conduct the experiments.

Table 4.1: Chemical composition (weight %) of austenitic stainless steel (SS 304).

C	Si	Mn	P	S	Cr	Ni	Al	Co
0.024	0.59	1.89	0.017	0.011	18.91	8.43	0.011	0.093
Cu	**Nb**	**Ti**	**V**	**Pb**	**Sn**	**Fe**		
0.478	0.052	0.041	0.045	0.014	0.002	Bal.		

Table 4.2: Chemical composition (weight %) of austenitic stainless steel (SS 316).

C	Si	Mn	P	S	Cr	Mo	Ni	Al
0.047	0.5	1.88	0.013	0.01	16.418	2.3	10.615	0.014
Co	**Cu**	**Nb**	**Ti**	**V**	**W**	**Fe**		
0.091	0.53	0.05	0.043	0.054	0.02	Bal.		

The welding process parameters for conducting the experiments are considered similar for both controlled atmosphere of argon and open atmospheric conditions to determine the characteristic difference between them. Table 4.4 and Table 4.5 denote the welding process parameters used for present investigations on 5 mm and 3 mm thickness plates. In this experimental setup, the laser head is mounted in Z-direction vertically (moveable), whereas workstation is CNC controlled and positioned stationary during operation. The welded sample was kept normal to the laser beam. Prior to the welding, the work pieces are cleaned with acetone. Figures 4.2 (a) and (b) depict the fiber laser welding experimental setup and schematic representation of controlled atmosphere setup, respectively.

Table 4.3: Experimental conditions of fiber laser welding system.

Mode of laser power	Continuous wave
Laser spot diameter	200 µm
Beam mode	Multi-mode and flat top surface
Beam angle	90 degrees
Wavelength	1080 nm
Shielding gas	Argon
Shielding gas flow rate	10 LPM
Fiber core diameter	50 µm
Focal point	0.5 mm below to the top surface for 3 mm plate
	1.0 mm below to the top surface for 5 mm plate

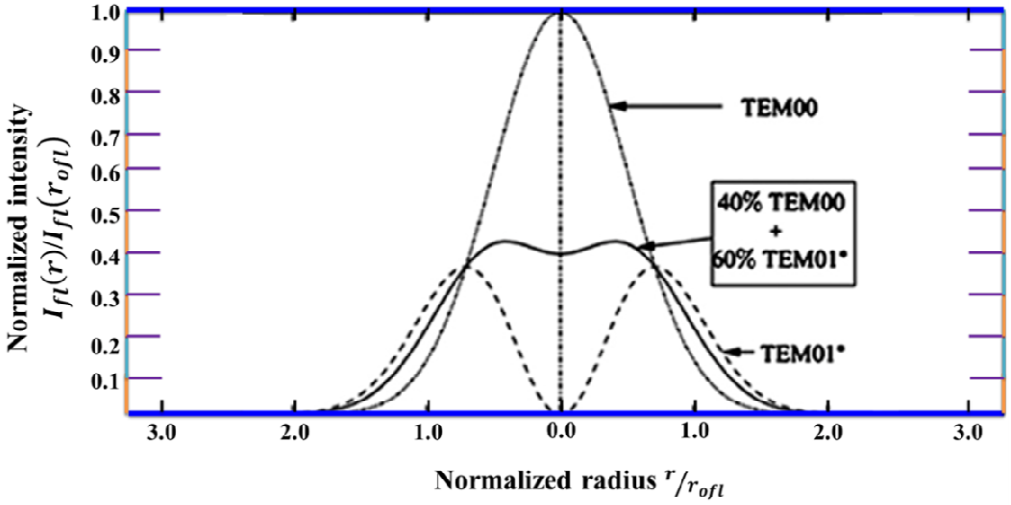

Figure 4.1: Schematic representation of intensity profiles of two different fundamental modes and their mixture.

Table 4.4: Fiber laser welding process parameters on SS304 and SS316 at open and controlled atmosphere of argon for 5 mm thick plate.

Data set	Laser power (W)	Welding velocity (mm/s)	Heat input per unit length (J/mm)
1	2000	18.33	109.09
2	2000	16.67	120.00
3	2000	15.00	133.33
4	2000	13.33	150.00
5	1800	18.33	98.18
6	1800	16.67	108.00
7	1800	15.00	120.00
8	1800	13.33	135.00
9	1600	18.33	87.27
10	1600	16.67	96.00
11	1600	15.00	106.67
12	1600	13.33	120.00

Table 4.5: Fiber laser welding process parameters on SS304 and SS316 at open and controlled atmosphere of argon for 3 mm thick plate.

Data set no.	Laser power (W)	Welding velocity (mm/s)	Heat input per unit length (J/mm)
1	1000	18.33	54.56
2	1000	16.67	59.99
3	1000	15.00	66.67
4	1000	13.33	75.02
5	900	18.33	49.10
6	900	16.67	53.99
7	900	15.00	60.00
8	900	13.33	67.52
9	800	18.33	43.64
10	800	16.67	47.99
11	800	15.00	53.33
12	800	13.33	60.02

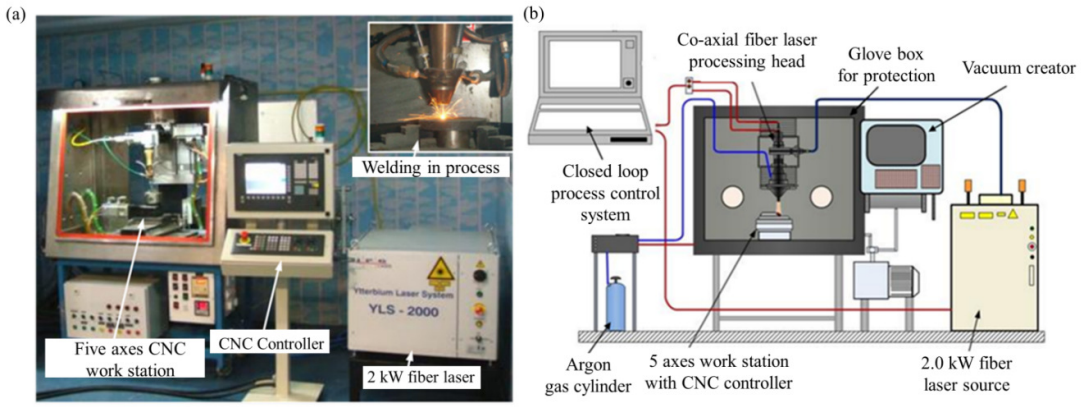

Figure 4.2: (a) Fiber laser welding experimental setup. (b) Schematic representation of protective atmosphere setup.

The metallographic analysis of welded samples are performed to measure the weld pool shape and dimensions; and to examine the microstructure formation in both laser and GTA welding processes. The welded samples were sectioned perpendicular to welding direction, polished with different grades of polishing papers (200, 400, 600, 800 and diamond

polish) and etched with Villella's reagent. The etched samples were analyzed on optical microscope. The weld pool shape, depth of penetration and bead width are measured for each experimental condition. The top surface appearance and top bead profile of the welded plate was also studied for both open and self-protective atmosphere of argon.

4.1.1 Controlled atmosphere of argon

The influence of welding ambient atmosphere plays a significant role in the weld joint quality. Hence, the molten weld pool protection is necessary to prevent the reaction with open atmospheric elements such as Oxygen, Nitrogen etc. The role of self-protective atmosphere is different from application of shielding gas in laser welding process. In present work, the influence of self-protective atmosphere of argon is examined and compared with open atmospheric conditions. When a controlled atmosphere of argon welding is performed, five axes CNC workstation was kept in glove box as shown in Fig. 4.2 (b). The welding system consists of four major subsystems. They are vacuum pump, CNC controller, ytterbium CW fiber laser source and CNC workstation in a glove box as shown in Fig. 4.2. The glove box is crucial for controlling the atmospheric conditions during laser welding process. High purity argon gas filled glove box is used to protect the weldment from the atmosphere. Moisture and air particle are the main impurities in atmosphere which influence properties of the weld joint. Henceforth, a self-protective fiber laser system was also integrated with moisture and oxygen analyzers. The desired purity levels of the glove box are accomplished by purging high purity grade argon gas. The purity level within glove box is retained by keeping the differential pressure just above the atmospheric pressure.

Figures 4.3 (a) and (b) show the measured values of weld widths and penetrations corresponding to process parameters depicted in Table 4.4 both for SS 304 and SS 316, respectively. The heat input per unit length is a signature parameter for the moving heat source to describe the effective heat energy that is utilized to melt a specific volume of substrate material of unit length. It is obvious from Fig. 4.3 that the weld pool dimensions are considerably higher for greater laser power or lower velocity since the energy input per unit length is more in both of these cases. Figure 4.4 (a)-(b) describes the experimentally measured values of weld bead dimensions corresponding to the data set of Table 4.5 both for SS 304 and SS 316, respectively.

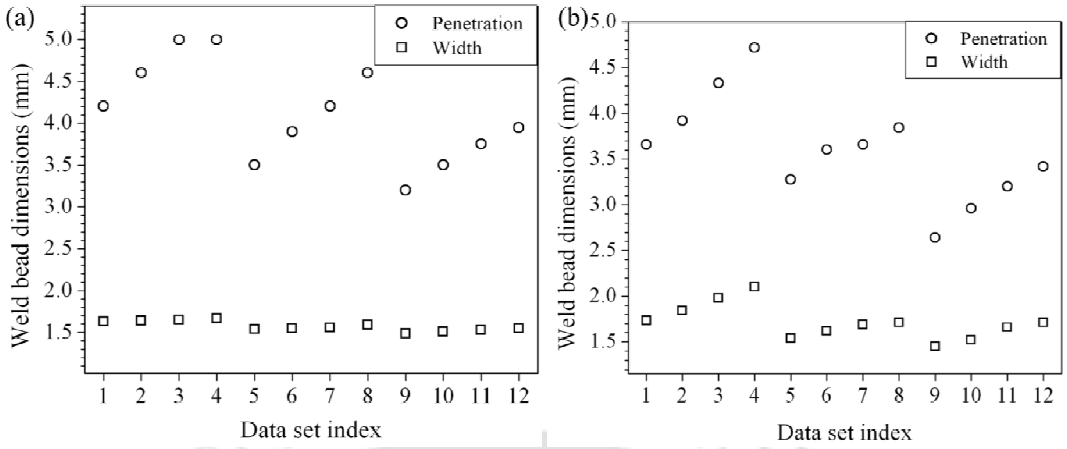

Figure 4.3: Weld bead dimensions of welds in controlled atmosphere corresponding to welding conditions given in Table 4.4, (a) SS 304 and (b) SS 316.

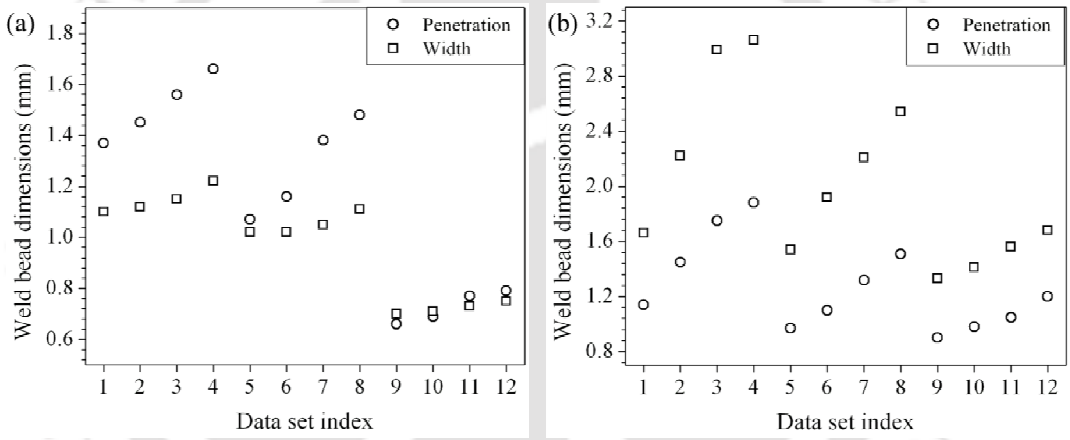

Figure 4.4: Measured weld bead dimensions corresponding to welding conditions given in Table 4.5, (a) SS 304 and (b) SS 316 in controlled atmosphere.

Overall, the process conditions indicate that the laser power varies from 800 ~ 2000 W, laser scanning speed 13.33 ~ 18.33 mm/s and corresponding energy input per unit length varies from 43.64 ~ 150.00 J/mm. It is thus obvious that a wide range of process variables are considered in present work where the inference may be justifiable in a boarder domain. It is imperative to say that with the increase of energy input per unit length, the weld pool dimensions increase and this trend is observed in both the figures 4.3 and 4.4.

The macrographs corresponding to welding conditions described in Table 4.4 are represented in Fig. 4.5 for SS304 and Fig. 4.6 for SS 316 respectively. With respect to the heat input per unit length, the similar trend (as in figures 4.3 and 4.4) in weld bead dimensions has been observed.

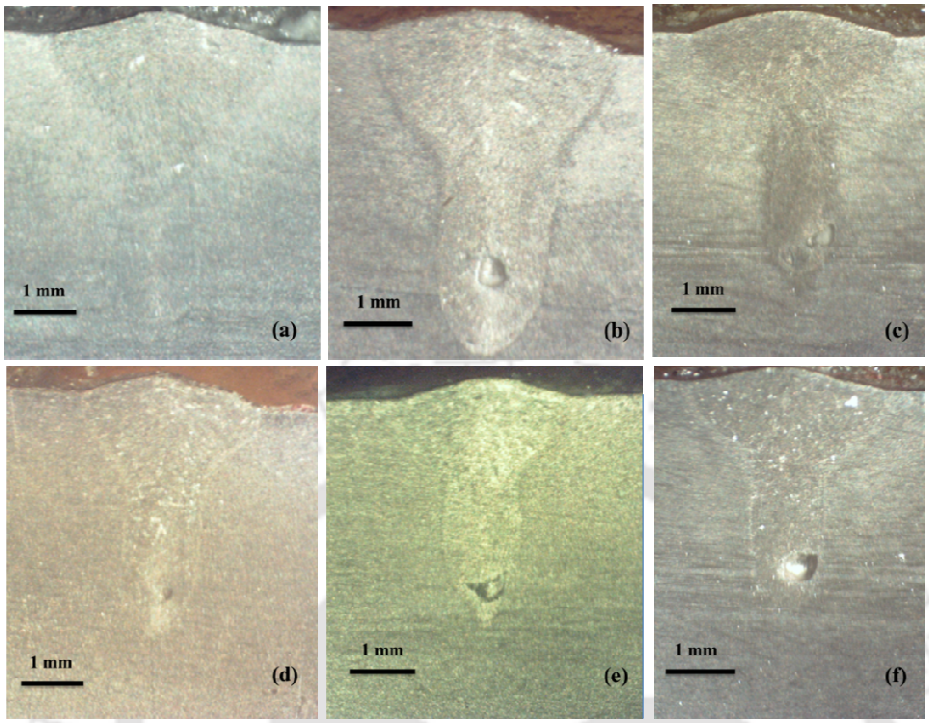

Figure 4.5: Controlled atmosphere weld macrographs of SS 304, 5 mm thickness plate corresponding to welding conditions (a) data set 1, (b) data set 3, (c) data set 6, (d) data set 9, (e) data set 10 and (f) data set 12 given in Table 4.4.

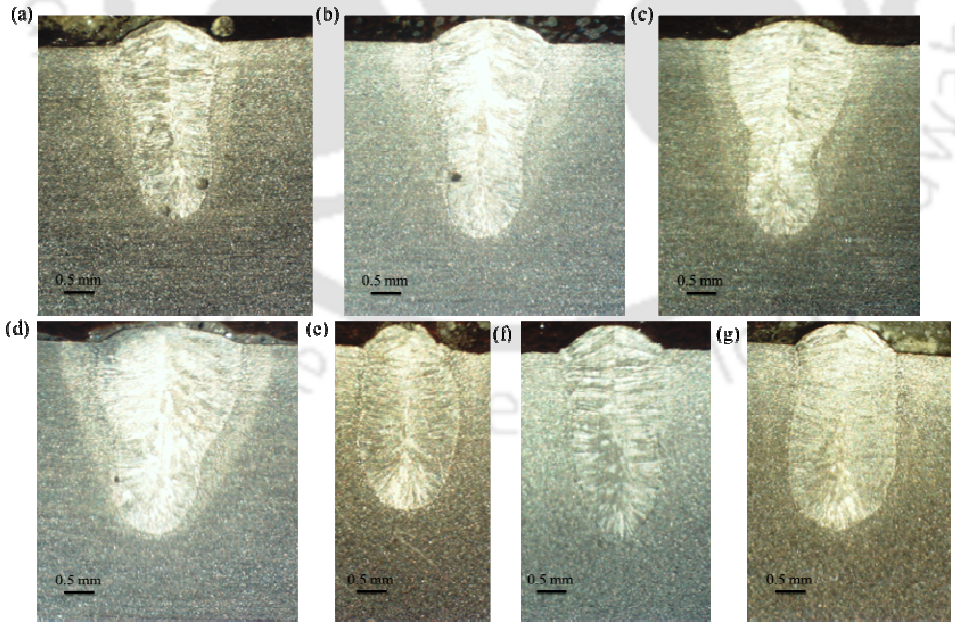

Figure 4.6: Experimental weld macrographs of 5 mm thickness plate in controlled atmosphere of argon corresponding to (a) data set 5, (b) data set 6, (c) data set 7, (d) data set 9, (e) data set 10, (f) data set 11 and (g) data set 12 given in Table 4.4.

Figures 4.7 and 4.8 represent the experimentally measured weld macrographs corresponding to welding conditions given in Table 4.5 for SS 304 and SS 316, respectively. The weld bead dimensions are increased with increase of heat input. However, the weld bead shape varies for two different materials, SS 304 and 316.

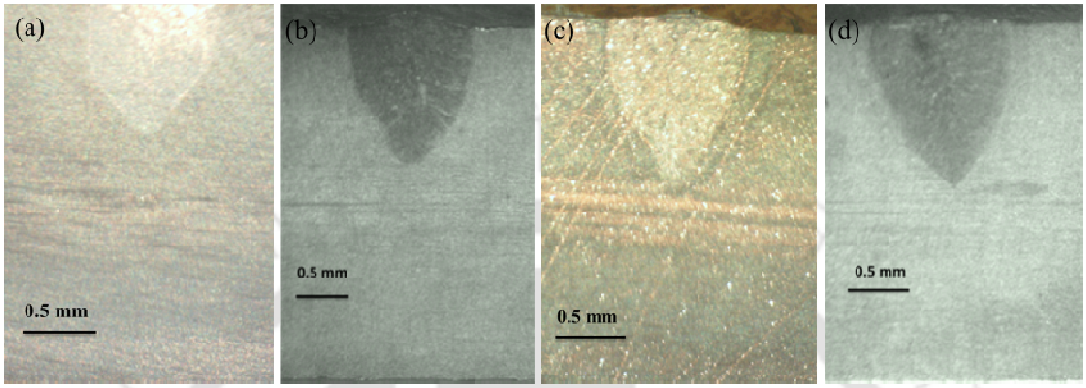

Figure 4.7: Weld macrographs in protective atmosphere corresponding to SS 304, 3 mm thickness plate welds of (a) data set 5, (b) data set 6, (c) data set 7 and (d) data set 8 given in Table 4.5.

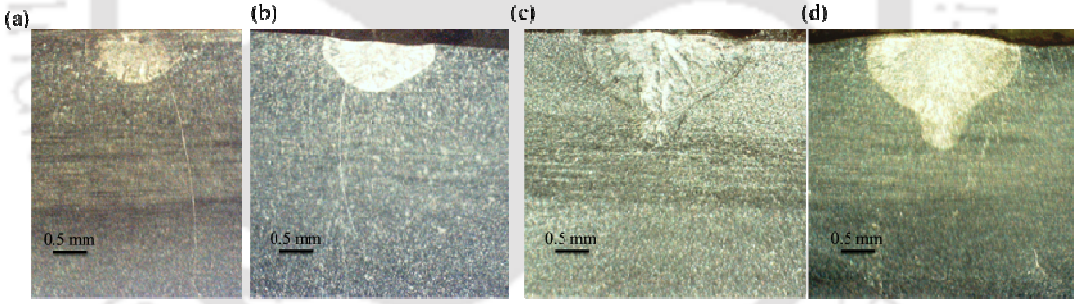

Figure 4.8: Experimental weld macrographs of SS 316, 3 mm thickness plate in controlled atmosphere of argon corresponding to (a) data set 1, (b) data set 2, (c) data set 3 and (d) data set 4 given in Table 4.5.

4.1.2 Open atmosphere

Laser welding experiments are also conducted in open atmosphere to examine the influence of welding ambient atmosphere. The experiments are carried out with similar process variables (Table 4.4 and 4.5) on SS 304 and SS 316 for 5 mm and 3 mm thickness plates. In this case, the work station was not in glove box. The measured weld bead dimensions are depicted from figures 4.9 and 4.10. In case of open atmosphere welding, the

weld bead dimensions as well as the aspect ratio are lesser as compared to the controlled atmospheric conditions.

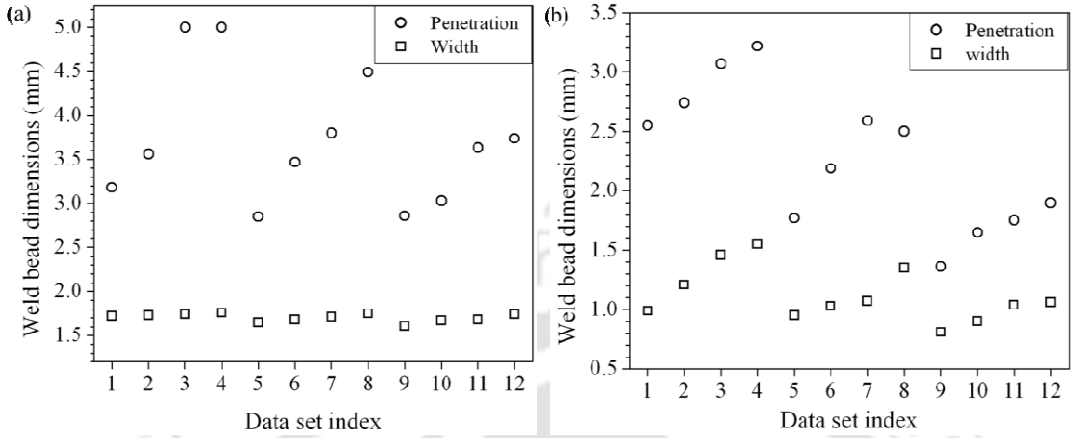

Figure 4.9: Open atmosphere weld bead dimensions corresponding to welding conditions given in Table 4.4, (a) SS 304 and (b) SS 316.

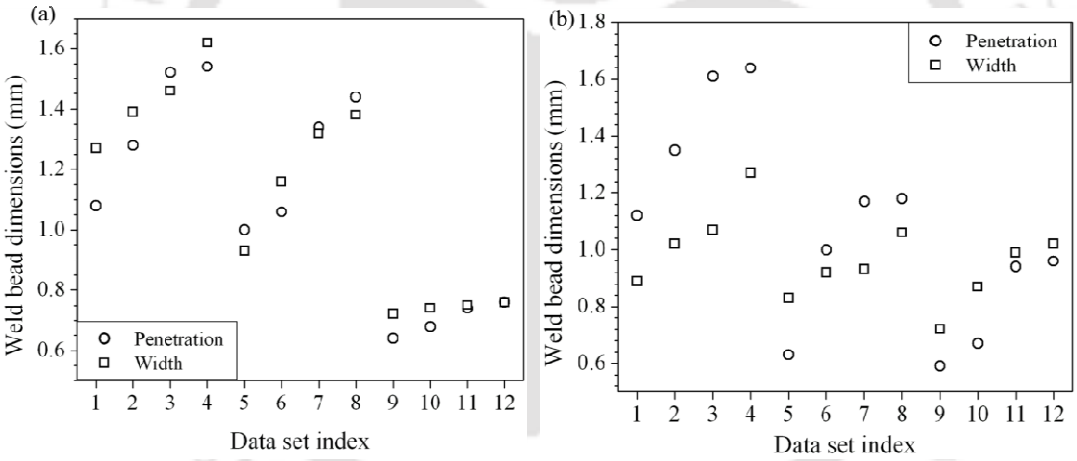

Figure 4.10: Measured open atmosphere weld bead dimensions corresponding to welding conditions given in Table 4.5, (a) SS 304 and (b) SS 316.

Figures 4.11 and 4.12 show the experimentally extracted weld macrographs corresponding to the welding conditions given in Table 4.4 for SS 304 and SS 316 respectively. It is noteworthy that the full penetration is achieved for laser power 2.0 kW at laser scanning speed of 15.0 and 13.33 mm/s. Figures 4.13 and 4.14 signify the measured weld macrographs of SS 304 and SS 316 corresponding to welding conditions of Table 4. In case of 5 mm thick material, the weld bead dimensions and shapes both are varied in open and controlled atmosphere of argon.

It is clearly observed from sections 4.1.1 and 4.1.2 that the welding ambient atmosphere is sensitive to the weld bead dimensions and shapes. In the following section, the characteristic difference between the controlled and open atmosphere welding is described comprehensively.

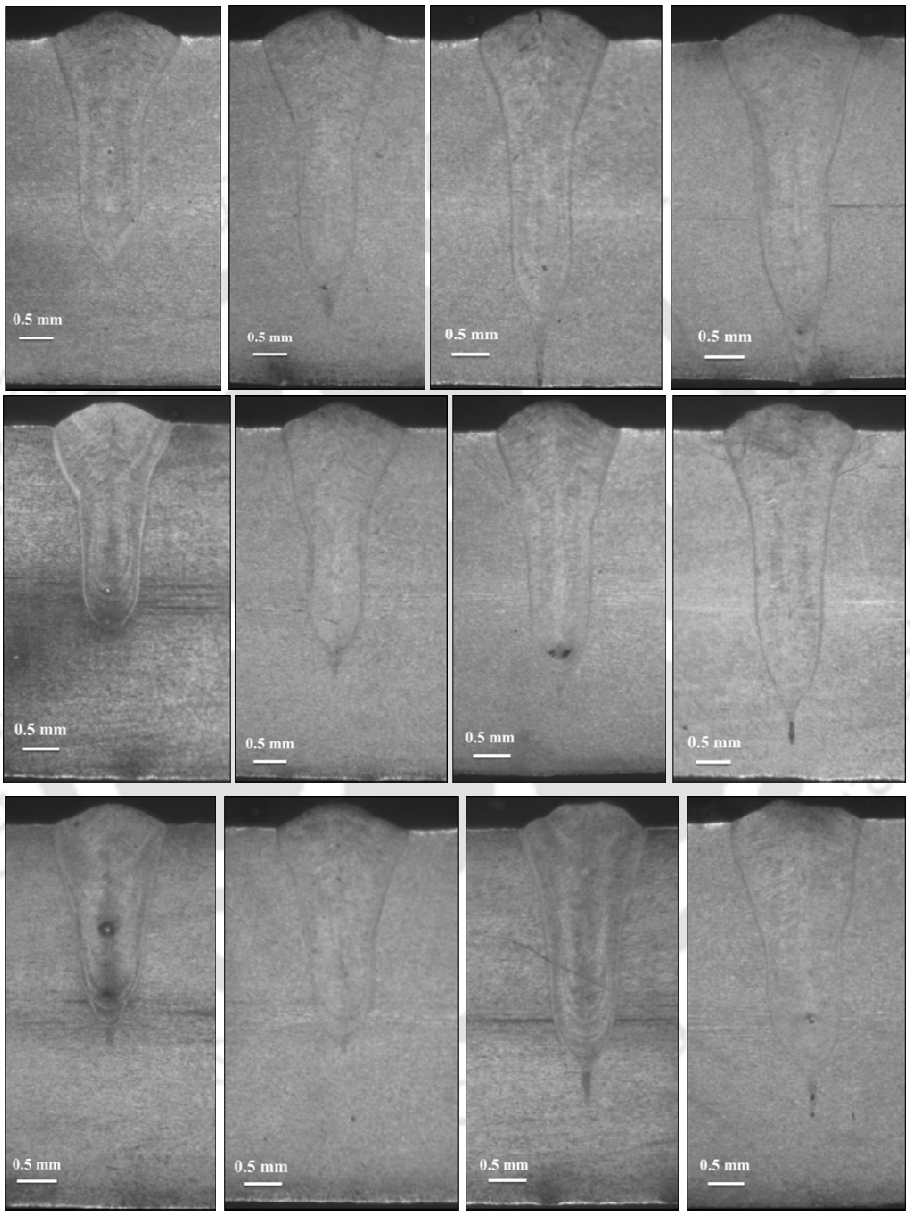

Figure 4.11: Experimental weld macrographs for welds in open atmosphere corresponding to welding conditions given in Table 4.4 of SS 304, 5 mm thickness plate.

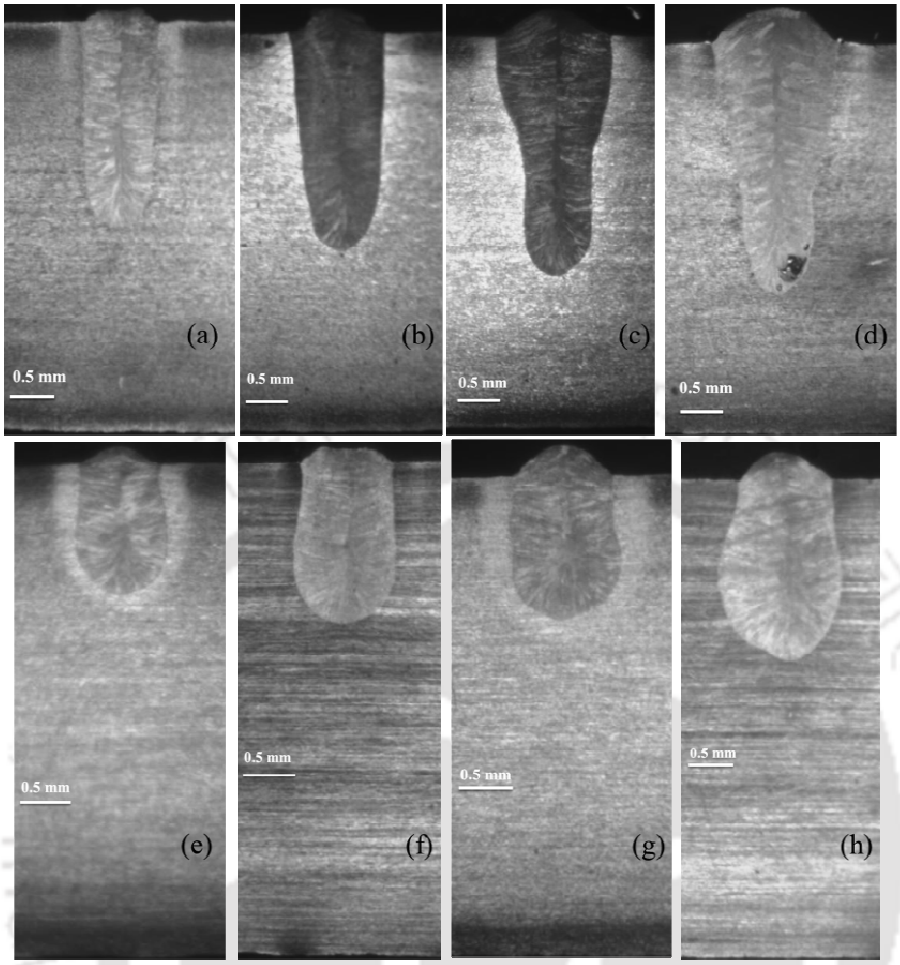

Figure 4.12: Experimental weld macrographs of SS 316, 5 mm thickness plate in open atmospheric conditions corresponding to (a) data set 1, (b) data set 2, (c) data set 3, (d) data set 4, (e) data set 9, (f) data set 10, (g) data set 11 and (h) data set 12 given in Table 4.4.

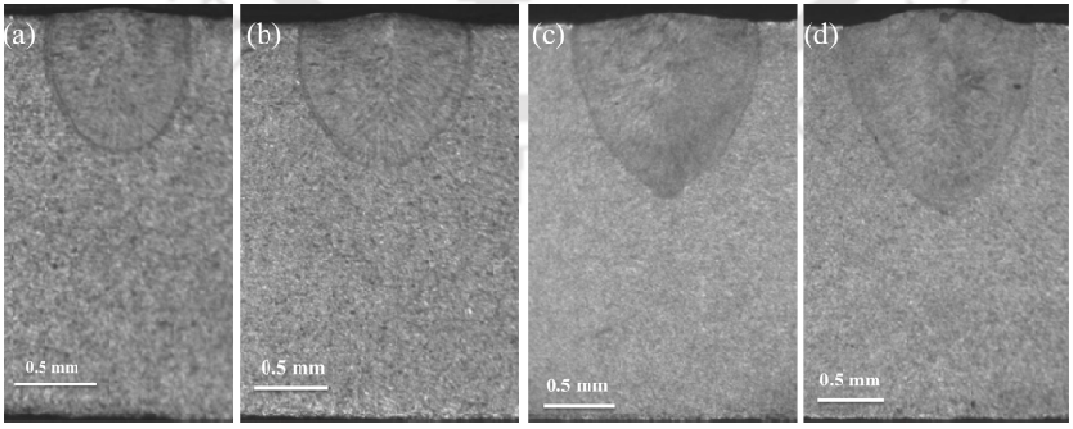

Figure 4.13: Weld macrographs corresponding to open atmospheric conditions for (a) data set 5, (b) data set 6, (c) data set 7 and (d) data set 8 given in Table 4.5 of SS 304, 3 mm thickness plate.

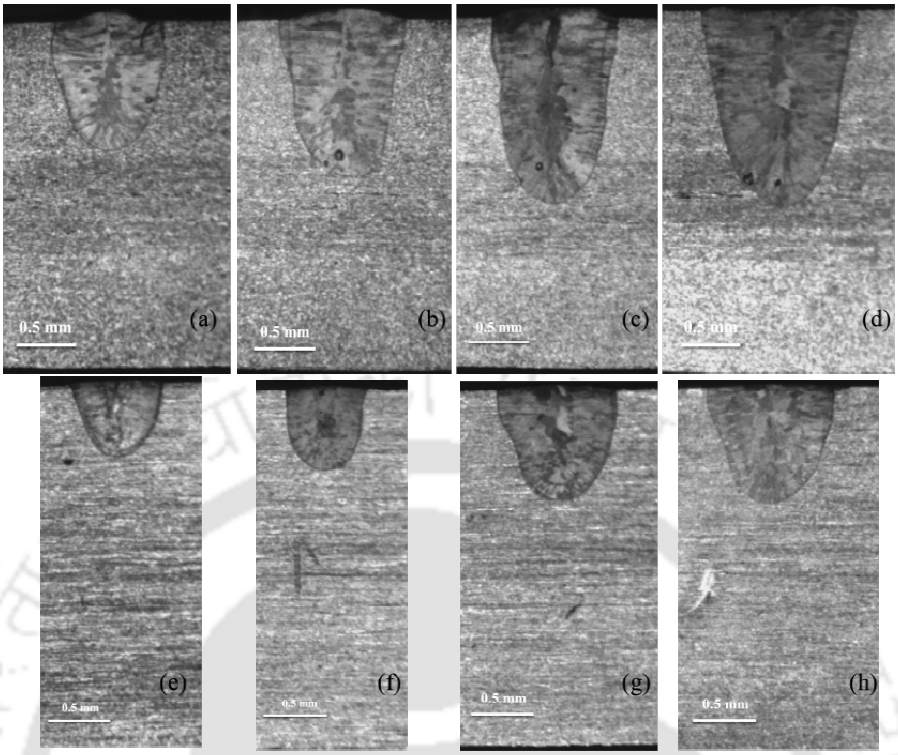

Figure 4.14: Experimental weld macrographs of SS 316, 3 mm thickness plate in open atmospheric conditions corresponding to (a) data set 1, (b) data set 2, (c) data set 3, (d) data set 4, (e) data set 5, (f) data set 6 and (g) data set 7 and (h) data set 8 given in Table 4.5.

4.1.3 Influence of welding ambient atmosphere

This section describes the influence of the welding ambient atmosphere during fiber laser welding with reference to weld dimensions. During fusion welding process, thermo-chemical reactions occur between weld pool and working atmosphere that severely affects the weld metal properties and weld joint quality. Therefore, the welding atmosphere influences notably on the quality of the weld joint.

Figure 4.15 represents the quantitative comparison of weld bead dimensions (SS 304) at two different welding atmospheres under similar welding conditions (data set 1 to data set 8) depicted in Table 4.5. The self-protective atmosphere welds attained maximum depth of penetration and minimum width. This resembles the fact that the presence of argon gas helps to constrict the laser beam and results in more concentrated heat flux. The maximum variation of the weld depth of penetration is 29% and weld width is 40%; and the minimum variation of the weld bead width is 9% and depth of penetration is 4% between two welding atmospheres. Figure 4.15 (c) denotes the aspect ratio which is well-defined by the ratio of weld depth of

penetration to bead width of a weld joint. The aspect ratio is one of the characteristic quantities to specify the efficiency of the joint. The numeric inside the Fig. 4.15 (c) depicts the welding conditions (data set 1 to data set 8) given in Table 4.5. In case of protective atmosphere, the maximum aspect ratio is achieved as 1.361 for the data set #4 given in Table 4.5. However, the minimum is 1.049 corresponding to data set # 5 of Table 4.5. In case of the open atmosphere, the minimum aspect ratio is 0.85 and maximum is 1.075 for the data set # 1 and 5, respectively of Table 4.5. Hence, the aspect ratio attained in a self-protective atmosphere of argon welding process is more as compared to open atmospheric condition.

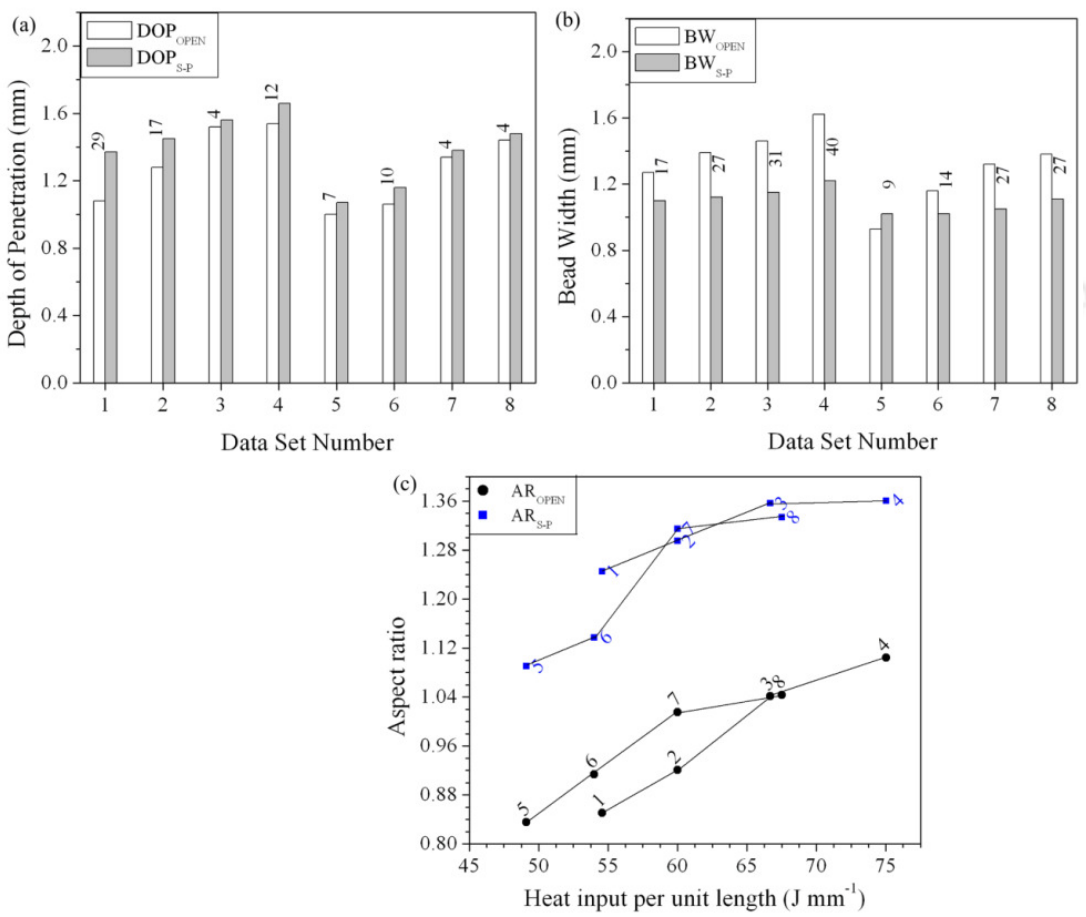

Figure 4.15: Comparison of SS 304 weld dimensions in open and controlled atmosphere of argon: (a) depth of penetration, (b) bead width and (c) aspect ratio corresponding to data set 1 to data set 8 given in Table 4.5.

Figure 4.16 describes the comparison of the weld macrographs between open atmosphere and a self-protective atmosphere of argon corresponding to welding conditions of data set # 1, 2, 3, and 4, respectively given in Table 4.5. The characteristic difference can be observed from this comparison in terms of weld pool size and shape at two different welding

atmospheres. In protective atmosphere, the weld bead shape is conical whereas it is different in case of open atmospheric condition. The weld depth of penetration is higher and weld bead width is lesser in argon atmosphere as compared to open atmospheric condition with similar welding conditions.

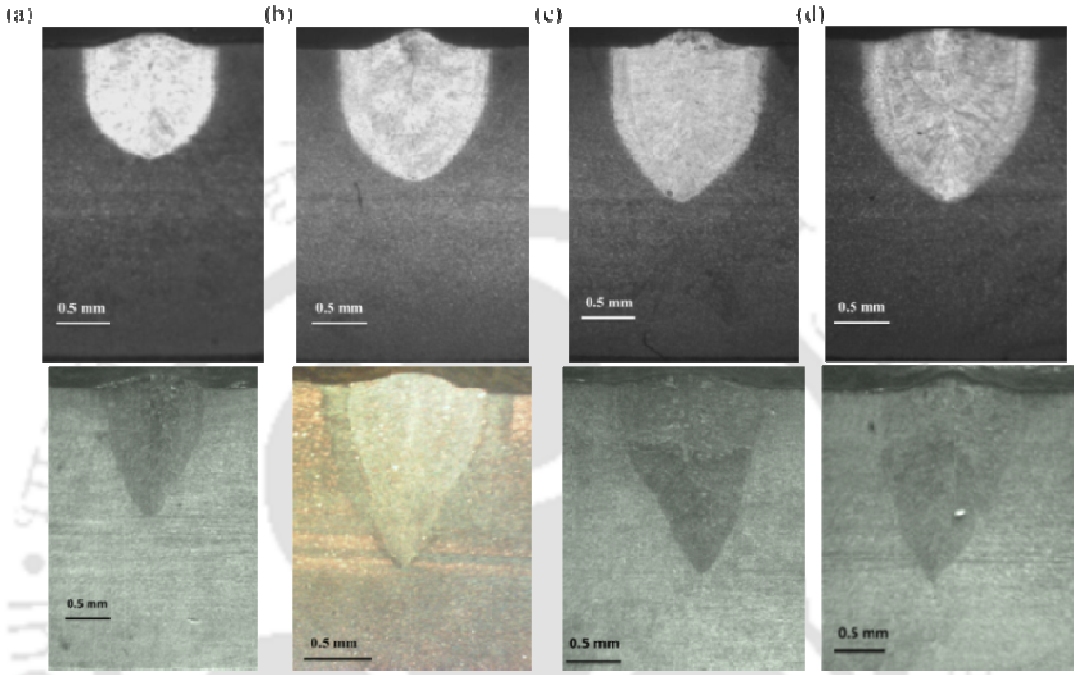

Figure 4.16: Comparison between open and self-protective atmosphere SS 304 weld macrographs corresponding to (a) data set 1, (b) data set 2, (c) data set 3 and (d) data set 4 given in Table 4.5.

The most significant finding in present experimental investigation is the noticeable difference in the appearance of weld bead surface. Figure 4.17 shows the comparison between open and a self-protective atmosphere of argon corresponding to welding variables of data set # 2, 3 and 8 given in Table 4.5. It is obvious that more neat and clean surface is observed in case of a self-protective atmosphere of argon welds as compared to open atmospheric condition. In open atmosphere, air particles such as nitrogen, oxygen, and hydrogen may react with molten weld pool. These reactions are result in high degree of rough surfaces, porosity, gas pores or pin holes. However, in a self-protective atmosphere of argon welding, the appearance of weld surface is clean with low degree of surface roughness, and less porosity. In open atmosphere welding process, the air particles in their elemental form may go inside the molten weld pool at high temperature gradients and during solidification they may try to escape from the weld pool. This may also causes the cracking of the weld joint and reduces

the weld joint quality. In case of self-protective atmosphere, the issues of the reaction with air particles which exists in atmosphere can be minimized/eliminated using self -protection by argon.

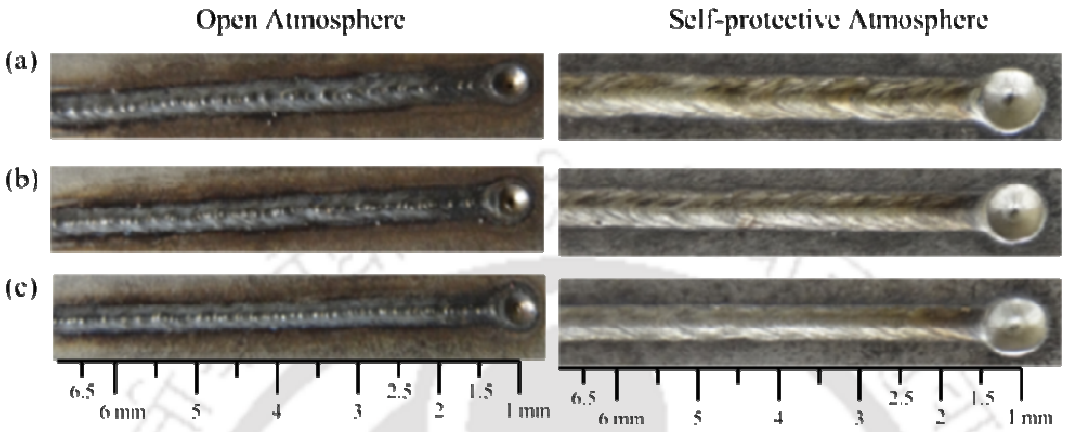

Figure 4.17: SS 304 top surface appearance corresponding to welding conditions of (a) data set 3, (b) data set 6 and (c) data set 8 given in Table 4.5.

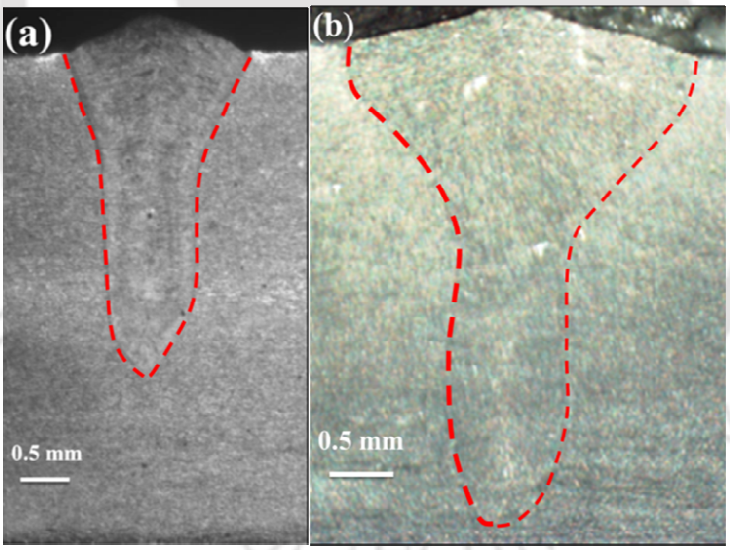

Figure 4.18: Weld macrographs corresponding to data set 1 given in Table 4.4; (a) open atmosphere and (b) controlled atmosphere welding.

Figure 4.18 describes the measured weld macrograph of SS 304 corresponding to laser power 2000 W and welding speed, 18.33 mm/s in open and controlled atmosphere of argon respectively. It is observed that the weld bead dimensions and aspect ratio is more in case of controlled atmosphere corresponding to similar welding conditions. Moreover, the weld bead dimensions increases with decreasing the welding speed at constant laser power. However,

the weld bead shapes and dimensions of open atmosphere and controlled atmosphere of argon welds are not similar in nature. Figure 4.19 refer to the experimental weld macrographs corresponding to SS 316 of laser power 1000 W and laser scan speed 18.33 mm/s. It is obvious that irrespective of weld material, the weld bead dimensions and aspect ratio is more in controlled atmosphere of argon as compared to open atmospheric condition. Figure 4.20 represents the top surface appearance of 5 mm thick SS 304 corresponding to data set 1 and data set 2 given in Table 4.4, respectively. More neat and clean surface is obtained in controlled atmosphere of argon welding as compared to open atmospheric condition.

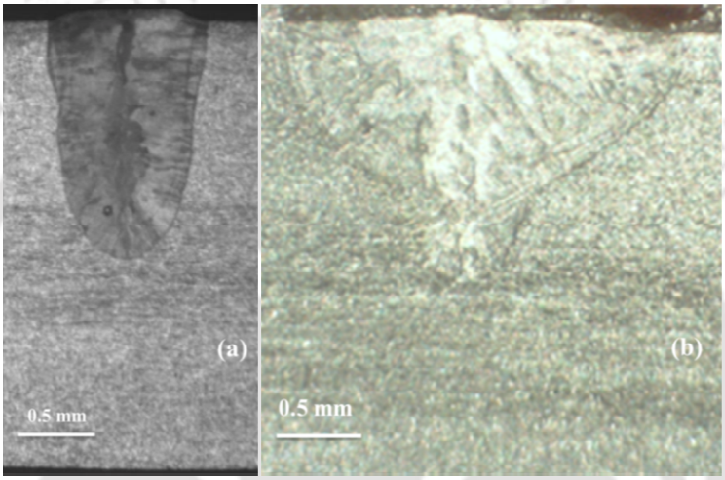

Figure 4.19: Comparison of experimental weld macrographs corresponding to SS 316 of data set 1 given in Table 4.5; (a) open atmosphere and (b) controlled atmosphere welding.

Figure 4.21 describes the quantitative comparison of the weld bead dimensions, depth of penetration, bead width and aspect ratio between open and controlled atmosphere of argon welds corresponding to SS 304, 5 mm thickness plate welding conditions data set 1 to data set 4 given in Table 4.4. For each data set index/number given in this figure, weld bead dimensions and aspect ratio are more in case of controlled atmosphere of argon as compared with open atmosphere welds. This resembles the fact that argon helps to constrict the laser beam and results in more concentrated heat flux. The maximum weld bead dimensions are achieved for the data set 4 given in Table 4.4. The aspect ratio which is well-defined by the ratio of weld depth of penetration to bead width of a weld joint is a characteristic quantity to specify the effectiveness of the formed weld joint. The maximum aspect ratio, 2.998 is achieved in controlled atmosphere of argon welding (data set 4 in Table 4.4) whereas the minimum is 2.02 (data set 1 in Table 4.4). In case of the welding in open atmospheric conditions, the maximum aspect ratio is 2.8 and the minimum is 1.8 for the data set 4 and 1,

respectively (Table 4.4). The aspect ratio achieved in controlled atmosphere of argon welding process is more when compared with the process of welding under open atmospheric conditions for the similar welding conditions plotted in Fig. 4.21.

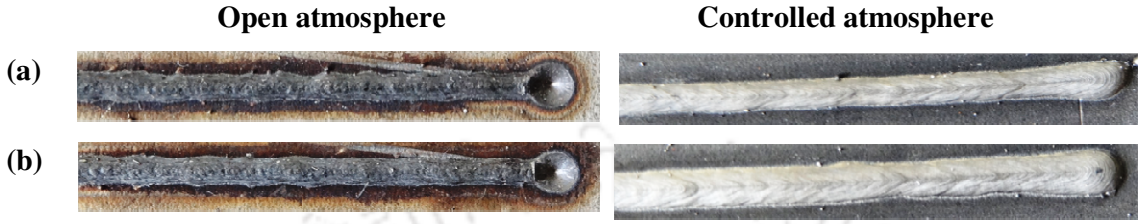

Figure 4.20: Top view appearance comparisons for open and controlled atmosphere welding corresponding to (a) data set 1 and (b) data set 2 given in table 4.4.

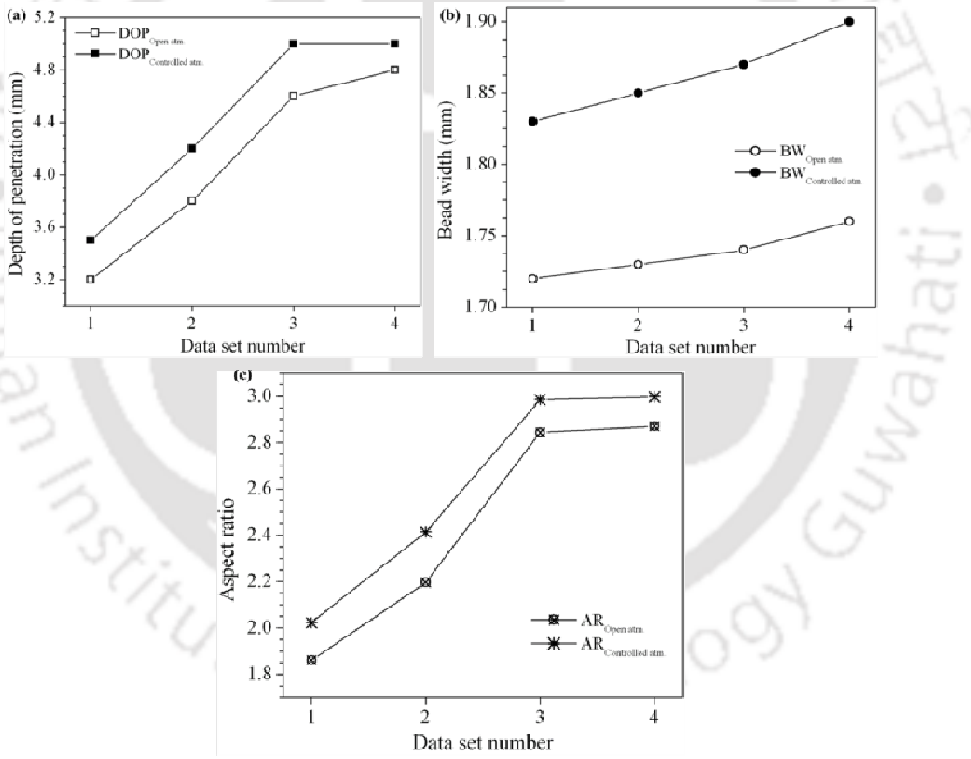

Figure 4.21: Comparison of weld bead dimensions of open and controlled atmosphere welding corresponding to welding conditions given in table 4.4.

Figure 4.22 describes the comparison of weld macrographs achieved for SS 316 material of 3 mm and 5 mm thickness plate in open and controlled atmosphere of argon corresponding to similar process variables. Though, weld bead dimensions and aspect ratios are more in case of controlled atmosphere, the weld macrograph shapes are also not the same. For 3 mm

thickness plate, weld macrographs in controlled atmosphere are uneven shaped. However, it is also observed that the macrographs for 5 mm thickness plate vary with welding atmosphere at similar processing variables.

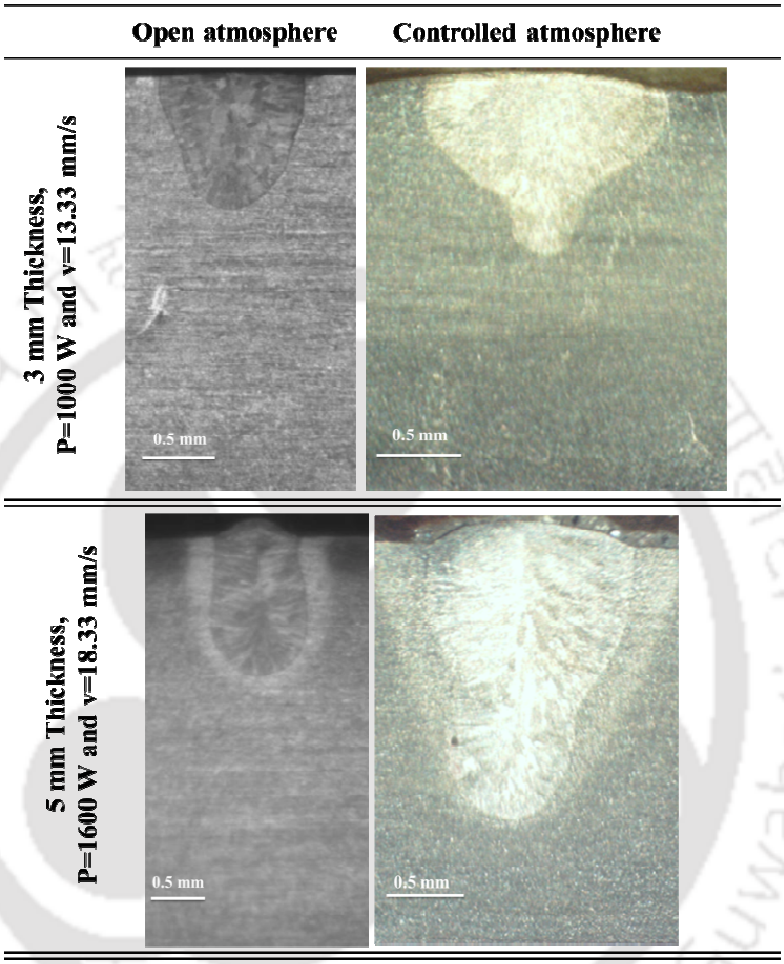

Figure 4.22: Comparison of weld macrographs made in open and controlled atmosphere of argon of SS 316, 3 mm and 5 mm thickness plate.

The most noteworthy observation in for this material is also the appearance of weld bead surface quality. Figure 4.23 (a)-(c) and (d)-(g) represents top view weld bead appearance comparison of open and controlled atmosphere welding on 3 mm and 5 mm thickness plates respectively. It is clearly observed from this figure that better and clean surface is achieved in controlled atmosphere due to protection of molten pool. Moreover, the problems of oxygen, nitrogen and hydrogen presence in welds can be minimized with controlled atmosphere of welding.

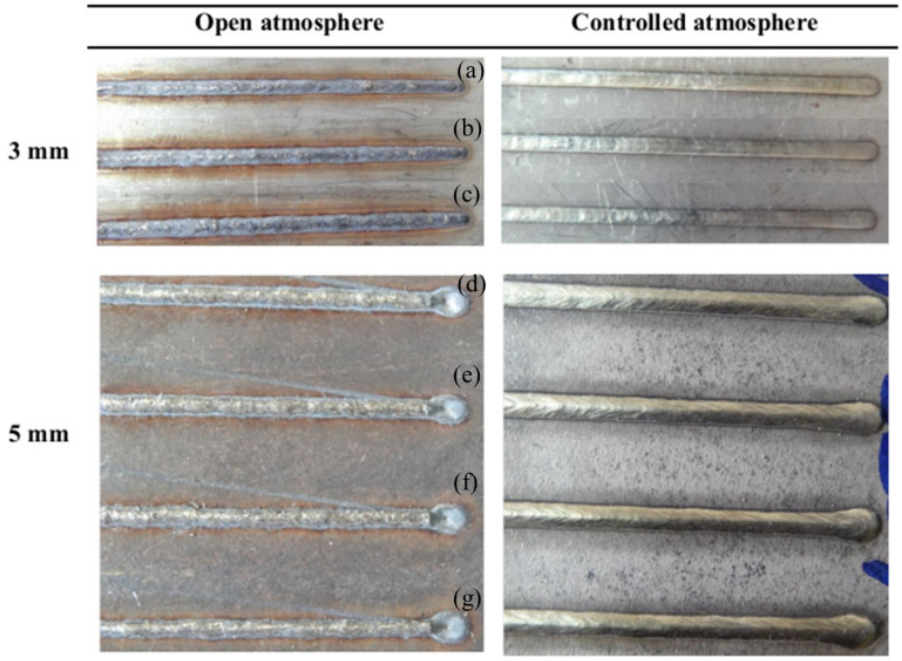

Figure 4.23: Top view appearance comparison of SS 316 open and controlled atmosphere welds corresponding to (a) data set 1, (b) data set 2 and (c) data set 3 given in Table 4.5; and (d) data set 1, (e) data set 2, (f) data set 3 and (g) data set 4 given in Table 4.4.

Figure 4.24 depicts the quantitative comparison of weld bead dimensions for open and controlled atmosphere corresponding to welding conditions of Tables 4.4 and 4.5. $DOP_{Open\ atm.}$, $DOP_{Controlled\ atm.}$, $BW_{Open\ atm.}$, $BW_{Controlled\ atm.}$ and 'Difference' depict the depth of penetration in open and controlled atmosphere, bead width in open and controlled atmosphere and difference between them respectively. At similar welding process variables, the aspect ratio and weld bead dimensions obtained in controlled atmosphere are more as compared to open atmosphere. The fact is that argon helps to penetrate the laser into deep due to inverse bremsstrahlung effect.

4.1.4 Distortion in fiber laser butt joint

The welding experiments are performed to investigate the distortion in square butt joint configuration at different welding parameters. These experiments comply with the computed results of the developed thermo-mechanical model. The deflections are measured in terms of average angular distortion in longitudinal direction. The configuration of angular distortion is presented in Fig. 4.25. The 2 kW fiber laser based welding system was used to perform welding on SS 304 and SS 316 of 3 mm and 5 mm thickness. High purity argon was

used as shielding gas with flow rate is 10 LPM. Table 4.6 and 4.7 depict the welding process variables corresponding to 5 mm plate and 3 mm plate butt welding respectively. The other process variables are same as given in Table 4.3.

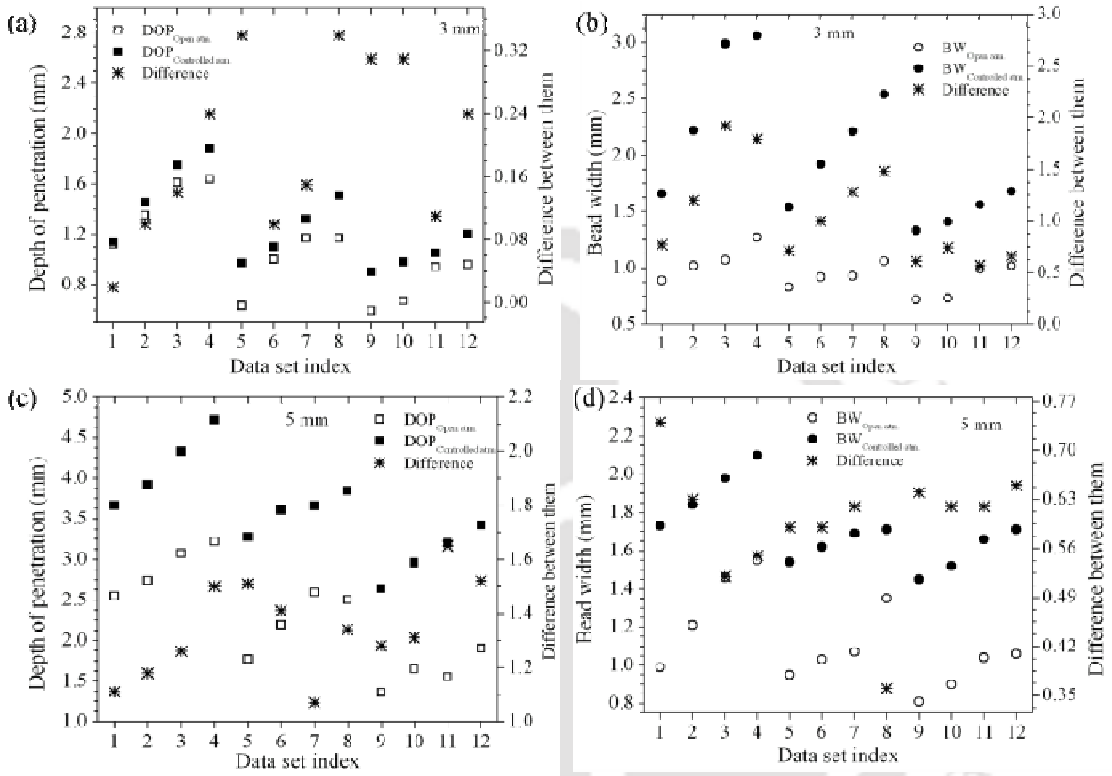

Figure 4.24: The quantitative comparison of SS 316 weld bead dimensions obtained from open and controlled atmosphere of argon welds along with difference between them, (a) depth of penetration (DOP) and (b) bead width (BW) corresponding to data given in Table 4.5; and (c) depth of penetration (DOP) and (d) bead width (BW) corresponding to welding conditions given in Table 4.4.

After re-solidification of fusion zone, the deflections are measured for each case. Digital height gauge is used to measure the deflections at various end locations and the average value is considered. After measuring the angular deflections, the metallographic analysis has performed to measure the weld macrographs.

Table 4.6: Square butt fiber laser welding process parameters for SS304 and SS316 stainless steel of 5 mm thick plate under open atmosphere.

Data set no.	Laser power (W)	Welding velocity (m/min.)	Heat input per unit length (J/mm)
1	2000	0.88	136.36
2	1800	0.9	120
3	1800	1.028	105.05
4	1600	1.06	90.57

Table 4.7: Square butt fiber laser welding process parameters for SS304 and SS316 stainless steel of 3 mm thick plate under open atmosphere.

Data set no.	Laser power (W)	Welding velocity (m/min.)	Heat input per unit length (J/mm)
1	1000	0.667	90
2	900	0.72	75
3	900	0.9	60
4	800	1.067	45

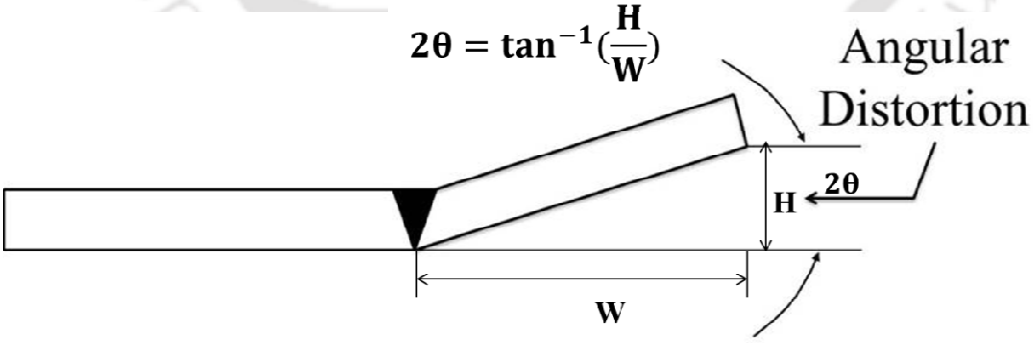

Figure 4.25: Schematic representation of angular distortion measurement.

Figure 4.26 represents the experimentally measured weld macrograph of SS 304, 5 mm thickness plate corresponding to data set 1, 2 and 3 respectively given in Table 4.6. It is obvious from this figure that the weld bead dimensions decreases as heat input per unit length

decreases. The weld joint profile is almost symmetrical that indicates a relatively better butt joint.

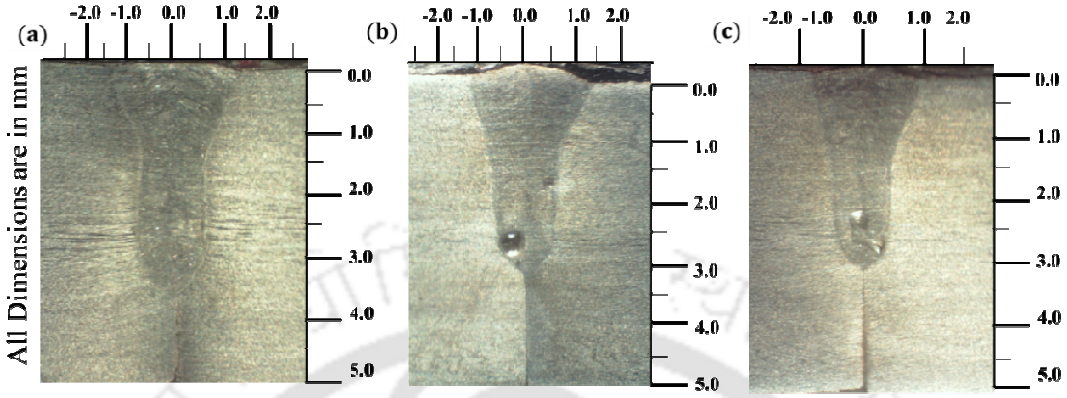

Figure 4.26: Weld macrographs of butt joint welds of SS 304, 5 mm thickness plate corresponding to (a) data set 1, (b) data set 2 and (c) data set 3 given in Table 4.6.

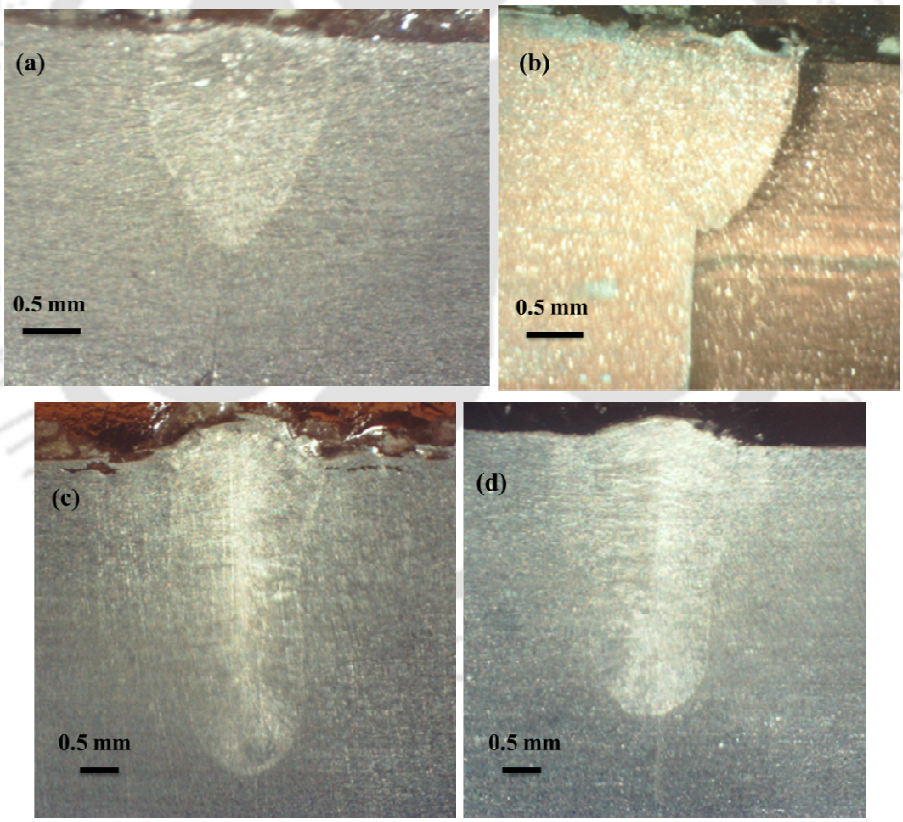

Figure 4.27: Butt joint weld macrographs (a) SS 304, data set 4, (b) SS 316, data set 1 given in Table 4.7; and (c) SS 316, data set 1 and (d) SS 316, data set 2 given in Tables 4.6.

Figures 4.27 (a) – (d) depict the measured square butt weld macrographs of SS 304 and SS 316, 3 mm and 5 mm thickness respectively. The corresponding welding conditions

are mentioned in this figure. Figures 4.28 and 4.29 describe the measured welding induced angular distortions of SS 304 and SS 316 plates of square butt joint. These angular distortions are corresponding to welding conditions given in Tables 4.6 and 4.7. It is observed from these figures (figures 4.28 and 4.29) that the angular distortion in more when the heat input per unit length is more. For the particular case of laser power 2000 W and laser scanning speed 0.88 m/min, the angular distortion is the maximum. The lower angular distortion was observed when the welds were made with laser power 1600 W and scanning speed of 1.06 m/min for 5 mm thick butt weld joint. Similar trend was followed for 3 mm thickness plate with respect to welding heat input per unit length, laser power and laser scanning speed.

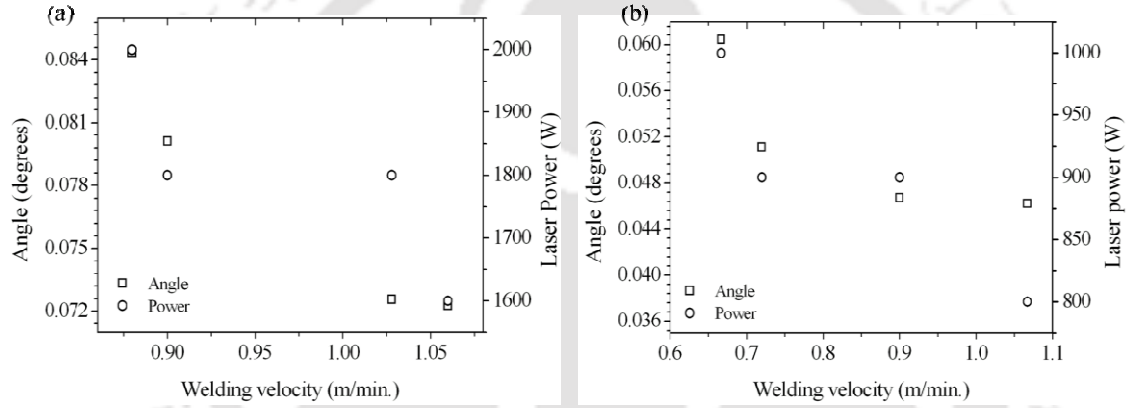

Figure 4.28: Angular distortions of fiber laser butt joint corresponding to SS 304 of thickness (a) 5 mm and (b) 3 mm.

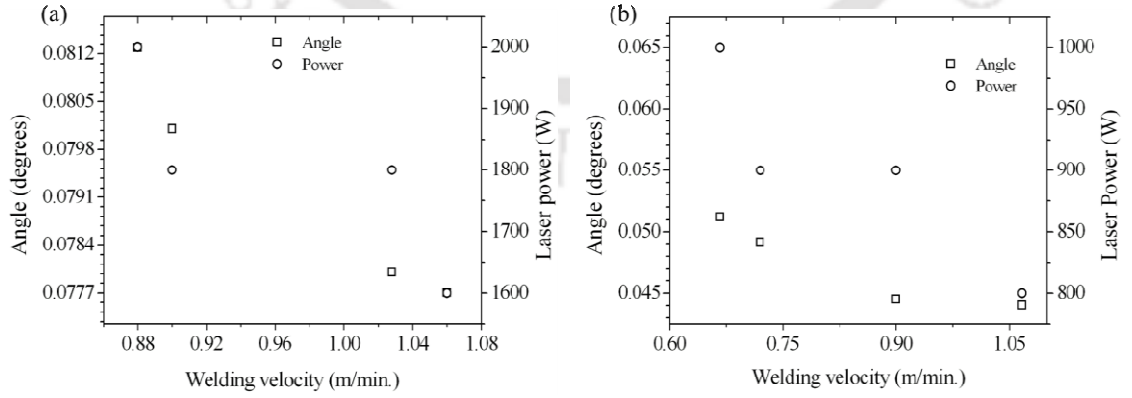

Figure 4.29: Welding induced angular distortions of fiber laser butt joint corresponding to SS 316 of thickness (a) 5 mm and (b) 3 mm.

4.1.5 Microstructure analysis

The microstructure of weldment reveals several facts on weld joint quality and consequently the influence of process variables. Hence, an investigation is carried out on the influence of ambient atmosphere in welded microstructure of SS 304 and SS 316. Apart from material composition, the thickness of the work piece greatly influences the solidification behavior and consequently the solidified structure.

Microstructure of the as-received material (SS 304) is shown in Fig. 4.30 (a). In general, the transverse section of the weld sample shows that the extension of the heat affected zone is very small. This is the distinctive advantageous effect associated with highly focused welding heat source [72]. The microstructure analysis reveals that there are no cracks formed in any one of the specimens examined. Even though some isolated pores were found mostly in open atmosphere weldment, no noticeable inclusions are observed in a controlled atmosphere of argon. In both ambient conditions, the obvious feature is the highly directional nature of the microstructure around the axis of the fiber laser beam due to the solidification of weld metal at high cooling rate. Figures 4.30 (b) and (c) describe the optical micrographs of heat affected zone (HAZ) and fusion zone (FZ) in open atmosphere weld at laser power of 2 kW and laser scanning speed of 18.33 mm/s. Fusion zone composition was insensitive to change in heat input. However, increase in welding speed and/or decrease in laser power resulted in a finer solidification structure due to low heat input. A dominant austenitic structure with no solidification cracking was obtained for all welds.

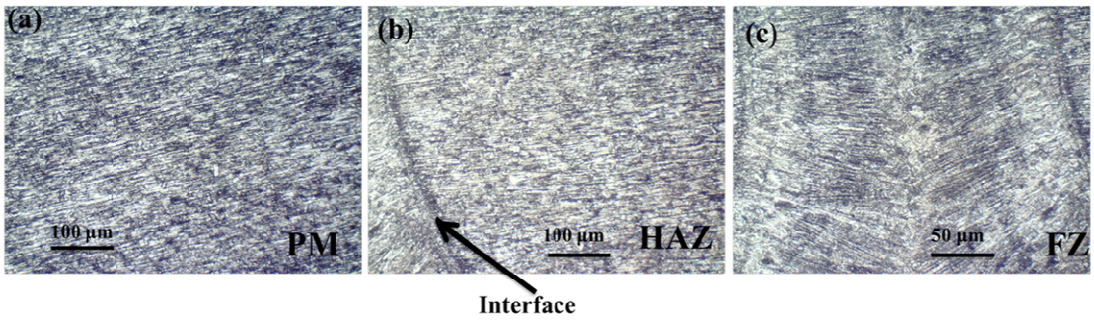

Figure 4.30: SS 304, 5 mm thickness plate optical microstructure of weldment in open atmospheric condition corresponding to data set 1 given in Table 4.4 at various zones, (a) parent material (PM), (b) heat affected zone (HAZ and (c) fusion zone (FZ).

The weld microstructure in controlled atmosphere of argon (figure 4.31) revels the fact that the solidification structure is dendritic containing austenite and a few percent of delta ferrite at the dendritic boundaries. Figures 4.31 (a) and (b) illustrate the HAZ and FZ micrographs of weld metal in a controlled atmosphere of argon corresponding to laser power of 2000 W and laser scan speed of 18.33 mm/s. It is obvious from Figs. 4.31 and 4.32 that there is variation of microstructure in open and a controlled atmosphere of argon with similar process variables. This difference in the microstructure is may be due to the solidification behavior of the weld metal varies for both the atmospheres. In addition to this, the chemical reactions between the molten weld pool and surrounding atmosphere may influence the formation of microstructure. In controlled atmosphere of argon, the degree of chemical reaction with atmospheric elements such as nitrogen, oxygen and hydrogen lead to minimum porosity or pin-holes formation. Figures 4.31 (c) and (d) represent the HAZ and FZ optical micrographs of weld metal using the laser power is 2000 W and welding speed of 13.33 mm/s in a controlled atmosphere of argon.

It is observed that the influence of the laser welding speed in a controlled atmosphere is almost similar as open atmosphere laser welds. However, the microstructures in the both welds are not similar. The higher the welding speed, the finer is the dendritic structure. This is attributed to an increase in both solidification and cooling rates due to low heat input resulted from high welding speed. Concerning the effect of laser power, the higher the laser power, the coarser is the dendritic structure due to decreasing cooling rate. However, the effect of laser power was relatively less than that of welding speed. The microstructures observed for present range of process parameters are always austenite with a few percent of delta-ferrite at the dendritic boundaries. Due to fine protection of weld pool in a controlled atmosphere; oxide, nitride, porosity and inclusion were formed minimum level in the weld metal. This may lead to the high efficiency of the weld joint in controlled atmosphere.

The microstructure of as-received SS 316 is shown in Fig. 4.32 (a). In general, the transverse section of weld sample after fiber laser welding shows that the extension of the heat affected zone is very small. No cracks are formed in any one of specimens examined. No isolated pores are observed in controlled atmosphere welding, but some isolated pores were found in open atmosphere weldment. There are no noticeable inclusions observed in a controlled atmosphere welding. Highly directional nature of the microstructure around the axis of fiber laser beam due to solidification at high cooling rate is observed. Figures 4.32 (b)-

(c) and (d)-(e) describes HAZ and FZ of SS 316 optical micrographs corresponding to data set #2 and #4 given in Table 4.4, respectively.

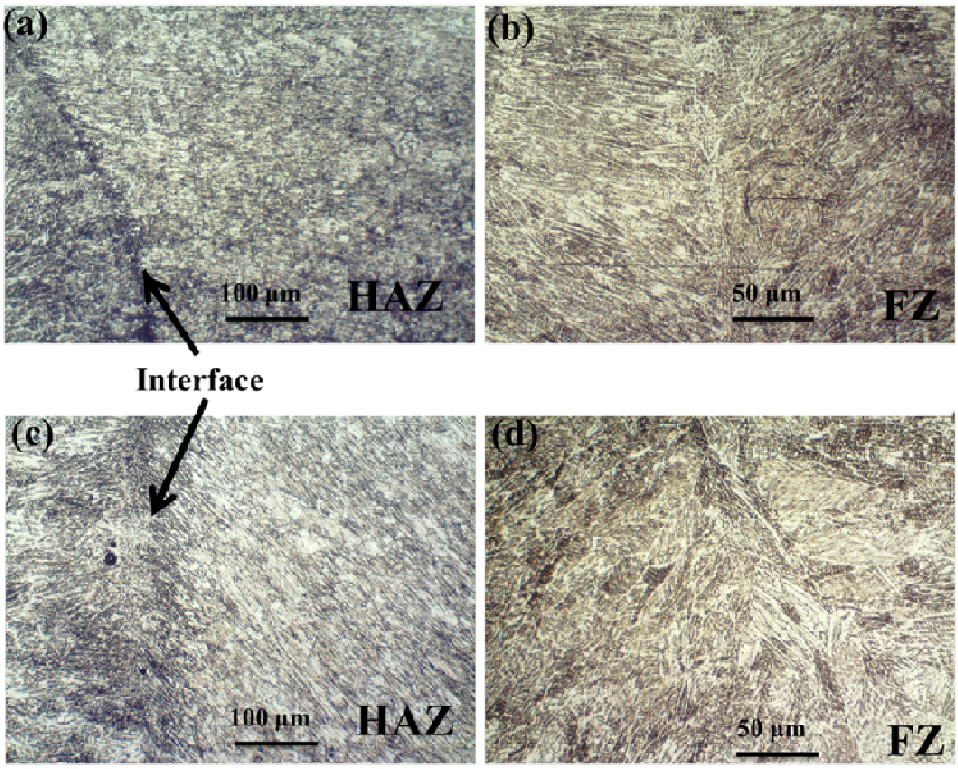

Figure 4.31: Microstructure of weldment in controlled atmosphere of argon corresponding to (a) data set 1, HAZ, (b) data set 1, FZ, (c) data set 4, HAZ and (d) data 4, FZ given in Table 4.4.

Figure 4.33 describes the microstructure of SS 316 welds produced in controlled atmosphere corresponding to data set #1, #2 and #4 of table 4.4. It is obvious that the microstructure formation in both the environments is certainly not the same due to variation of solidification rate in two atmospheres. Due to controlling/avoiding the chemical reaction of atmosphere particles with molten pool, the porosity or pin-holes formation is less in controlled atmosphere.

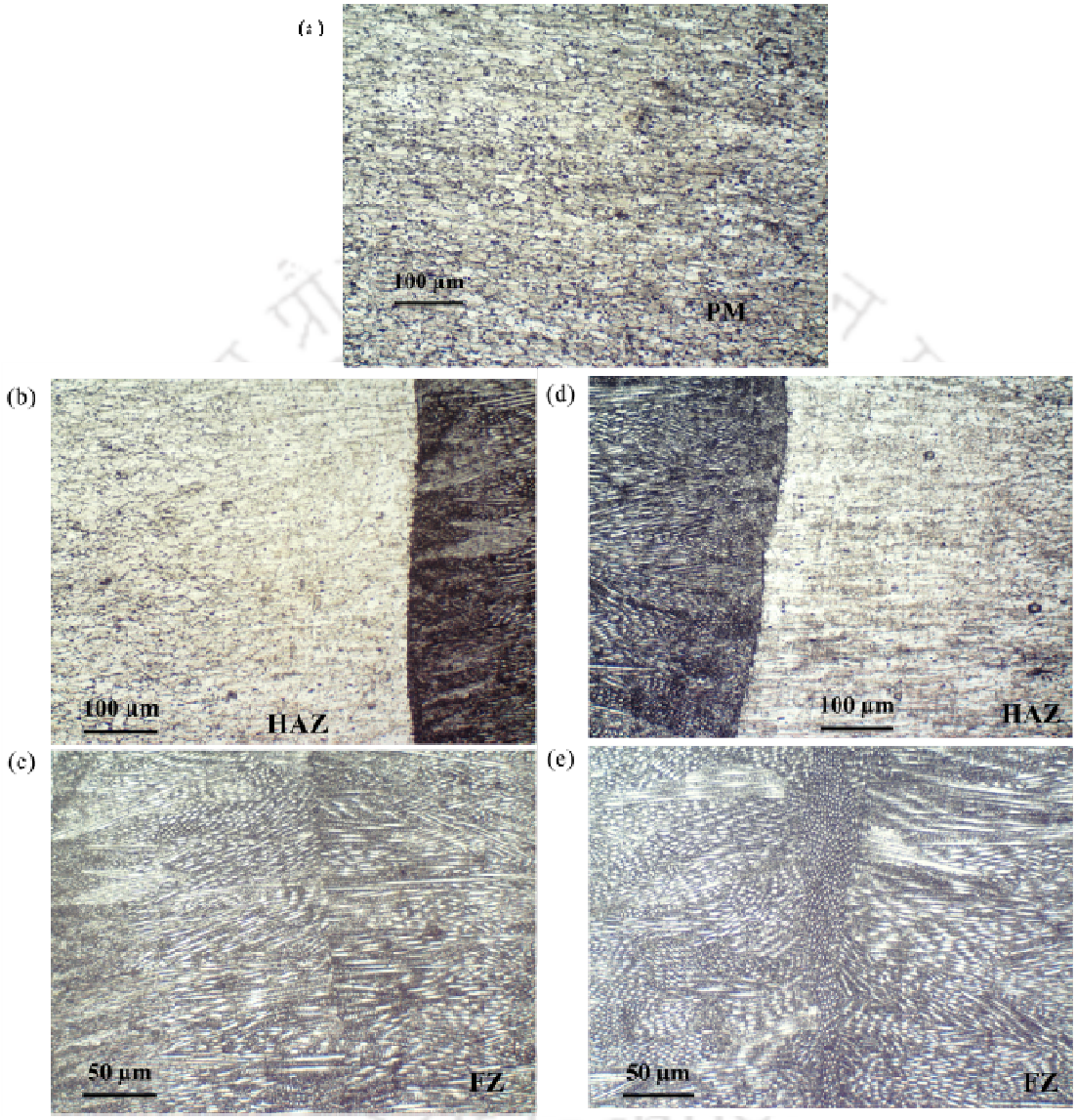

Figure 4.32: Optical microstructure of SS 316, 5 mm thickness plate weldment in open atmospheric condition, (a) parent material (PM); (b) heat affected zone (HAZ) and (c) fusion zone (FZ) corresponding to data set 2; (d) HAZ and (e) FZ corresponding to da set 4 given in Table 4.4.

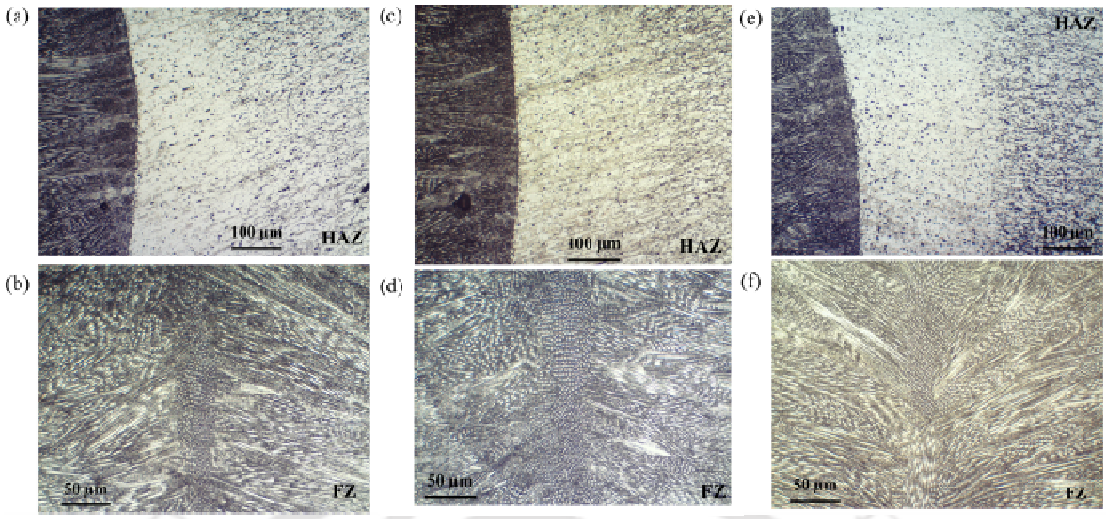

Figure 4.33: Microstructure of controlled atmosphere welds corresponding to (a) HAZ (b) FZ corresponding to data set 1; (c) HAZ, (d) FZ corresponding to data set 2; (e) HAZ and (f) FZ data set 4 given in Table 4.4.

4.2 Gas tungsten arc (GTA) welding

The GTA welding are carried to produce deep penetration welding using different activating fluxes. A thorough investigation is carried out to examine the differential influence of the surface active elements on weld dimensions. A bead-on-plate welding is performed on SS 316 of 5 mm thickness plate with thin layer of activating fluxes such as TiO_2, SiO_2, Al_2O_3 and mixture of fluxes. The linear GTA welding conditions are furnished in Table 4.8. The welding current varies from 130 A to 190 A whereas welding velocity is kept constant as 2.91 mm/s. The experiments are conducted with heat input per unit length from 90.57 J/mm to 136.36 J/mm. The primary objective of this experimental study is to produce deep penetration in linear GTA welding process by adopting simple and tractable approach using surface active elements. The GTA welds with and without activating fluxes were conducted using DCEN power source (Pi 400 Plasma from ***Migatronic*** that can be used for both plasma arc and GTA welding processes). The in-house developed experimental setup is shown in Fig. 4.34. The time–temperature history is measured using K-type thermocouples at different locations illustrated in Fig. 4.35.

Table 4.8: GTA welding process parameters with and without flux.

Data set no.	Current (A)	Welding velocity (mm/s)	Heat input per unit length (J/mm)
1	130	2.91	136.36
2	160	2.91	120
3	190	2.91	90.57

Figure 4.34: In-house developed GTA welding experimental setup along with thermocouples.

4.2.1 GTA welding using activating flux

The experiments are conducted using thin layer of activating fluxes such as TiO_2, SiO_2, Al_2O_3 and mixture of these. Prior to the welding, the surface of each specimen was roughly ground with 240 grit (silicon carbide) flexible abrasive paper to remove all impurities and was cleaned with acetone. The compounds TiO_2, SiO_2, Al_2O_3 supplied in powder form are selected as activated flux because their simple composition facilitate the penetration of TIG welds. The information regarding these powders is shown in Table 4.9. Before welding process, the flux powder was uniformly mixed with acetone to form a paint-like consistency, and was subsequently applied with a paintbrush as shown in Fig. 4.36. In the present work, the thickness of the flux layer is considered approximately 2 ~ 3 mm. In GTA welding, the

welding current and travel speed are the process parameters that are primarily used to determine the weld shape. In the present investigation, only welding current is varied and travel speed is kept constant to investigate the influence of activating fluxes.

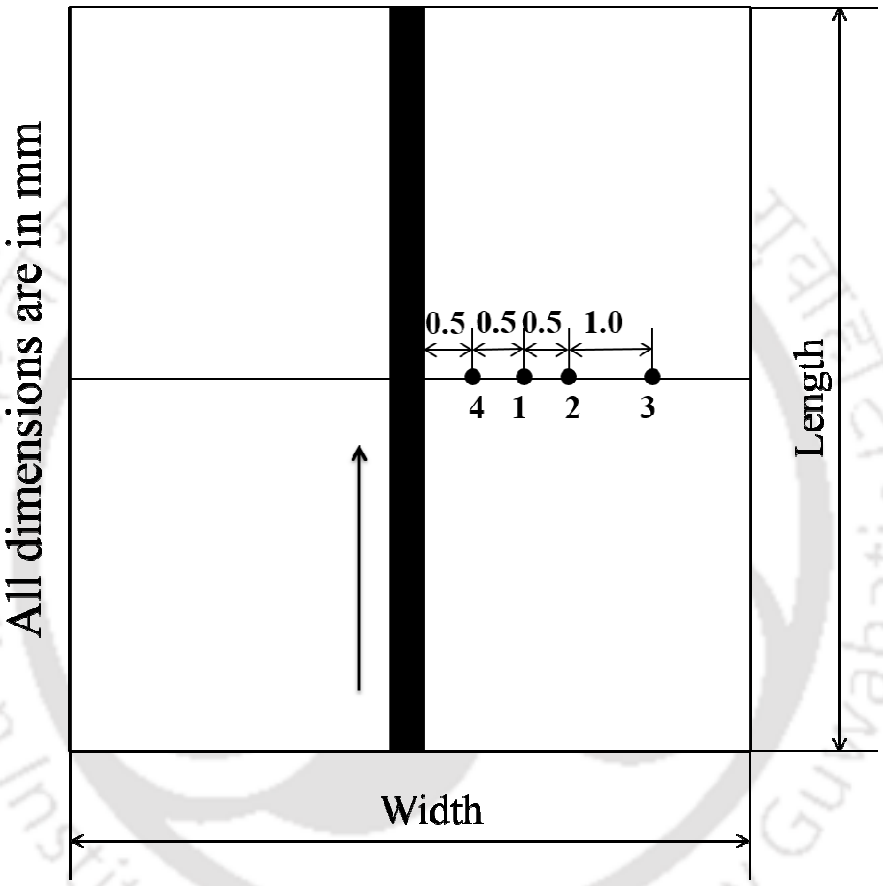

Figure 4.35: Schematic representation of thermocouples location on work piece during GTA welding.

Table 4.9: Information of flux powders used.

Flux powder			
	TiO_2 powder	**Al_2O_3 powder**	**SiO_2 powder**
Origin	Merck Specialities Pvt. Ltd.	Merck Specialities Pvt. Ltd.	Merck Specialities Pvt. Ltd.
Molar mass	79.90 g/mol	101.96 g/mol	60.08 g/mol
Density	4.2 g/cm^3		2.6 g/cm^3
Melting point	2128.15 K		1923.15 K
Boiling point	3245.15 K		2503.15 K
Calcium (Ca)	-	Less than or equal to 0.15%	-
Chloride (Cl)	-	Less than or equal to 0.05%	-
Portion elutable with water	-	Less than or equal to 0.2%	-
pH-value (10% aqueous suspension)	-	6.8-7.8	-
Substances soluble in water	Less than or equal to 0.5%	-	-
Substances soluble in diluted hydrochloric acid	Less than or equal to 0.5%	-	-
Sulfate (SO_4)	Less than or equal to 0.05%	-	-
Heavy metals (as Pb)	Less than or equal to 0.005%	-	-
Arsenic (As)	Less than or equal to 0.0005%	-	-
Iron (Fe)	Less than or equal to 0.005%	-	-

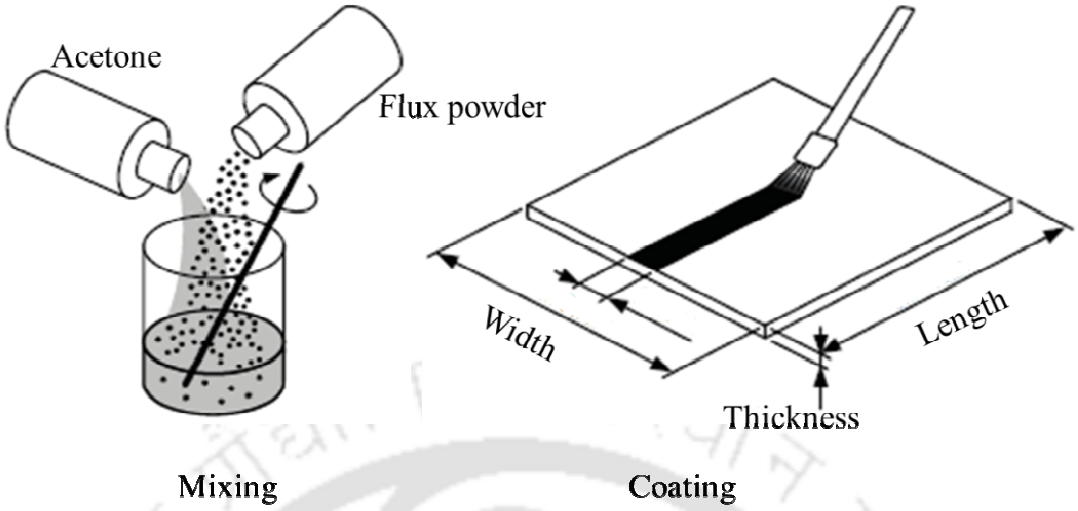

Figure 4.36: Schematic representation of flux preparation and coating.

Figures 4.37 - 4.39 represents weld macrographs of GTA welding with activating flux TiO_2, SiO_2, and Al_2O_3 corresponds to welding condition of data set 1 and 2 given in Table 4.8. The effect of different activating fluxes leads to various pattern of weld bead shapes. The welding by using TiO_2 provides the higher depth of penetration and bead width as compared to the other two activating fluxes. Moreover, the experiments by using Al_2O_3 flux produce a shallow penetration weld. The reasons for this patters and weld pool behaviour are explained in the subsequent section.

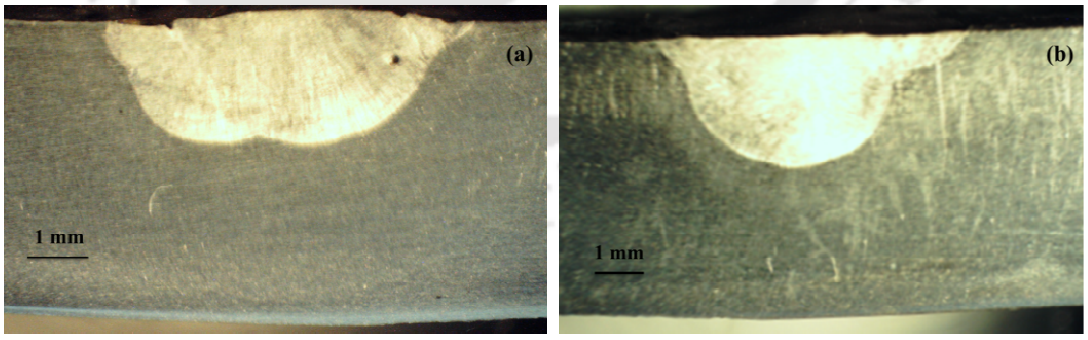

Figure 4.37: GTA Welds macrographs using TiO2 activating flux corresponding to (a) data set 1 and (b) data set 2 given in Table 4.8.

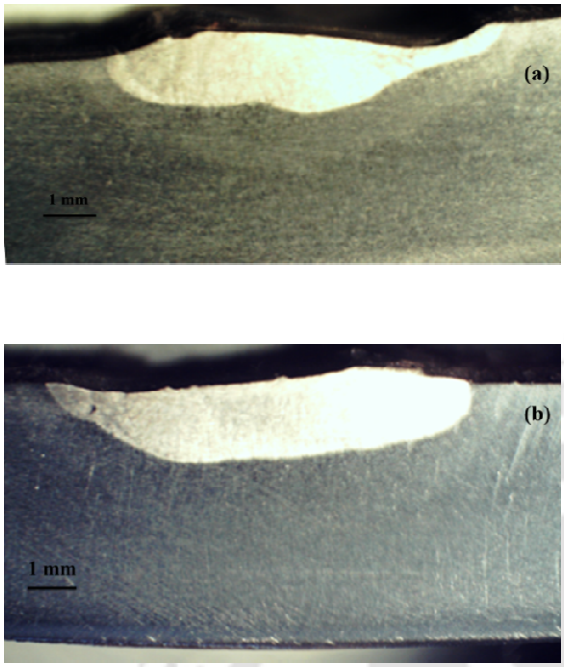

Figure 4.38: GTA weld macrographs using Al_2O_3 activating flux corresponding to (a) data set 1 and (b) data set 2 given in Table 4.8.

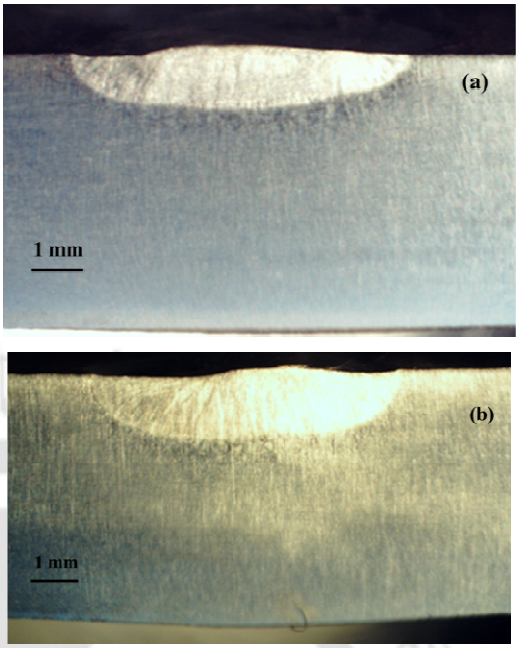

Figure 4.39: Experimental GTA weld macrographs With SiO2 flux corresponding to (a) data set 1 and (b) data set 2 given in Table 4.8.

4.2.2 GTA welding without any activating flux

The GTA welding experiments are also carried out without any activating flux to examine the influence of activating fluxes. These experiments are conducted with the similar process variables as given in Table 4.8. Figures 4.40 (a) and (b) show the weld macrographs corresponding to data set 1 and 2 of Table 4.8.

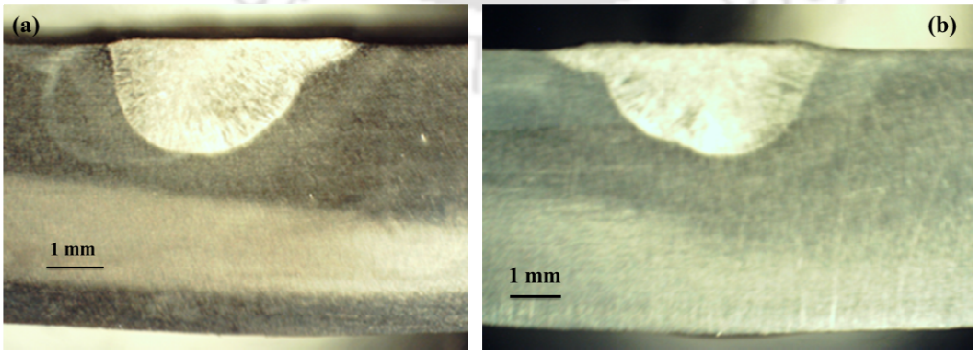

Figure 4.40: Weld macrograph of GTA welds made without any flux corresponding to (a) data set 1 and (2) data set 2 given in Table 4.8.

Figure 4.41 depicts the overall comparison of weld depth of penetration and bead width of GTA welds made with and without activating flux. The weld bead dimension is higher in case of welding using TiO_2 activating flux as compared to other activating fluxes. Figure 4.41 shows the variation of weld depth of penetration and bead width as a function of welding current for welds with and without activating flux.

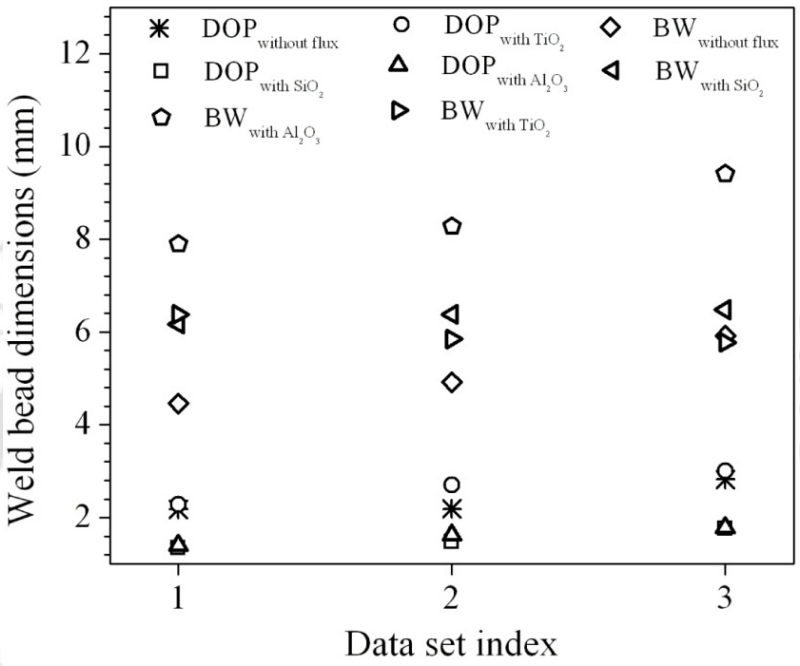

Figure 4.41: GTA weld bead dimensions using different activating fluxes and without using any activating flux.

4.2.3 Effect of surface active elements

The literature indicates that the fluid flow direction in the molten pool affects the weld morphology [114-117]. A significant factor in driving the direction of fluid flow in molten weld pool is the temperature coefficient of surface tension. Figure 4.42 represents the morphology of GTA welds corresponding to the welding current of 190 A and travel speed of 2.91 mm/s. During welding process, it is very difficult to measure the temperature in the molten pool because this area is surrounded by hot plasma. Nevertheless, it is well known that the temperature gradient always exists on the surface of the GTA weld accompanied by higher temperatures in the pool center under the arc and lower temperatures at the molten pool edge.

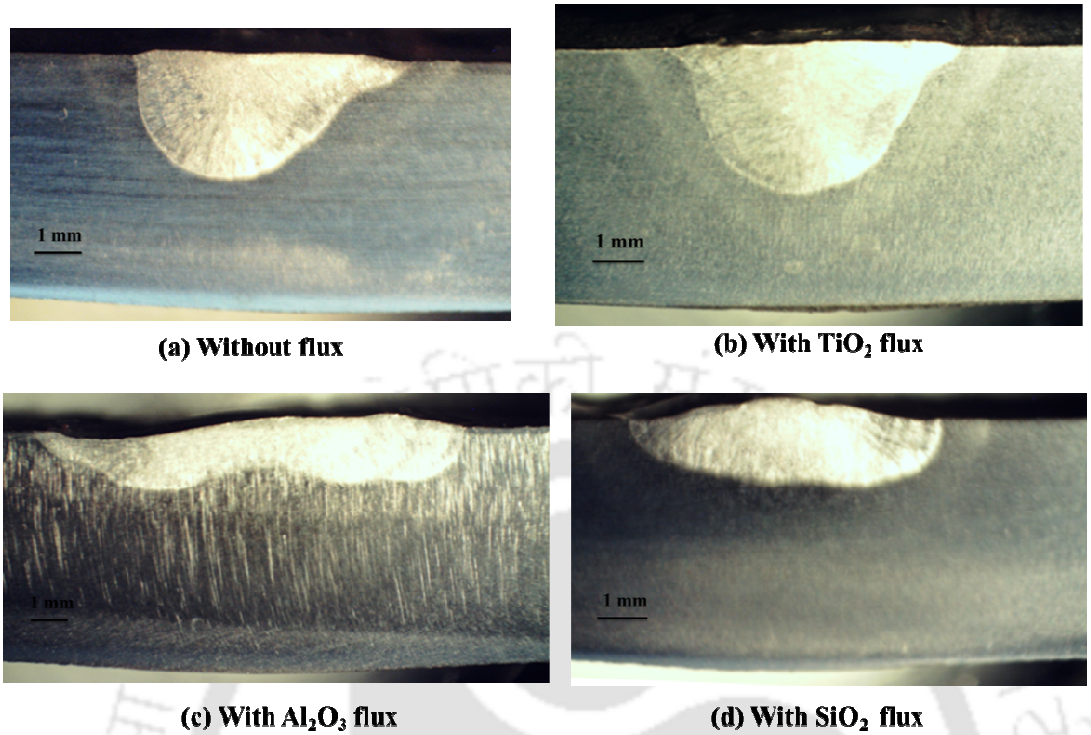

(a) Without flux (b) With TiO_2 flux

(c) With Al_2O_3 flux (d) With SiO_2 flux

Figure 4.42: Comparison of GTA weld macrographs with and without activating flux corresponding to data set 3 given in Table 4.8.

Figure 4.43 illustrates the geometric characteristics of GTA welds which are produced without and with TiO_2, Al_2O_3 fluxes. A considerable increase in depth of penetration is achieved using TiO_2 flux. The TiO_2 flux can help in creating GTA weld with a high penetration in 316 stainless steel. A weld with a high aspect ratio is characterized by an increased energy density of the welding heat source which yields an adequate concentration of heat energy. Moreover, the energy density is inversely proportional to the duration over which the heat source acts on the work piece. When the energy density of the welding heat source increases, the overall heat required per unit length of the weld deposit decreases. The critical improvement of applying an activated flux to conventional GTA welding is the reduction of arc heat necessary to attain a deep-penetration weld. With the similar welding process variables, the GTA welding with TiO_2 activating flux can increase the depth of penetration with high aspect ratio. However, the shallow penetration and wide bead width welds are achieved in GTA welding with Al_2O_3 flux.

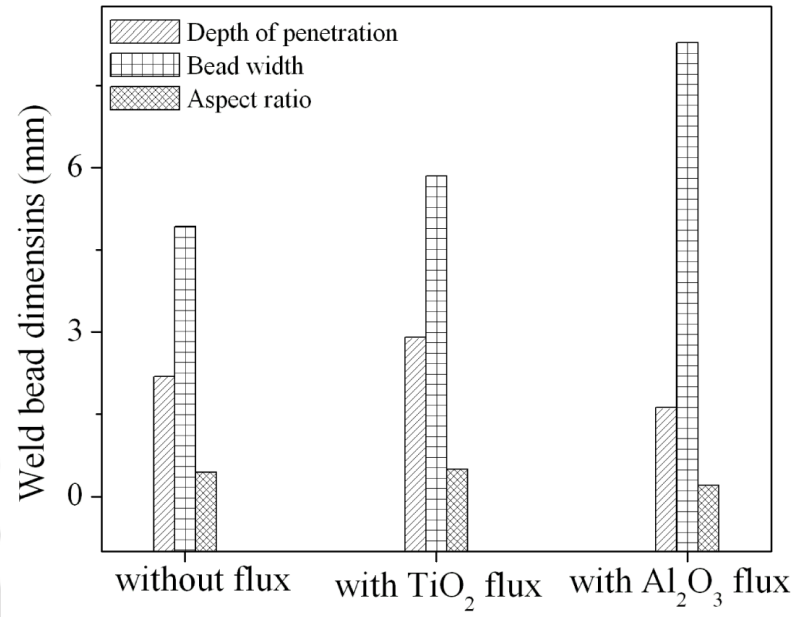

Figure 4.43: Quantitative comparison of weld bead dimensions and aspect ratio with and without flux corresponding to data set 2 given in Table 4.8.

Figure 4.44 describes the GTA weld macrographs made with different combinations of activating fluxes. Figure 4.44 refers to the combined influence of activated flux on weld macrographs. The combinations of any activating fluxes used in present investigation provide wide bead width and shallow penetration. Hence it is recommended that the use of combined activating fluxes is not favorable.

On the basis of the present results, it is considered that the surface tension gradient plays a significant role in increasing the penetration of activated GTA weld joint. As a result of the existence of oxygen in the oxide flux, the temperature coefficient of surface tension on the molten weld pool changed from the negative to the positive, which initiated centripetal Marangoni convection mode. Thus, a constricted anode root was formed and higher current density and energy concentration in the arc column further support the centripetal Marangoni convection in the molten pool driven by Lorentz force, which in turn brought about a greater arc forces acting on the molten pool. Even though further research must clarify the physical mechanisms involved in this phenomenon, this study mainly verified the influence of specific activated flux on the GTA welds.

The temperature coefficient of surface tension on the molten weld pool generally exhibited a negative value during GTA welding without any flux. If the surface tension in the weld pool center is less than the temperature at the pool edge, the surface tension gradient

dσ/dT generates centrifugal Marangoni convection in the molten pool as illustrated Fig. 4.45 (a). In this situation, the flow of the molten on the surface transfers easily from the pool center to the edges, yielding a wide and less penetration weld.

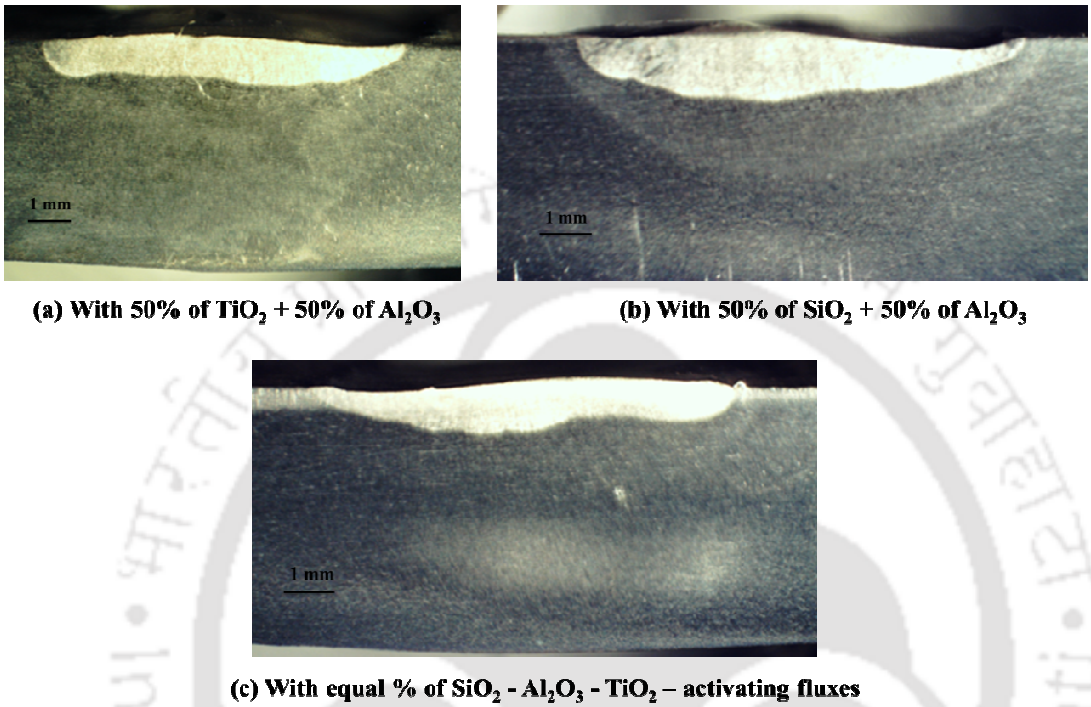

(a) With 50% of TiO_2 + 50% of Al_2O_3

(b) With 50% of SiO_2 + 50% of Al_2O_3

(c) With equal % of SiO_2 - Al_2O_3 - TiO_2 – activating fluxes

Figure 4.44: Combined influence of activating fluxes of corresponding to data set 2 given in Table 4.8.

While GTA welding with TiO_2 and SiO_2 fluxes, the temperature coefficient of surface tension on the molten pool changed from a negative to a positive value. Henceforth, the surface tension at the molten pool center was higher as compared to the pool edge. This phenomenon specifies that the surface tension gradient introduces centripetal Marangoni convection in the molten pool as shown in Fig. 4.45 (b). The fluid flow of the molten pool surface simply transfers from the pool edge to the center, and then downward direction. Figure 4.45 (b) demonstrates that this results in a significantly deep penetration welding. Figure 4.44 shows that the Al_2O_3 flux has a negative effect on the activated GTA weld morphology. Moreover, not all oxide fluxes can change the Marangoni convection mode by altering the temperature coefficient of surface tension. The increment of depth of penetration for welds using activating flux depends on the composition and purity levels of the used flux.

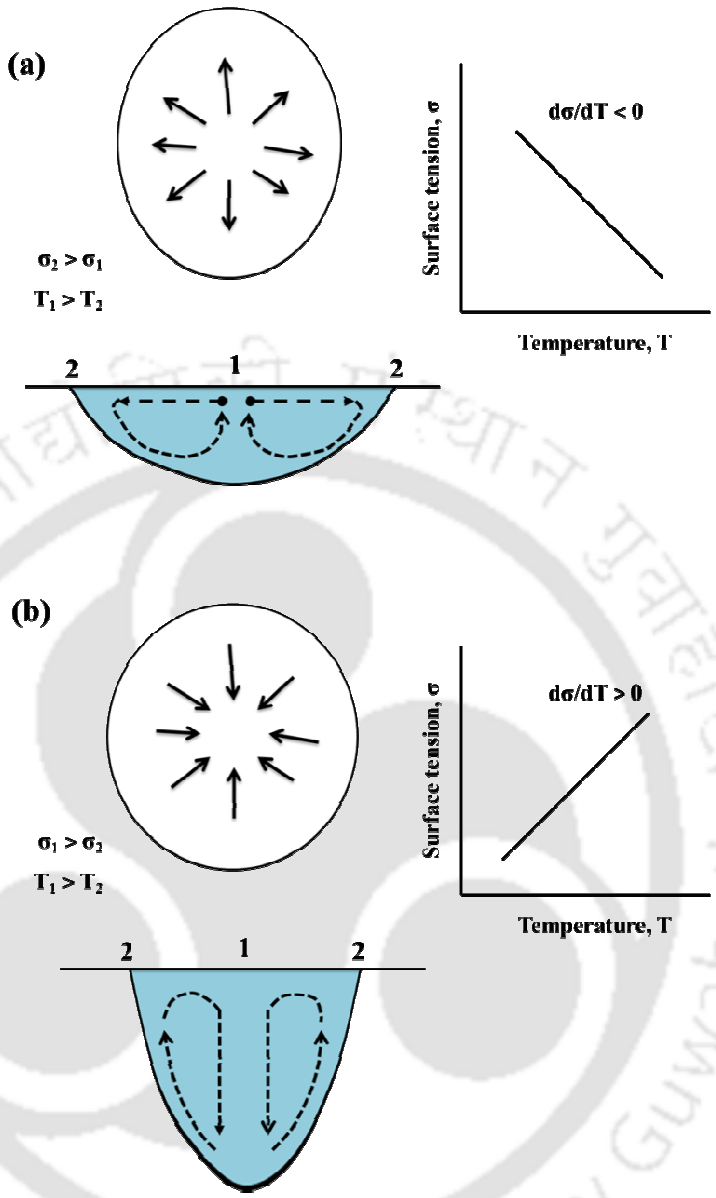

Figure 4.45: Schematic diagram of Marangoni convection mode (a) centrifugal and (b) centripetal.

Figure 4.46 schematically shows the Marangoni convection mode for aluminum oxide particles. The GTA welding with Al_2O_3 flux yields a radially outward flow from the pool center and an aluminum oxide particle-free band forms along the pool edge. This flow pattern in the molten pool surface simply transfers heat to the pool edge and creates wider and shallower welds as compared to conventional GTA welding. This phenomenon may be related to the thermodynamic stability of aluminum oxide. According to the Ellingham diagram [114-117], which plots the Gibbs free energy change in oxidation reaction versus temperature, aluminum oxide has a high degree of thermodynamic stability. Since the

temperature of the outer region of the arc may be lower than the dissociation temperature of the Al_2O_3 flux, aluminum oxide is particularly difficult to dissolve. Hence, there is no lessening in the number of electrons in the cooler outer region of the arc, and no constriction of the arc column. This situation causes an aluminum oxide particle-free band to be formed along the edge of the molten weld pool, creating residual slag on both sides of the welded surface.

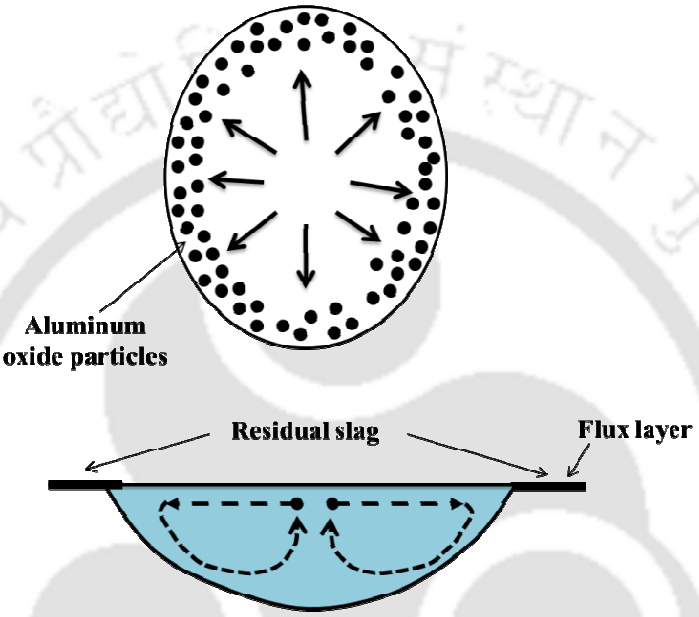

Figure 4.46: Schematic diagram of Marangoni convection for aluminum oxide particles.

4.2.4 Time-temperature history

The time temperature history during GTA welding with TiO_2 and without activating flux have been measured using K-type thermocouples at four different locations (point 1, point 2, point 3 and point 4) as shown in Fig. 4.35. However, the thermocouple locations are at middle of the work piece length. Figure 4.47 (a)-(b) describes the thermal cycles of GTA welding without any flux corresponding to data set 1 and data set 2 of Table 4.8. The thermal cycles are specified for the thermocouple locations, point 1 and point 2. This Fig. 4.47 denotes that the time-temperature history for point 1 and 2 varies due to the distance between welding centre line and thermocouple locations. When the distance between the weld centre line and thermocouple location increases the time temperature profile converges to similar value. Figure 4.48 depict the time-temperature history of GTA welding with activating flux

TiO_2 at two different locations, point 1 and point 2, corresponding to data set 1 and 2 of Table 4.8. It is observed from this figure that the thermal cycle for two different locations varies for data set 1 whereas it is almost same for data set 2.

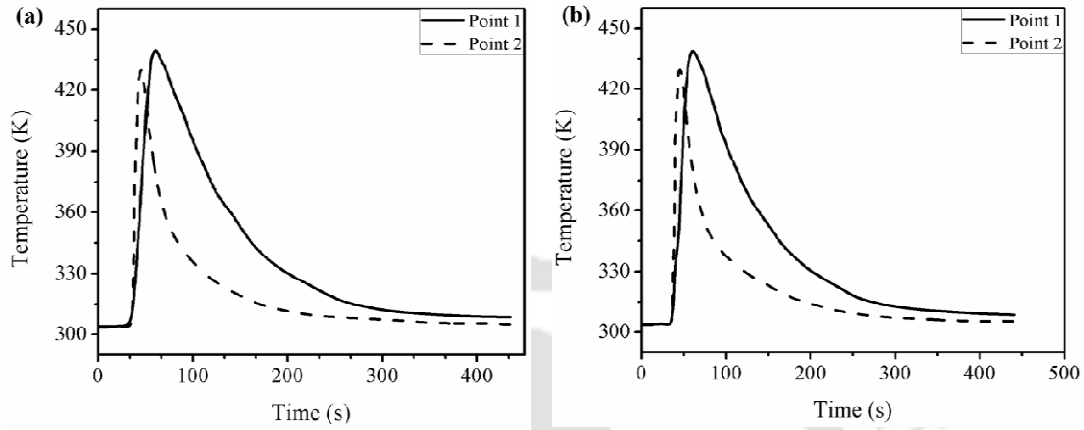

Figure 4.47: Time-temperature history corresponding to GTA welds without any activating flux, (a) data set 1 and (b) data set 2 given in Table 4.8.

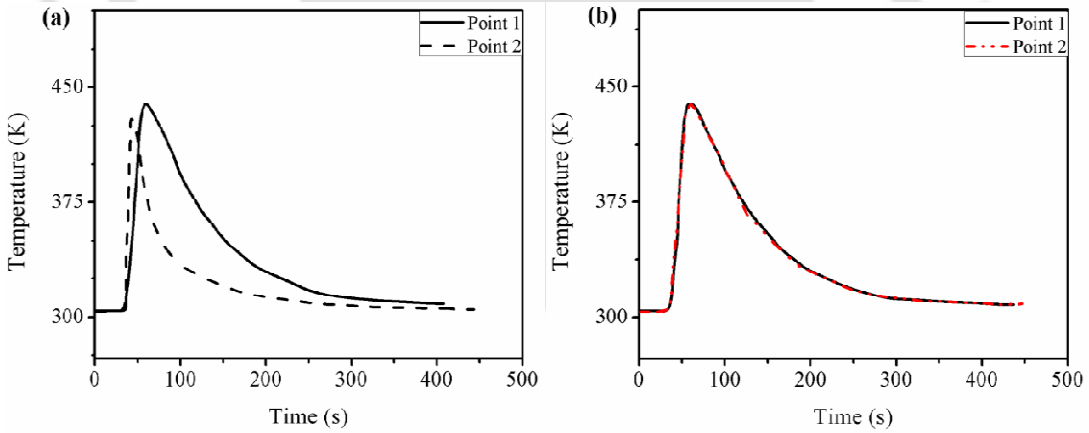

Figure 4.48: Time-temperature history corresponding to GTA welds with TiO_2 activating flux, (a) data set 1 and (b) data set 2 given in Table 4.8.

Figure 4.49 describe the comparisons of weld thermal cycles for the welding made with activation flux TiO_2 and without any activating flux corresponding to data set 3 of Table 4.8 at two different locations, point1 and point 2. The thermal cycles at point 1 varies for both the flux and without flux condition. When the distance of thermocouple location increases from the weld centre line, the time-temperature history is almost same. This is due to the fact that GTA welding with TiO_2 flux, the temperature coefficient of surface tension on the molten

pool changed from a negative to a positive value. Henceforth, the surface tension at the molten pool center was higher as compared to the pool edge.

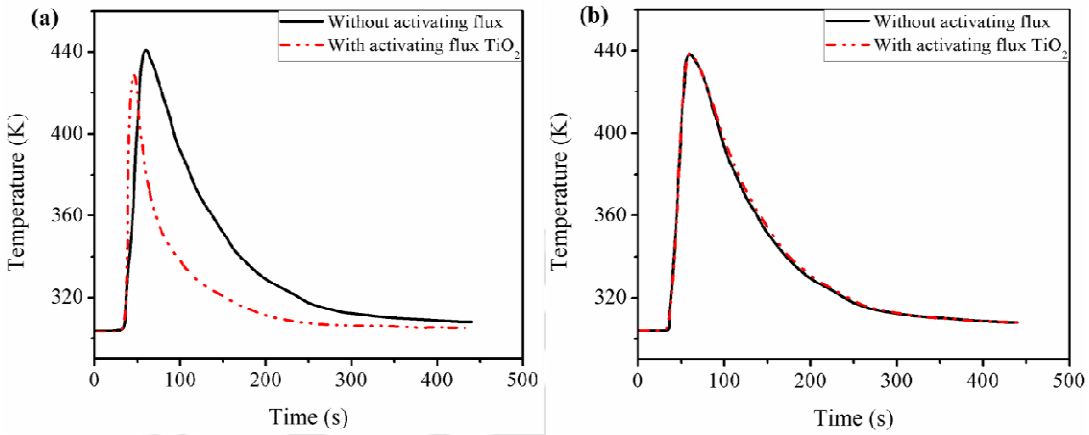

Figure 4.49: Comparison of thermal cycles with activating flux TiO_2 and without activating flux corresponding to data set 3 given in Table 4.8, (a) point 1 and (b) point 2.

4.3 Experimental data from literatures

Some experimental results of linear GTA and laser welding processes are considered from independent literature [120, 227-231] for extensive validation of integrated numerical model and for the calibration of newly developed heat source model. Table 4.10 depicts the measured weld bead dimensions along with process variables for bead-on-plate GTA welding of SS 304 with 3.0 mm thick plate [227]. It is obvious from Table 1 that the weld dimensions increases with weld velocity or heat input per unit length (P/v), where P is weld power (V*I).

Table 4.10: Welding conditions for gas tungsten arc welding experiments of stainless steel [227].

Data set no.	Current (A)	Voltage (V)	Welding velocity (mm/s)	Width (mm)	Depth (mm)	Heat input per unit length (J/mm)
1	150	13.1	8.5	3.56	1.03	231.17
2	140	12.8	7.3	3.96	1.15	245.48
3	150	13.3	5.2	4.31	1.59	383.65
4	180	14.6	4	4.92	2.11	657.00

To analyze the influence of surface active elements, the results obtained from the integrated numerical model are validated with experimentally measured data reported in the

independent literature [120]. The welding experiments were performed on SUS 304 as a bead-on-plate joint configuration. A mixture of pure argon and oxygen had been used as shielding gas with gas flow rate of 10 and 20 L/min, weld current 160 A, welding speed 2 mm/s, electrode gap of 3 mm, electrode diameter of 1.6 mm with DCEN polarity. The chemical composition of the material used in this study is given in Table 4.11.

Table 4.11: Chemical composition of SUS 304 stainless steel.

C	Si	Mn	Ni	Cr	P	S	O	Fe
0.06	0.44	0.96	8.19	18.22	0.027	0.001	0.0038	Bal.

The oxygen content in the shielding gas and the resulting weld dimensions (width and penetration) are presented in Table 4.12. It is observed that the oxygen concentration in the final weld joint increases with increase in shielding gas up to a certain limit and remains almost constant thereafter. High oxygen concentration in shielding gas lowers the adverse effect of surface tension force that is alleviated by almost constant oxygen concentration in the final weld joint. It is thus obvious from experimental data that the weld pool shape as well as aspect ratio changes even at similar welding conditions. However, the weld penetration as well as aspect ratio is the maximum at a specific oxygen concentration in the shielding gas (in between 3000 to 5000 ppm oxygen). Afterward, the aspect ratio remains almost constant. The nature of convection within the weld pool owing to a difference in surface tension force makes a significant contribution to decide the weld pool shape and size. Hence, an effort has been made to numerically simulate the weld pool convection as a function of surface active elements such as oxygen in the present work.

Table 4.13 depicts the process variables corresponding to autogenous laser welding process. The material used for the investigation was 500 × 125 × 4mm ASTM A131 steel; grade DH36. The composition of the same is given in Table 4.14 [228].

The experimental results of gas tungsten arc welding process of AZ91 magnesium alloy [229] and high-power diode laser welding process of aluminium alloys 5083 and 6082 [230-231] under conduction regime are considered from independent literature. Table 4.15 depicts the experimental process variables along with measured weld bead dimensions. The chemical compositions of magnesium alloy and aluminium alloys are given in Table 4.16 [229, 230-231].

Table 4.12: Approximate values of weld pool dimensions at different oxygen concentration at initial gas flow rate (a) 10 L/min, and (b) 20 L/min [120].

Oxygen content in shielding gas (ppm)	10 L/min			20 L/min		
	Oxygen content in weld (ppm)	Width (mm)	Depth (mm)	Oxygen content in weld (ppm)	Width (mm)	Depth (mm)
0	25	7.0	1.9	31	6.5	2.2
1000	35	8.9	1.8	40	9.5	1.6
2000	67	8.9	1.9	75	7.5	2.3
3000	132	7.0	3.8	150	6.9	3.6
4000	182	6.9	3.9	243	7.3	4.0
5000	229	8.0	3.8	268	7.9	3.6
6000	225	8.0	3.5	196	8.9	2.3
7000	214	9.8	1.8	208	9.7	2.0
8000	207	9.9	1.9	232	9.8	1.9
9000	207	9.8	2.0	244	9.9	1.6
10000	213	9.0	1.9	197	9.9	1.5

Table 4.13: Details of welding processes and parameters [228].

Process variables	Autogenous laser
Laser power (kW)	4.50
Laser spot size (mm)	0.63
Welding speed (mm/s)	41.7
Heat input/unit length (W/mm)	108

Table 4.14: Chemical composition of DH36 steel.

C	Mn	Si	S	P	Al	Nb	V	Cu
0.18 max	0.9-1.6	0.1-0.5	0.04 max	0.04 max	0.015 max	0.015-0.05	0.05-0.1	0.35
Cr	**Ni**	**Mo**	**Fe**					
0.2	0.4	0.08	Bal.					

Table 4.15: Welding experimental conditions and non-dimensional heat input index of (a) gas tungsten arc welding [229], and (b) laser welding of aluminum alloy 6082 and (c) laser welding of aluminum alloy 5083 [230-231].

(a)

Data set	Welding current (A)	Welding voltage (V)	Welding speed x10^{-3} (m/s)	Depth of penetration (mm)	Bead width (mm)	N_{HI}
1	100	12	3.33	1.17	5.78	6.59
2	100	12	6.67	0.76	4.8	9.28
3	200	13	6.67	2.49	8.68	7.13
4	100	12	13.3	0.31	2.95	1.65
5	200	13	13.3	1.44	5.92	3.57

(b)

Data set	Laser power (kW)	Welding speed x10^{-3} (m/s)	Depth of penetration (mm)	Bead width (mm)	N_{HI}
1	1.5	5	1.93	4.09	31.27
2	1.5	50	0.71	2.31	3.12
3	2.0	5	2.38	4.67	41.69
4	2.0	100	0.8	2.34	2.08
5	2.5	5	2.72	5.34	52.11
6	2.5	100	0.84	2.48	2.60

(c)

Data set no.	Laser power (kW)	Welding speed x10^{-3} (m/s)	Depth of penetration (mm)	Bead width (mm)	Heat input per unit length (J/mm)
1	2.0	3.33	1.85	4.09	600.60
2	2.0	5.0	1.20	3.21	400.00
3	2.5	3.33	2.11	4.67	750.75
4	2.5	5.0	1.45	3.82	500.00
5	2.75	3.33	2.29	5.07	825.83
6	2.75	5.0	1.54	3.89	550

Table 4.16: Chemical composition (wt. %) of (a) AZ91 alloy according to ASTM B93-94, (b) aluminum alloy 5083-T0 and (c) aluminum alloy 6082-T6.

(a)

Al	Zn	Mn	Si max	Fe max	Cu max	Ni max	Others each max
8.5/9.5	0.45/0.9	0.17/0.4	0.05	0.005	0.03	0.002	0.02

(b)

Si	Fe	Cu	Mn	Mg	Zn	Cr	Pb	Ti	Ga	V	Al
0.1	0.3	0.02	0.5	4.22	-	0.08	0.01	0.02	0.01	0.01	94.73

(c)

Si	Fe	Cu	Mn	Mg	Zn	Cr	Pb	Ti	Ga	V	Al
1.03	0.34	0.06	0.57	0.87	0.01	0.01	0.01	0.03	0.01	-	97.04

In this section, the experimental data that are considered from independent literature are reported. These data are useful to validate the developed numerical model of heat transfer and material flow. Moreover, the author has conducted GTA welding using in-house developed experimental facility at central workshop of IIT Guwahati, India. The laser welding

experiments are also conducted at *Laser Material Processing Division*, *Raja Ramanna Centre for Advanced Technology* (RRCAT), Indore, India.

4.4 Summary

A detailed experimental investigation is undertaken in the present work to validate the integrated modeling approach both for GTA and laser welding processes. The experiments are conducted to examine the influence of welding ambient atmosphere during fiber laser welding and to study the influence of surface active elements during GTA welding process. The fiber laser welding is carried out for wide variation of process variables. Two different types of materials i.e., SS 316 and SS 304 are used in the experimental investigation having thickness of 3 mm and 5 mm. The macrographs of weld cross section are evaluated first for various welding conditions both in GTA and laser welds and then the corresponding weld bead dimensions are measured from the macrographs. The thermal cycles are also measured in case of GTA welds. The laser power density used in present investigation generally confirm to the conduction mode laser welding and keyhole mode laser welding for few cases. The weld bead dimensions increase with the heat input per unit length. In fiber laser welding, the weld bead dimensions as well as aspect ratio are more in case of controlled atmosphere of argon as compared to open atmospheric condition. In GTA welding, the influence of activating flux is significant and the weld bead dimensions are more in case of welds with activating fluxes, TiO_2 and SiO_2. The experimentally measured weld bead shapes and dimensions are adapted from independent literatures to validate the results obtained from the numerical model simulation.

Chapter – 5

Results and Discussion

5.0 Introduction

The present chapter consists of the computed temperature and velocity distributions in autogenous GTA and laser welding processes. The results include thermal cycles, cooling rates, solidification parameters, weld bead shapes and dimensions, keyhole profile, welding induced distortions and residual stresses in GTA and laser welding processes. The calculated results for finite element model of both the conduction heat transfer and the transport phenomena based heat transfer and fluid flow model are validated with corresponding experimentally measured values conducted in-house as well as reported in independent literatures. Moreover, the computed welding induced distortions are compared with corresponding experimental results of fiber laser but joint.

The necessary model data such as temperature dependent material properties, solution domain and computational aspects are presented first. The sensitivity of the calculated values

of weld bead dimensions on the unknown model input parameters are presented next. Subsequently, the calculations in the direction of estimating the suitable values of these unknown model input parameters by using the integrated process models are presented. A comparative study among the computed results from different heat source models is included to comprehend the suitable heat source model for various welding processes and conditions. The novelty and limitations of developed egg-configuration heat source model are presented along with conduction heat transfer analysis using the same model. The estimated keyhole profiles based on point-by-point energy balance on the keyhole wall are presented next. The calculated thermal cycles in and around the fusion zone are utilized to estimate the evolution of cooling rate and solidification parameters that are important to compute final microstructure and mechanical properties of weld joint.

The transport phenomena based heat transfer and fluid flow results are presented to examine the influence of surface active elements in linear GTA welding process. Finally, the welding induced distortions and residual stresses are illustrated to investigate the influence of heat source parameters in linear GTA welding process and laser butt joint.

5.1 Observation from experimental investigation

The purpose of the numerical model is to represent the physical process as real as possible in a mathematical system of equations and solution of the same using various techniques. Hence the experimental investigation provides the information about physical mechanism of the process that facilitates to improve the phenomenological modeling approach. With this objective the detail experimental investigations procedure and the observations are reported in *chapter 4*. The summary of the observations from experimental investigation are as follows.

The depth of penetration in fiber laser welding under controlled atmosphere of argon is more as compared to open atmospheric condition whereas the width is more in open atmospheric condition. It is obvious from the nature of macrographs that there is sharp gradient of fusion zone in case of controlled atmosphere as compared to open atmospheric condition. It is also possible to minimize or avoid the chemical reaction of molten weld pool with air by using the controlled atmosphere process. The top surface profile and the appearance of the controlled atmosphere is better as compared to open atmospheric results. The estimated maximum power density of fiber laser for present set of experiments is ~

$6.37x10^6$ Wcm^{-2}. Therefore, few welding experiments are produced with the formation of keyhole. The change of laser welding process parameters influences more on weld penetration as compared to weld width. The presence of argon gas in fiber laser welding of controlled atmosphere helps to constrict the keyhole plasma and results in more concentrated heat flux. In GTA welding process, a significant increase in penetration is achieved in the presence of surface active elements of TiO_2 flux. However, the shallow penetration and width are achieved in GTA welding with Al_2O_3 flux.

5.2 Numerical model parameters

The numerical modeling of conduction heat transfer analysis, transport phenomena based heat transfer and fluid flow analysis and thermo-mechanical analysis during fusion welding process greatly depends on proper material properties, mesh size and other model parameters. A fine mesh will tend to increase the accuracy of results at the expense of computational time. However, these conflicting effects can be counterbalanced by selecting an optimum mesh size devoid of losing the accuracy of computed results. The present section describes the thermal and mechanical properties of austenitic stainless steel and other materials considered in the present work. The model geometry, mesh size selection, time step and load step selection are also presented in this section.

5.2.1 Mechanical and thermal properties

Figures 5.1 (a) to (c) show the temperature dependent thermal properties of SS 304, SS316 and ASTM A131 steel: grade DH36 respectively that are used for finite element simulation. Table 5.1 describes the temperature independent values of other physical properties utilized in the FE model. Figure 5.1(a) shows the temperature dependent material properties of austenitic stainless steel, SS 304 [173, 214, 232-233]. For this material, the value of the thermal conductivity increases linearly till 1672 K. The thermal conductivity decreases at temperature 1672 K to 1727 K and increases linearly thereafter. The value of specific heat also increases almost linearly.

Figures 5.1 (b) and (c) describe the temperature dependent thermal properties of austenitic stainless steel, SS 316 and ASTM A131 steel; grade DH36 respectively [192, 234-236]. For SS 316, the value of thermal conductivity increases linearly up to temperature around 1700 K and remain constant after that. The value of the specific heat also increases

linearly up to 1000 K and increases between 1700 K and 1900 K possibly due to phase change effect. It reduces to certain value and remains constant thereafter. The variation of thermal conductivity and specific heat of ASTM A131 steel; grade DH36 with respect to temperature can be seen from Fig. 5.1 (c).

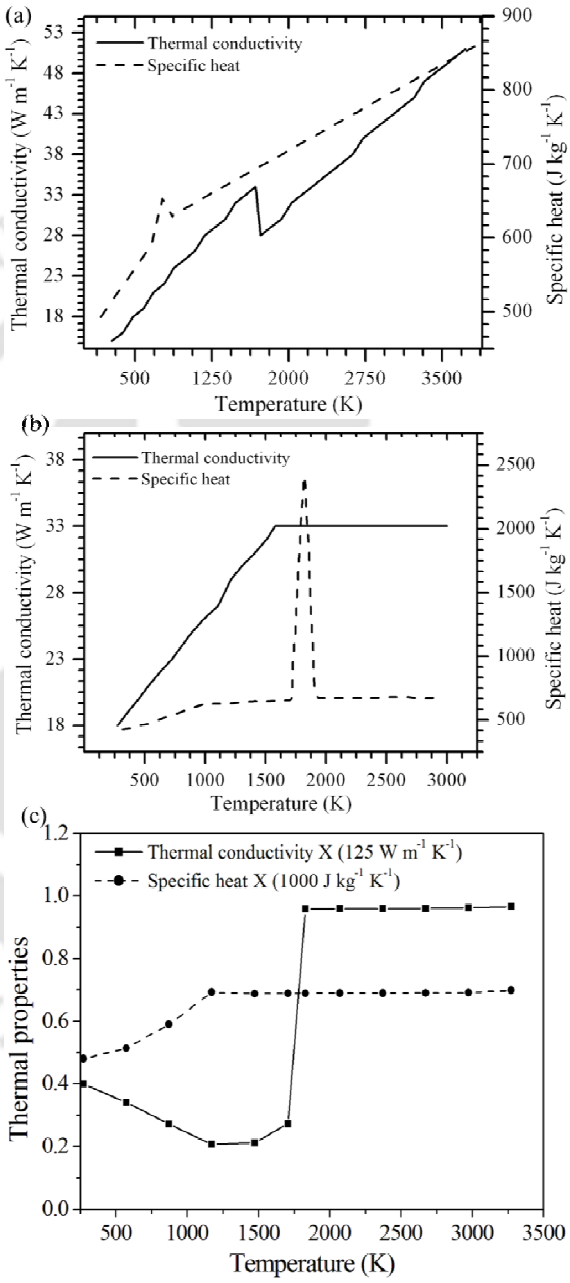

Figure 5.1: Temperature dependent various materials thermal properties used in the present numerical work, (a) austenitic stainless steel, SS 304; (b) austenitic stainless steel, SS 316 and (c) DH36 steel.

Table 5.1: Constant material properties of SS 304, SS 316 and DH-36 steel used in the numerical model [173, 192, 214, 232-236].

Parameter	Value			Unit
	SS 304	SS 316	DH-36 steel	
Density (ρ)	7.2×10^3	7.2×10^3	7860	kg m^{-3}
Molecular viscosity (μ)	6.7×10^{-3}	6.7×10^{-3}	6.7×10^{-3}	kg m^{-1} s^{-1}
Solidus temperature (T_S)	1697	1648	1690	K
Liquidus temperature (T_L)	1727	1673	1723	K
Ambient temperature (T_0)	300	300	300	K
Specific heat (C_p)	711.8	500.0	710.6	J kg^{-1}
Thermal conductivity (k_s)	19.26	16.2	21	J s^{-1} m^{-1} K^{-1}
Latent heat (L)	2.47×10^5	3×10^5	2.47×10^5	J kg^{-1} K^{-1}
Temperature coefficient of surface tension $\left(\frac{d\gamma}{dT}\right)$	-0.43×10^{-3}	-0.43×10^{-3}	-0.5×10^{-3}	N m^{-1} K^{-1}
Magnetic permeability (μ_m)	1.26×10^{-6}	1.26×10^{-6}	1.26×10^{-6}	N A^{-2}
Coefficient of thermal expansion (β)	1.96×10^{-5}	1.96×10^{-5}	1.96×10^{-5}	K^{-1}

Figures 5.2 (a)-(c) describe temperature dependent density, specific heat and thermal conductivity of aluminum alloy 6082, magnesium alloy AZ 91 and aluminum alloy 5083 respectively [237-240]. Figure 5.2 (b) describes the variation of thermal conductivity and specific heat of magnesium alloy AZ 91 with respect to temperature. For this material, the thermal conductivity decreases linearly till 800 K and then constant thereafter. Specific heat increases linearly and decreases thereafter. However, the specific heat value is constant beyond 1600 K. The variation of material properties with respect to the temperature for aluminum alloys Al-6082 and Al-5083 is shown in figures 5.2 (a) and (c). The other temperature independent material properties of aluminum alloy 6082, magnesium alloy AZ 91 and aluminum alloy 5083 used in FE calculations is provided in Table 5.2.

Figure 5.3 (a)-(b) show the temperature dependent mechanical properties of austenitic stainless steel, SS 304 and ASTM A131 steel; grade DH36 respectively. The temperature dependent yield stress elastic modulus, thermal expansion coefficient and Poisson's ratio of

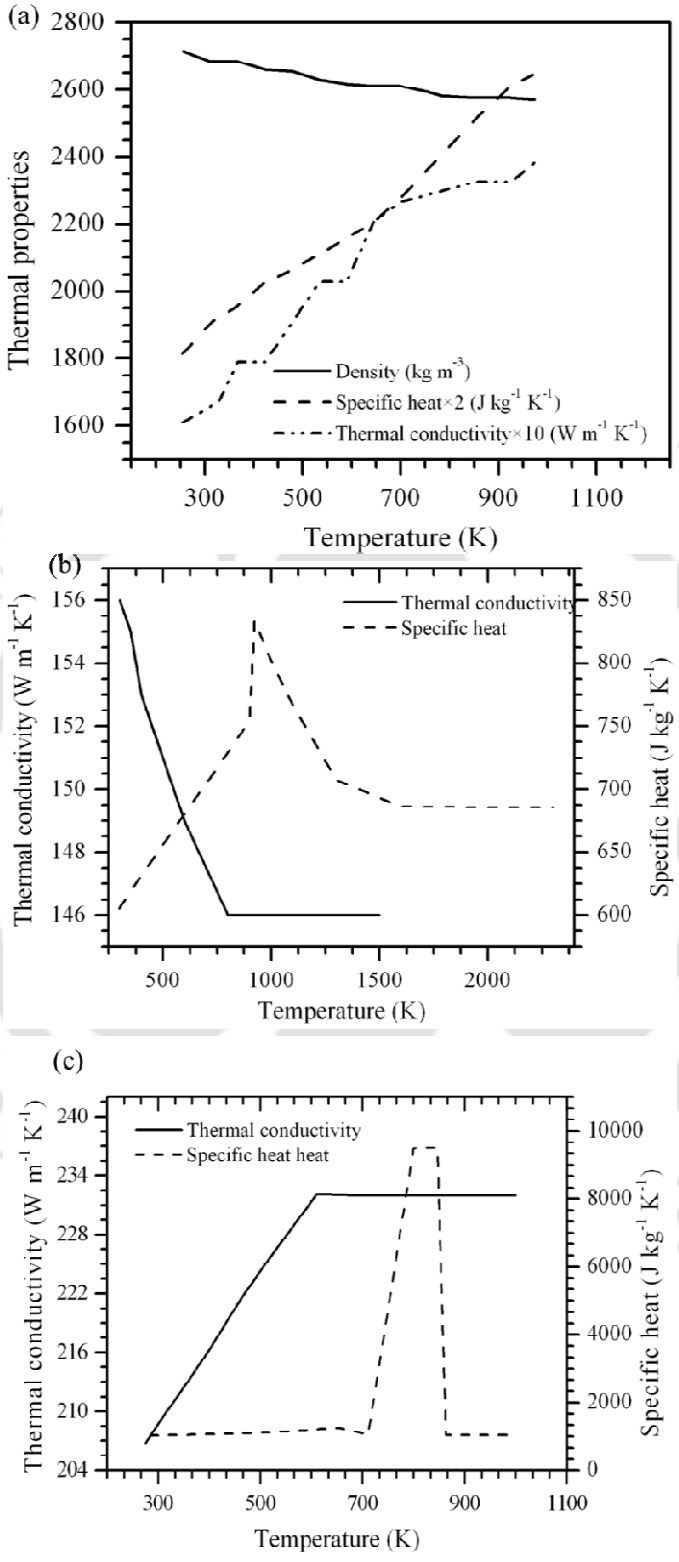

Figure 5.2: Temperature dependent thermal materials properties used in the present work, (a) aluminum alloy 6082, (b) magnesium alloy AZ 91 and (c) aluminum alloy 5083.

ASTM A131 steel; grade DH36 used in FE model and is given in Fig. 5.3 (b).

Table 5.2: Temperature independent material properties of AZ 91 Magnesium alloy, Aluminum alloy 6082 and Aluminum alloy 5083 used in the computations [237-240].

Physical property	**AZ91 Magnesium alloy**	**Aluminum alloy 5083**	**Aluminum alloy 6082**
Specific heat at room temperature (J/kg K)	1020	900	894
Density (kg/m^3)	1810	2650	2700
Liquidus temperature (K)	870	843	828
Solidus temperature (K)	740	796	780
Thermal efficiency (%)	0.6	0.8	0.8
Emissivity	0.5	0.12	0.12
Latent heat of fusion (kJ/kg)	373	397	300
r_{eff} (mm)	2.472	1.02	1.02

5.2.2 Model geometry

In the present work, thermo-mechanical analysis is carried out using ANSYS Parametric Design Language (APDL). The element SOLID70 is chosen for thermal analysis and SOLID45 is used for mechanical analysis. The geometrical size of the welding plate for the simulation and experiment is the same. In the present work, non-uniform meshes are used and shown in figures 5.4 and 5.5. For bead-on-plate welding, half of the welding plate was considered (Fig. 5.4). For some cases of butt joint welding, a full geometry was considered (Fig. 5.5) for analysis. The finer mesh is considered near and along the weld centre line to assure the accuracy of the simulated results and the mesh size increases for rest of the metal plate in order to reduce the computational cost.

5.2.3 Calibration of numerical model

The computational cost of finite element based numerical model is approximately linearly proportional to the number of elements in the mesh, number of time steps, number of non-linear iterations per time step and the time required for each non-linear iteration.

Therefore, the selection of these parameters, mesh size, number of sub-steps and load steps are significant. The following sections describe the selection methodology for these parameters.

5.2.3.1 Selection of mesh size

The calculated results of thermal cycles, weld bead dimensions, welding induced distortions and residual stresses from FE model are sensitive to the element size and the distribution of elements within the model geometry. The accuracy of computed results increases by fine mesh. However, at the same time it increases the computational time. For the solution geometry, a trade-off is thus essential to choose on a mixture of non-uniform meshing, a fine mesh in and around the FZ and coarse mesh away from FZ without compromising the accuracy of computed results.

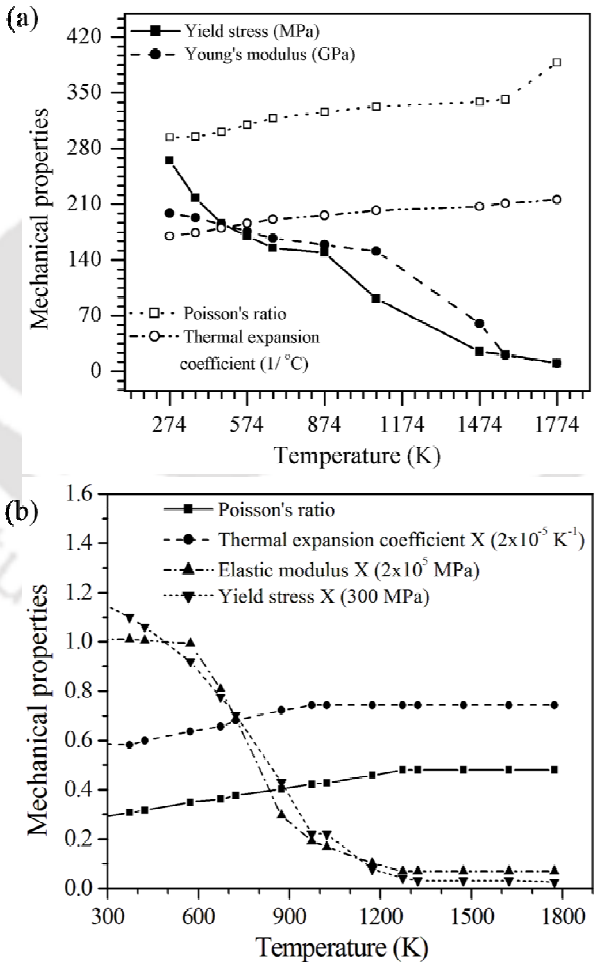

Figure 5.3: Temperature dependent mechanical properties of (a) SS 304 and (b) ASTM A131 steel; grade DH36.

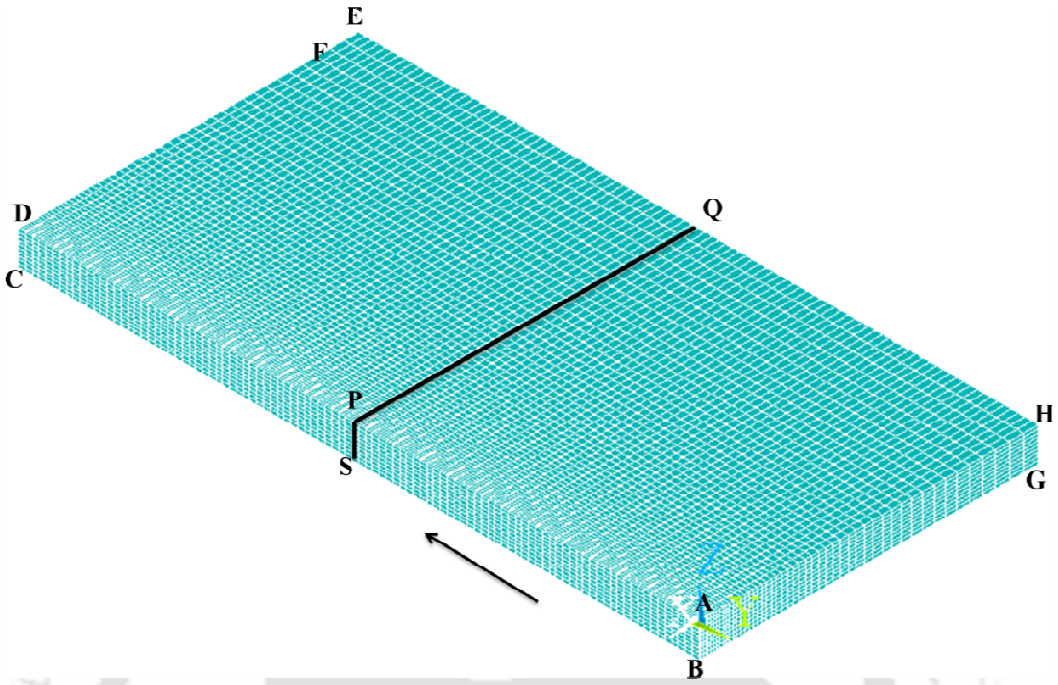

Figure 5.4: Half plate FE model along with mesh for symmetric analysis.

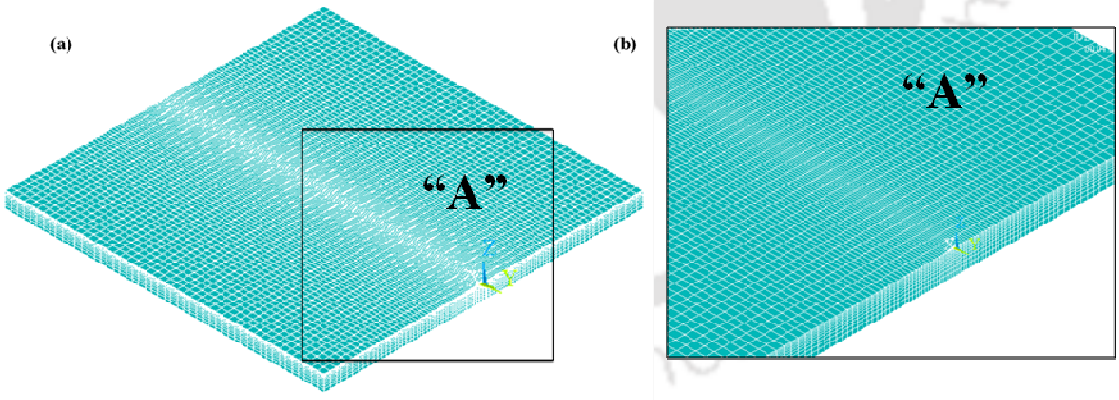

Figure 5.5: Full plate FE model with mesh for butt joint analysis.

Figures 5.4 and 5.5 show the typical geometric model with mesh considered in the present work. Since the heat source is symmetric in the transverse direction, only half section is considered for the analysis. It is imperative to say that the heat input to the nodes under the welding heat source is calculated assuming a Gaussian distribution of energy. To accumulate accurate heat input, the minimum number of nodes and elements must be present under the arc or laser beam [241-242]. Goldak [241] suggested a minimum number of four elements

within the welding heat source to capture the surface heat input in the case of linear elements. Reddy et al. [242] presented that a minimum of five nodes in depth direction are appropriate for capturing the arc heat input for double ellipsoidal heat source model. In the present numerical model, the solution geometry is discretized in a manner so that a minimum number i.e. six nodes are at least available under the laser beam or arc.

The selection of mesh size in the solution domain of fluid flow analysis is more intricate than the heat conduction analysis. In general, the smaller size elements are required to capture the dynamics of fluid flow. The minimum element size in a fluid zone is estimated by Chakraborty et al. [56]. Using an appropriate scaling analysis with regard to the stationary molten pool for laminar flow in GTA welding process, they estimated the viscous boundary layer thickness (δ_v) at the top surface [243]

$$\delta_v \approx \frac{\mu \times U_s \times R}{\Delta T \times \left|\frac{\partial \gamma}{\partial T}\right|} \tag{5.1}$$

where U_s is the characteristic surface velocity, R is the radius of molten pool which is roughly equal to r_{eff} and ΔT is the characteristic temperature difference between the locations corresponding to the bottom of the electrode and phase changing interface which can be roughly scaled as L/C_p. Therefore, equation (5.1) can be modified as

$$\delta_v \approx \frac{\mu \times U_s \times C_p \times r_{eff}}{L \times \left|\frac{\partial \gamma}{\partial T}\right|} \tag{5.2}$$

For a typical GTA welding process on SUS 304 stainless steel, having characteristic velocity, U_s = 2 mm/s and effective arc radius, r_{eff} = 1.8 mm, the estimated boundary layer thickness is of the order of 0.161×10^{-6} m/s. Similarly, for SS 316 stainless steel having characteristic velocity 2.91 mm/s and effective arc radius 1.9 mm, the boundary layer thickness of the order of 0.144×10^{-6} m/s. It is thus obvious that, in principle, a finer mesh (a very small element size) in the fluid region is required and it increases the number of elements. However, related mesh independence investigations with respect to heat transfer and fluid flow analyses in welding reported by independent researchers [54, 56, 244] recommends that a finer mesh system does not alter the results noticeably. The minimum size of node spacing is followed as 0.37 mm, in fluid flow analysis of GTA welding process [54, 56, 244]. Hence, the present work has followed similar meshing strategies following the guidelines mentioned by earlier researchers [54, 56, 244, 245].

5.2.3.2 Selection of time step and load step

The transient analysis in numerical modeling of linear GTA and laser welding processes are carried out by dividing the total solution time into a large number of time steps. The converged solutions of temperature and velocity fields are henceforth attempted in each of these small time steps. The total load is divided into number of small increments in the quasi-steady state analysis such that the non-linearity arising out of the evolution of temperature and velocity variables can be traced till the complete load is applied. In the present work, the discretization of temporal variable is followed the Galerkin weighted residual method, and is considered to be unconditionally stable [246]. Nevertheless, spurious oscillations of the field variable introduces when too large time step used [247]. The time step is thus taken by the following limiting case [246]

$$\Delta t_c \leq \frac{(\Delta d_n)^2 \times \rho \times C_p}{k} \tag{5.3}$$

where Δt_c is critical time step, Δd_n is the minimum distance between the nodes, and k, ρ and C_p depicts the thermal conductivity, density and specific heat respectively at room temperature. Based on equation (5.3), the critical time steps for minimum nodal distance of 0.05 mm and 2 mm, are 4 x10^{-4} s and 6 x10^{-3} s respectively. In the present analysis, the time step for GTA welding is considered as 10^{-3} s and for laser welding it is taken as 10^{-5} s.

5.2.4 Non-dimensional heat input index

In order to realize the influence of the welding heat source parameters and thermo-physical material properties, an integrated non-dimensional heat input index (N_{HI}) is defined for each data set in both GTA and laser welding processes. This N_{HI} is defined by [62]

$$N_{HI} = \frac{\frac{P.\eta}{\pi r_{eff}^2 . v}}{\rho C_p (T_L - T_0) + \rho L} \tag{5.4}$$

where P is the arc power (W), η is an arc efficiency or absorption coefficient, r_{eff} is effective arc radius (m), v is weld velocity (m s^{-1}), ρ is density of the material (kgm^{-3}), C_p is the specific heat of the material (J kg^{-1} K^{-1}), T_L is the liquids temperature of the material, T_0 is the ambient temperature of the material and L is the latent heat of fusion (J kg^{-1}). In equation (5.4), the numerator can be assumed as the whole incident welding heat source per unit volume. In case of laser welding this welding heat source is a laser power and in case of

GTAW it is the multiplication of the welding voltage and current. The denominator corresponds to the enthalpy which is needed to heat the unit volume of the material from ambient temperature to liquidus temperature.

Table5.3: Ranges of non-dimensional heat input index for various materials.

		N_{HI}	
Material	**Plate thickness**	**Minimum**	**Maximum**
SS 304	3	243.55	418.63
SS304	5	487.1	837.26
SS 316	3	269.98	464.05
SS 316	5	539.95	928.1
Aluminum alloy 6082	4	75.36	155.58
Aluminum alloy 5083	3	2.08	52.11
Magnesium alloy AZ91	15	1.65	9.28

Table 5.3 depicts the ranges of non-dimension heat input index for different materials and welding processes. The magnitude of N_{HI} corresponding to GTA welding of magnesium alloy AZ91 varies from 1.65 to 9.28 whereas it is from 2.6 to 52.11 for laser welding of Aluminum alloy 5083. In case of fiber laser welding of SS 304, 3 mm plate, the magnitude of N_{HI} varies from 243.55 to 418.63 where as it is from 269.98 to 464.05 for laser welding of SS 316, 3 mm plate. In case of 5 mm thickness plate SS 304 and SS 316 it varies from 487.1 to 837.26 and 539.95 to 928.1 respectively. The wide variation of N_{HI} signifies that the selected process parameters cover a wide range of welding conditions.

5.3 Identification of unknown and uncertain model parameters

The simulation of conduction heat transfer and transport phenomena based heat transfer and fluid flow in GTA and laser welding processes demands several input parameters such as work piece geometry, welding process variables, experimental setup conditions and material properties. Some of these parameters such as solution geometry, process parameters like laser beam power, welding speed, welding current and voltage can be straight away specified with a reasonable degree of certainty. On the other hand, few of the model

parameters cannot be specified certainly with confidence and these parameters are termed as unknown parameters in finite element based numerical model.

During fusion welding, only a portion of energy is transferred from the heat source to the work piece material. The amount of energy transferred is significant since it directly affects the shape and size of the weld pool, the temperature distribution in the HAZ and welding induced distortions. The arc efficiency/absorption coefficient (ŋ) in arc/laser welding process defines the actual heat input to the system and finally contributes to the calculations of the weld pool dimensions. The arc efficiency mostly depends on work piece surface condition, chemical composition of work piece material, the shielding gas environment and the instantaneous temperature distribution. The value of 'ŋ' is calculated and described for several welding processes and conditions [25, 51, 60-62, 196, 204, 205]. However, the efficiency varies significantly even for apparently similar welding conditions. Therefore, the arc efficiency is considered as unknown model parameter.

The area on the top surface of work piece come into contact with welding arc is represented as effective arc radius (r_{eff}) in GTA welding process. In general, the effective arc radius depends on electrode shape and size, type of shielding gas used and also on the range of operating welding currents and voltages [25, 47, 54]. Moreover, it is difficult to determine the actual value of r_{eff} with confidence beforehand. Hence, r_{eff} is considered as an uncertain model input parameter in simulation of GTA welding process.

Moreover, the effective thermal conductivity (k_{eff}) and the effective viscosity (μ_{eff}) values in molten pool are significant in transport phenomena based modeling, since they allow accurate modeling of the high rates of transport of heat and mass in systems with strong fluctuating velocities that are inevitable in small weld pools with very strong convection currents. The values of effective conductivity and viscosity are properties of the specific welding system and not inherent physical properties of the liquid metal [25, 47, 51, 54, 60-62, 128, 196, 200, 204-205, 208]. Although the values of these variables are often assigned from past experience, currently there is no unified basis to accurately prescribe the values of these variables based on scientific principles. Hence, in undertaking heat transfer and fluid flow simulation of weld pool, the effective thermal conductivity (k_{eff}) and effective viscosity (μ_{eff}) in melt pool are considered as uncertain model input parameters.

Double-ellipsoidal volumetric heat with Gaussian distribution of heat intensity is one of the most popular heat source model used in fusion welding process simulations. However,

the major difficulty of this kind of heat source model is to define the parameters before start of simulation. It is common practice to define the heat source parameters from experimental measurement of weld dimensions for a particular welding condition that meet the demand of two parameters i.e. weld width and penetration. Till date, the definition of front and rear length of double ellipsoidal is to-some-extent arbitrary in linear welding. Therefore, the ratio of rear and front lengths of double ellipsoidal heat source model is assumed by trial-and-error method or with past experience [30, 31, 194, 241]. But, this ratio depends on welding speed and other process parameters. It is not possible to measure this ratio exactly from weld bead dimensions. Therefore, this ratio is considered as uncertain model parameter indirectly to estimate the correlation between welding velocity and front and rear length ratio.

5.3.1 Identification of optimum (a_r/a_f) ratio of double ellipsoidal heat source model in linear GTA welding

The objective here is to determine the uncertain or unknown parameter, a_r/a_f ratio that is a function of welding velocity. A 3D conduction heat transfer model is used to originate the weld bead dimensions from the known welding conditions. The various combinations of unknown parameter, a_r/a_f ratio is assumed. A sensitivity study of the ratio of rear and front length of double-ellipsoidal parameter (a_r/a_f) on weld dimensions for data set #4 in Table 4.10 is depicted in Fig. 5.6 (a). It has been recognized from the observed trend that the weld dimensions decrease with increase of a_r/a_f ratio almost in linear way. Actually, high value of a_r/a_f ratio promotes to reduce the distributed heat intensity that finally reduces the weld pool dimensions. The weld penetration is more sensitive to the change of a_r/a_f ratio as compared to weld width. Figure 5.6 (b) shows the variation of weld dimensions with respect to weld velocity at two different values of a_r/a_f ratio. The weld dimensions diminish with increase of velocity that resembles the fact of reducing heat input per unit length. At low velocity (~ 4 mm/s), the change in dimensions is more as compared to higher velocity (~ 7.4 mm/s) due to a jump of heat input per unit length. It is noteworthy from Fig. 5.6 (b) that with the increase of a_r/a_f ratio, the weld dimensions decreases. Therefore, the sensitivity study depicted in Fig. 5.6 clearly indicates that the a_r/a_f ratio may not be defined arbitrarily. An organized approach is necessary to find the optimum value of a_r/a_f ratio corresponding to a particular welding condition. In present work, it is assumed that a_r/a_f changes with weld velocity and a suitable trend is adopted that fit best considering the present set of experimental data.

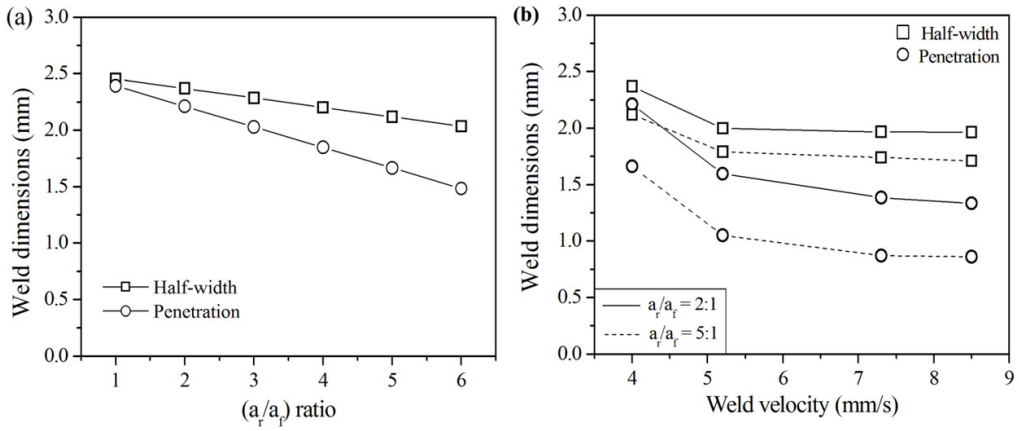

Figure 5.6: Sensitivity on weld dimensions: (a) (a_r/a_f) ratio for data set #4 in Table 4.10, and (b) weld velocity for (a_r/a_f)= 2:1.

The GA based optimization algorithm, PCX G3 model is integrated with the heat transfer model to investigate the optimum trend of a_r/a_f ratio. The trend of a_r/a_f ratio must satisfy the following two constraints: one is a_r/a_f =1:1 at velocity v = 0 which resembles with stationary heat source and a_r/a_f ratio tends to infinity at very high velocity. Several functional forms are possible that satisfy these two constraints. However, several trend of a_r/a_f ratio have been tried and concluded that a third-order polynomial fits best considering the availability of present set of experimental data. The polynomial function is defined by

$$\chi = 1.0 + A_1 v + A_2 v^2 + A_3 v^3 \tag{5.5}$$

Figure 5.7 (a) describes the initially generated population i.e. the distribution of coefficients (A_1, A_2, A_3) to find the best suitable combination of these coefficients to minimize the objective function (equation (3.74)). The feasible range of these coefficients is depicted in Table 5.4. It is obvious from Fig. 5.7 (a) that the initial population is diversely distributed over the space and having equal chance to reach the global optimum condition.

Table 5.4: Optimum calculation of coefficients.

Initial range			Optimum value			Objective function
A_1	A_2	A_3	A_1	A_2	A_3	
0.1×10^{-1} 1.8×10^{-1}	1×10^{-3} 18×10^{-3}	1×10^{-3} 10×10^{-3}	1.0×10^{-1}	5.48×10^{-3}	2.97×10^{-3}	1.29×10^{-2}

Figure 5.7 (b) shows the objective function space after 90 generations which is assumed as optimum condition corresponding to the objective functional value of 1.29×10^{-2}. Further improvement of objective function in successive generations was not possible. The zone marked by enclosed curve (dotted line) in Fig. 5.7 (b) indicated the F_0 value less than 0.01. Increasing A_2 and decreasing A_1 follow similar trend of F_0 value which is less than 0.01 and it indicates that there exists several local minimum within the solution space. However, the global optimum values of coefficients achieved in this case are depicted in Table 5.4. The optimum trend of a_r/a_f ratio as a function of weld velocity is depicted in Fig. 5.7 (c) where third order polynomial fit better.

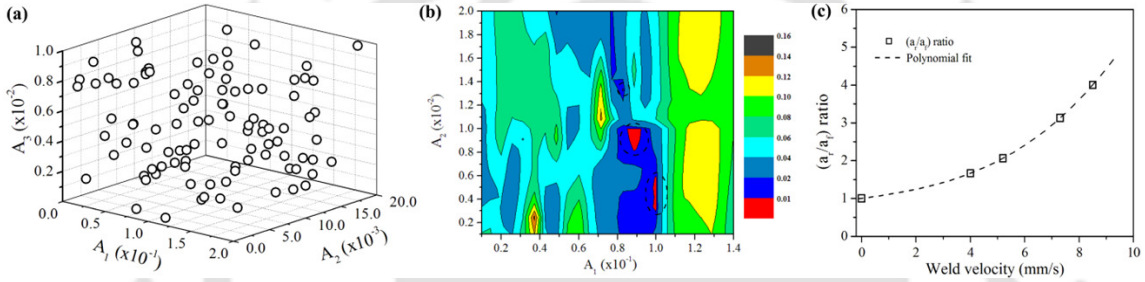

Figure 5.7: Optimization of unknown coefficients: (a) Initial population, (b) final population after 90 generations, and (c) optimum trend of (a_r/a_f)ratio with respect to weld velocity.

5.3.2 Estimation of optimum ŋ, r_{eff}, k_{eff} and μ in linear GTA welding

The objective of the optimization problem here is to determine the optimum values of uncertain parameters, ŋ, r_{eff}, k_{eff} and μ. First of all, FE based numerical model is used to examine the influence of uncertain model parameters on weld bead dimensions. An inverse approach is followed to calculate four uncertain model parameters using few experimental data depicted in Table 4.12. The detail flowchart of this approach has been described in chapter 4. Table 5.5 represents the set of uncertain parameter obtained by integrated approach using DE. DE starts with generation of initial population within range of specified limit depicted in Fig. 5.8. The feasible solution space is created based on the experience gained from literature related to the process [39, 60, 125, 214]. The number of initial individuals influences the overall computational time. Hence, the number of individuals is considered as 40 (~ 10 times of 4 parameters). The range of these parameters is selected in non-dimensional form depicted in third column of Table 5.5.

Table 5.5: Optimization of uncertain model input parameters.

Uncertain parameters (P)	**Reference value (P_r)**	**Non-dimensional Range ($P^* = P/P_r$)**	**Optimum value (P^*_{opt})**	**Effective values (P_{eff})**
Arc efficiency (η)	0.40	1.0 ~ 2.0	1.58	0.63
Arc radius (r)	0.8 mm	1.0 ~ 5.0	2.28	1.82 mm
Thermal conductivity (k)	24.0 W m^{-1} K^{-1}	1.0 ~ 15.0	9.38	225.2 W m^{-1} K^{-1}
Viscosity (μ)	0.01 Kg m^{-1} s^{-1}	1.0 ~ 15.0	7.0	0.07 Kg m^{-1} s^{-1}

It is observed in Figures 5.8 (a) and (b) that the individuals are distributed diversely over the solution space and each individual has equal potential to achieve the optimum value after successive evolutions. The minimum value of objective function in initial population is ~ 0.04 and the maximum value is ~ 0.45. The fourth column of Table 5.5 describes the optimum values of uncertain parameter set ($\mathbf{P^*_{opt}}$) corresponding to the minimum value of objective function. The minimum value of objective function is achieved after 47 generations. Further improvement of the objective function was not possible in the context of predefine values of control parameters (crossover constant, mutation factor and number of initial population). The optimum set of parameter has been chosen from a cluster of closely similar values of objective function resembles similar range of uncertain parameter sets. However, the minimum value of objective function (~ 0.0012) is considered as the best solution for the optimization problem. It is noteworthy that the estimation of optimum parameters is independent of surface active elements (weight percentage) since a fixed set of optimum parameter value has been used for all simulations irrespective of oxygen concentration in the process. It is observed from Table 5.5 that the effective values of arc radius, thermal conductivity, and viscosity are equivalent to several times enhancement over their reference values. The reference value for arc radius is the radius of electrode (~ 0.8 mm), for thermal conductivity and viscosity are the numerical values at room temperature i.e. 24 W m^{-1} K^{-1} and 0.01 Kg m^{-1} s^{-1}, respectively.

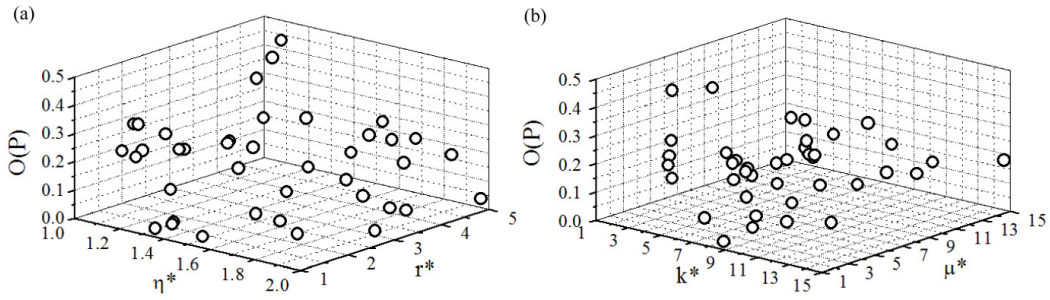

Figure 5.8: Initial population of uncertain parameters within the range depicted in Table 5.5.

5.4 Conduction mode heat transfer analysis

The direct measurement of high peak temperature, rapid change of weld thermal cycle and resulting thermal distortion and associated stresses are difficult to measure experimentally for fusion welding process and hence the contemporary demand of reliable quantative models are ever increasing. In the current welding research standpoint, a three dimensional (3D) transient non-linear sophisticated numerical model is necessary to investigate the molten pool formation and temperature distribution during fusion welding process. The conduction heat transfer model based on finite element method is often preferred as compared to convective heat transfer analysis since former is more appropriate where fast and repetitive calculation of temperature field is of main concern.

A 3D finite element based conduction heat transfer model using two different types of volumetric heat source is developed. The element SOLID 70 which has 8 nodes with temperature as degree of freedom is used in heat transfer analysis. The transient temperature fields of GTA and laser welding processes were simulated using ANSYS 14.0 [223] with APDL subroutine. The temperature dependent thermal conductivity and specific heat are considered for the simulation. The material properties used in numerical simulation are reported in figures 5.1 to 5.3 and Tables 5.1-5.2. In conduction heat transfer analysis, the thermal conductivity of molten material is increased artificially for several folds to account the enhanced heat transfer due to high convective flow of liquid molten metal within the weld pool.

5.4.1 Influence of heat source parameters during linear GTA welding

The sensitivity analysis of double-ellipsoidal heat source parameters shows that the ratio of front and rear length ratio has significant effect on weld dimensions as well as thermal distortion and residual stress of final weld joint. This problem has been addressed in present thesis work where the optimum value of the ratio of front and rear length of double ellipsoidal heat source model is designed within the kernel of an integrated optimization algorithm (PCX-G3). The ratio is assumed as function of weld velocity and a suitable functional form is designed over a range of welding current and velocity. The proposed trend of ratio along with optimum values demonstrate fair agreement of experimentally measured weld dimensions for linear gas tungsten arc (GTA) welding process.

Table 4.10 depicts the experimental process variables along with bead width and penetration for a bead-on-plate GTA welding on 3 mm thick SS304. It is obvious from Table 4.10 that the weld dimensions increases with weld velocity or heat input per unit length (P/v), where P is weld power (V*I). Inclusion of temperature dependent material properties in numerical simulation makes the solution non-linear and computational intensive. Using the optimum value of a_r/a_f ratio the numerical analysis has been performed.

Figure 5.9 shows the three dimensional temperature distribution at three different positions (at 4/5.2 s, 14/5.2 s and 24/5.2 s) with velocity of 5.2 mm/s corresponding to welding conditions of data set #3 in Table 4.10 using the optimum value of a_r/a_f ratio. In figure 5, the region surrounded by the liquids temperature 1700K represents the weld pool, and its intercepts along the Z-axis and X-axis depict the weld penetration and the half-width, respectively. Figure 5.10 shows the comparison between experimentally measured weld macrograph (right side) and computed temperature profile (left side) corresponding to data set #3 in Table 4.10. Moreover, Fig. 5.11 depicts the quantitative comparison of experimental and computed weld dimensions using the optimum set of a_r/a_f ratio. It is obvious that relatively fair agreement of the shape and size of computed temperature profile endorse the correct estimation of a_r/a_f ratio in the simulation of linear welding process.

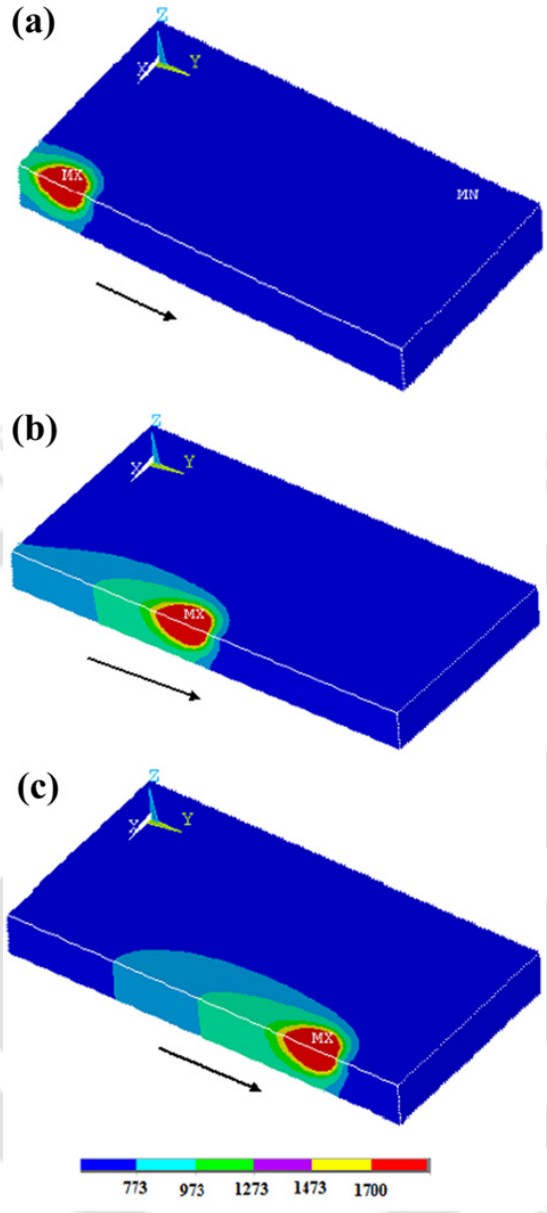

Figure 5.9: Three dimensional computed temperature distribution corresponding to welding condition of data set #3 in Table 4.10 at three different locations.

Since direct estimation of front and rear length of a double ellipsoidal heat source model are nearly intractable for fusion welding process, the demand of reliable quantitative models for heat transfer is ever increasing. The present work is a contribution in this direction.

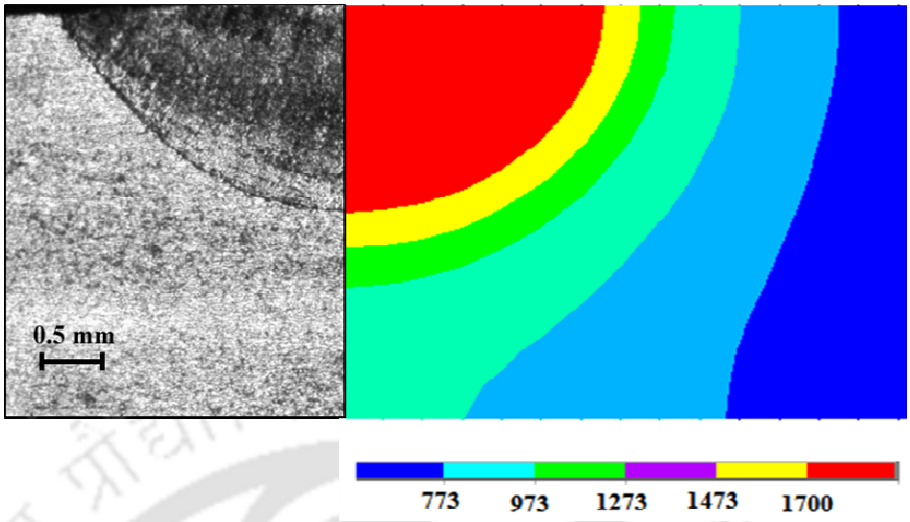

Figure 5.10: Comparison between computed and experimentally measured macrograph corresponding to welding condition of data set #3 in Table 4.10.

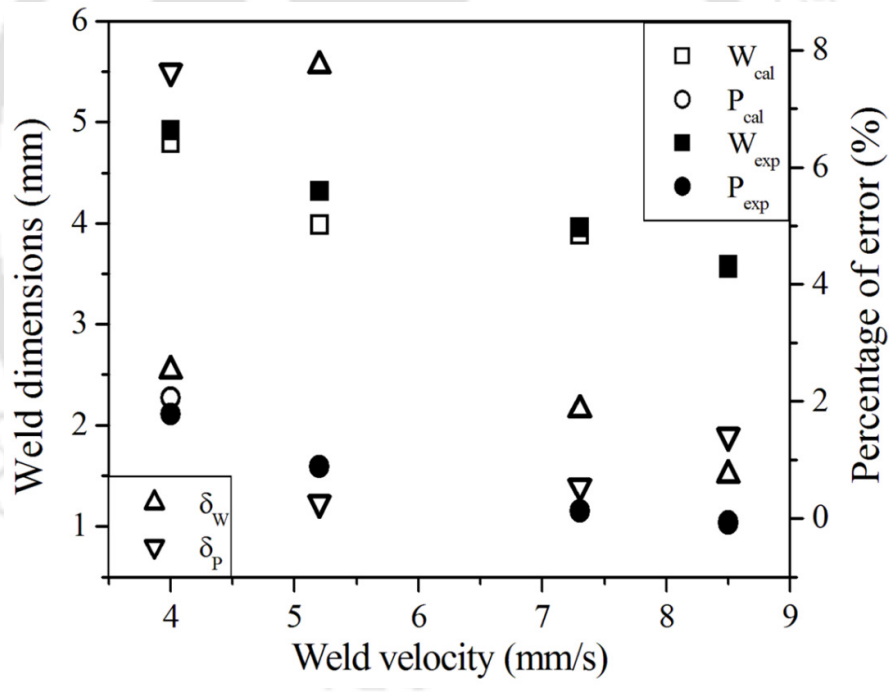

Figure 5.11: Comparison between computed and experimentally measured weld dimensions corresponding to welding conditions given in Table 4.10.

5.4.2 Transient heat transfer in fiber laser welding

The computational exercise with the conduction heat transfer analysis is attempted next for linear laser welding process. Typically in the physical modeling of a linear welding process, welding heat source generally moves with a constant velocity along the original weld joint interface, a moving heat source concept is required to be implemented. This can be done in two ways. The first way is that in which it can be considered that the welding heat source moves with relative to the work piece and applies the heat input at different positions on the work piece (weld line) as a function of time. This approach referred to the Lagrangian. One significant disadvantage of this approach is the fact that a large solution domain is necessary to map the actual length of the weld joint. On the other hand, a quasi-steady method can be followed in which the main consideration is that the work piece is satisfactorily large enough and the thermal cycles around the heat source does not necessarily change with time over the complete length of the weld joint, apparently except towards the end of the work piece. The later method allows the solution domain to be comparatively smaller than the actual weld joint dimensions and hence, has mostly been followed in the contemporary computational welding research works.

5.4.2.1 Fiber laser welding of austenitic stainless steel, SS 304

Figure 5.12 refers to computed 3D transient temperature distribution for data set # 8 in Table 4.5 at four different times of 0.54 s, 1.44 s, 2.22 s and 2.88 s, respectively. The red color area along X-direction and Z-direction represents the half-weld bead width and depth of penetration, respectively. The color bar in this figure actually defines the fusion zone, and heat affected zone in terms of corresponding isotherm. It is obvious that with the movement of laser the subsequent zone solidifies.

The development of weld pool is demonstrated in Fig. 5.13 at the initial stage of welding. The temperature distribution at four different times of 0.06 s, 0.23 s, 0.38 s, 0.53 s and 0.68 s respectively are simulated corresponding to data set 8 given in Table 4.5. It is obvious from the figure that temperature field is in transient nature from 0 to 0.53 s, which is generally refer as initial transient zone. Figure 5.14 represents the temperature field corresponding to quasi-stationary zone at time 1.275 s, 2.026 s, 2.551 s and 3 s respectively.

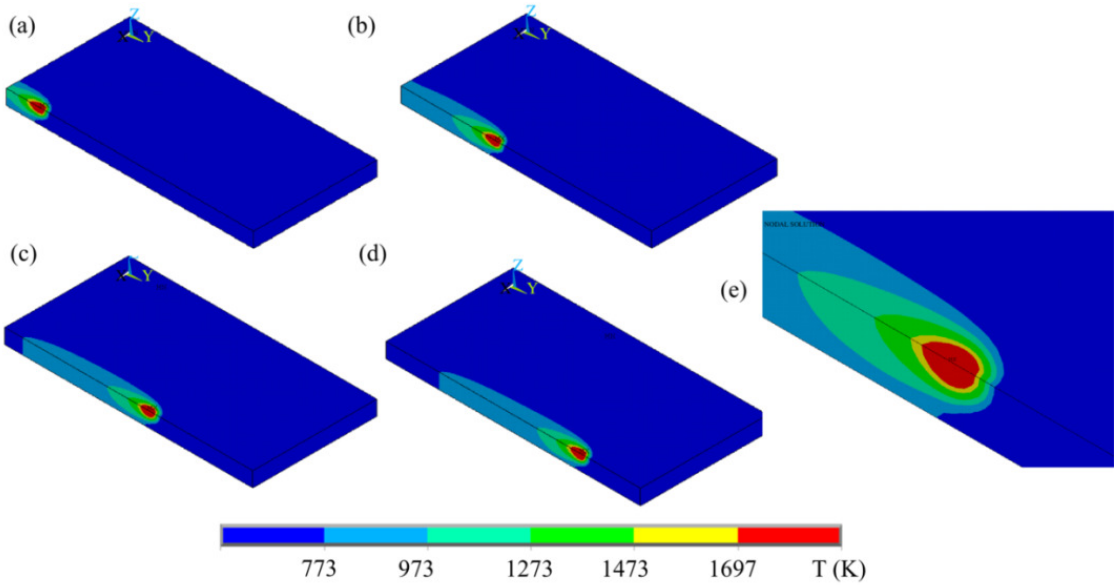

Figure 5.12: 3D transient temperature distribution for open atmospheric welding condition of data set 8 given in Table 4.5, at (a) 0.54 s, (b) 1.44 s, (c) 2.22 s, (d) 2.88 s and (e) zoomed view of (c).

In this zone the temperature distributions are almost stationary and produce similar type of isotherms with the advancement of laser source. Figure 5.15 represents the temperature field at the end of welding corresponding to weld time 3.48 s, 3.58 s and 3.676 s, respectively. When the heat source reaches towards end of the plate, temperature field varies from one location to another. At the transient zone of the specimen, three modes of heat transfer are more active. In quasi-stationary zone, heat transfer is mainly more due to conduction as compared to convection and radiation.

Figure 5.16 depicts the comparison of the open atmosphere computed weld bead shape (left side) with experimentally measured (right side) weld macrographs for welding process parameters corresponding to data set # 3, 6 and 7 respectively given in Table 4.5. A fair agreement between the computed and experimental weld macrographs shows the robustness of the developed numerical model. The area surrounded by 1697 K (red in colour) represents the weld fusion zone. Overall quantitative comparisons of estimated and measured weld bead dimensions are described in Fig. 5.17. Figure 5.17 (a) depicts the comparison of computed and experimental weld depth of penetration (DOP) for the welding conditions (data set 1 to data set 8) given in Table 4.5.

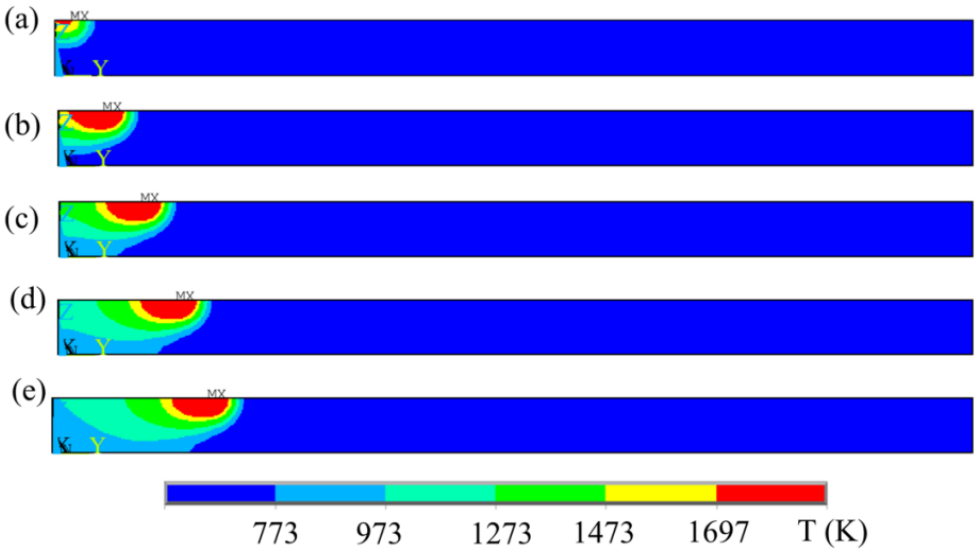

Figure 5.13: 2D temperature field corresponding to laser power 900 W and welding speed of 13.33 mm/s at (a) 0.06 s, (b) 0.23 s, (c) 0.38 s, (d) 0.53 s and (e) 0.68 s.

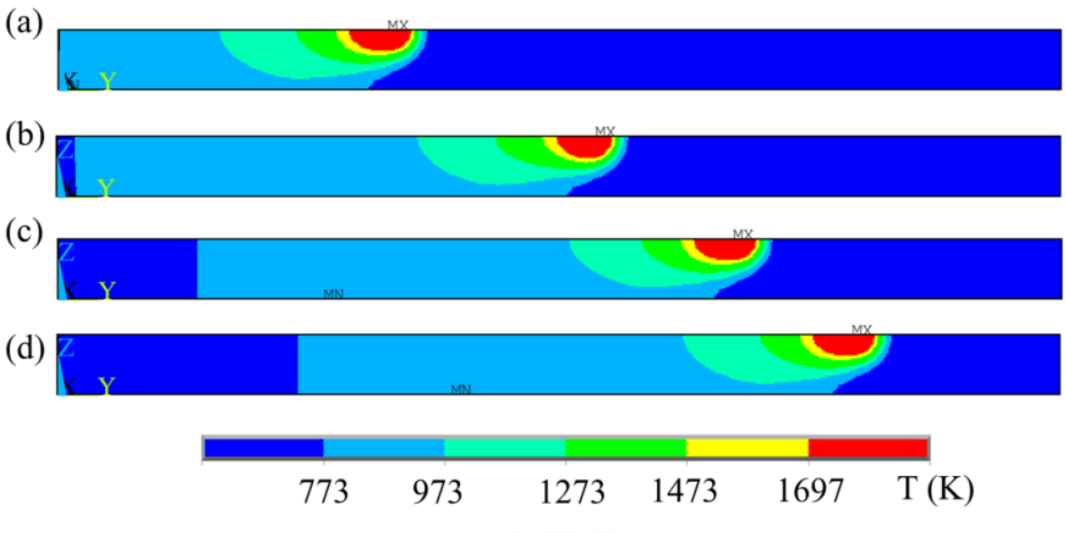

Figure 5.14: 2D temperature distribution corresponding to laser power 900 W and welding speed of 13.33 mm/s at (a) 1.275 s, (b) 2.026 s, (c) 2.551 s and (d) 3 s.

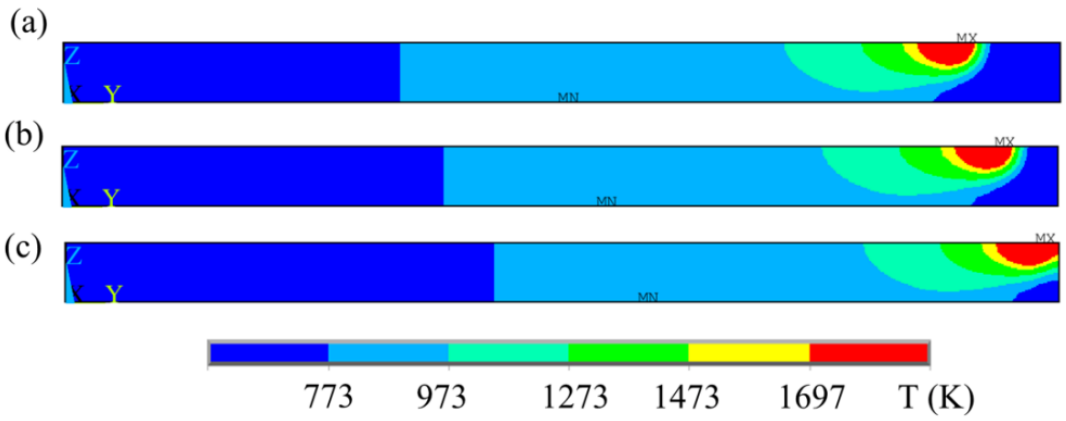

Figure 5.15: 2D temperature field corresponding to laser power 900 W and welding speed of 13.33 mm/s at (a) 3.48 s, (b) 3.58 s and (c) 3.676 s.

The values in Fig. 5.17 on bars illustrate the percentage error between the computed and measured weld pool dimensions. Figure 5.17 (b) describes the comparison of experimental bead width and computed values for the same welding conditions given in Fig. 5.17 (a). The maximum error in case of DOP comparison is 7.46 and minimum is 3.7 for data sets 7 and 1 respectively. It is obvious that the error percentage in calculation of weld dimensions is within acceptable limit of less than 8 %.

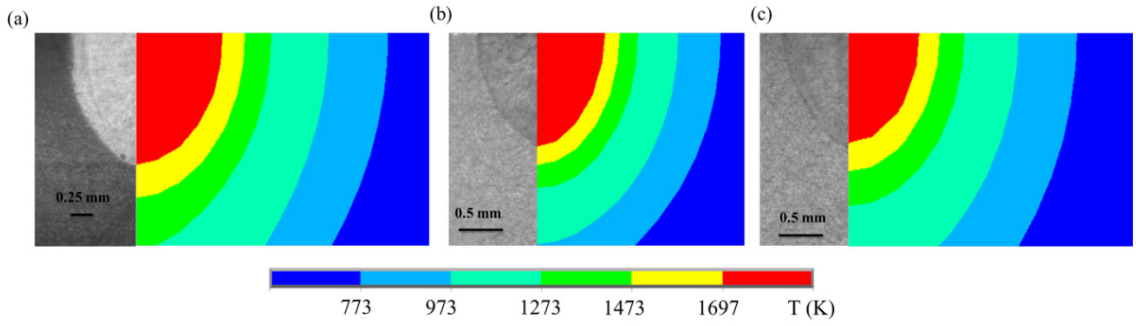

Figure 5.16: Comparison between experimental and computed weld macrographs at open atmosphere corresponding to (a) data set 3, (b) data set 6, and (c) data set 7 given in Table 4.5.

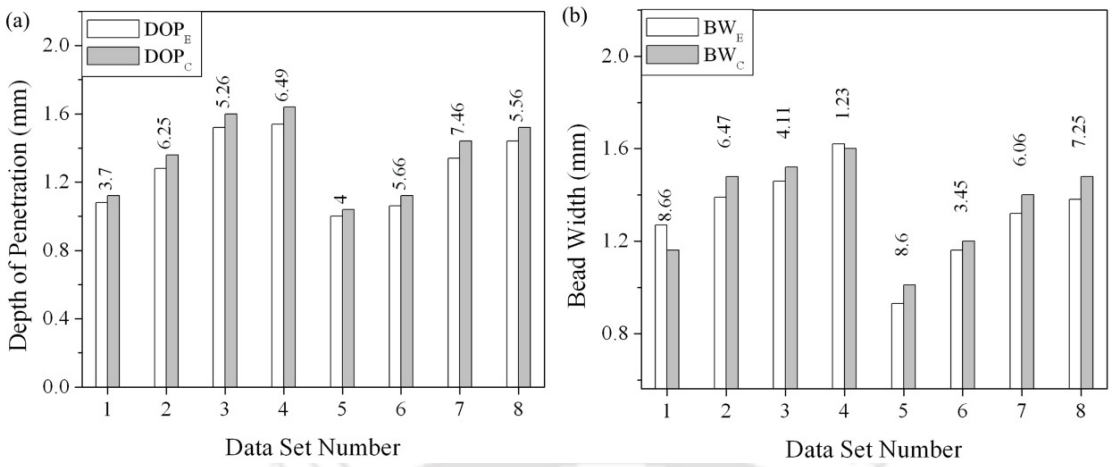

Figure 5.17: The quantitative comparison of computed and predicted weld pool dimensions along with percentage error in open atmosphere welding process corresponding to data 1 to data set 8 of Table 4.5: (a) weld depth of penetration and (b) weld bead width.

The heat transfer analyses of self-protective atmosphere of argon fiber laser welding have been performed using a conical heat source model. Figure 5.18 illustrates the comparison of the self-protective atmosphere experimentally measured weld macrograph (left side) with computed weld bead shape (right side) for welding process variables corresponding to data set # 1 and data set # 4 given in Table 4.5. Satisfactory agreement between experimental and computed weld macrographs has been achieved using a conical heat source model. The area surrounded by melting point temperature (red colour) signifies the fusion zone in Fig. 5.18. It is noteworthy that sharp temperature gradient exists in the formation of fusion zone is case of argon shielding gas (macrographs) as compared to open atmosphere. Hence the conical heat source model is more appropriate as compared to double-ellipsoidal heat source model. Figure 5.19 describes the overall quantitative comparisons of measured and estimated weld pool dimensions corresponding to self-protective atmosphere welding variables (data set 1 to data set 8) given in Table 4.5. In Fig. 5.19, the numbers on bars show the percentage error between measured and predicted weld bead dimensions. The maximum percentage error between computed and measured weld bead penetration is 6.97 and minimum is 3.62 for data sets 2 and 7 respectively. It is obvious that the error percentage in calculation of weld dimensions is less than 7 % in case of self-protective atmosphere welding.

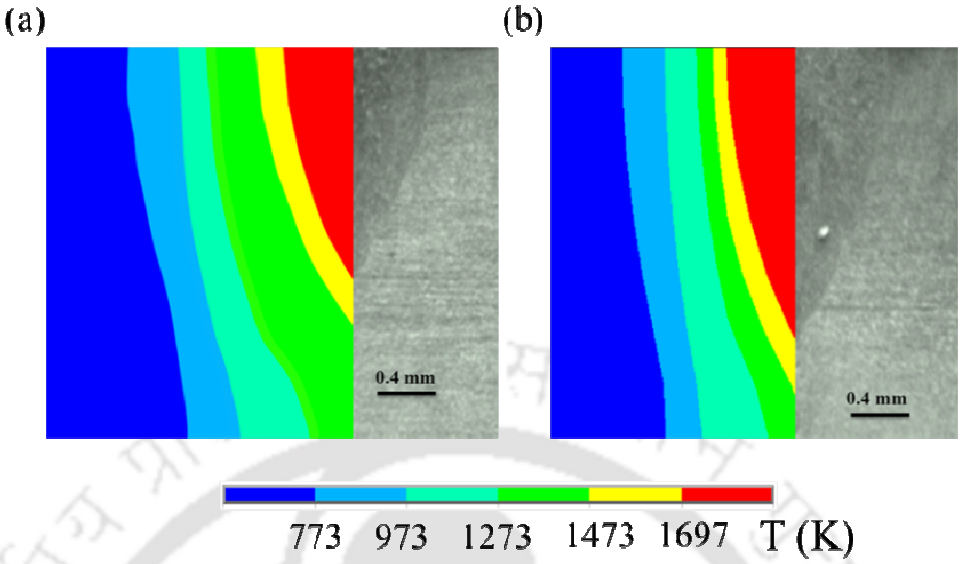

Figure 5.18: Comparison between experimentally measured and computed weld macrographs at protective atmosphere of argon corresponding to (a) data set 1 and (b) data set 4 given in Table 4.5.

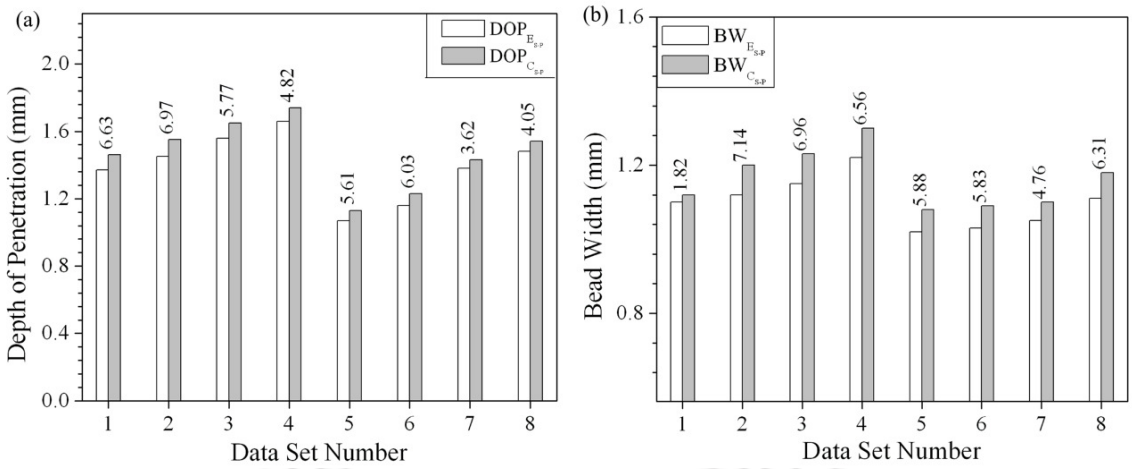

Figure 5.19: Comparison between computed and measured weld pool dimensions corresponding to self-protective atmosphere welding variables (data set 1 to data set 8) given in Table 4.5: (a) weld penetration and (b) weld width.

In fusion welding processes, the nature of thermal cycle and cooling rate greatly affects the microstructure and mechanical properties of the welded joint. Therefore, the numerical model is also used further to estimate the thermal cycles and cooling rates experienced at a number of representative points within the weld pool and heat affected zone. Figure 5.20 depicts the calculated weld thermal cycles corresponding to laser power 900W

and welding velocity 13.33 mm/s at six different locations on X-Z plane. The located points 1, 2, 3 and 4 in Fig. 5.20 correspond to weld centre line and at a distance of 0.4 mm, 0.9 mm and 1.4 mm away from the weld centre line. Also, fixed locations of points 5 and 6 are through thickness directions at 0.4 mm and 1.6 mm. It is obvious that the temperature of points 1, 2, 3 and 4 increases gradually and decreases subsequently. Moreover, thermal cycles are stiffer and the peak temperature magnitude varies from point to point. Also, there is a delay to reach peak temperature for fixed points away from welding centre line. Similar trend can be observed corresponding to points 5 and 6. With the similar process variables and at same locations, it is noticeable that the peak temperatures are different for open and self-protective atmosphere welding processes. In case of open atmosphere welding corresponding to point 1 and 2, the maximum temperature attained are 2299 K and 2066 K; whereas it is 2667 K and 2278 K for self-protective atmosphere welding process. Furthermore, the point which is away from the welding line experiences less heating and it is expected that there is no significant changes in weld joint properties. The numerical model is further utilized and demonstrated its capability in computing cooling rate (CR).

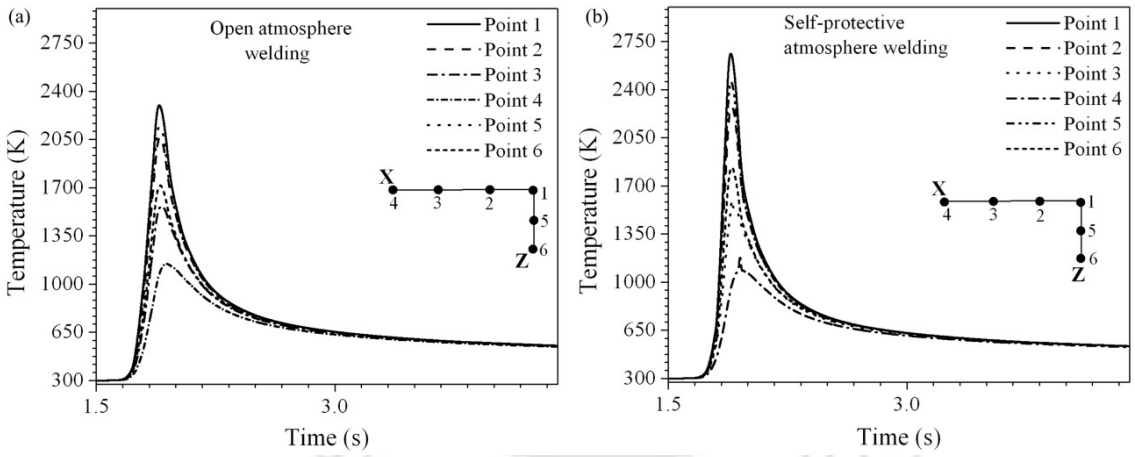

Figure 5.20: Computed weld thermal cycles corresponding laser power 900 W and welding velocity 13.33 mm/s at six different points, for (a) Open atmosphere welding and (b) self-protective atmosphere welding process.

Figure 5.21 describes the peak temperature and cooling rate corresponding to data set 8 given in Table 4.5 for fixed thermocouple location shown in Fig. 5.20. The maximum peak temperature is achieved 2667 K in self-protective atmosphere welding. The magnitude of the maximum cooling rate for open atmosphere welding process is 305×10^3 K/s and minimum is 153×10^3 K/s whereas it is 354×10^3 K/s and 145×10^3 K/s, respectively for controlled

atmospheric condition. Figure 5.21 (a) indicates that the variation of maximum cooling rate along weld width (X-direction) is more as compared to thickness (Z) direction.

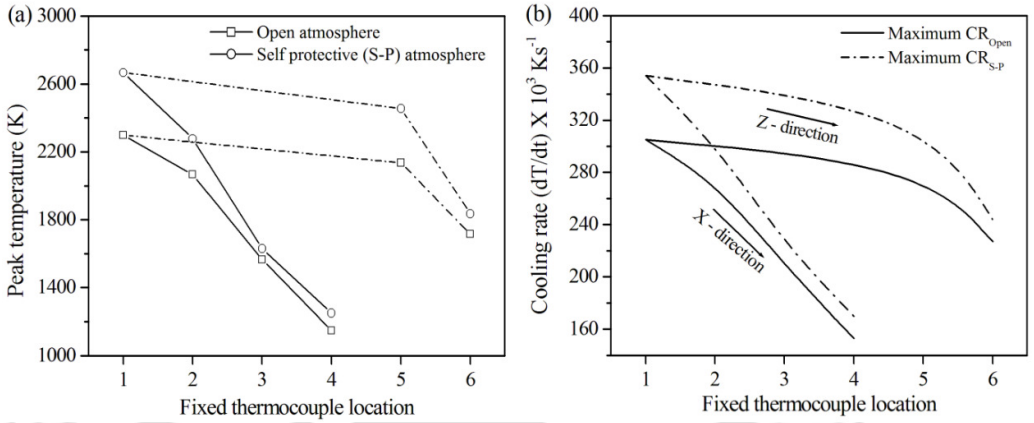

Figure 5.21: Comparison of peak temperatures and maximum cooling rates at different locations corresponds to open and self-protective atmosphere of argon welding.

To investigate the combine influence of process parameters and thermal properties of substrate material, the non-dimensional heat input index (as discussed in section 5.2.4) is considered. The parameters used to predict N_{HI} are described in Table 4.15. Figure 22 (a) describes the variation and nature of non-dimensional heat input index with welding speed which is not exactly linear. The wide variation of N_{HI} signifies that the selected process parameters cover a wide range of welding conditions. The average values of cooling rates in and around the weld pool corresponding to three different transformation temperatures are plotted in Fig. 22 (b) with respect to N_{HI} corresponding to data set 4, 5 and 8 given in Table 4.5. It is evident that that at lower values of N_{HI}, the computed values of cooling rate at higher temperature (1698 K) are more than the same at 1497 K and 997 K. Moreover, as the value of N_{HI} increases, the values of average cooling rates decrease considerably and become nearly same corresponding to temperatures 1698 K, 1497 K and 997 K. At higher values of N_{HI}, the weld pool size increases noticeably thereby reducing the value of the average cooling rate.

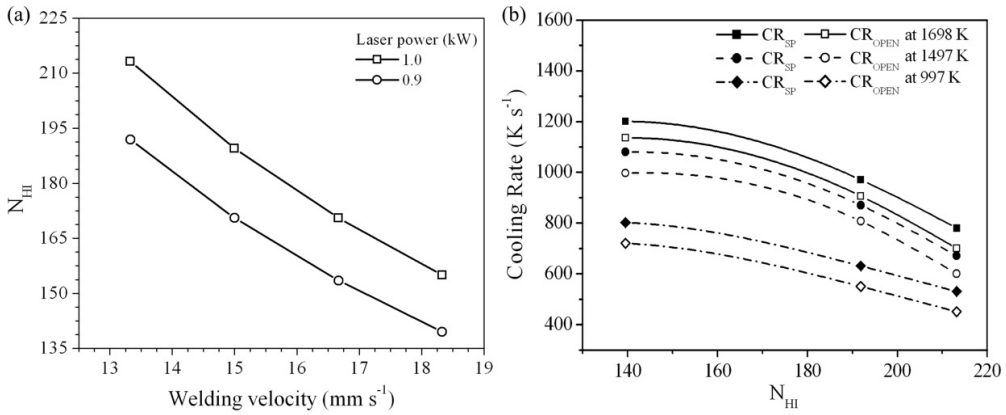

Figure 5.22: (a) Variation of non-dimensional heat input index with respect to welding velocity and (b) influence of N_{HI} on cooling rate.

5.4.2.2 Fiber laser welding of austenitic stainless steel, SS 316

The conduction mode heat transfer analysis is also performed for fiber laser welding on SS 316, 3 mm thickness plate. The temperature dependent material properties (Fig. 5.1 (b)) and other constant material properties (Table 5.1) are used in simulation. The latent heat of melting and solidification was also incorporated into the material model through increase or decrease of specific heat of the material and emissivity is considered as 0.9.

Figure 5.23 describes the 3D transient temperature distribution for data set 2 given in Table 4.5 at three different locations. Figures 5.23 (a), (b), and (c) respectively, refer to the temperature distribution at time 0.9 sec., 2.25 sec., and 3.45 sec. The region surrounded by the liquidus temperature 1727 K denotes the weld pool, and its intercepts along the Z-axis, X-axis, and Y-axis respectively represents the depth of penetration, half bead width and weld length. It is also observed from this figure that the temperature distribution is symmetrical about the YZ plane; on the other hand, it is asymmetric nature with respect to other planes as a result of the laser beam movement along the positive Y-axis.

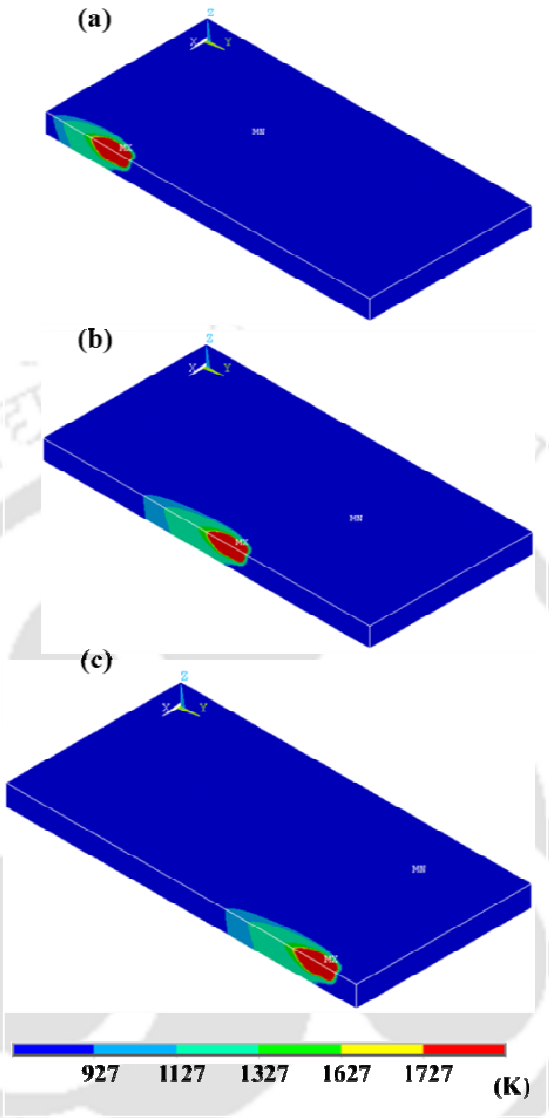

Figure 5.23: Three dimensional transient temperature distributions for data set 2 in Table 4.5 at three different times; (a) at time 0.9 s (b) at 2.25 s and (c) at 3.45 s.

Figure 5.24 shows the comparison between the experimentally measured (left side) and computed weld macrographs (right side). Moreover, figures 5.24 (a), (b), and (c) respectively, depict the comparison of the two dimensional transverse cross-section of the experimentally observed weld pool shapes against the calculated weld macrographs for data set 2, 6, and 7 given in Table 4.5. Moreover, the area enclosed by the base material liquidus temperature, 1727 K indicates the weld molten pool and its intercepts along the, X-axis and Z-axis depict, half weld bead width and the weld penetration respectively. Figure 5.24 also clearly show a fair agreement between the actual weld macrographs shape and sizes and corresponding calculated weld shapes and sizes for the similar welding conditions.

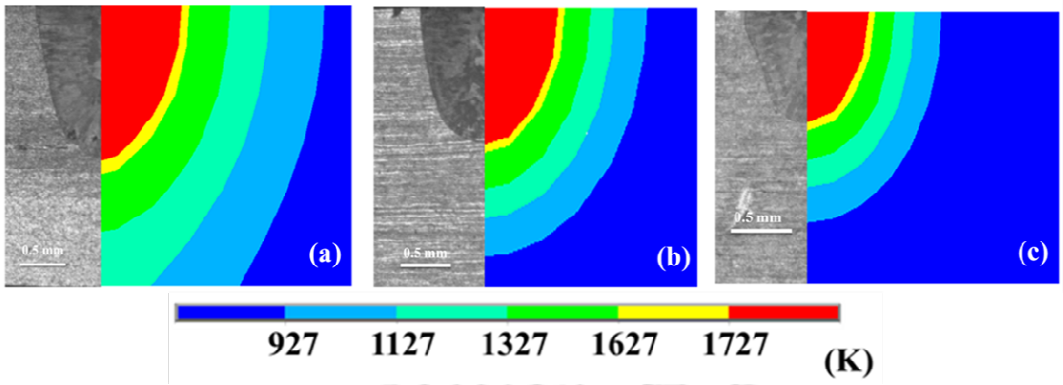

Figure 5.24: Comparison of experimental (left hand side) and computed (right hand side) transverse cross-section weld macrographs, (a) for data set 2, (b) for data set 6 and (c) for data set 8 in Table 4.5.

Moreover, Fig. 5.25 illustrates the measurable comparison of experimental and computed weld dimensions for welding conditions data set no.'s 1, 3, 5, 7, 9 and 11 given in Table 4.5. It may be observed from the results shown in Fig. 5.25 that when keeping laser power as constant and decreasing the welding velocity, the depth of penetration increases and bead width also increases but it is nominal in magnitude. Similarly, when welding velocity is constant and decreases the laser power, weld penetration decreases and bead width also decreases that is substantial in magnitude.

The maximum depth of penetration is 1.64 mm for the data set 3 given in Table 4.5 and the minimum is 0.6 mm for data set 9 given in Table 4.5 is experimentally observed for the range of process variables given in Table 4.5. The percentage of error between the experimentally measured weld pool dimensions and corresponding calculated weld pool dimensions are below 8 percent and this can be realized from Fig. 5.25.

5.4.2.3 Laser welding of DH 31 steel plate

In present work, a quasi-steady state heat transfer analysis of laser welding process is performed first to simulate the temperature distribution within the solution domain. Figure 5.26 schematically represents one sheet of butt joint geometry to be welded along the interface A–B–C–D. The heat source is irradiated on the top surface along the interface say, at a point 'O' at any time instant. The clamps are placed nearby to E, F, G, H points, respectively. Due to symmetric nature of the problem, half of the work-piece is considered for analysis. This symmetric profile is obtained with respect to YZ plane since the torch is moving along Y-direction and assuming similar type of material is joining. The welding

conditions are depicted in Table 4.13. The temperature dependent thermal material properties are used as given in Fig. 5.1 (c). The constant material properties used in numerical model is depicted in Table 5.1.

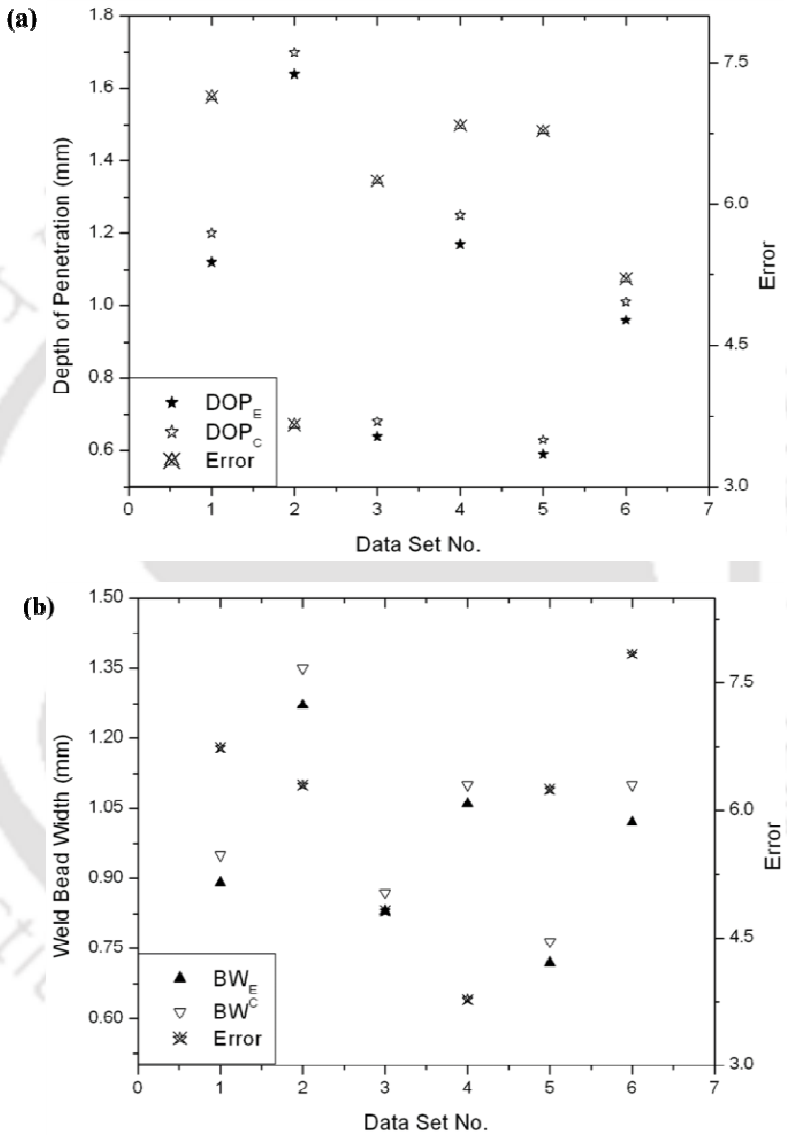

Figure 5.25: Quantitative comparison of calculated and experimental weld dimensions along with error between them for welding conditions of data set 1, 3, 5, 7, 9 and 11 given in Table 4.5; (a) weld penetration comparisons and (b) weld bead width comparisons.

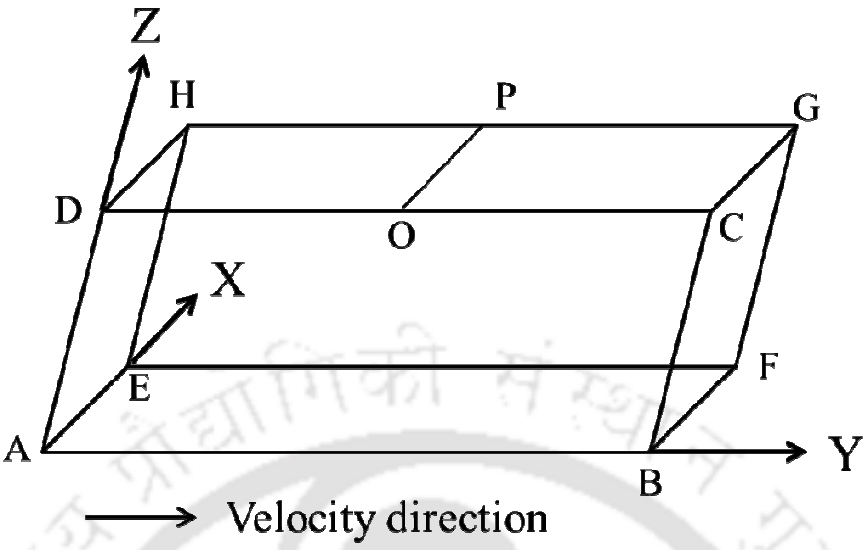

Figure 5.26: Schematic presentation of butt joint geometry.

Figure 5.27 depicts the simulated temperature distribution for autogeneous laser welding process when the laser is at the middle of the whole work-piece. It seems from the nature of temperature distribution that the laser is moving at certain speed and is stopped at this position. This resembles the quasi-steady state nature of heat transfer analysis in fusion welding process. The red zone in this figure indicates the molten pool size e.g. from the centre of focused laser, the length along X- direction is half-width (W_w) and depth (W_p) along Z-direction. The estimated power density is ~ 0.36 x10^6 W/m^2. Hence it may be assumed as conduction mode laser welding where the aspect ratio (W_p/W_w ratio) is around ~ 0.5. The time-temperature cycle in quasi-steady state analysis is performed by assuming the loading period from one edge to the middle of work-piece. The laser beam is stopped (as well as switched-off) at the middle position of work-piece and it is allowed to cool to room temperature. The loading period depends on the weld velocity and is calculated in present case as ~ 2.9 s.

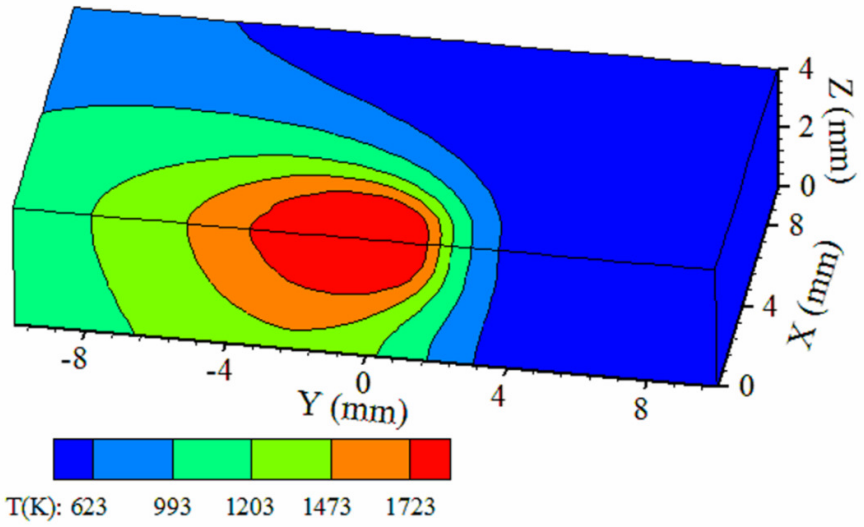

Figure 5.27: Simulated temperature profile of autogeneous laser welding.

The time temperature history for autogeneous laser welding is depicted in Fig. 5.28. The temperature profiles have been calculated along X-direction on the top of work piece at various distances from the centre of the heat source. It is obvious that peak temperature achieved for laser welding is below 3000 K at the centre very rapidly. During cooling period there exists a pleatu region (the part of the work-piece that cross the solidus temperature) possibly in between solidus and liquidus temperature due to release of latent heat which effectively consider the phase change effect. The cooling period is longer as compared to heating period. Figure 5.29 depicts the comparison between experimentally measured peak temperatures and computed one at three different welding conditions. In numerical simulation, the peak temperature has been considered along the line OP when heat source is assumed at the Centre point 'O'. Due to a concentrated heat source, temperature in the weld pool changes rapidly with the distance from the weld center line, i.e. the highest temperature is limited to the domain of the heat source with the lower temperature zone fanning out. Moreover, the computational model is further utilized to estimate the fusion zone area and compared with that of experimental results. The experimentally measured fusion zone area is 4.1 mm^2, whereas the calculated fusion zone area is 4.3 mm^2. The percentage error between the computed and experimental fusion zone area is 4.88 %. Henceforth, the computational approach followed here is providing relatively fair results.

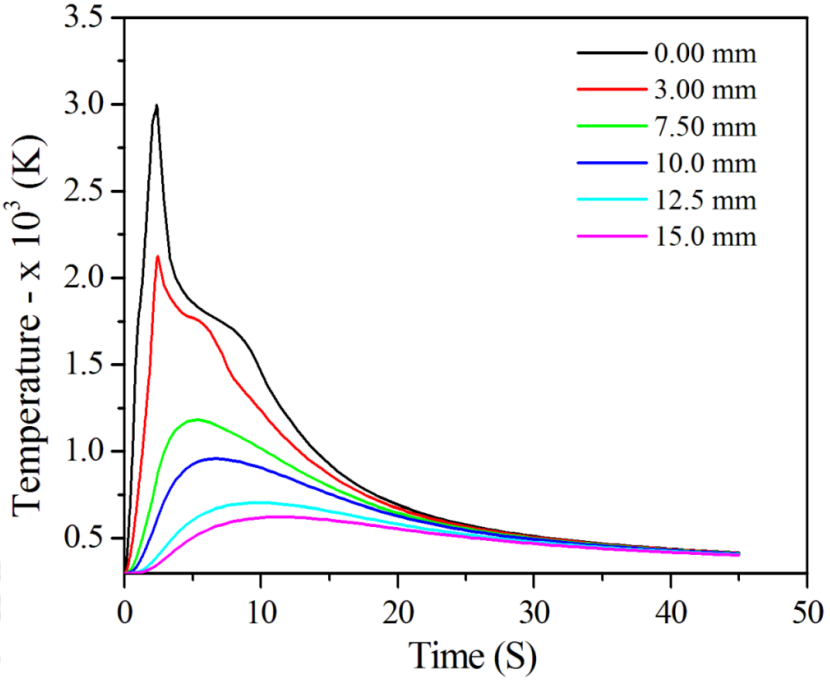

Figure 5.28: Time-temperature history of autogeneous laser welding.

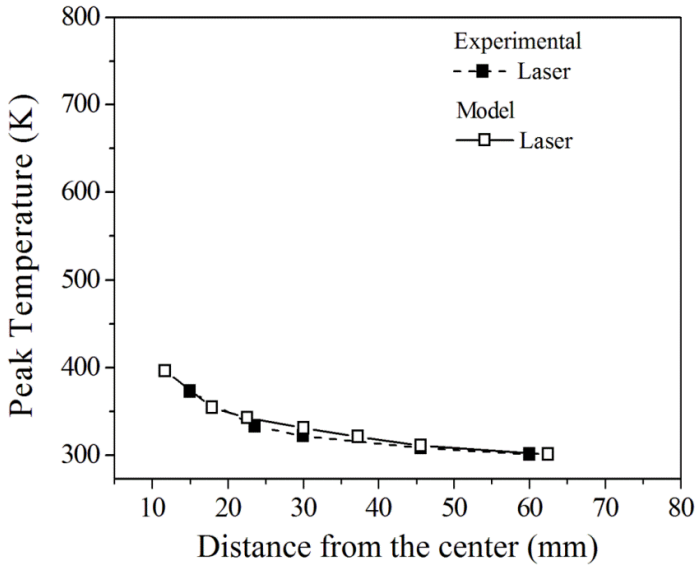

Figure 5.29: Comparison between experimental and numerical model results of thermal analysis: peak temperature.

5.4.2.4 Laser butt joint of SS 304

The effort on conduction heat transfer analysis based on finite element method has been further extended to simulate the fiber laser butt joint welding on SS 304 of 3 mm

thickness plate. In this section, the thermal results are presented and the mechanical analysis results are given in section 5.6. The conduction heat transfer analysis is performed considering two plates with neglecting contact resistance.

Figure 5.30 shows the three dimensional temperature distribution of the butt welding plates when the laser beam passes the position at the coordinate of y = 50 mm (at time 4.498 s) in the welding direction corresponding to laser power 1000 W and scan speed 0.667 m/min. The region surrounded by the liquidus temperature 1727 K (red portion in figure 5.24) represents the fusion zone (FZ) and its intercepts along the X-axis and Z-axis represent the weld bead width and depth of penetration, respectively. High temperatures are existent at an immediate vicinity of the fusion zone, which describes the heat affect zone (HAZ).

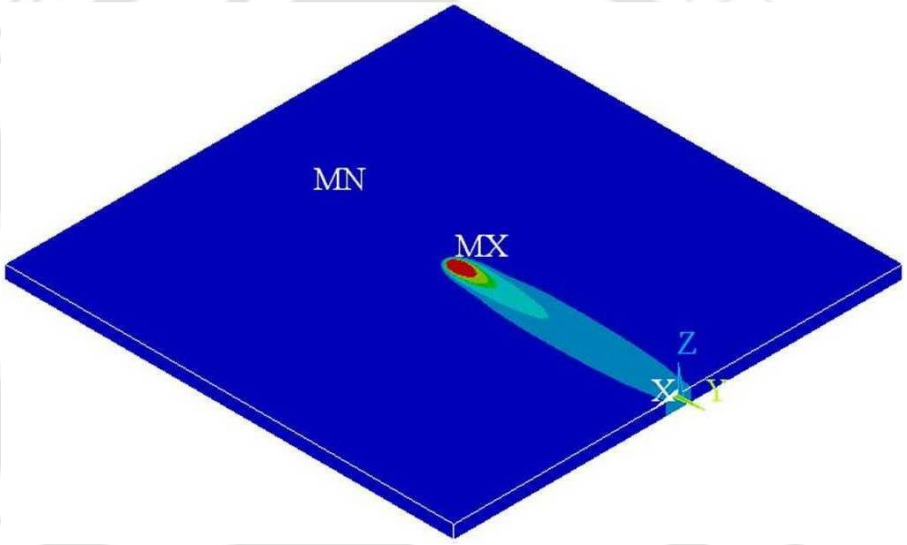

Figure 5.30: Three dimensional view of temperature distribution at 4.498 s after beginning of welding corresponding to data set #1 in Table 4.7 (red color zone represents fusion zone).

Figure 5.31 (a)-(b) illustrates the comparison of experimental and computed weld bead dimensions corresponding to welding conditions given in Table 4.7. The depth of penetration is more when the welds are made of laser power 1000 W and laser scan speed 0.667 m/min. Moreover, when the heat input per unit length decreases the weld bead dimensions are also decreases. The maximum percentage error between computed and measured penetration and bead width are achieved 7.5 and 5.56. A fair agreement between measured and calculated weld bead dimension can be seen from the Fig. 5.31. Furthermore, thermo-mechanical analysis has been performed in this work to estimate the welding induced residual stresses and distortions (section 5.6).

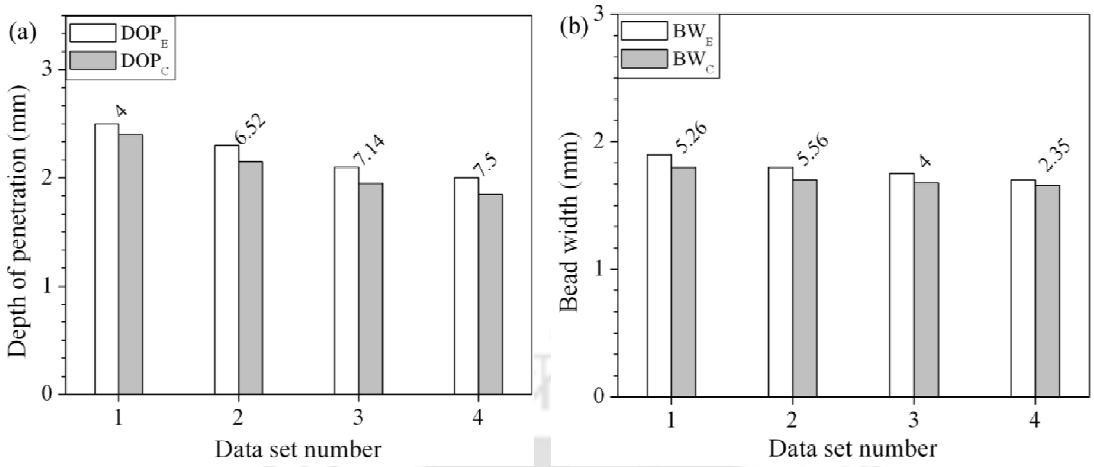

Figure 5.31: Comparison of experimental and calculated weld bead dimensions of fiber laser welding on SS 304, 3mm thickness plate corresponding to welding conditions given in Table 4.7.

5.4.3 Heat transfer analysis using newly developed egg-configuration heat source model

The egg-configuration heat source model is developed to reduce the model parameters during simulation of linear fusion welding process. In order to verify the flexibility and soundness of the egg-configuration heat source model, two relatively unlike welding processes such as linear GTA and laser welding are considered for simulation. In both the welding processes a non-linear three dimensional transient heat transfer model is developed to study the validity and flexibility of the proposed heat source model. For the simulation of these problems, the symmetric one-half of the plate is considered. The following assumptions are made in the formation of the finite element modelling: the work piece initial temperature is 300 K i.e. no preheating effect. The work piece is fixed while the heat source moves to attain prescribed relative velocity. The experimental results of gas tungsten arc welding process of AZ91 magnesium alloy and high-power diode laser welding process of aluminium alloy 5083 and 6082 under conduction regime are considered. Table 4.15 (a)-(c) shows the welding process parameters along with measured weld dimensions used to validate the numerical model. The chemical compositions of magnesium alloy AZ 91, aluminium alloy 5083 and 6082 are given in Table 4.16 (a), (b) and (c) respectively.

In order to realize the influence of the welding heat source parameters and thermo-physical material properties, an integrated non-dimensional heat input index N_{HI} is defined for

each data set in both the welding processes. The parameters used to estimate N_{HI} are described in Table 4.15. In equation (5.4), r_{eff} value in case of GTAW is considered as 2.5 mm [248]. The magnitude of N_{HI} corresponding to GTAW welding varies from 1.65 to 9.28 (Table 4.15(a)) whereas it is from 2.6 to 52.11 (Table 4.15(c)) for laser welding of aluminum alloy 5083. The wide variation of N_{HI} signifies that the selected process parameters cover a wide range of welding conditions.

Table 5.6: List of proposed heat source model parameters for GTA and laser welding processes.

Welding Process	a	b	c	m	N_f	N_r
GTAW (data set #1 in Table 4.15 (a))	2.89	4.34	1.17	0.2	1.25	0.75
Laser (data set #5 in Table 4.15 (c))	2.67	4.01	2.72	0.2	1.23	0.77

Figure 5.32 (a)-(c) describe the transient 3D calculated temperature distribution corresponding to data set #5 in Table 4.15 (b) at three different locations corresponding to weld time 1.502 s, 3.904 s, and 6.907 s, respectively using the proposed heat source model. The liquidus temperature of the base material is considered as 828 K. Therefore, the area enclosed by the liquidus temperature of the base material depicts the weld fusion zone and its intercepts along X-axis and Z-axis denote the half of the weld bead width and depth of penetration, respectively.

Figure 5.33 (a)-(c) describes the comparison between the experimentally measured weld pool shapes (left side) and computed weld pool shapes (right side) corresponding to data set #1, #3 and #4 given in Table 4.15 (b) using egg shape heat source model. A fair agreement between the computed and corresponding experimental weld macrographs indicates the robustness of the proposed 'egg' shape heat source model. Figure 5.34 describes the quantitative comparison between computed weld pool dimensions and the experimental measured weld pool dimensions as given in Table 4.15(b). In Fig.5, DOP_E, DOP_C, BW_E, BW_C, ER_P and ER_W depict experimental and computed depth of penetration, experimental and computed bead width, percentage error between computed and experimental depth of penetration and bead width respectively.

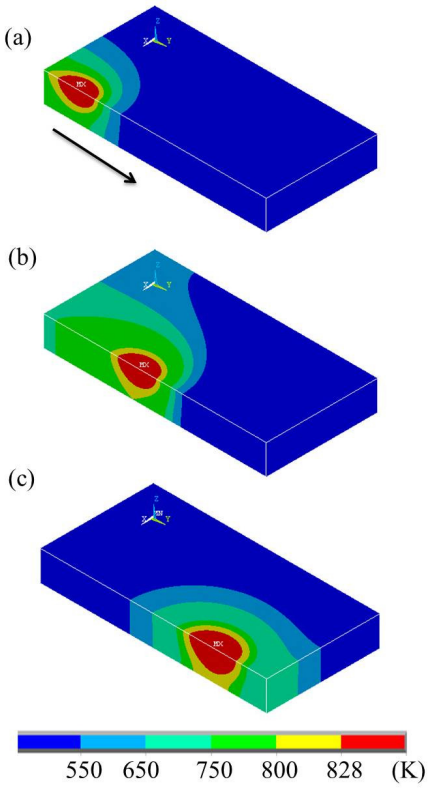

Figure 5.32: 3D transient temperature distribution for data set 5 given in Table 4.15 (b) after (a) 1.502 s, (b) 3.904 s and (c) 6.907 s. plate dimensions: 15 mm×30 mm×4 mm

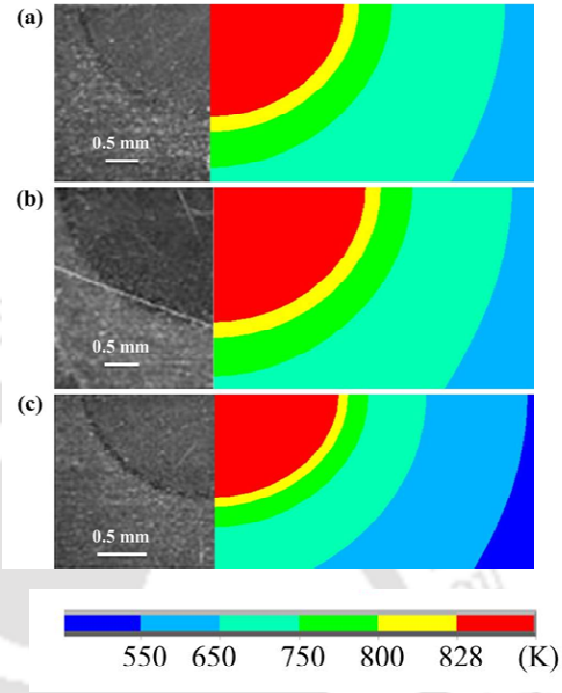

Figure 5.33: Comparison between experimental and computed weld macrographs: (a) data set #1, (a) data set #3 and (a) data set #4 given in Table 4.15 (b).

It is clear from the Fig.5 that the error percentage in calculation of weld bead dimensions is within acceptable limit (< 7 %). Moreover, the percentage error between computed and experimental depth of penetration is maximum of 6.9 % for data set #4 and is minimum of 1.75% for data set #5 given in Table 4.15 (b). Likewise, the percentage error between computed and experimental weld bead width is minimum of 2.31 % for data set #6 and maximum of 5.78 % for data set #3 given in Table 4.15 (b).

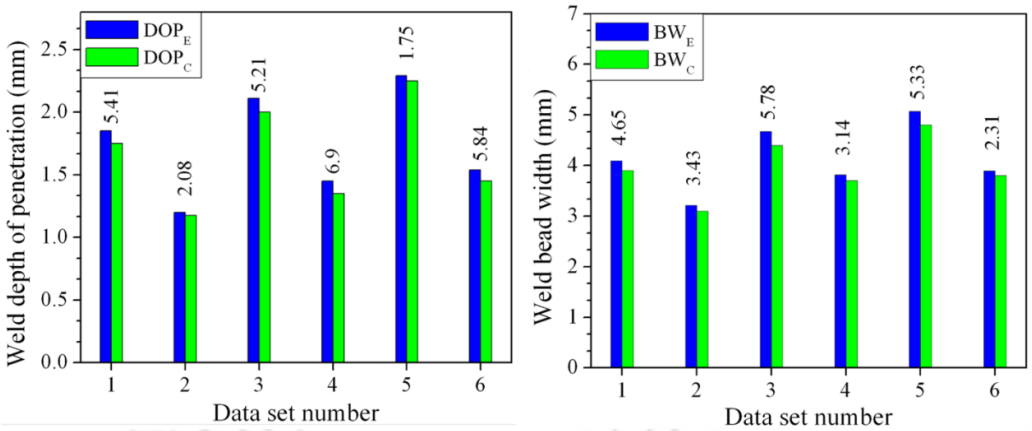

Figure 5.34: Quantitative comparison of experimental and computed weld pool dimension corresponding to process variable given in Table 4.15 (b).

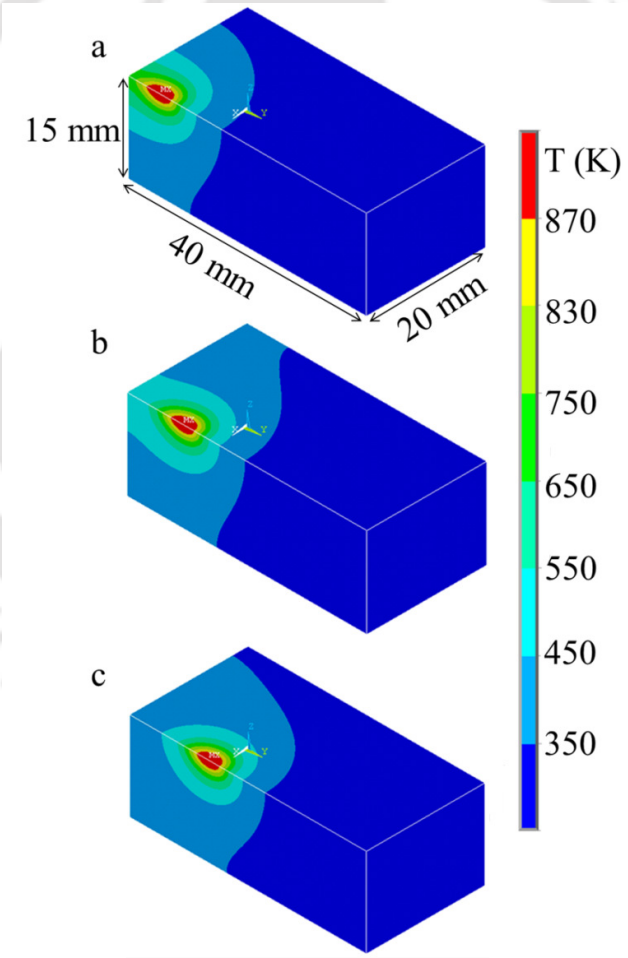

Figure 5.35: Calculated transient temperature field in GTAW weldment corresponding to data set #1 in Table 4.15 (a), (a) using proposed heat source model: (a) at 1.8018 s, (b) at 3.003 s, and (c) at 4.2042 s.

The proposed model parameters are considered from the experimentally measured weld pool dimensions. This approach has been followed by several researchers [30, 42, 125, 144]. Therefore, in this work, the heat source model parameters were mapped with the actual weld pool size. Table 5.6 describes the typical model parameters used for egg configuration heat source model. Table 4.15 (a) shows the process parameters of GTAW along with the experimentally measured weld pool dimensions. The proposed model is verified for welding speeds from 3.33 mm/s to 13.3 mm/s. Figure 5.35 (a)-(c) show the three dimensional predicted temperature distribution of GTAW at three different locations (at time t = 1.8018 s, 3.003 s, and 4.2042 s respectively) corresponding to data set #1 in Table 4.15 (a) using a proposed egg configuration heat source model. In Fig. 5.35 (a)-(c), the area enclosed by the liquidus temperature of AZ91 magnesium alloy is 870K, depict the fusion zone, and its intercepts along the Z-axis and X-axis represents the depth of penetration and half of the bead width, respectively. Figure 5.36 (a)-(c) describe the 3D computed temperature distribution for laser welding of aluminum alloy 5083 corresponding to data set #1 in Table 4.15 (c) at three different positions corresponding to weld time 6/50 s, 14/50 s, and 22/50 s, respectively using a proposed heat source model. The liquidus temperature of the aluminium alloy is considered as 843 K. Numerical simulation is performed for lower speed of laser welding (5 mm/s) to relatively higher speed welding (100 mm/s). In the present work, the simulations are also performed using a double ellipsoidal heat source model to understand the perfection of the proposed model for linear fusion welding process. Figure 5.37 (a) and (b) show the comparison between computed isotherms of two types of heat source model corresponding to data set # 5 in Table 4.15 (c). It is observed from this figure that the computed weld macrographs are almost similar in shape and size. However, the values of the weld width and depth of penetration are not same due to the variation of the lengths in moving direction of heat source. Figures 5.38 (a) and (b) depict the overall comparison of weld depth of penetration and width using two heat source models along with percentage error corresponding to experimental data in Table 4.15 (c).

Figures 5.39 (a)-(c) depicts the comparison of experimentally measured weld pool shapes (left side) and computed weld pool shapes (right side) corresponding to data set #2, #3 and #5 of Table 4.15 (c) using a proposed heat source model. Fair agreements between calculated and experimental weld bead cross sections indicate the robustness of numerical simulation using egg-configuration heat source model. Overall quantitative estimation of weld dimensions from numerical model and a comparative study over experimentally measured

weld dimensions are illustrated in figures 5.40 and 5.41 using the proposed heat source model.

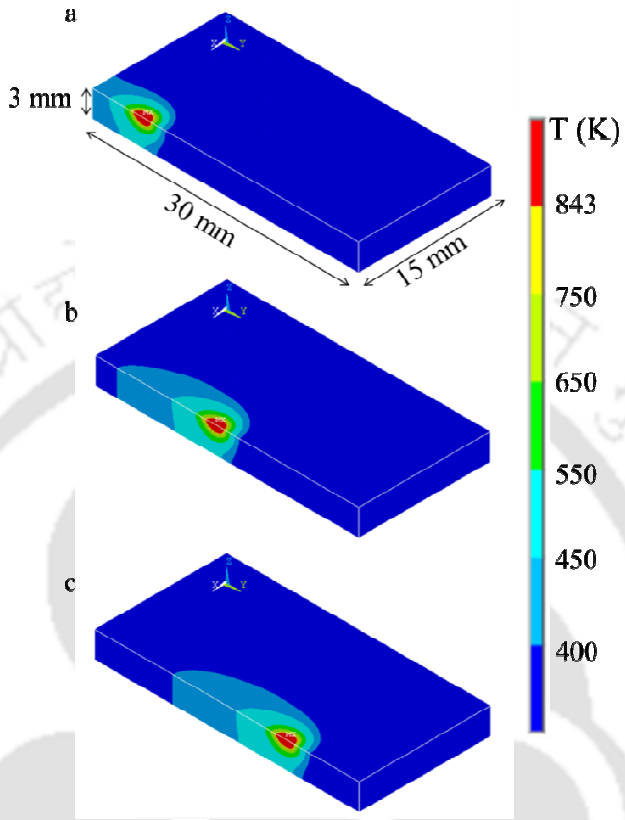

Figure 5.36: Calculated transient temperature field in diode laser weldment corresponding to data set #2 in Table 4.15 (c), (c) using proposed heat source model: (a) at 6/50 s, (b) at 14/50 s, and (c) at 22/50 s.

Figure 40 (a) and (b) illustrates the comparison of computed and experimental weld pool dimensions for the welding conditions given in table 4.15 (b) for depth of penetration and weld bead width respectively. The values in figures on bars illustrate the percentage error between the computed and measured weld pool dimensions. The comparison of weld pool dimensions for GTAW indicates fair agreement for a wide range of process parameters (N_{HI} = 1.65 ~ 9.28). Figures 41 (a) and (b) depicts the quantitative comparison of the experimentally measured (Table 4.15 (c)) and calculated weld pool dimensions for laser welding over a wide range of N_{HI} (2.6 ~ 52.11) for depth of penetration and weld bead width respectively. It is obvious that both the cases, the error percentage in calculation of weld dimensions is within acceptable limit (< 8 %).

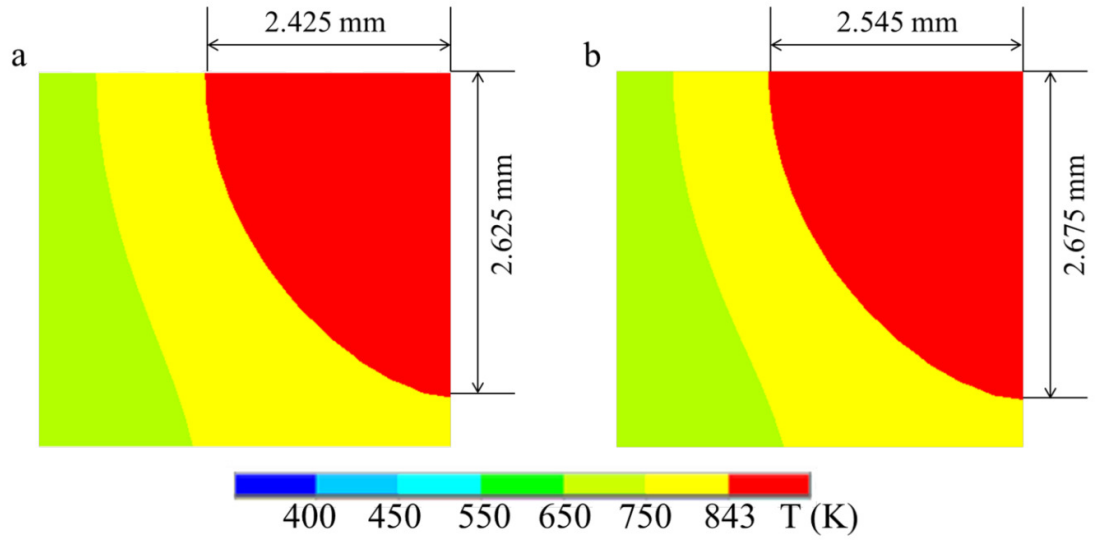

Figure 5.37: Comparison between computed weld macrographs using double ellipsoidal (left side) and egg-configuration heat source model (right) for data set 5 of Table 4.15 (c).

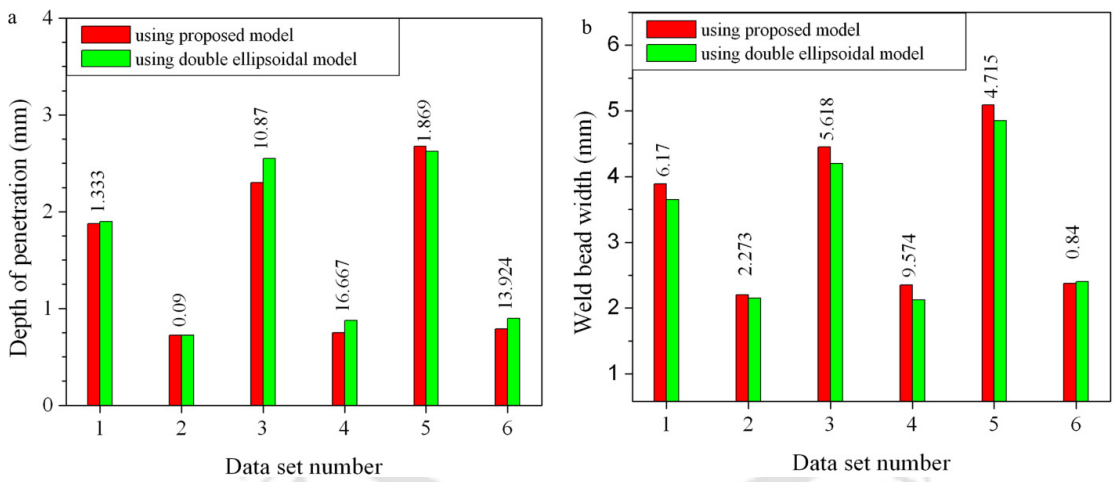

Figure 5.38: Comparison between computed weld pool dimensions using double ellipsoidal and egg-configuration heat source model corresponding to welding conditions of Table 4.15 (b): (a) depth of penetration and (b) weld bead width.

In welding process, the thermal histories and cooling rates strongly influence the microstructure and mechanical properties of the welded joint. A quantitative knowledge on the cooling in and around the weld zone is useful for understanding phase transformation kinetics which influences the final microstructure of the joint. To keep the calculations simple, the thermodynamics and kinetics of the solidification process are not incorporated and the degree of undercooling is assumed zero.

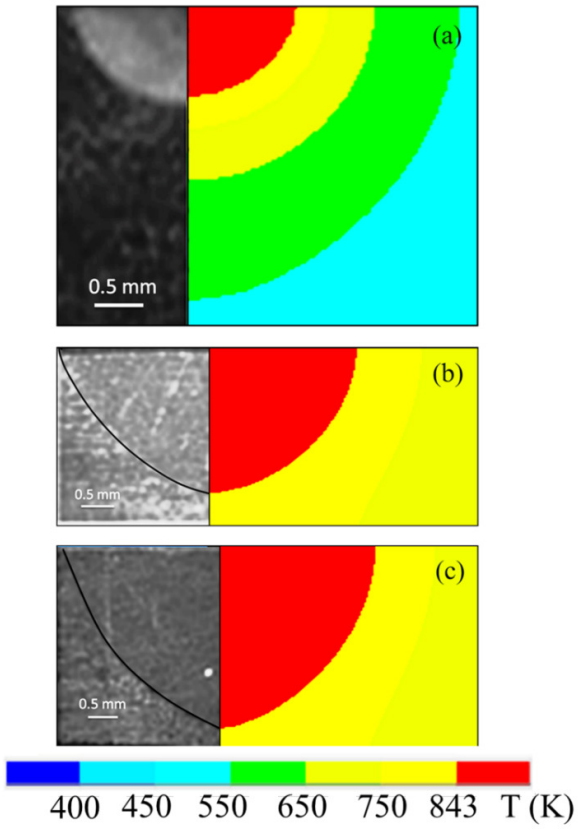

Figure 5.39: Comparison of experimental weld macrograph (left side) with computed thermal profile using proposed heat source model corresponding to (a) data set #2, (b) data set #3, and (c) result set #5 in Table 4.15 (c).

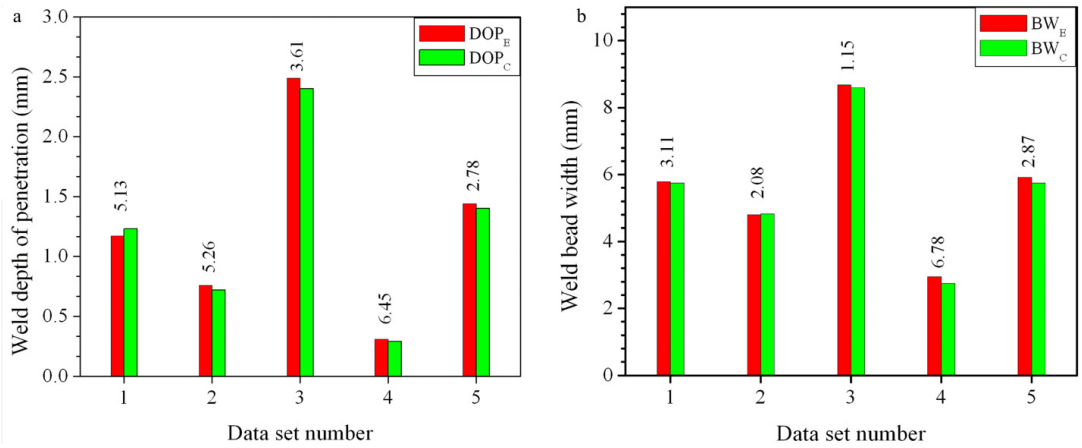

Figure 5.40: Comparison between experimentally measured weld dimensions with computed dimensions using proposed heat source model during GTAW corresponding to welding conditions of Table 4.15 (a): (a) depth of penetration and (b) weld bead width.

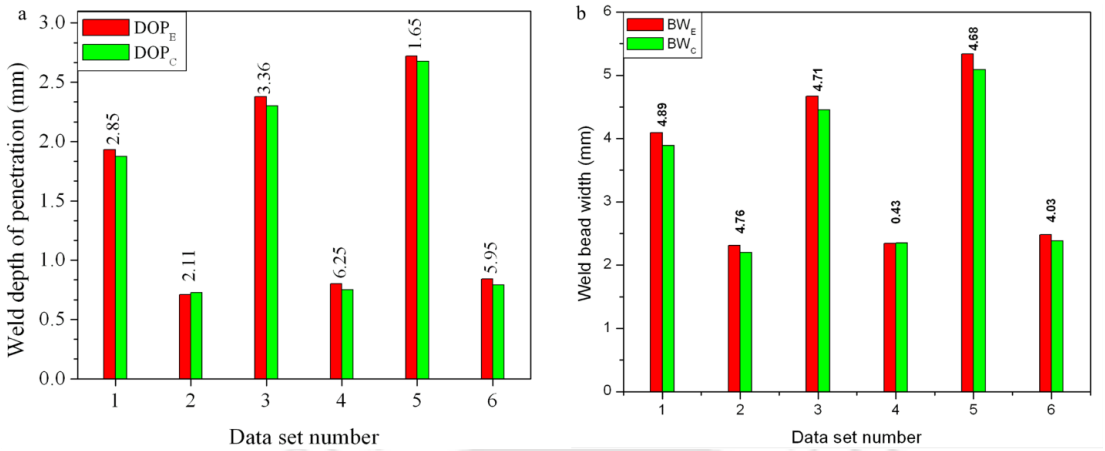

Figure 5.41: Comparison between experimentally measured weld dimensions with computed dimensions corresponding to welding conditions of Table 4.15 (c): (a) for depth of penetration and (b) for weld bead width.

Figures 5.42 (a) and (b) depict the estimated time-temperature history of GTAW corresponding to data set #1 given in Table 4.15 (a) and laser welding corresponding to data set #2 given in Table 4.15 (c) at four different locations from the weld centre line. In Fig. 5.42 (a), the time-temperature history for fixed locations of points 1, 2, 3 and 4, illustrates the temperature variation over time at a distance of 0.5 mm, 1.0 mm, and 4 mm away from the weld centre line and before the middle of the work piece. Figure 5.42 (a) demonstrates that the temperature of each point increases gradually and decreases subsequently. The magnitude of the peak temperature varies from point to point. There is a delay to attain peak temperature for fixed points away from welding centre line. Figure 5.42 (b) describes the calculated thermal cycles of laser welding process at points 1, 2, 3, and 4. The corresponding locations of points are indicated in the figure. It is obvious that the peak temperatures are different for these two processes. In GTAW, the maximum peak temperature is 940 K whereas 1060 K for laser welding process. However, the process parameters are not same for both the processes. Overall, the time-temperature cycle is stiffer for laser welding and is widen for GTAW welding process. The temperature gradient as well as high rate of heating and cooling takes place in laser welding as compared to GTAW. Moreover, the point which is away from the welding line experiences less heating and it is expected that there is no significant changes in properties. The numerical heat transfer model is next utilized to demonstrate its capability in computing cooling rate (CR). Figures 5.43 (a) and (b) illustrate the cooling rate with respect to time for both GTAW and laser welding processes, respectively corresponding to the special

points indicated in Fig. 5.42. The cooling rate is estimated by the ratio of change in temperature with change of time and is defined by

$$CR = \frac{dT}{dt} \approx \left|\frac{T_2 - T_1}{t_2 - t_1}\right| \quad (5.6)$$

where T_2 and T_1 are the temperatures corresponding to time t_2 and t_1 ($t_2 > t_1$). It is customary to note that rate of change of temperature during heating period is also termed as cooling rate. In Fig. 5.43 (a), the cooling rate is initially zero since there is little effect of welding heat source to develop the temperature or to change the temperature on fixed points. When the heat source approaches toward the fixed points, the cooling rate increases gradually to half of the total welding time. At the half of the total welding time, cooling rate suddenly becomes zero since there is no change in temperature at that time. The cooling rate further increases, attains maximum value, and reduces thereafter when the heat source moves away from the fixed region. This trend follows for laser welding although the magnitude of the cooling rate is different. The magnitude of the maximum cooling rate for GTAW are 603 K/s, 580 K/s, 517 K/s, and 122 K/s corresponding to points 1, 2, 3, and 4, respectively. In case of laser welding (Fig. 5.43 (b)), the cooling rate varies from 11.1 x 10^3 K/s for point 1 to 0.435 x 10^3 K/s for point 2. Although the distance from the weld centre line is same for both GTAW and laser welding, the cooling rate for laser welding experiences wide variation. This signifies that the laser welding involves concentrated heat distribution that affects considerably low geometric space. Since direct measurement of high peak temperature, rapid change of weld thermal cycle and resulting thermal distortion and associated stresses are difficult to measure experimentally for fusion welding process, the contemporary demand of reliable quantitative models are ever increasing. Present work is an effort to demonstrate heat transfer analysis using proposed egg-configuration heat source model for autogenous fusion welding process. Further validation of time-temperature history, cooling rate and influence of cooling rate on mechanical properties of weld joint are necessary to enhance the reliability of process model reported in this work.

5.4.3.1 Novelty and limitation of egg-configuration heat source model

The egg-configuration volumetric heat source model is developed and is tested to simulate temperature distribution for GTAW and laser welding processes. The developed heat source model consists of limited number of model parameters with asymmetric heat density

distribution for linear fusion welding process. The effect of welding speed on volumetric heat is dealt with changes of measurable weld dimensions and is adjustable by the parameter 'm'. The heat source model is limited to equal semi axis length along the welding direction, however, capable to yield non-uniform volumetric heat in front and rear parts of the proposed egg shape.

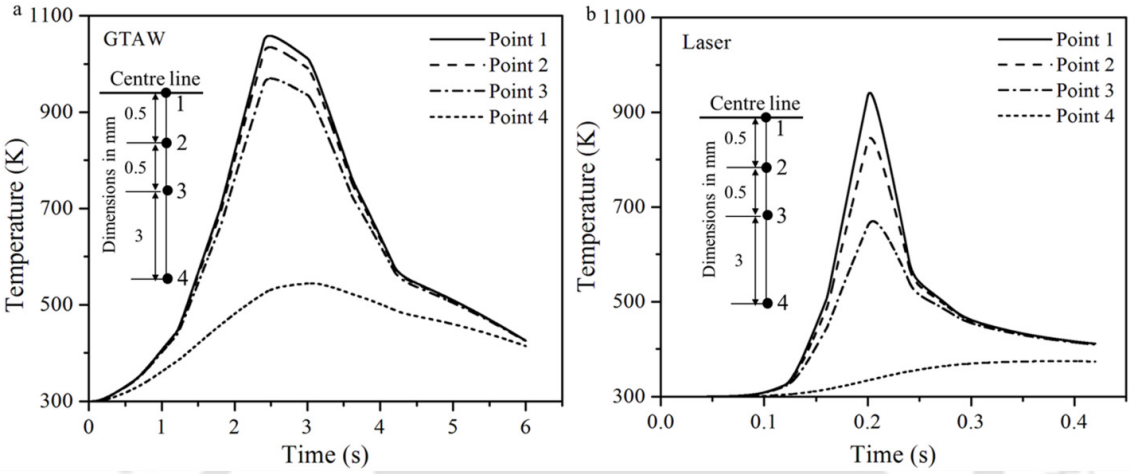

Figure 5.42: Estimated time-temperature history for (a) GTAW corresponding to data set #1 in Table 4.15 (a), and (b) diode laser welding corresponding to data set #2 in Table 4.15 (c).

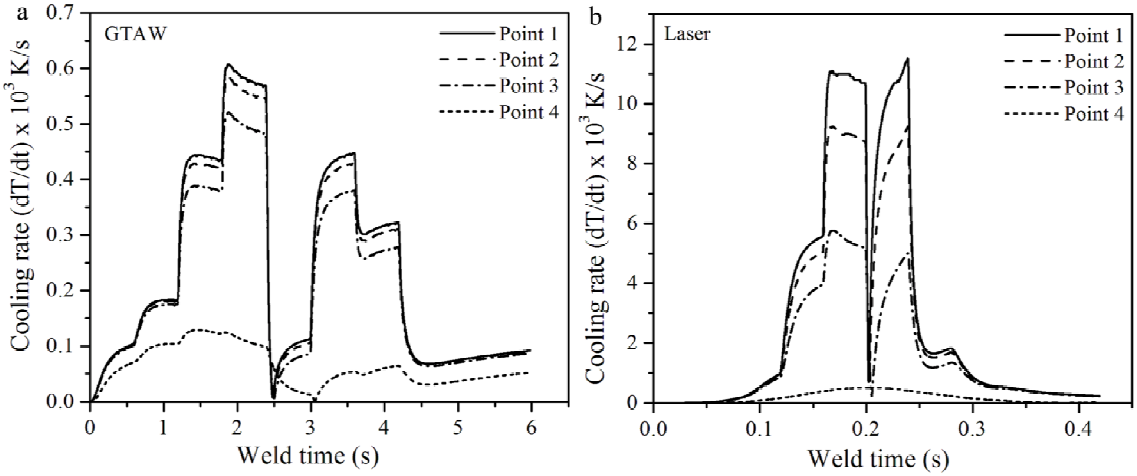

Figure 5.43: Estimated of cooling rate for (a) GTAW and (b) diode laser welding corresponding to thermal cycles of Fig. 5.42.

Overall, from the results it is revealed that the developed heat source model is flexible enough to accommodate different type of fusion welding process and hence the casting of the heat source parameters are needed to fit for a specific application. However, the estimation of heat source parameters from the mathematical basis demands an organized approach using

optimization algorithm which is the future scope of work for further exploration of egg configuration heat source model.

5.4.5 Keyhole formation in laser welding

The keyhole geometry is estimated from a separate mathematical model, a point-by-point energy balance on the keyhole wall where the temperature was assumed to be equal to the boiling point of the alloy. The mathematical model computes keyhole geometry depending on several parameters which include geometrical parameters, material properties and welding process variables. The modeling approach of the keyhole is described in chapter 4. Data utilized for the estimation of the keyhole geometry are listed in Table 5.1. A typical calculated keyhole profile is shown in Fig. 5.44 corresponding to laser power 2000 W and laser scan speed 18.33 mm/s of SS 316, 5 mm thickness plate in open atmospheric conditions. The maximum power density corresponding to laser power 2000 W and other welding conditions given in Table 4.6 is 6.37×10^{6} W cm^{-2}. Generally, if the maximum power density is more than 10^{6} W cm^{-2} then the keyhole may form during welding [69]. Henceforth, the welding conditions considered in this section will lead to keyhole formation in welds.

It is observed from the keyhole profile that the beam axis intersects the front keyhole wall. The front keyhole wall has a larger angle with the beam axis than does the rear keyhole wall. During welding, the laser beam comes across cold material first and approaches to the front keyhole wall. The material near the rear wall has been heated then. Therefore, the heat flux into the front wall is higher than that into the rear wall. To facilitate the balance of the heat loss, the front wall was more inclined so that more beam energy could be intercepted and absorbed. Henceforth, the estimated keyhole geometry was asymmetric with the rear wall being steeper than the front wall. Figure 5.45 depict the mapping of keyhole profile with experimentally extracted weld macrograph. The keyhole boundary is marked by the yellow lines. Figures 5. 45 (a) and (b) are corresponding to welding data set 3 and 4 given in Table 4.5 of SS 316 fiber laser welds. It is observed from the results that the estimated keyhole profile is larger for the low welding speed (13.33 mm/s) as compared to welding speed of 15 mm/s.

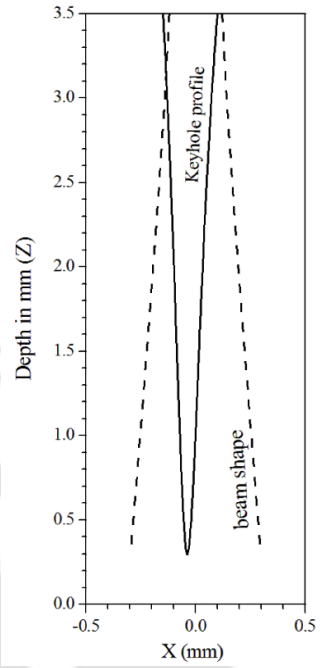

Figure 5.44: Estimated keyhole profile for fiber laser welding at laser power 2 kW and scanning speed 18.33 mm/s in open atmospheric.

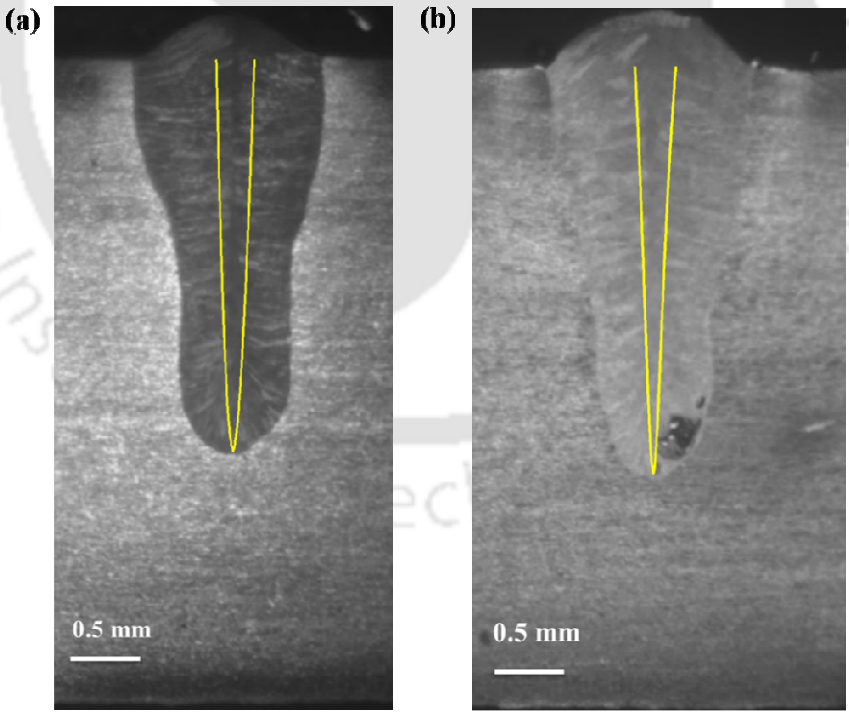

Figure 5.45: Mapping of estimated profile with experimentally obtained SS 316, 5 mm thickness plate weld macrograph corresponding to laser power 2000 W and laser scan speed (a) 15 mm/s and (b) 13.33 mm/s.

5.5 Heat transfer and fluid flow in GTA welding

The conduction heat transfer analysis of fusion welding process using volumetric heat source model has provided with reasonably accurate weld bead dimensions in linear GTA and laser welds corresponding to a number of experimentally measured results. Nevertheless, the conduction heat transfer analysis alone is not sufficiently enough of accounting for the convective transport of heat that occurs in molten weld pool. Only heat conduction analysis might not be sufficient to consider the effect of surface-active elements. In the liquid metal flow, the most significant driving force is the surface tension force and it is incorporated through temperature- and concentration-dependent coefficients of surface tension. Other forces such as buoyancy force due to presence of density differences and electromagnetic force due to presence of electric arc also significant. Therefore, it is necessary to perform an analysis involving the effect of such driving forces on the convective heat transport in weld pool. In such an effort, it is required to solve the conservation of energy, mass and momentum equations within the solution domain. Hence an effort is made to examine the influence of surface active elements in linear GTA welds using an enhanced transport phenomena based heat transfer and fluid flow model based on finite element method. The uncertain model parameters for fluid flow analysis are extracted from integrated modeling approach using optimization algorithm. It should be point out that in the case convective heat transfer analysis; the volumetric heat source model is not required.

5.5.1 Influence of Oxygen as surface active element

The influence of surface-active elements such as Oxygen on linear GTA welds using transport phenomena based heat transfer and fluid flow model is presented. To analyze the overall performance of the process, an error analysis has been executed on the comparative study of calculated and experimental results. The error analysis consists of individual component errors and relative reliability of the predicted solution sets. The estimation of most appropriate optimum values of uncertain model parameters in convection based model is presented in section 5.3.2. The experimental welding process variables and the corresponding measured weld bead dimensions used for the optimization of uncertain parameters are given in Table 4.12. In this work, arc efficiency, arc radius, thermal conductivity and viscosity are considered as uncertain model input parameters. The optimization method starts with randomly generated initial population and each individual consists of four values of uncertain

parameters. The feasible range and optimum values of uncertain parameters are described in Table 5.5. The optimum values attained, of arc efficiency, arc radius, thermal conductivity and viscosity are 0.63, 1.83 mm, 225.2 W m^{-1} $K^{-1}$and 0.07 kg m^{-1} s^{-1} respectively. Using these optimum values, a transport phenomenon based heat transfer and fluid flow analysis is performed to examine the influence of surface active elements. The results obtained from integrated numerical model are validated with experimental data given in Table 4.12.

Numerical simulation of heat transfer and fluid flow is performed on plate dimensions of 30 mm X 15 mm X 5 mm. To gain in computational time, the solution geometry is shorter than the actual work piece dimensions. However, the model has been calibrated accordingly. Figure 5.46 depicts the special distribution of temperature and velocity field in quasi-steady state condition at 20 L/min gas flow rate and 243 ppm oxygen concentration in weld.

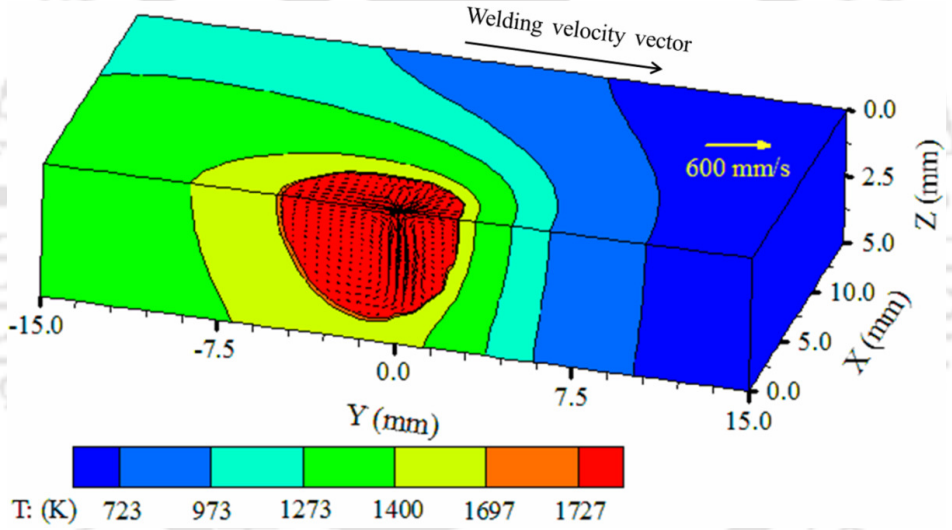

Figure 5.46: Three dimensional temperature and velocity distribution in weld pool at gas flow rate 20 L/min and oxygen concentration in shielding gas 4000 ppm.

The quasi-steady state resembles the fact that the moving welding torch is stopped at the middle of work-piece. Two anti-clockwise circulation loops are observed on the symmetric plane and the liquid metal flows from outward periphery to the weld centre. The oxygen concentration in weld (~ 243 ppm) is relatively high and produces positive temperature coefficient of surface tension that favours high weld penetration and low weld width. The flow reversals occurred at low oxygen concentration owing to negative surface tension coefficient. It is thus obvious from analogy that high penetration weld joint is possible even in gas tungsten arc welding process. The computed weld dimensions are measured by isotherm above solidus temperature (~ 1697 K) and the mushy zone is defined by isotherm of

solidus and liquidus temperature (~ 1727 K). The weld dimensions are measured on cross-section along X-Z plane and the molten zone is defined corresponding to solidus isotherm of 1697 K for stainless steel. The intercepts along X-axis and Z-axis by molten zone are calculated as half-width (W^c) and penetration (D^c), respectively. The comparison between computed weld zone and experimentally measured weld macrograph at similar welding conditions for two different welding conditions (gas flow rate = 10 L/min and oxygen concentration = 4000 ppm and gas flow rate = 20 L/min and oxygen concentration = 3000 ppm) are illustrated in Fig. 5.47.

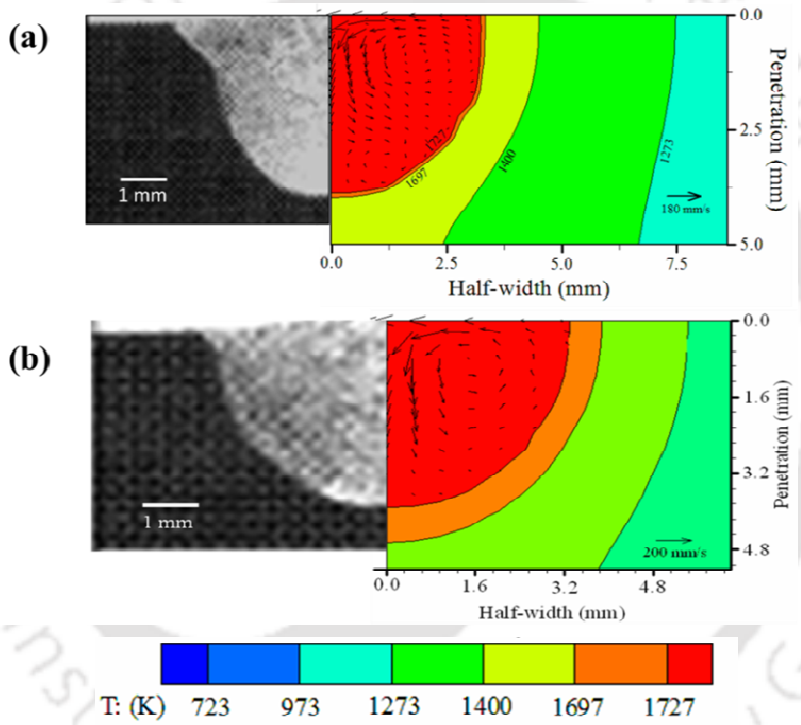

Figure 5.47: Comparison between numerically obtained macrograph (right) and experimentally measured macrograph (left), (a) at gas flow rate 10 L/min and oxygen concentration 4000 ppm and (b) at gas flow rate 20 L/min and oxygen concentration of 3000 ppm.

The anticlockwise circulation loop favours high penetration with low width owing to positive surface tension coefficient. The convective motion of liquid metal is mainly driven by surface tension force whereas the electromagnetic and buoyancy forces influence to a lesser extent. The complex nature of resultant driving force also produce a small clockwise circulation loop observed in Fig. 5.47 and this nature of flow try to widen the weld pool at the bottom of weld joint. However, the influence of this loop is weaker as compared to overall

anticlockwise circulation loop. To validate the fluid flow model, an order of magnitude analysis of the maximum velocity due to surface tension force is estimated as

$$U_{ST}^{3/2} \approx \left|\frac{\partial\gamma}{\partial T}\right|\left|\frac{dT}{dy}\right|_{y=W/4} \frac{W^{1/2}}{0.664\rho^{1/2}\mu^{1/2}} \tag{5.7}$$

where $\frac{dT}{dy}$ to the average temperature gradient on the top of weld pool at y = W/4, ρ and μ are density and viscosity of liquid material, respectively. The maximum velocity is estimated of the order of ~ 180 mm/s corresponding to welding condition depicted in Figure 5.47 (a). The magnitude is very closer to numerically calculated maximum velocity. The relative importance of heat transport by conduction and convection within the weld pool is well prescribed by Peclet number. The estimated Peclet number is well above one for all welding conditions and indicates the importance of convective heat transport within weld pool. Relatively decent agreement between experimental and simulated results depicted in Figure 5.47 reflects the effectiveness of numerical model as a consequence of flow dynamics to capture the effect of surface active elements in weld pool modelling.

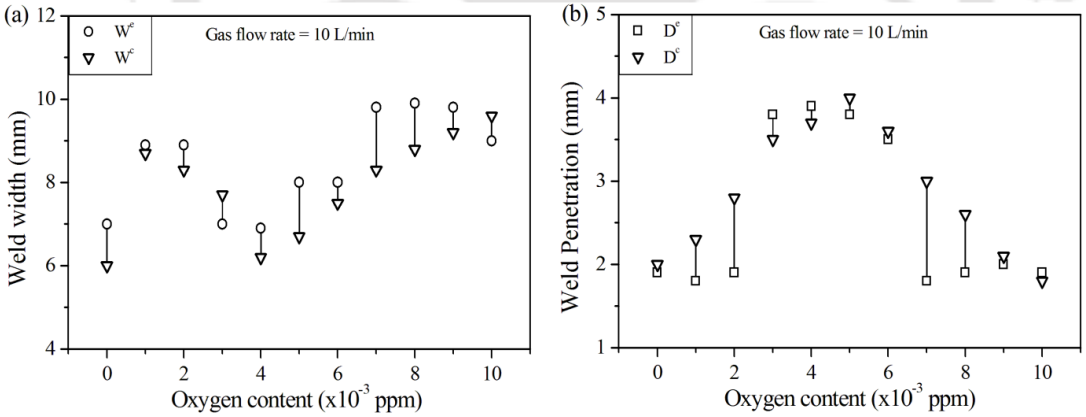

Figure 5.48: Comparison between experimentally measured and numerically calculated weld dimensions at gas flow rate 10 L/min for different oxygen concentration in shielding gas: (a) weld width, and (b) weld penetration.

However, high oxygen concentration with shielding gas produces a relatively thick layer of oxygen that restricts the movement of liquid metal. It seems that the surface free energy between the liquid molten pool and oxide layer reduces with increase of oxygen concentration. This phenomenon is simulated assuming weaker surface tension force i.e. in

aggregate positive surface tension force with low magnitude. It results in inward flow of liquid metal with wide weld pool shape.

Figures 5.48 and 5.49 describe the comparison between experimental and numerically computed weld width and penetration using optimum uncertain parameters depicted in Table 5.5 at the gas flow rate of 10 L/min and 20 L/min, respectively. Irrespective of the gas flow rate, it is clearly observed that the weld penetration increases with oxygen concentration in shielding gas up to a certain limit (~ 182 ppm and ~ 243 ppm oxygen in final weld, respectively for 10 L/min and 20 L/min gas flow rate). Afterwards the weld penetration decreases and diminishes the effect of extra oxygen addition since almost a constant level of oxygen (~ 210 – 250 ppm) in weld pool is maintained. This observation accomplishes the fact that large amount of oxygen concentration presents in weld may not always favour to obtain high penetration or aspect ratio. There exists an optimum quantity of surface active element that produces the maximum weld depth for a specific welding condition. Therefore, the numerical model can be exploited to take into the effect of oxygen presents in weld pool as well as thickness of oxide layer when excess amount of oxygen will be added through shielding gas. Figures 5.50 (a) and (b) depict the comparison between the experimental and numerically calculated ratio of weld penetration to weld width (D/W ratio) at gas flow rate of 10 L/min and 20 L/min, respectively.

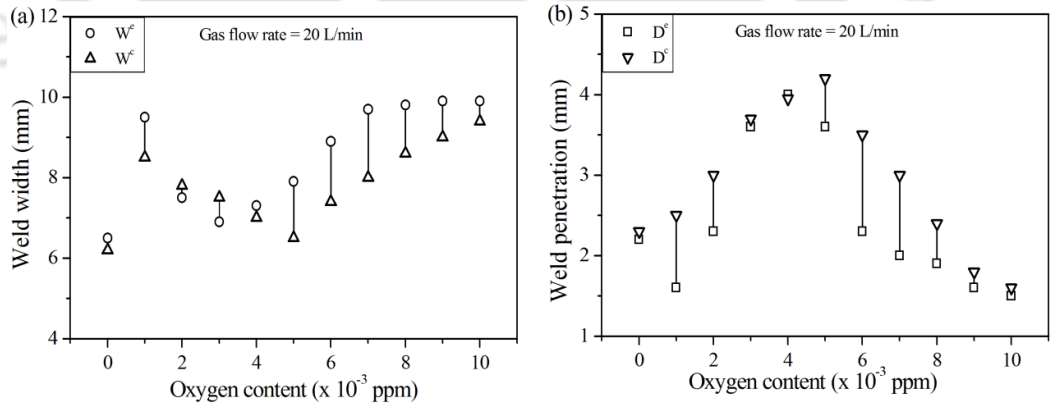

Figure 5.49: Comparison between experimentally measured and numerically calculated weld dimensions at gas flow rate 20 L/min for different oxygen concentration in shielding gas: (a) weld width, and (b) weld penetration.

It is observed that a definite range of oxygen content in the weld joint (130 ~ 250 ppm), a large D/W ratio (~ 0.5) is obtained both from experimental and numerically evaluated results. However, out of this range (oxygen content) the D/W ratio is less than 0.5. It is

noteworthy that the oxygen content in the weld and consequent D/W ratio are not sensitive to the shielding gas flow rate.

It is thus obvious from Figs 5.47-5.49 that there is discrepancy in few cases during comparison between calculated and experimental results (oxygen concentration $2x10^3$, $6x10^3$, $7x10^3$ ppm). There is abrupt change of weld dimensions as compared to nearest welding conditions which directly influence the surface tension model, i.e., the estimation of coefficient of surface tension.

To analyze the overall performance of the process, an error analysis has been executed on the comparative study of calculated and experimental results. The error analysis consists of individual component errors and relative reliability of the predicted solution sets. The non-dimensional predictable errors can be defined as

$$E_w = (1 - \frac{W^c}{W^e}); \quad E_d = (1 - \frac{D^c}{D^e}) \qquad (5.8 \text{ and } 5.9)$$

where 'c' and 'e' represent the numerically computed and experimentally measured values of weld width and penetration. Envisaging the fact that the computational error in either numerically calculated weld width or penetration is mutually exclusive and equally important for the reliability of the overall prediction, the individual reliabilities are connected to be in series, and the overall reliability R_s can be calculated as

$$R_s = (1 - |E_w|) \times (1 - |E_d|) \qquad (5.10)$$

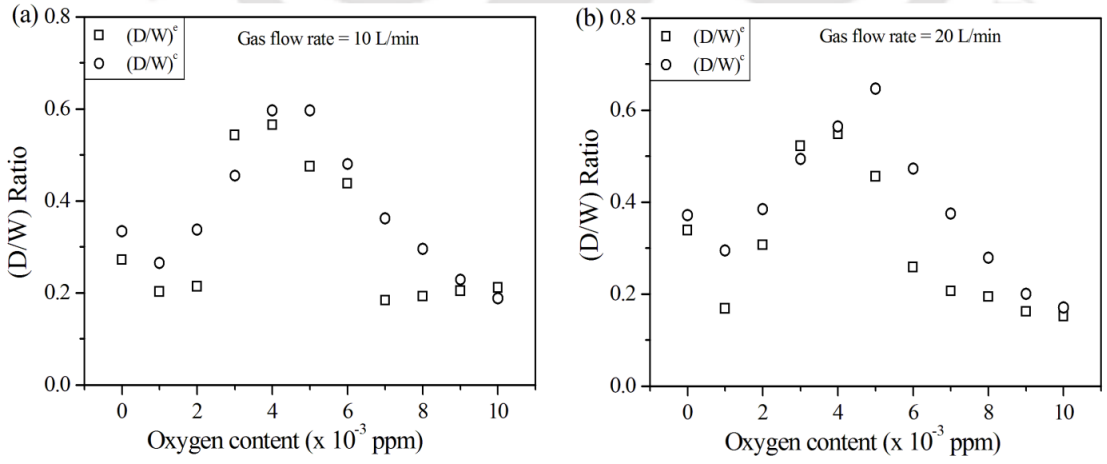

Figure 5.50: Comparison between experimentally measured and numerically calculated depth/width ratio for different oxygen concentration in shielding gas: (a) at gas flow rate 10 L/min, and (b) at gas flow rate 20 L/min.

Figures 5.51(a) and (b) depict the variation of the error components and overall reliability at the gas flow rate of 10 L/min and 20 L/min, respectively. At shielding gas flow rate of 10 L/min, the variation of error components is observed as $-0.1 \leq E_w \leq 0.163$ and $-0.667 \leq E_d \leq 0.079$. The maximum reliability is achieved 0.91 whereas the minimum value is 0.282 considering the optimum solution set depicted in Table 5.5. In similar way, Fig. 5.31(b) shows the ranges of the errors and the overall reliability as $-0.087 \leq E_w \leq 0.177$; $-0.562 \leq E_d \leq 0.0125$ and $0.391 \leq R_s \leq 0.94$. More than 50% data predict the reliability above 0.8 and it essentially strengthens the overall quantative prediction by present approach of integrated modeling and subsequent error analysis.

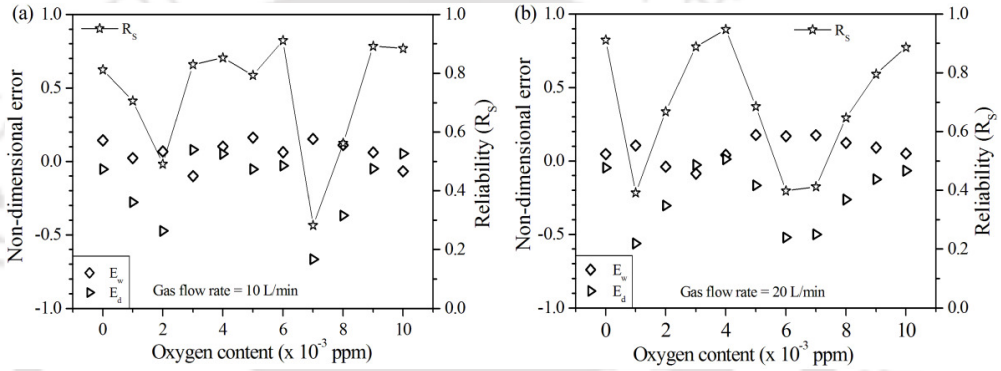

Figure 5.51: Evaluation of entity error and overall reliability for all solution sets: (a) at gas flow rate 10 L/min, and (b) at gas flow rate 20 L/min.

Based on obtained results in this section, it is concluded that the DE algorithm assisted heat transfer and fluid flow model has been successfully developed and is used in this work to estimate the effect of surface active elements e.g. oxygen on weld pool shape and size. Moreover, the error analysis along with reliability calculation of predicted results further elaborates the scope of process design.

5.6 Distortion and residual stress analysis

In the mechanical analysis, the similar finite element model for thermal analysis is employed. The only difference is the element type and boundary conditions. The element type used in mechanical analysis is SOLID 45 and is defined by eight nodes having three degrees of freedom at each node (translations in the nodal x, y, and z directions). The necessary boundary conditions are presented at an appropriate place for each case study with the help of schematic representation. The procedure followed for the mechanical analysis is presented in *chapter 3*.

5.6.1 Influence of heat source parameters

In order to estimate the influence of front and rear length ratio of double ellipsoidal heat source model, thermo-mechanical analysis was also performed and calculated welding induced residual stresses, distortions and strains. In the course of mechanical analysis, the same thermal analysis FE model has been used along with mechanical analysis boundary conditions. The displacement normal to the weld interface i.e. symmetric surface is zero and the weld specimen rigidly clamped on four corner points and hence all the displacement degrees of freedom are zero at these four points.

As the front and rear length ratio is not same for all velocities, the heat intensity on front and rear lengths also changes that directly impact on the thermal behaviour of the weld pool as well as mechanical behaviour of surrounding welded zone. Figures 5.52 to 5.54 illustrate the mechanical behaviour when heat source is at the middle of work-piece and subsequently solidified to ambient temperature. The residual stress, strain, and displacement are derived along thickness and width of plate for the ratio a_r/a_f of 2:1 and 6:1, respectively corresponding to the welding condition of data set #3 in Table 4.10. It is noteworthy that the influence of cooling rate on mechanical properties of substrate material is not considered in present analysis.

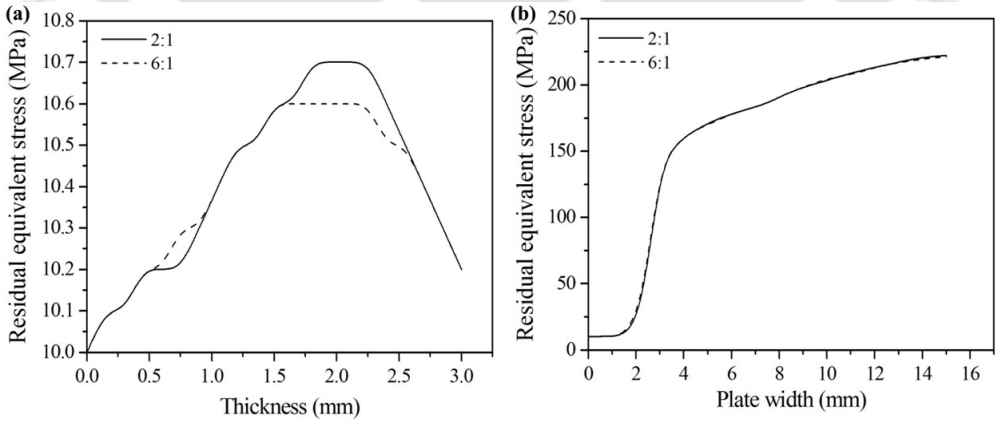

Figure 5.52: Distribution of residual stress for data set #3 (in Table 4.10) corresponding to (a_r/a_f)ratios of 2:1 and 6:1, respectively.

Figure 5.52 (a) depicts the calculated values of the residual equivalent stresses along thickness direction. The maximum value of the residual stress is obtained as 10.7 MPa that is reasonable significant with respect to flow stress of the material. There is also significant variation of the magnitude of residual equivalent stress (maximum ~ 0.1 MPa i.e. 1 %) at two

different front and rear length ration of heat source model. However, at width direction the change of residual stress level is more significant that is at the maximum 5 MPa i.e. 15 %.

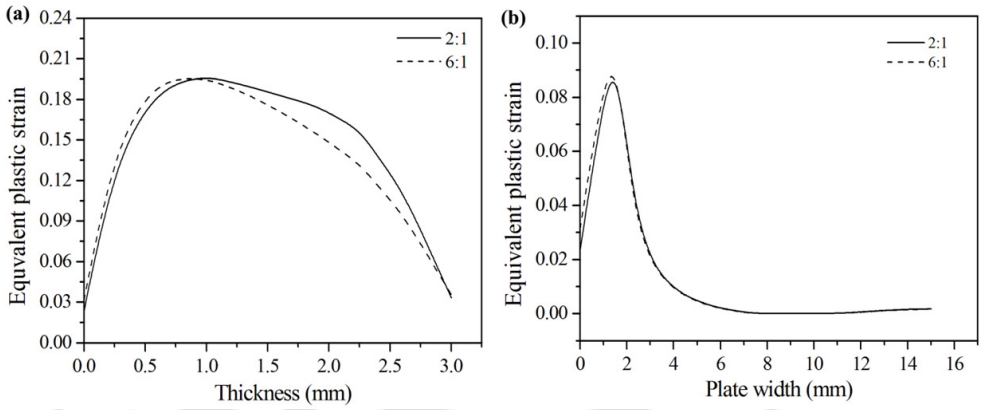

Figure 5.53: Distribution equivalent plastic strain for data set #3 (in Table 4.10) corresponding to (a_r/a_f)ratios of 2:1 and 6:1, respectively.

Figure 5.53 depicts the calculated values of the equivalent plastic strain along the thickness and width direction of work-piece, respectively. It is obvious from Fig. 5.53 (a) that at the ratio of 2:1, the magnitude of the equivalent plastic strain is more as compared to the ratio of 6:1. There exists a maximum deviation of equivalent plastic strain of 0.025 i.e. maximum 19 % variation is observed when there is change of a_r/a_f ratio from 2:1 to 6:1. However, for both the ratios the magnitude of the plastic equivalent strain varies with the same pattern.

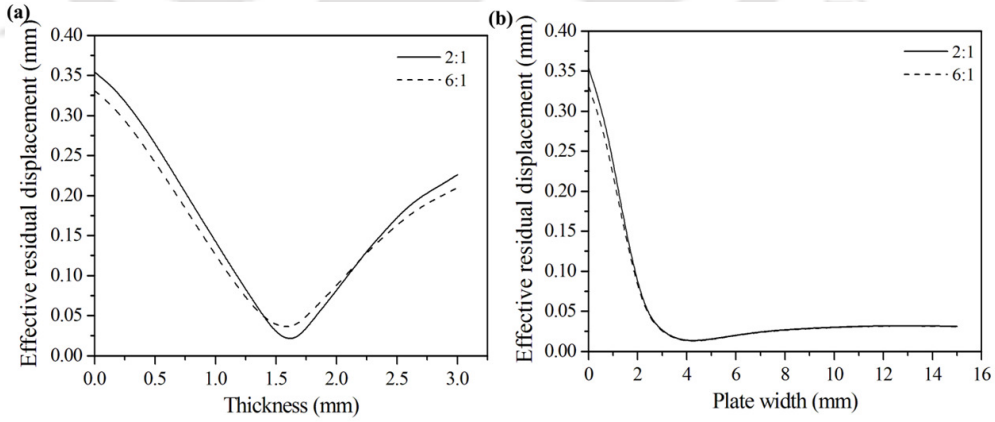

Figure 5.54: Effective residual displacement for data set #3 (in Table 4.10) corresponding to (a_r/a_f)ratios are of 2:1 and 6:1, respectively.

Similarly, Fig. 5.53 (b) depicts the equivalent plastic strain in the direction of the width from the centre of the heat source and it is obvious that there is variation of the plastic strain in the order of ~0.007 i.e. 7 %.

Figure 5.54 describes the effective residual displacement that refers to the vector sum of the computed displacements in all three normal directions. The maximum value of effective residual displacement at the centre of heat source is 0.35 mm and gradually reduces to 0.025 mm at the border of weld pool. Again it increases to 0.22 mm within heat affected zone. The magnitude of the effective residual displacement is more at a_r/a_f ratio 2:1 as compared to the ratio 6:1. Figure 5.54 (b) depicts that the computed effective residual displacement along the width of plate that is maximum at the centre and gradually decreases away from the centre. However, the maximum difference of displacement magnitude is ~0.024 mm along depth direction whereas it is ~0.020 mm along width direction. Overall, it is observed that the variation of properties is more significant along thickness direction as compared to the width of plate. This may be attributed by the fact the heat transfer is more turbulent along thickness direction whereas due to large in dimension along weld width, the change of temperature distribution is less vibrant. This temperature distribution directly affects the mechanical analysis.

5.6.2 Butt joint in laser welding

5.6.2.1 Butt joint in fiber laser welding of SS 304

In order to estimate the welding induced distortions and residual stresses, a thermo-mechanical analysis has been performed. However, in this work, the full geometry is considered for simulations. Figure 5.55 is a schematic representation of the solution domain along with mechanical boundary conditions. The point A in Fig. 5.55 is constrained in the X, Y and Z directions, and point B is constrained only in the Z-direction. ‘A’ and ‘B’ are the start and end points of the weld centerline of the FE model, respectively. The mechanical analysis is performed by using the nodal temperature results presented in thermal analysis (section 5.4.2.4 5). However, the same FE model and mesh used in thermal analysis is employed here.

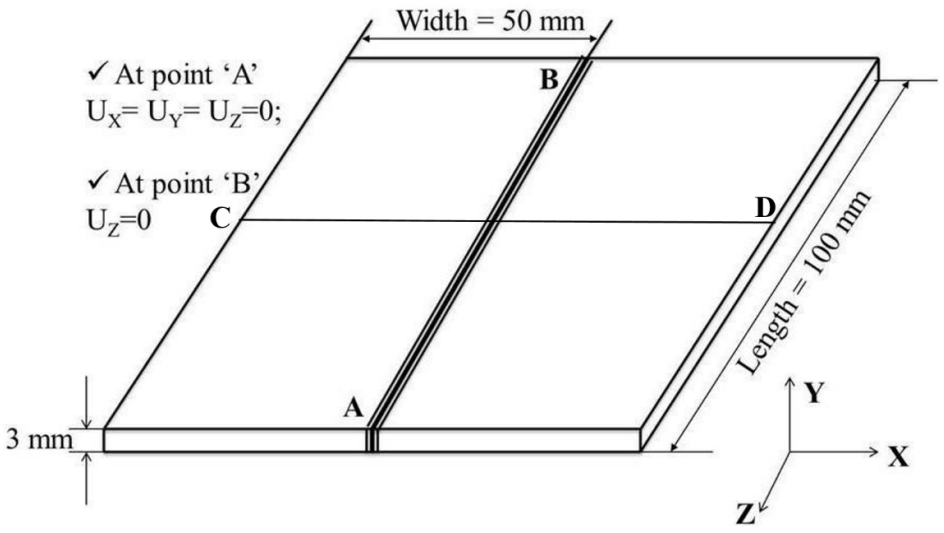

Figure 5.55: Solution domain along with mechanical boundary conditions.

Figure 5.56 represents the three dimensional computed longitudinal residual stress distribution (SY) corresponding to welding speed of 0.667 m/min. of data set 1 given in Table 4.7. It is observed that SY is tensile in FZ and HAZ, and this is more as compared to yield strength of the parent material 304 stainless steel at room temperature. However, there is also compression stress on the weld metal plate away from the weld center line. Moreover, the computed maximum tensile stress is 420 MPa at FZ and the minimum compressive stress is 210 MPa at away from the weld center line.

Figure 5.57 compares the bottom and top surface longitudinal residual stresses (SX) distribution along welding line AB (defined in Fig. 5.55). To elucidate the difference between the top and bottom surface residual stresses, the simulated results of bottom surface along welding line is also plotted in this figure. From this figure, it can be seen that the value of longitudinal residual stress of both top and bottom surface within the range approximately from Y= 20 mm to Y= 85 mm is almost constant, however, the small variation is observed with up and down. Moreover, the bottom and top surface longitudinal residual stresses are not same. Near the weld end-start location the magnitudes are compressive. Furthermore, the top surface residual stress (SX) is more as compared to the residual stresses obtained from bottom surface stresses. Similarly, Fig. 5.58 describes the comparison of bottom and top surface residual stresses (SY) along welding line AB. The similar trend can be observed in both the cases for bottom and too surface stresses. However, in case of SY along welding line, the bottom surface stresses are almost constant from Y=18 mm to Y= 85 mm. Nevertheless, for this range the stresses are varying in case of top surface distribution.

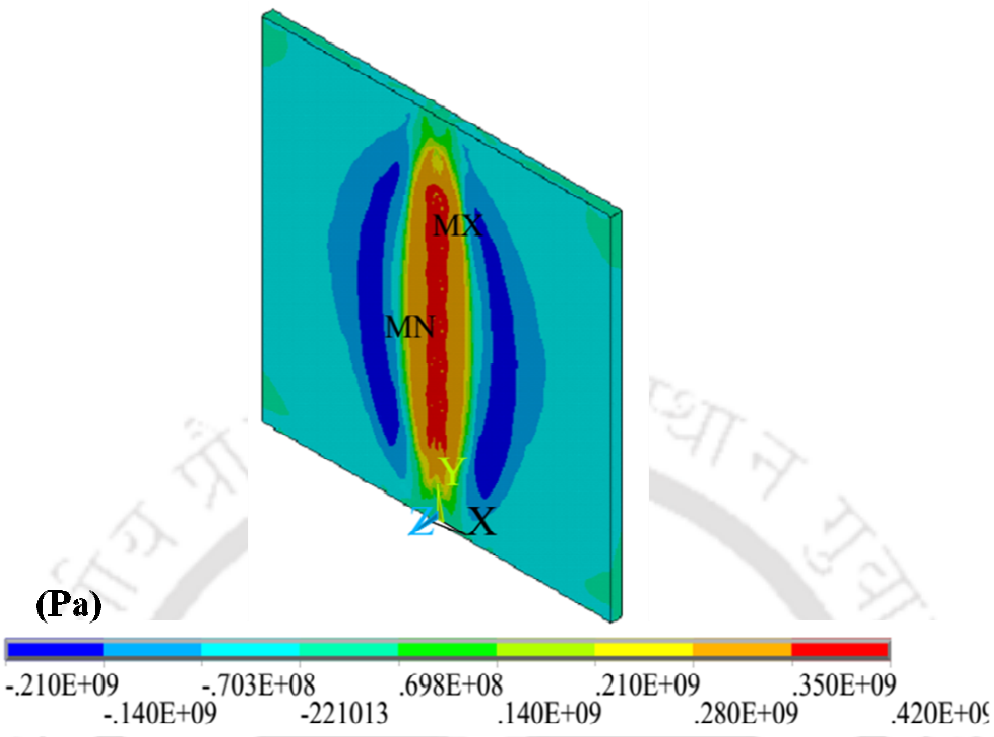

Figure 5.56: Three dimensional longitudinal residual stress distribution (SY) of data set #1 given in Table 4.7.

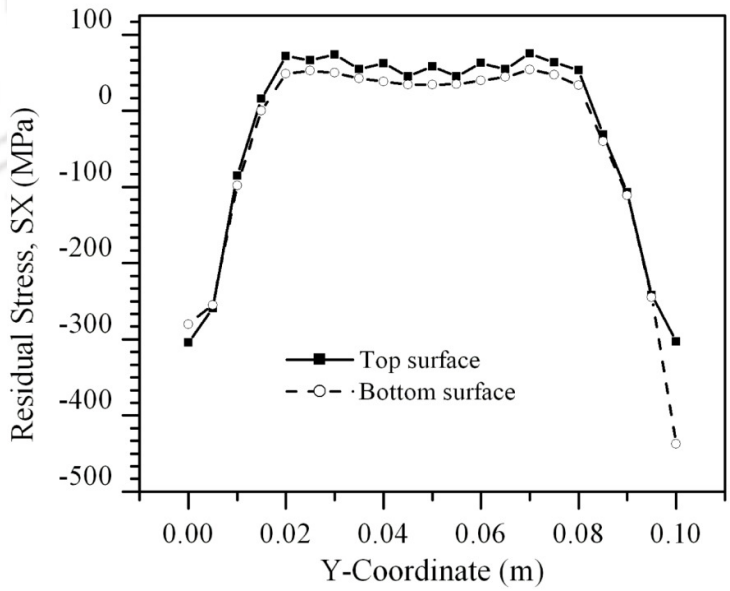

Figure 5.57: Comparison of top and bottom surface longitudinal residual stress (SX) along welding line.

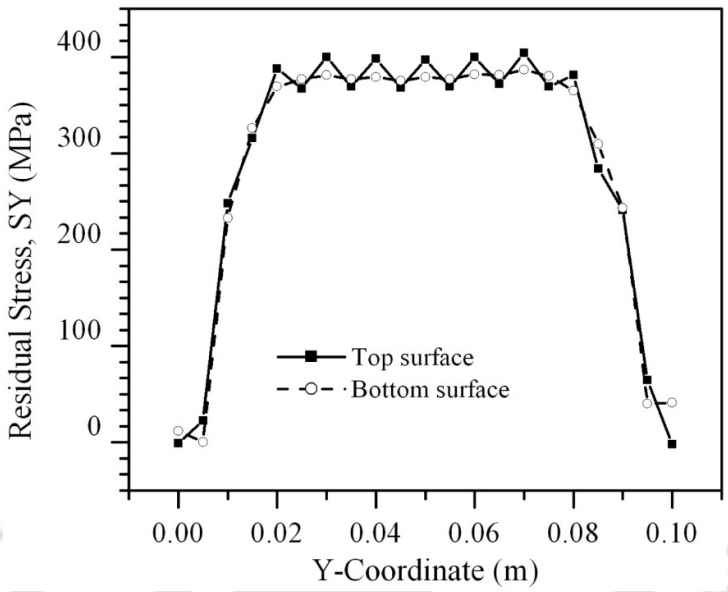

Figure 5.58: Transverse residual stress (SY) comparison along welding line of bottom and top surfaces.

Figures 5.59, 5.60 and 5.61 illustrate the residual stresses, SX, SY and SZ of both on top and bottom surfaces respectively. The magnitude and distribution of transverse and longitudinal residual stresses show a significant difference. However, the distribution pattern of residual stresses for bottom and top surfaces is same and the magnitude of them is not equal. The numerically predicted maximum transverse residual stresses along mid-section CD for top and bottom surface are 397 MPa and 379 MPa respectively. This variation in the residual stresses between top and bottom surfaces is due to the difference in temperature gradient. Moreover, SX along mid-section CD gradually increases from X= 0 to X= 40 mm and them decreases up to X = 45 mm. the longitudinal residual stress (SY) along mid-section CD is more significant and maximum is achieved at X = 50 mm. The bottom and top surface residual stresses distributions along CD (SY) follow same pattern, however, the magnitudes are not same. Similarly, the SZ bottom and top surface distribution along mid-section CD can be seen in Fig. 5.61.

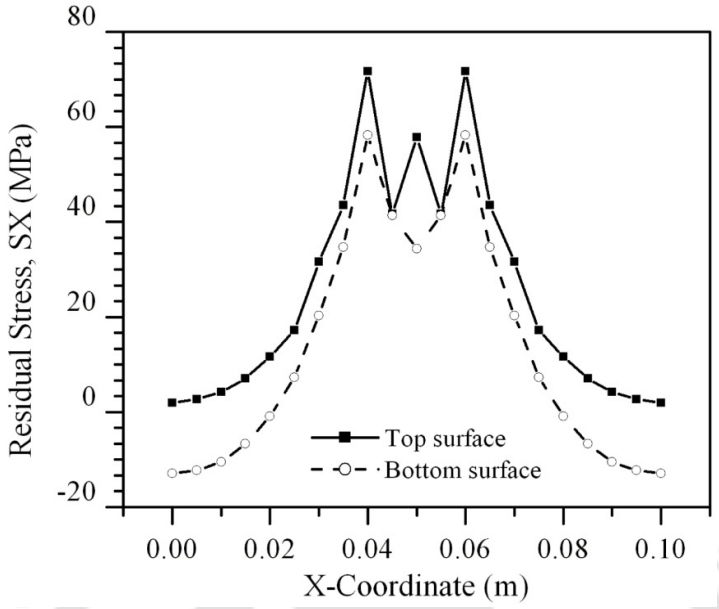

Figure 5.59: Comparison of top and bottom surface longitudinal residual stress (SX) along mid-section CD.

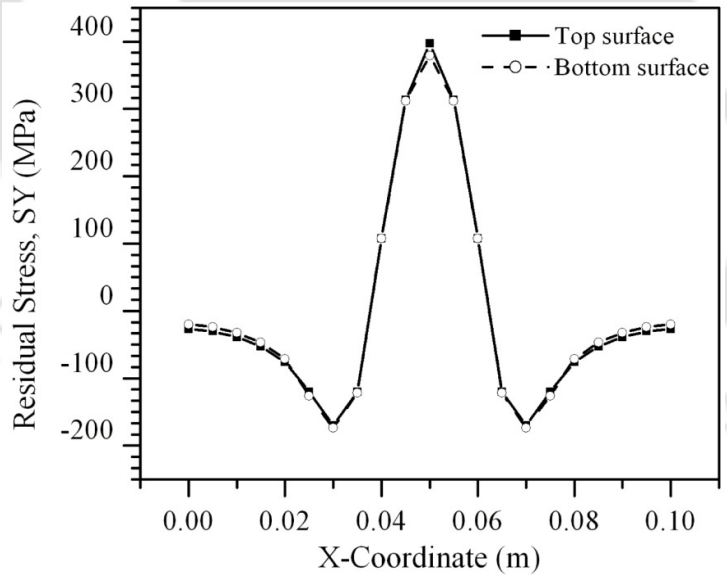

Figure 5.60: Top and bottom surface transverse residual (SY) comparison along mid-section CD.

Due to a relatively large out-of-deformation generated after welding, there is a difference between the longitudinal stress (SX) of the top surface and that of the bottom surface. On the contrary, there is almost no difference between the longitudinal stress of the top surface and that of the bottom surface in case of SY. There is also a significant difference

between the transverse residual stresses (SZ) of the top surface and that of the bottom surface. It is very clear that in the fusion zone and the HAZ the transverse residual stress of the top surface is much larger than that of the bottom surface. The difference results from the transverse bending deformation.

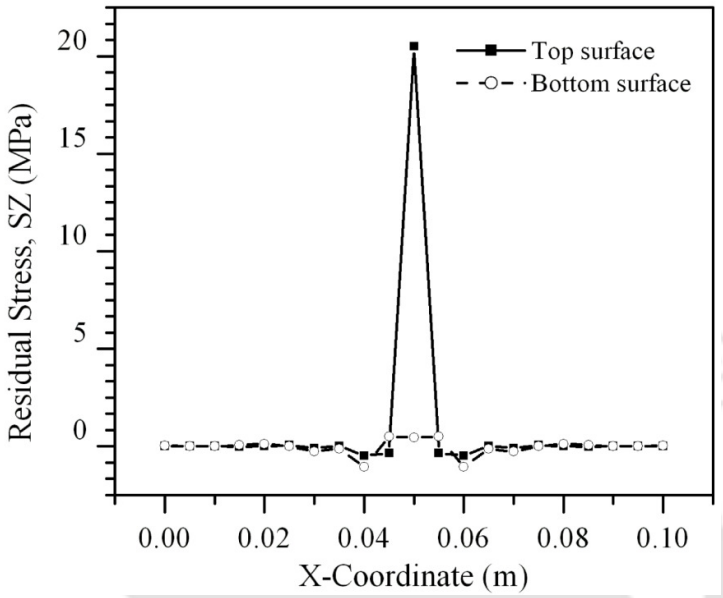

Figure 5.61: Comparison of top and bottom surface residual stress (SZ) along mid-section CD.

Figures 5.62 and 5.63 illustrates the comparison of bottom and top surface Von Mises and plastic equivalent stress distributions along mid-section CD. The numerically computed maximum Von Mises and plastic equivalent stresses values along mid-section CD is same, 360 MPa. However, the Von Mises stress is minimum at the weld start and increases gradually from X = 0 to X = 30 mm and then decreases up to X= 40 mm. Then, the stress rapidly increases from X= 40 mm to X = 50 mm and reaches to maximum of 306 MPa. Similarly, in case of plastic equivalent stress along mid-section CD the value gradually increases from X = 0 to X = 40 mm and then suddenly increases up to X = 50 mm (this can be seen from Fig. 5.63). However, the magnitudes of top and bottom surface stresses are not same.

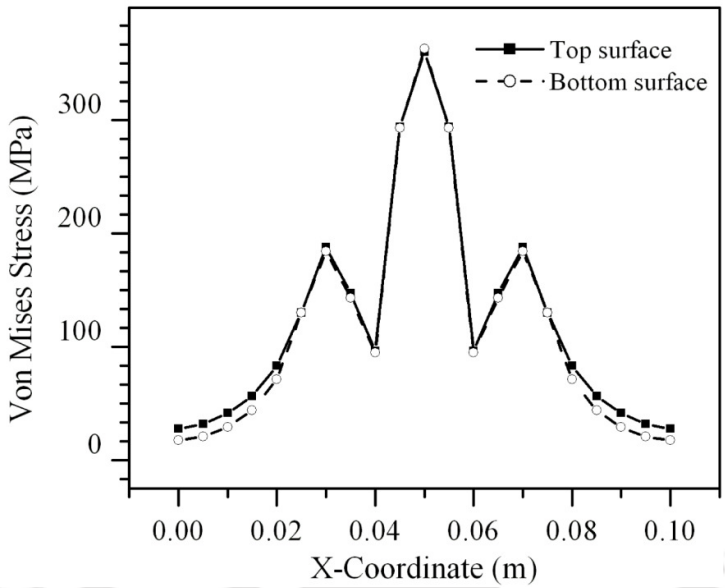

Figure 5.62: Von Mises Stress distribution of top and bottom surface along mid-section CD.

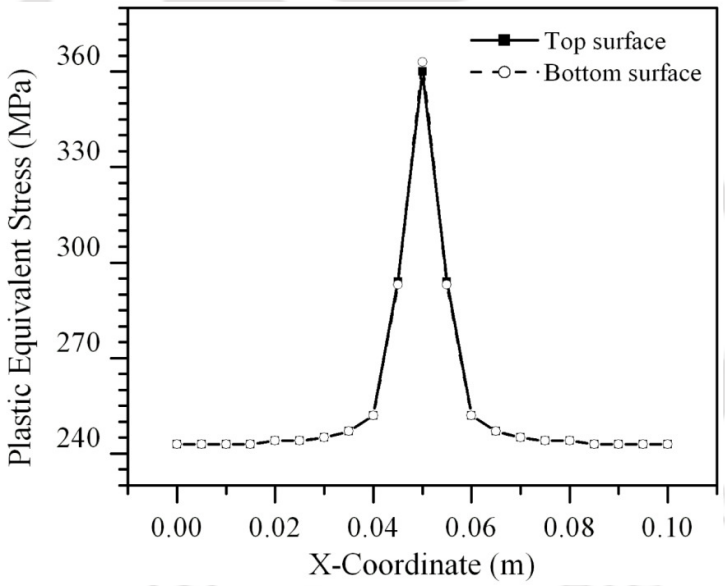

Figure 5.63: Comparison of top and bottom surface plastic equivalent stresses along mid-section CD.

Figures 5.64 and 5.65 illustrates the Y-component of displacement and displacement vector sum along welding line AB respectively. The maximum and minimum displacement vector sums are 1.05 mm and 0.00 mm at welding start and end locations along welding line AB. However, the Z-component of displacement is randomly changing from weld start to end along welding line AB.

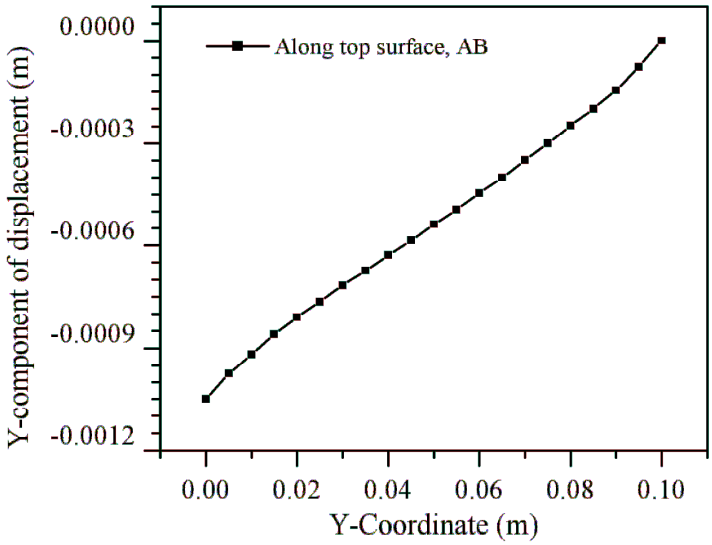

Figure 5.64: Y-component of displacement (UY) along welding line AB.

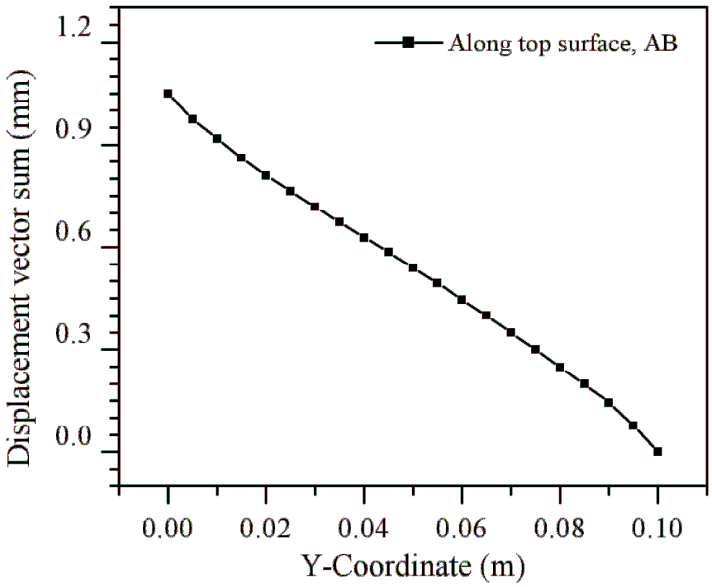

Figure 5.65: Displacement vector sum (USUM) along welding line AB.

Figures 5.66 to 5.69 describe the various components of displacements and displacement vector sum along mid-section CD. Figure 5.66 shows the comparison of X-directional displacement distribution of the middle section. Comparing the transverse shrinkage of the bottom surface with that of the top surface, it can be observed that the former is smaller than the latter. However, the difference is very small.

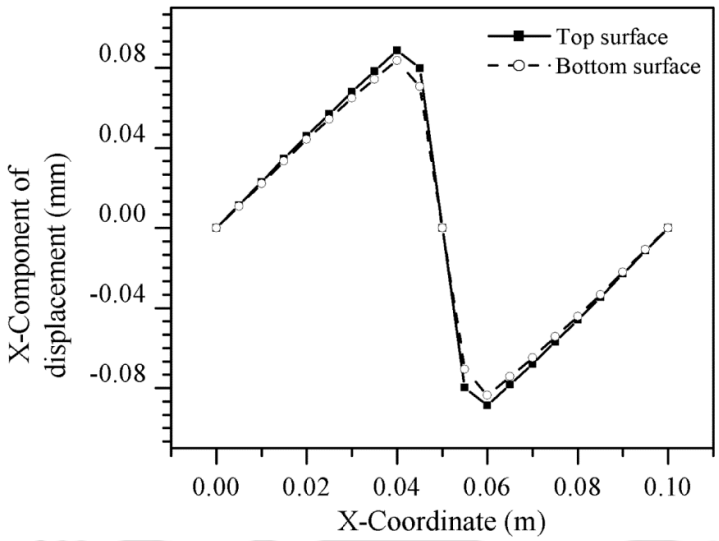

Figure 5.66: X-component of displacement (UX) along mid-section CD.

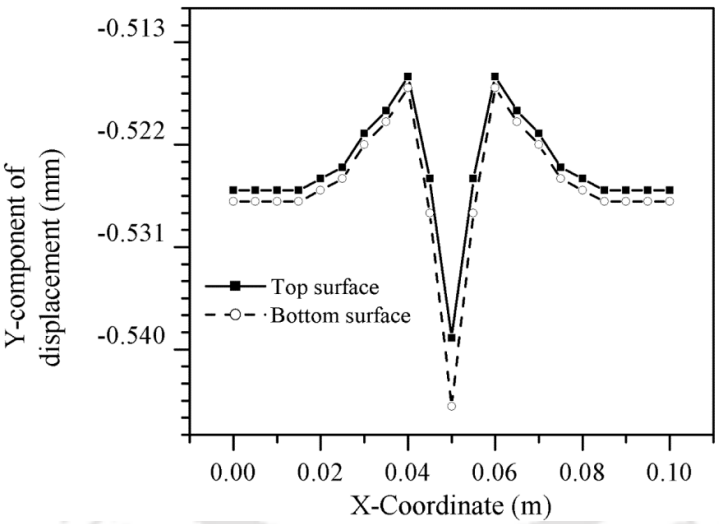

Figure 5.67: Y-component of displacement (UY) along mid-section CD.

Figure 5.67 shows the Y-directional displacement distribution of the middle section of both top and bottom surfaces. This figure indicates that the UY is almost same for both top and bottom surfaces. However, the Z-component of displacement along mid-section CD is not same for top, middle and bottom surfaces as shown in Fig. 5.68. Figure 5.69 describes the displacement vector sum along mid-section CD of bottom and top surfaces. However, the bottom surface welding induced distortion is more as compared to that of top surface distortion.

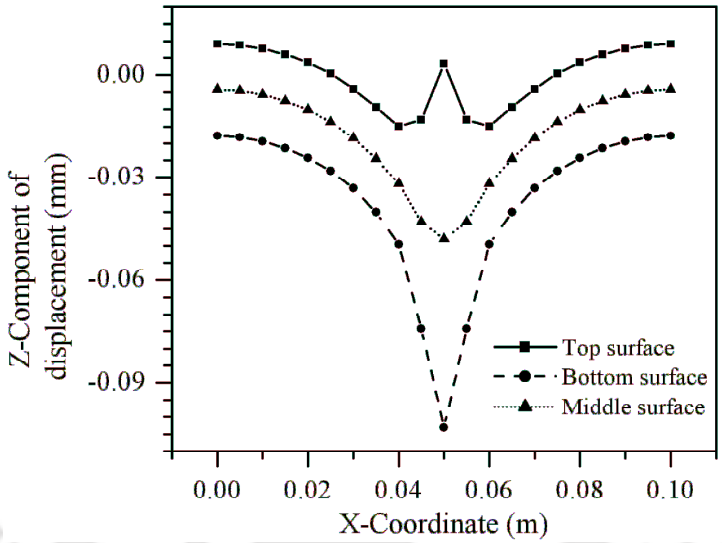

Figure 5.68: Z-component of displacement (UZ) along mid-section CD.

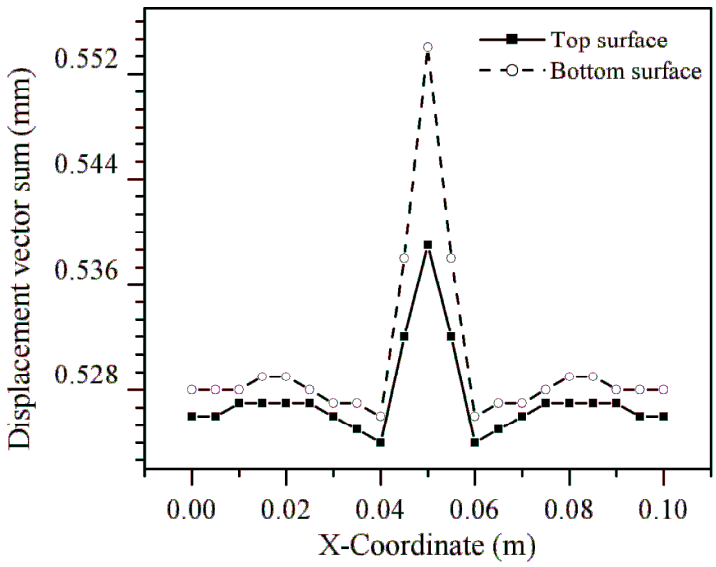

Figure 5.69: Displacement vector sum (USUM) along mid-section CD.

Figure 5.70 shows the longitudinal, transverse, von Mises and equivalent plastic strain distributions of the middle section corresponding to data set 2 given in Table 4.7. Based on these calculated results (Fig. 5.70), it has been observed that the transverse and longitudinal plastic strains are negative and spread narrowly over the fusion zone and its surrounding area. However, the von Mises and equivalent plastic strains are positive and having maximum values of 0.0185 and 0.0329 respectively.

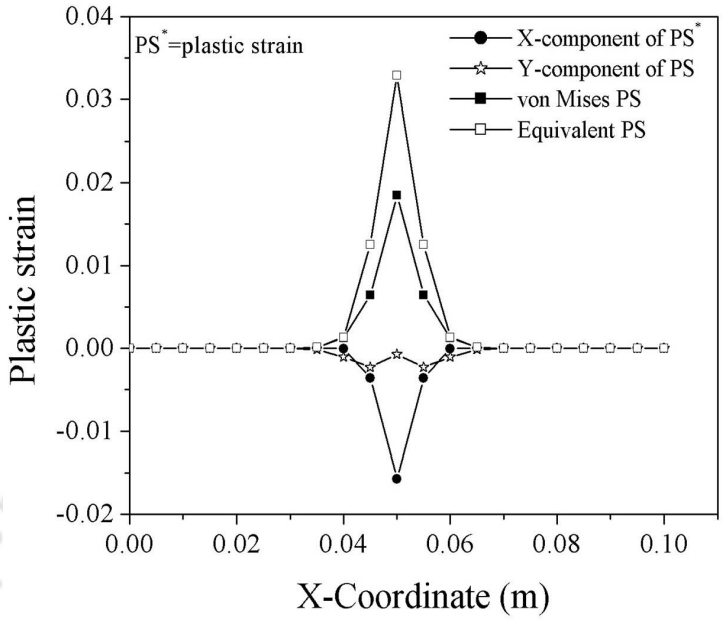

Figure 5.70: Plastic strain distribution of the middle section corresponding to data set #2 given in Table 4.7.

Furthermore, the welding deflections are calculated and compared with the measured value for similar process variables. For instant, the maximum measured and computed welding deflections at both ends of the plate corresponding to data set 2 given in Table 4.7 are 1.656 mm and 1.53 mm, respectively. The percentage error in calculation of welding deflection is within the acceptable limit (< 8 %).

5.6.2.2 Laser Butt joint on DH 36 steel

The mechanical analysis is performed of laser butt joint on DH 36 steel plates. The three dimensional distribution of equivalent residual strain for autogeneous laser is depicted by figures 5.71 and 5.72. The maximum magnitude of residual strain is ~ 0.03 when heat source is at the middle of work piece (Fig. 5.71) and is ~ 0.15 when heat source reaches at the end of work-piece (Fig. 5.72). Similarly, figures 5.73 and 5.74 indicates the maximum distortion for autogeneous laser welding is ~ 0.09 mm when laser travels at the middle of work-piece (Fig 5.73) and is ~ 0.3 mm when laser reaches the end of work-piece (Fig. 5.74). It is noteworthy that the distortion spans over a narrow zone in autogeneous laser welding process.

The numerical simulation of autogeneous laser welding process has been performed to determine longitudinal residual stresses. Figure 5.75 depicts the longitudinal residual stress level on the top surface of work-piece for autogeneous laser.

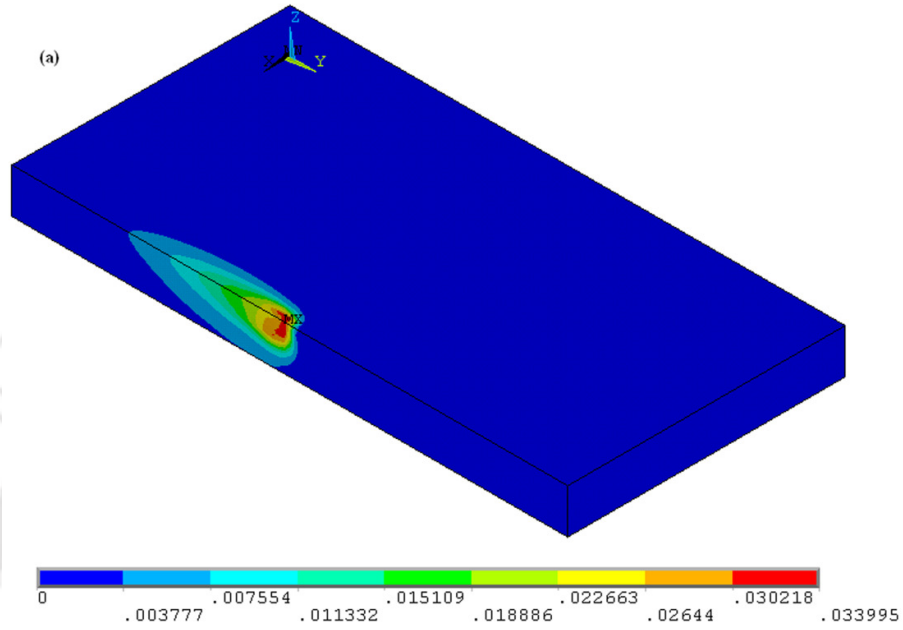

Figure 5.71: Three dimensional numerical simulation of residual equivalent strain of autogeneous laser welding: (a) the welding torch is stopped at middle.

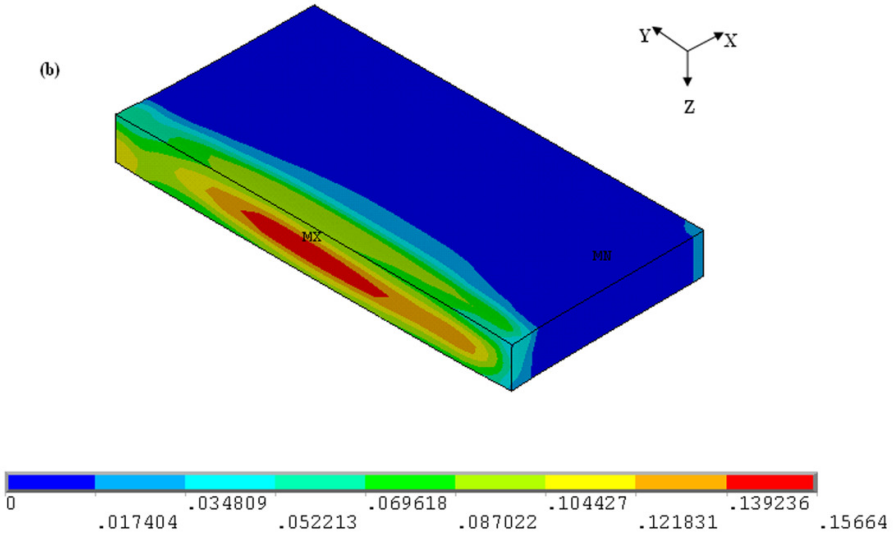

Figure 5.72: Three dimensional numerical simulation of residual equivalent strain of autogeneous laser welding: (b) the welding torch cover whole work-piece.

The residual stress magnitude is nearly equal to the yield stress of the material. The range of stress is narrow for the autogenous laser process and broader for the remaining welding processes.

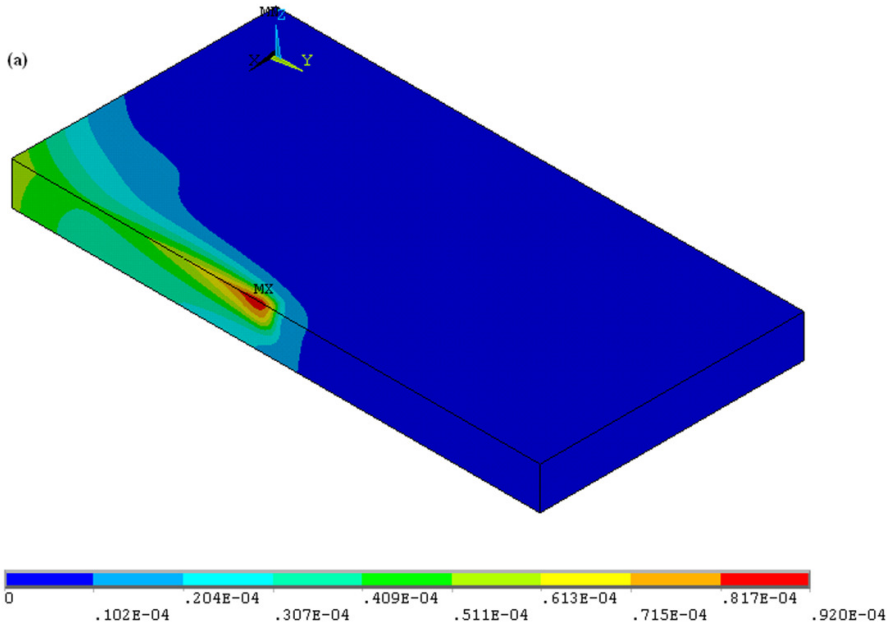

Figure 5.73: Three dimensional numerical simulation of residual equivalent displacement of autogeneous laser welding: (a) the welding torch is stopped at middle.

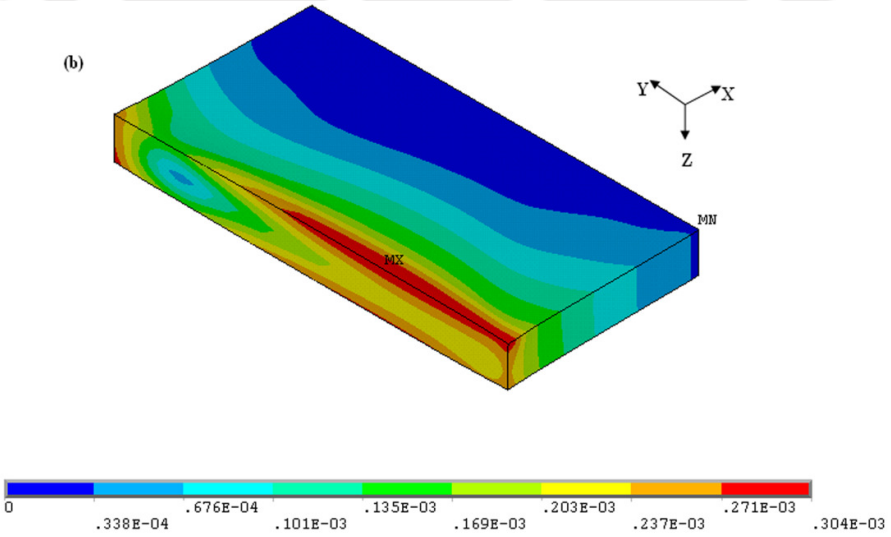

Figure 5.74: Three dimensional numerical simulation of residual equivalent displacement of autogeneous laser welding: (b) the welding torch cover whole work-piece.

Both width as well as the magnitude of the tensile stress regime for laser welding processes is in good agreement with experimental results.

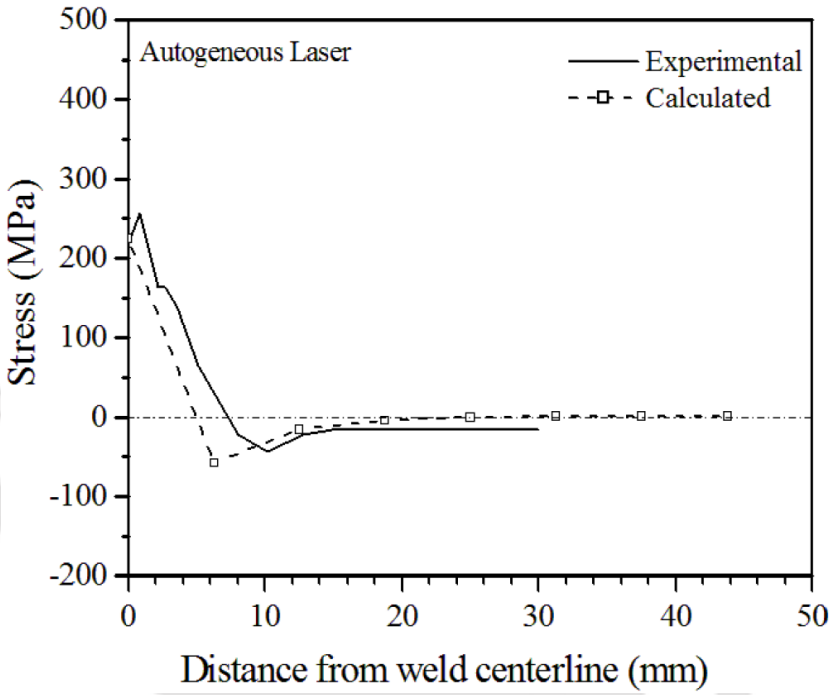

Figure 5.75: Comparison between experimental and numerically calculated longitudinal residual stress for autogeneous laser welding process.

The simulated results in present case is improved and possibly better as compared to numerical results depicted in reference [228]. This is due to the fact that the thermal model in present case is more phenomenological and possibly better due to implementation of adaptive volumetric heat source. In the welded zone a high tensile stress is generated, and then decreases to zero, finally becoming compressive away from the welded zone. Due to the self-equilibrium of the weldment, the tensile and compressive residual stresses exist at the welded region and away from the welded zone, respectively.

Since direct measurement of weld thermal cycle, and resulting thermal distortion and residual stresses are expensive for fusion welding processes, the demand of reliable quantitative heat transfer models and coupled thermo-mechanical analysis for fusion welding process is ever increasing. The present work is a contribution in this direction. Further validation of the calculated results of weld pool dimensions and associated thermal distortion for different welding conditions are necessary to reliably establish the process model reported in this work.

5.7 Summary

The present chapter demonstrates the performance of integrated modeling approach in which a GA based optimization algorithm is integrated with numerical model to find out the uncertain or unknown model parameters. At first, the conduction heat transfer analysis has been performed and integrated this process model with optimization module to estimate the front and rear length ratio (a_r/a_f) of double-ellipsoidal heat source model. The sensitivity analysis indicates that the weld dimensions decrease with increase in the a_r/a_f ratio almost in linear way. However, the depth of penetration is more sensitive to the change of ratio as compared to weld width. The a_r/a_f ratio of double-ellipsoidal heat source model is represented as a third order polynomial function of weld velocity. The coefficients of this polynomial function are estimated by integrated modeling approach using PCX-G3 GA model.

A new volumetric heat source model called as egg-configuration heat source is developed for the simulation of temperature in autogenous fusion welding process. The proposed heat source model is presented in generalized form and several other existing heat source models are special cases of developed model. This heat source model is having less number of model parameters without violating the non-symmetry heat intensity for linear fusion welding processes. The egg-configuration heat source model is calibrated with two distinct fusion welding processes i.e GTA and laser welding processes. Using this heat source, the maximum percentage error between experimentally measured and calculated weld bead dimensions is predicted as less than 7%. The magnitude of the maximum cooling rate for GTA welding is 603 K/s whereas it is 11.1 x 10^3 K/s for laser welding process.

The conduction heat transfer model has been developed for simulation of fiber laser welding process of two different grades of stainless steel at two different ambient atmospheres. The heat transfer analysis was performed using double ellipsoidal heat source model for welding in open atmosphere and using conical heat source model for welding in controlled atmosphere of argon. The percentage error between the experimentally measured weld pool dimensions and corresponding calculated results are below 8 %. The magnitude of the maximum cooling rate for open atmosphere welding process is 305×10^3 K/s and whereas it is 354×10^3 K/s for controlled atmospheric condition. However, few experimental conditions produce keyhole formation in fiber laser welding process. Hence, a semi-analytical approach based on point-by-point energy balance is considered to estimate keyhole profile in deep penetration fiber laser welding process.

To investigate the influence of surface active elements on GTA weld pool formation, a transport phenomenon based heat transfer and fluid flow analysis was performed. The uncertain model parameters are evaluated by integrated modeling approach using DE module. The uncertain parameters for GTA welding is estimated as arc efficiency of 0.63, arc radius of 1.82 mm, effective thermal conductivity of 225.2 W m^{-1} K^{-1} and viscosity of 0.07 kg m^{-1} s^{-1} for the welding conditions considered in the present work. It is concluded that a definite range of oxygen content in the weld joint (130 ~ 250 ppm), a large depth by width ratio (~ 0.5) is obtained both from experimental and numerically evaluated results. More than 50% data predict the reliability above 0.8 and it essentially strengthens the overall quantative prediction by present approach of integrated modeling and subsequent error analysis.

Finally, in the course of estimating welding induced distortions and residual stresses, a thermo-mechanical analysis was performed using sequentially coupled thermal data (nodal temperature) along with mechanical boundary conditions. The residual stress magnitude is nearly equal to the yield stress of the material. The numerical process model possibly avoids many repetitious experiments.

Chapter – 6

Conclusions and Future Scope

6.0 Introduction

One of the desirable objectives of fusion welding process is to produce deep penetration to enhance butt weld joint efficiency. The fiber laser generally produces high depth of penetration as compared to other type of lasers with proper choice of process parameters. Moreover, presence of argon atmosphere in fiber laser welding process enhances the depth of penetration as compared to open atmospheric condition. GTA welding is not as much efficient like laser welding process to produce high depth of penetration. However, the addition of surface active elements to the material during GTA welding process can be used beneficially to enhance the penetration depth of welding. Present investigation was motivated in that direction and the intuitive processes like GTA and fiber laser welding are analyzed through

physical modeling and experimental verification of the same with the aim of generating high depth of penetration.

The phenomenological modeling of a fusion welding process is a complex phenomenon that involves a lot of interactive physical phenomena. It is apparent from the literature that the modeling of the heat source is an important issue in computation of the temperature distribution. The most commonly used heat source model is double-ellipsoidal volumetric heat source that are used for moving arc or laser beam welding process. Even though several other heat source models are available in literature, they are commonly lacking of well-defined heat source parameters. There is a trend of estimating the heat source parameters and/or other model input parameters by inverse approach. To calculate the unknown parameters, the optimization algorithm with the aid of mathematical model has been used in several cases. It has been envisaged that temperature distribution also plays an important role to influence the mechanical analysis of a welded joint. Due to the non-uniform cooling and heating and non-uniform expansion and contraction, residual stresses and weld induced distortions occurs in weld zone. These residual stresses and distortions may harm the life of the welded joint. Hence, an accurate estimation of residual stresses is necessary and the accuracy depends on precise thermal model.

The fiber laser and GTA welding experiments are carried out to validate the developed process model and to investigate the influence of surface active elements. The fiber laser experiments are carried out in two different welding ambient atmospheres to study the effect of welding ambient atmosphere on weld bead dimensions. The GTA welding experiments are also carried out to investigate the influence of activating flux in the formation of weld pool. The following conclusions and possible directions of further research work are arrived at on the basis of the present work.

6.1 Conclusions

The primary deed of the present work lies in the development of an indigenous heat conduction model using finite element method that is capable of undertaking 3D transient heat transfer for linear welding process. A generalized form of egg-configuration volumetric heat source model is developed that is implemented in conduction heat transfer based model. Furthermore, the heat conduction model is enhanced to transport phenomena based heat transfer and fluid flow model to analyze the influence of surface active elements in GTA

welding process. Finally, the finite element based model to predict the weld induced distortion and residual stresses are developed for deep penetration fiber laser welding process. Moreover, the numerical models are enhanced with two optimization modules, real parameter based PCX-G3 based GA and DE module to estimate the uncertain model parameters.

The following conclusions are arrived at in the course of studying previous literature, developing the computational exercise and conducting the experiments on laser and GTA welding processes.

- The conduction based numerical model attempt to consider Gaussian distributed surface heat flux or volumetric heat source. It is realized that the surface heat flux may not be sufficient for deep penetration laser welding process. In that case, the volumetric heat source is more appropriate and *a-priori* knowledge of solidified weld dimensions from experiment is required. It was conceived that the consideration of a volumetric heat source with less number of parameters will be effective in conduction mode heat transfer analysis.
- In numerical modelling of fusion welding process, the input model parameters such as arc efficiency, effective thermal conductivity, arc radius and effective viscosity cannot be assigned with confidence based on scientific principles alone. But, the parameters like welding power, welding speed etc. can be correctly specified. To estimate the correct values of uncertain model parameters, an effort towards integration of suitable optimization tool with numerical model is required.
- During fusion welding process, thermo-chemical reactions occur between weld pool and working atmosphere that severely affects the weld metal properties and weld joint quality. Therefore, the welding atmosphere influences notably on the quality of the weld joint.
- It is experienced that a rigorous thermo-mechanically analysis will be of significant help in understanding the welding induced distortion and residual stresses. The initial attempts were empirical and analytical which had significant limitations in terms of general use and reliability. The numerical models for calculating the welding induced distortion and residual stresses have shown a promise to be able to undertake most of realities that are present in real weld design.
- The quantitative understanding of time-temperature history, velocity fields, keyhole formation and welding induced distortions and residual stresses in fusion welding process are indispensable to estimate the final weld bead dimensions, resulting microstructure, solidification morphology, and mechanical behaviour of the weld joint.

- A more practical approach has been adopted to estimate the effect of double-ellipsoidal volumetric heat source parameters in thermal and mechanical analysis of linear GTA welding process, in particular the effect of front and rear length of the double ellipsoidal heat source model on weld pool dimensions, and welding induced distortions and residual stresses. However, the other parameters of double ellipsoidal heat source model are approximated from the experimentally measured weld bead dimensions. The population-based method, a parent-centric operated generalized generation gap (PCX-G3) genetic algorithm (GA) has been used to find the optimum ratio of front and rear length of double-ellipsoidal heat source model.
- The influence of the rear and front length ratio on weld pool dimensions is significant. When a_r/a_f ratio increases the weld bead dimensions decrease. There exists a suitable functional form of a_r/a_f ratio that varies with welding velocity. A third degree polynomial represents better this functional form. The simulated thermal results are well agreed with experimentally measured weld dimensions at optimum values of a_r/a_f ratio. The variation of calculated values of final residual stress, equivalent plastic strain and residual stress has indicated that precise information of front and rear length ration is necessary in Double-ellipsoidal heat source model.
- A detailed sensitivity study of the computed weld dimensions on uncertain model input parameters such as a_r/a_f ratio, η, r_{eff}, k_{eff} and μ is carried out. It is comprehended that there is a necessity to develop a reference frame to identify their appropriate values to bring the reliability in model calculations of heat transfer, material flow and weld induced distortion and residual stresses.
- The optimized values of these unknown model input parameters are successfully achieved by intrinsically supporting the process FE model through the real parameter Genetic algorithm (PCX operated G3 model) based optimization technique and DE. It is also noticed that only a very few sets of experimentally measured weld bead dimensions are adequate to act as the reference for such optimization exercise. The reliability and robustness of the overall integrated process model is enriched by the assistance of optimization module.
- The integrated model is also developed to the extent that the same can compute quantitative information of thermal cycles and cooling rate using the optimum value of unknown model parameters.

- An egg-configuration volumetric heat source model is developed to simulate temperature, time-temperature history, and cooling rate during autogeneous fusion welding process. The application of the heat source model is confirmed by three dimensional heat conduction analyses for two distinct welding processes (GTA and laser welding).
- The proposed egg-configuration heat source model consists of limited number of model parameters for the simulation of moving heat source problem. The existed heat source models such as Pavelic's disc, Paley and Hibbert volumetric heat source, Westby's heat source model and semi-ellipsoidal heat source models are the special cases of the proposed egg-configuration heat source model. It has been revealed that the numerical model is also capable of estimating the cooling rate from time temperature history which is significant to predict the microstructural properties of weld joint.
- From this study it is observed that only heat conduction analysis might not be sufficient to consider the effect of surface active elements. A three dimensional heat transfer and fluid flow model is developed to account the effect of flow dynamics during formation of weld pool. The effect of oxygen as surface active element on the development of weld pool during autogeneous GTA welding process is studied. In the liquid metal flow, the most significant driving force is the surface tension force and it is incorporated through temperature and concentration dependent coefficients of surface tension.
- To estimate the uncertain model parameters such as effective arc radius, arc efficiency and material properties at high temperature, DE based optimization algorithm is integrated with the developed numerical model. Present work is practically significant to obtain high penetration as well as high aspect ratio weld joint in GTA welding. The maximum benefit can be obtained with an optimum value of oxygen for a specific welding condition. The same has been analysed using developed numerical model. The overall reliability analysis of predicted results signifies the robustness of present integrated modelling approach.
- The investigation is carried out on fiber laser welding of austenitic stainless steel at two different atmospheric conditions i.e. self-protective atmosphere of argon and open atmosphere. The application of shielding gas is performed in a controlled chamber that eliminates the gas flow rate locally around the weld zone. The depth of penetration as well as aspect ratio under controlled atmosphere of argon is more when compared with the open atmospheric condition. It is also possible to minimize or avoid the chemical reaction of molten weld pool with air by using the controlled atmosphere process. The top surface

profile and clear appearance of the controlled atmosphere is better as compared to open atmospheric results.

- The presence of inert gas constricts the keyhole plasma and in effect the depth of penetration as well as aspect ratio is more as compared to open atmospheric condition. The bead width decreases in presence of argon gas. The maximum variation of the weld depth of penetration is 29% and weld width is 40% due to presence of argon gas.
- Double ellipsoidal volumetric heat source model is suitable for open atmosphere condition whereas conical heat source model is utilized for self-protective atmosphere of argon since the weld pool shape is analogous to stiff temperature gradient. The computed and experimentally measured weld macrographs for both atmospheric conditions are in fair agreement. The percentage error in calculation of weld dimensions is less than 8 %. The computed cooling rate differs considerably between two atmospheric conditions and hence the possibility of differences in expected macrostructure.
- The formation of keyhole entrains the penetration depth of fiber laser welding process. The fiber laser welding of SS 316, 5 mm thickness is assumed to form keyhole in present set of experimental conditions. The keyhole geometry is calculated by semi-analytical mathematical model based on point-by-point energy balance.
- It is obvious that surface active elements produce high depth of penetration in GTA welding. The GTA welding experiments are conducted using thin layer activating fluxes of TiO_2, SiO_2, and Al_2O_3. The weld bead dimension is higher in case of welding using TiO_2 activating flux as compared to other activating fluxes. However, the shallow penetration and wide bead width are achieved in GTA welding with Al_2O_3 flux. It is concluded that the narrow range of surface active elements acts positively to produce high depth in present system of welding process. However, more experimental verification is needed in this effect.
- Finally, the calculation method and quantative knowledge extracted from this research work in fusion welding process will expected to serve as a basis for the control of fusion welding processes aimed at achieving enhanced reliability.

6.2 Scope of future work

Although the efforts towards the development of a new heat source model for the simulation of fusion welding processes, conduction heat transfer analysis and a comprehensive thermo-fluid model assuming laminar flow of molten metal in the present

work is a significant direction to predict weld dimensions and transient thermal cycles in fusion welding, it is expected that the consideration of turbulent flow within weld pool may influence the shape, size and temperature distribution of weld pool and surrounding area. Even though, the developed new heat source model calibrated for two distinct fusion welding processes, the calculation of heat source parameters from the mathematical basis demands a systematic approach using optimization algorithm which is the future scope of further research on egg configuration heat source model. One of the significant assumptions of the present convection heat transfer analysis is flat surface of fusion zone which may not be the real case of fusion welding process. The amalgamation of turbulent flow in weld pool along with free surface modeling in the present numerical model for finding the influence of surface active elements on weld pool formation will be worth attempting to robust modeling approach.

Although the characteristic difference during fiber laser welding of austenitic stainless steel between controlled and open atmospheric condition are analyzed in terms weld dimensions, preliminary microstructures and top surface appearance, it is expected that the consideration of more reactive materials and their quantative formation of porosity analysis is the future scope of the research work on controlled atmosphere. The influence of the ratio front length to rear length with respect to welding speed has been studied in this work; however, this ratio may be affected by the change of power density. Henceforth, the estimation of this ratio with respect to both welding speed and power density is the future research work in this direction. The weld pool and its surrounding area experience uneven thermal expansion and contraction when the heat source moves from one end to other end on weld center line, it may lead to dimensional inaccuracy of welded plates and to form residual stresses. Though the primary quantitative study of thermo-mechanical analysis has been carried out, a further detailed and extensive research of thermo-mechanical analysis, specifically the experimental measurement of residual stress is the future research work in this direction. The effect of activating flux on formation of weld pool during GTA welding has been studied. However, more elaborate study on the effect of several other active elements, the application techniques of the active elements on the workpiece and the characterization of welded joint are future scope of work. A coupled thermo-mechanical analysis for weld joint can serve as an effective *a-priori* design tool for planning of proper weld schedules to minimize the distortion and residual stresses.

Appendix I

In Pavelic's disc heat source model, the power density distribution in Gaussian manner can be articulated as follows

$$q(r) = q(o) \times \exp(-Cr^2) \quad \text{(i)}$$

where q(r) is the surface heat flux at radius 'r' in W/m^2, q(o) is the heat flux at the centre of the heat source (maximum) in W/m^2, r is the radial distance from the centre of the heat source (m), and C is the concentration coefficient in m^{-2}. The alternative form of the Pavelic's disc heat source model for moving arc which is recommended by Friedman, Krutz, and Segerlind is expressed as

$$q(x, \xi) = \frac{3Q}{\pi c^2} \times \exp\{\frac{-3}{c^2}(x^2 + \xi^2) \quad \text{(ii)}$$

where Q is the energy input rate in W, 'c' is the characteristic radius of flux distribution in m. It is opportune to fix an (x, y, z) coordinate system in work piece and also a lag factor τ is necessary to define the position of the heat source at time t = 0, then the change linking the fixed and moving coordinate systems is

$$\xi = z + v(\tau - t) \quad \text{(iii)}$$

where v is the welding velocity in m/s. The Gaussian distribution of the power density in a proposed egg shape configuration heat source model with the centre at (0, 0, 0) and semi-axes a, b, c parallel to coordinate axes x, y, z can be stated as

$$q(x, y, z) = q_m \exp[-\{By^2 + (Ax^2 + Cz^2).t(y)\}] \quad \text{(iv)}$$

where $t(y) = \frac{1}{my + m^2y^2 + 1}$ (v)

q_m is the maximum value of the power density at the centre of a proposed egg shape and A, B, C and m are the distribution parameters. Conservation of energy requires the intensity of heat distributed inside the half of the egg shape and is expressed as

$$2Q = \int_{-\infty}^{\infty}\int_{-\infty}^{\infty}\int_{-\infty}^{\infty} q(x, y, z)dxdydz \quad \text{(vi)}$$

$$2Q = 4\int_0^{\infty}\int_0^{\infty}\int_0^{\infty} q_m \times \exp\left\{-\left[By^2 + (Ax^2 + Cz^2) \times \left(\frac{1}{my + m^2y^2 + 1}\right)\right]\right\} dxdydz$$
$$+ 4\int_0^{\infty}\int_0^{\infty}\int_0^{\infty} q_m$$
$$\times \exp\left\{-\left[By^2 + (Ax^2 + Cz^2) \times \left(\frac{1}{-my + m^2y^2 + 1}\right)\right]\right\} dxdydz \quad \text{(vii)}$$

After simplifying the above equation (vii), the q_m can be estimated as given below

$$\Rightarrow q_m = \frac{4BQ \times sqrt(ABC)}{\pi \times sqrt(\pi)[2B + m^2]} \quad \text{(viii)}$$

To estimate A, B, C, the semi-axes of a proposed egg shape a, b, c in the x, y, z axes directions respectively, are defined such that the heat density falls to $0.05q_m$ at the surface of proposed egg shape. In x-direction;

$$q(a, 0, 0) = q_m \times \exp(-Aa^2) = 0.05 \times q_m \quad \text{(ix)}$$

$$\Rightarrow \exp(-Aa^2) = 0.05 \quad \text{(x)}$$

$$\Rightarrow A \approx \frac{3}{a^2} \quad \text{(xi)}$$

Similarly,

$$B \approx \frac{3}{b^2}, \qquad C \approx \frac{3}{c^2} \quad \text{(xii, xiii)}$$

Now, substituting A, B, and C values in equation (x), we found the maximum heat density q_m as

$$\Rightarrow q_m = q_m = \frac{36Q \times sqrt(3)}{\pi \times sqrt(\pi)[6 + m^2 b^2]} \quad \text{(xiv)}$$

Substituting A, B, C, and q_m in equation (iv), the power density distribution in a proposed egg shape is expressed as

$$q(x, y, z) = \frac{36 \times sqrt(3) \times Q}{\pi \times abc \times sqrt(\pi) \times [6 + b^2 m^2]} \times e^{-\left[\frac{3y^2}{b^2} + \left(\frac{3x^2}{a^2} + \frac{3z^2}{c^2}\right) \times \left(\frac{1}{my + m^2y^2 + 1}\right)\right]} \quad \text{(xv)}$$

The effect of welding speed taking into account, the heat distribution should not be symmetrically distributed; it should be asymmetric, ahead of arc and behind it. From the Eq. (xviii) it is obvious that, if 'm' is equal to zero then the power density becomes equal to power

density of semi-ellipsoidal heat source model. The heat source models such as Pavelic's disc source, Paley and Hibbert volume heat source and Westby's heat source model are special cases of semi-ellipsoidal heat source model. The heat density distribution inside the front part and rear part of the proposed egg shape configuration can be expressed as

$$q_f(\mathrm{x,y,z}) = \frac{36\times\mathrm{sqrt}(3)\times\mathrm{Q}\times N_f}{\pi\times\mathrm{abc}\times\mathrm{sqrt}(\pi)\times[6+b^2\mathrm{m}^2]} \times \mathrm{e}^{-\left[\frac{3\mathrm{y}^2}{\mathrm{b}^2}+\left(\frac{3\mathrm{x}^2}{\mathrm{a}^2}+\frac{3\mathrm{z}^2}{\mathrm{c}^2}\right)\times\left(\frac{1}{\mathrm{my}+\mathrm{m}^2\mathrm{y}^2+1}\right)\right]} \quad \text{(xvi)}$$

$$q_r(\mathrm{x,y,z}) = \frac{36\times\mathrm{sqrt}(3)\times\mathrm{Q}\times N_r}{\pi\times\mathrm{abc}\times\mathrm{sqrt}(\pi)\times[6+b^2\mathrm{m}^2]} \times \mathrm{e}^{-\left[\frac{3\mathrm{y}^2}{\mathrm{b}^2}+\left(\frac{3\mathrm{x}^2}{\mathrm{a}^2}+\frac{3\mathrm{z}^2}{\mathrm{c}^2}\right)\times\left(\frac{1}{-\mathrm{my}+\mathrm{m}^2\mathrm{y}^2+1}\right)\right]} \quad \text{(xvii)}$$

where v, τ, and t depict the welding speed, a lag factor, and time respectively. Here, N_f and N_r are the fractions of heat deposited in the front and the rear sections respectively. For the front section, the heat deposition is determined as follows

$$2\int_0^\infty\int_0^\infty\int_0^\infty \mathrm{q(x,y,z)dxdydz} = \frac{1}{2}(\mathrm{N_fQ}) \quad \text{(xviii)}$$

Solving equation (xviii) for N_f as follows

$$2\int_0^\infty\int_0^\infty\int_0^\infty \mathrm{q(x,y,z)dxdydz} = \frac{36\times\mathrm{sqrt}(3)\times\mathrm{Q}}{\pi\times\mathrm{abc}\times\mathrm{sqrt}(\pi)\times[6+b^2\mathrm{m}^2]}\times 2 \times\int_0^\infty\int_0^\infty\int_0^\infty \mathrm{e}^{-\left[\frac{3\mathrm{y}^2}{\mathrm{b}^2}+\left(\frac{3\mathrm{x}^2}{\mathrm{a}^2}+\frac{3\mathrm{z}^2}{\mathrm{c}^2}\right)\times\left(\frac{1}{\mathrm{my}+\mathrm{m}^2\mathrm{y}^2+1}\right)\right]} dxdydz \quad \text{(xix)}$$

$$\Rightarrow \left(\frac{[6\times sqrt(\pi)+2\sqrt{3}\times bm+b^2m^2\times sqrt(\pi)]\times Q}{[2\times sqrt(\pi)\{6+b^2m^2\}]}\right) = \frac{1}{2}(\mathrm{N_fQ}) \quad \text{(xx)}$$

$$\Rightarrow N_f = \frac{[6\times sqrt(\pi)+2\sqrt{3}\times bm+b^2m^2\times sqrt(\pi)]}{sqrt(\pi)\{6+b^2m^2\}} \quad \text{(xxi)}$$

Similarly, for the rear section, heat deposition is can be determined as follows

$$2\int_0^\infty\int_0^\infty\int_0^\infty \mathrm{q(x,y,z)dxdydz} = \frac{1}{2}(\mathrm{N_rQ}) \quad \text{(xxii)}$$

Solving equation (xxii) for N_r as follows

$$2\int_0^{\infty}\int_0^{\infty}\int_0^{\infty} q(x,y,z)dxdydz$$

$$= \frac{36 \times \text{sqrt}(3) \times Q}{\pi \times abc \times \text{sqrt}(\pi) \times [6 + b^2m^2]} \times 2$$

$$\times \int_0^{\infty}\int_0^{\infty}\int_0^{\infty} e^{-\left[\frac{3y^2}{b^2}+\left(\frac{3x^2}{a^2}+\frac{3z^2}{c^2}\right)\times\left(\frac{1}{-my+m^2y^2+1}\right)\right]} dxdydz$$

(xxiii)

$$\Rightarrow \left(\frac{[6\times sqrt(\pi)-2\sqrt{3}\times bm+b^2m^2\times sqrt(\pi)]\times Q}{[2\times sqrt(\pi)\{6+b^2m^2\}]}\right) = \frac{1}{2}(N_r Q) \quad \text{(xxiv)}$$

$$\Rightarrow N_r = \frac{[6\times sqrt(\pi)-2\sqrt{3}\times bm+b^2m^2\times sqrt(\pi)]}{sqrt(\pi)\{6+b^2m^2\}} \quad \text{(xxv)}$$

Therefore, the sum of the N_f and N_r can be as follows

$$\Rightarrow N_f + N_r = \frac{[6 \times sqrt(\pi) + 2\sqrt{3} \times bm + b^2m^2 \times sqrt(\pi)]}{sqrt(\pi)\{6 + b^2m^2\}} + \frac{[6 \times sqrt(\pi) - 2\sqrt{3} \times bm + b^2m^2 \times sqrt(\pi)]}{sqrt(\pi)\{6 + b^2m^2\}}$$

(xxvi)

$$N_r + N_f = 2 \quad \text{(xxvii)}$$

References

1. T. DebRoy and S. A. David: Physical processes in fusion welding, *Reviews of Modern Physics*, **67**, 1995, 85-112.

2. S. A. David and T. DebRoy: Current issues and problems in welding science, *Science*, **257 (5069)**, 1992, 497-502.

3. J. G. Andrews and D. R. Atthey: Hydrodynamic limit to penetration of a material by a high-power beam, *Journal of Physics D: Applied Physics*, **9**, 1976, 2181-2194.

4. J. Kross, U. Gratzke and G. Simon: Towards a self-consistent model of the keyhole in penetration laser beam welding. *Journal of Physics D: Applied Physics*, **26**, 1993, 474–480.

5. A. Kaplan: A model of deep penetration laser welding based on calculation of the keyhole profile, *Journal of Physics D: Applied Physics*, **27 (9)**, 1994, 1805–1814.

6. H. Zhao and T. DebRoy: Macroporosity free aluminum alloy weldments through numerical simulation of keyhole mode laser welding, *Journal of Applied Physics*, **93**, 2003, 10089-96.

7. Ø. Grong: Metallurgical Modeling of Welding, 2nd edition, The Institute of Materials, London, 1997.

8. J. F. Lancaster: The Physics of Welding, 2nd Edition, Pergamon, Oxford, 1986.

9. K. Easterling: Introduction to the Physical Metallurgy of Welding, 2nd Edition, Butterworth-Heinemann, Oxford, 1992.

10. S. Kou: Welding Metallurgy, 2nd edition, John Wiley & Sons, Hoboken, New Jersey, 2003.

11. K. Masubuchi: Analysis of Welded Structures, Pergamon Press, Oxford, 1980.

12. K.J. Son, Y.S. Yang and H.G. Beom: Analysisof angular distortion in weldment using laminated plate theory, *Science and Technology of Welding and Joining*, **5**, 2000, 245-249.

13. D. Deng, H. Murakawa and W. Liang: Prediction of welding distortion in a curved plate structure by means of elastic finite element method, *Journal of Materials Processing Technology*, **203**, 2008, 252–266.

14. J. T. Liu, D. C. Weckman and H. W. Kerr: The effects of process variables on pulsed Nd:YAG laser spot welds: Part I. AISI 409 stainless steel, *Metallurgical and Materials Transactions B*, **24**, 1993, 1065-1076.

15. C. M. D. Starling, P. V. Marques, P. J.Modenesi: Statistical modelling of narrow-gap GTA welding with magnetic arc oscillation, *Journal of Materials Processing Technology*, **51 (9)**, 1995, 37-49.

16. D. C. Weckman, H. W. Kerr and J. T. Liu:The effects of process variables on pulsed Nd:YAG laser spot welds: Part.II. AA 1100 aluminum and comparison to AISI 409 stainless steel, *Metallurgical and Materials Transactions B*, **28B**, 1997, 687-699.

17. Y. F. Tzeng: Pulsed Nd:YAG laser seam welding of zinc coated steel, *Welding Journal*, **78(7)**, 1999, 238-244.

18. G. Lothongkum, P. Chaumbaiand P. Bhandhubanyong: TIG pulse welding of 304L austenitic stainless steel in flat, vertical and overhead positions, *Journal of Materials Processing Technology*, **89-90**, 1999, 410-414.

19. M. Pastor, H. Zhao, R. P. Martukantiz and T. DebRoy: Porosity, underfill and magnesium loss during continuous wave Nd:YAG laser welding of thin plates of Aluminium alloys 5182 and 5754, *Welding Journal*, **78**, 1999, 207-216.

20. M. Jou: Experimental study and modeling of GTA welding process, *Journal of Manufacturing Science and Engineering*, **125**, 2003, 801-808.

21. C. A. Walsh, H. D. K. H. Bhadeshia, A.Lau, B. Matthias, R. Oesterlein and J. Drechsel: Characteristics of high-power diode-laser welds for industrial assembly, *Journal of Laser Applications*, **15(2)**, 2003, 68-76.

22. M. G. Deutsch, A. Punkari, D. C. Weckman and H. W. Kerr: Weldability of 1.6 thick aluminium alloy 5182 sheet by single and dual beam Nd: YAG laser welding, *Science and Technology of Welding and Joining*, **8 (4)**, 2003, 246-256.

23. K. Y. Benyounis, A. G. Olabi and M. S. J. Hashmi: Effect of laser welding parameters on the heat input and weld-bead profile, *Journal of Materials Processing Technology*, **165**, 2005, 978-985.

24. V. Pavelic, R. Tanbakuchi, O. A. Uyehara and P. S. Myers: Experimental and computed temperature histories in gas tungsten-arc welding of thin plates, *Welding Journal*, **48(7)**, 1969, 295-305.

25. T. Zacharia, S.A. David, J. M. Vitek and T. Debroy: Weld pool development during GTA and laser beam welding of Type 304 stainless steel Part II-experimental correlation, *Welding Journal*, **68 (12)**, 1989, 510-519.

26. H. Ki, J. Mazumder and P. S. Mohanty: Modeling of laser keyhole welding: Part II. Simulation of keyhole evolution, velocity, temperature profile, and experimental verification, *Metallurgical and Material Transactions A*, **33**, 2002, 1831-1842.

27. P. J. Withers and H. K. D. H. Bhadeshia: Residual stress: Part 1–Measurement techniques, *Materials Science and Technology*, **17**, 2001, 355-365.

28. D. Rosenthal: Mathematical theory of heat distribution during welding and cutting, *Welding Journal*, **20(5)**, 1941, 220-234.

29. D. Rosenthal: The theory of moving sources of heat and its application to metal treatments, *Transactions of ASME*, **43(11)**, 1946, 849-865.

30. J. A. Goldak, A. Chakravarti and M. Bibby: A new finite element model for welding heat sources, *Metallurgical Transactions B*, **15 (2)**, 1984, 299-305.

31. J. Goldak, M. Bibby, J. Moore, R. House and B. Patel: computer modeling of heat flow in welds, *Metallurgical Transactions B*, **17**, 1986, 587-600.

32. A. Kar and J. Mazumder: Three dimensional transient thermal analysis for laser chemical vapour deposition on uniformly moving finite slabs, *Journal of Applied Physics*, **65 (8)**, 1989, 2923-2934.

33. S. K. Jeong and H. S. Cho: An analytical solution to predict the transient temperature distribution in fillet arc welds, *Welding Journal*, **76 (6)**, 1997, 223s-232s.

34. T. Kasuya and N. Shimoda: Stefan problem for finite liquid phase and its application to laser or electron beam welding, *Journal of Applied Physics*, **82**, 1997, 3672-3678.

35. S. H. Kang and H. S. Cho: Analytical solution for transient temperature distribution in gas tungsten arc welding with consideration of filler wire, *Journal of Engineering and Manufacture B*, **213 (8)**, 1999, 799-811.

36. N. T. Nguyen, A. Ohta, K. Matsuoka, N. Suzuki and Y. Maeda: Analytical solutions for transient temperature of semi-Infinite body subjected to 3-D moving heat sources, *Welding Journal*, **78 (6)**, 1999, 265s-274s.

37. M. R. Frewin, D. A. Scott: Finite element model of pulsed laser welding, *Welding Research Supplement*, **78(1)**, 1999, 15-22.

38. U. Tanriver, J. Longobardi, W. P. Latham and A. Kar: Effect of absorptivity, shielding gas speed, and contact media on sheet metal laser welding, *Science and Technology of Welding and Joining*, **5**, 2000, 310-316.

39. E. A. Bonifaz: Finite element analysis of heat flow in single-pass arc welding, *Welding Research Supplements*, **79 (5)**, 2000, 121-125.

40. J. Du, J. Longobardi, W. P. Latham and A. Kar: Weld geometry and tensile strength in laser welded thin sheet metals, *Science and Technology of Welding and Joining*, **5 (5)**, 2000, 304-309.

41. W. Guo and A. Kar: Determination of weld pool shape and temperature distribution by solving three dimensional phase change heat conduction, *Science and Technology of Welding and Joining*, **5 (5)**, 2000, 317-323.

42. A. De, S. K. Maiti, C. A. Walsh and H. K. D. H. Bhadeshia: Finite element simulation of laser spot welding, *Science and Technology of Welding and Joining*, **8 (5)**, 2003, 377-384.

43. V. A. Karkhin, A. S. Ilin, H. J. Pesch, A. A. Prikhidovsky, V. V. Plochikhine, M.V. Makhutin and H. W. Zoch: Effect of latent heat of fusion on thermal processes in laser welding of aluminium alloys, *Science and Technology of Welding and Joining*, **10 (5)**, 2005, 597-603.

44. V. A. Vinokurov: Welding Stresses and Distortion, The British Library, Boston Spa, England, 1977, 118-119.

45. C. Chan, J. Mazumder and M. M. Chen: A two dimensional transient model for convection in laser melted pool, *Metallurgical and Materials Transactions A*, **15**, 1984, 2175-84.

46. K. C. Tsao and C. S. Wu: Fluid flow and heat transfer in GMA weld pools, *Welding Journal*, **67 (3)**, 1988, 70-75.

47. T. Zacharia, S.A. David, J. M. Vitek and T. Debroy: Weld pool development during GTA and laser beam welding of Type 304 stainless steel Part II-experimental correlation, *Welding Journal*, **68** (12), 1989, 510s-519s.

48. V. Babu, A. K. Korpela and N. Ramanan: Flow and temperature fields in a weld pool formed by a moving laser, *Journal of Applied Physics*, **67,** 1990, 3990-3999.

49. R. T. C. Choo and J. Szekely: The possible role of turbulence in GTA weld pool behaviour, *Welding Journal*, **73 (2)**, 1994, 25-31.

50. W. H. Kim, H. G. Fan and S. J. Na: Effect of various driving forces on heat and mass transfer in arc welding. *Numerical Heat Transfer A*, **32**, 1997, 633–652.

51. A. Paul and T. DebRoy: Free surface flow and heat transfer in conduction mode laser welding, *Metallurgical and Materials Transactions B*, **19**, 1998, 851-857.

52. K. Hong, D. C. Weckmann, A. B. Strong and W. Zheng: Modelling turbulent thermo-fluid flow in stationary gas tungsten arc weld pools, *Science and Technology of Welding and Joining*, **7 (3)**, 2002, 125-136.

53. H. He, P. W. Fuerschbach and T. DebRoy: Heat transfer and fluid flow during laser spot welding of SS 304 stainless steel, *Journal of Physics D: Applied Physics*, **36**, 2003, 1388-1398.

54. W. Zhang, G. G. Roy, J. W. Elmer and T. DebRoy: Modelling of heat transfer and fluid flow during gas tungsten arc spot welding of low carbon steel, *Journal of Applied Physics*, **93 (5)**, 2003, 3022-3033.

55. A. De, C. A. Walsh, S. K. Maiti and H. K. D. H. Bhadeshia: Prediction of cooling rate and microstructure in laser spot welds, *Science and Technology of Welding* and *Joining*, 2003, **8 (6)**, 391-399.

56. N. Chakraborty and S. Chakraborty: Influences of sign of surface tension coefficient on turbulent weld pool convection in a gas tungsten arc welding (GTAW) process: A comparative study, *Journal of Heat Transfer*, **127 (4)**, 2005, 848-862.

57. V. A. Karkhin, V. V. Plochikhine and H. W. Bergmann: Solution of inverse heat conduction problem for determining heat input, weld shape, and grain structure during laser welding, *Science and Technology of Welding and Joining*, **7 (4)**, 2002, 224-231.

58. L. Quintino, A. Costa, R. Miranda, D. Yapp, V. Kumar and C. J. Kong: Welding with high power fiber lasers – A preliminary study, *Materials and Design*, **28**, 2007, 1231-1237.

59. H. Zhao and T. DebRoy: Weld metal composition change during conduction mode laser welding of aluminum alloy 5182, *Metallurgical and Materials Transactions B*, **32**, 2001, 163-172.

60. A. De and T. DebRoy: A smart model to estimate effective thermal conductivity and viscosity in weld pool, *Journal of Applied Physics*, **95** (9), 2004, 5230-5240.

61. A. Kumar and T. DebRoy: Guaranteed fillet weld geometry from heat transfer model and multivariable optimization, *International Journal of Heat and Mass Transfer*, **47,** 2004, 4793-5806.

62. A. De and T. DebRoy: Reliable calculations of heat and fluid flow during conduction mode laser welding through optimization of uncertain parameters, *Welding Journal*, **84** (7), 2005, 101s - 112s.

63. K. Deb and R. B. Agrawal: Simulated binary crossover for continuous search space, *Complex Systems*, **9 (2)**, 1995, 115-148.

64. F. Herrera, M. Lozano and J. L. Verdegay: Tackling real-coded genetic algorithms: Operators and tools for behavioural analysis, *Artificial Intelligence Review*, **12 (4)**, 1998, 265-319.

65. K. Deb, A. Anand and D. Joshi: A computationally efficient evolutionary algorithm for real-parameter optimization, *Evolutionary Computation*, **10,** 2002, 371-395.

66. R. Storn: Diferential evolution design of an IIR-filter with requirements of magnitude and group delay, *Proceedings of the IEEE Conference on Evolutionary Computation*, 1996, 268-273.

67. R. Storn: System design by constraint adaptation and differential evolution, *IEEE Transactions on Evolutionary Computation,* **3 (1)**, 1999, 22-34.

68. R. Nandan, B. Prabu, A. De and T. DebRoy, Improving reliability of heat transfer and fluid flow calculations during friction stir welding of dissimilar aluminum alloys, *Welding Journal*, **86 (10)**, 2007, 313-322.

69. J. Norrish: Advanced welding processes, Woodhead publishing Ltd., Cambridge, England, 2006.

70. G. R. Eisler and P. W. Fuerschbach: An extensible suite of codes for weld analysis and optimal weld schedules, SAND 96-2622C, 1997.

71. W. Dong, H. Kokawa, S. S. Yutaka and S. Tsukamoto: Nitrogen absorption by iron and stainless steels during CO_2 laser welding, *Metallurgical and Materials Transactions B*, **34**, 2003, 75-82.

72. A. Zambon, P. Ferro and F. Bonollo, Microstructural, compositional and residual stress evaluation of CO_2 laser welded superaustenitic AISI 904L stainless steel, *Materials Science and Engineering A*, **424**, 2006, 117-127.

73. A. G. Paleocrassas and J. F. Tu: Low-speed laser welding of aluminum alloy 7075-T6 using a 300-W, single-mode, Ytterbium fiber laser, *Welding Journal*, **86**, 2007, 179-186.

74. S. M. Chowdhury, D. L. Chen, S. D. Bhole, E. Powidajko, D. C. Weckman, and Y. Zhou: Microstructure and mechanical properties of fiber-laser-welded and diode-laser-welded AZ31 magnesium alloy, *Metallurgical and Materials Transactions A*, **42**, 2011, 1974-1989.

75. Abdel-Monem El-Batahgy: Effect of laser welding parameters on fusion zone shape and solidification structure of austenitic stainless steels, *Materials Letters*, **32 (2-3)**, 1997, 155-163.

76. S. Katayama, Y. Kawahito and M. Mizutani: Latest progress in performance and understanding of laser welding, *Physics Procedia*, **39**, 2012, 8-16.

77. M. Balasubramanian, V. Jayabalan and V. Balasubramanian: effect of pulsed current gas tungsten arc welding parameters on microstructure of titanium alloy welds, *Journal of Manufacturing Science and Engineering*, **131**, 2009, 064502-1-4.

78. K. Abderrazak, W. B. Salem, H. Mhiri, P. Bournot, and M. Autric: Nd:YAG Laser welding of AZ91 Magnesium alloy for aerospace industries, *Metallurgical and Materials Transactions B*, **40**, 2009, 54-61.

79. S. H. Chowdhury, D. L. Chen, S. D. Bhole, E. Powidajko, D. C. Weckman, and Y. Zhou: Fiber laser welded AZ31 magnesium alloy: the effect of welding speed on microstructure and mechanical properties, *Metallurgical and Materials Transactions A*, **43**, 2012, 2133-2147.

80. R. H. Zhang, J. L. Pan and S. Katayama: The mechanism of penetration increase in A-TIG welding, *Frontiers of Materials Science*, **5(2)**, 2011, 109-118.

81. M. Moradi and M. Ghoreishi: Influences of laser welding parameters on the geometric profile of NI-base superalloy Rene 80 weld-bead, *International Journal of Advanced Manufacturing Technology*, **55**, 2011, 205-215.

82. A. G. Paleocrassas and J. F. Tu: Inherent instability investigation for low speed laser welding of aluminum using a single-mode fiber laser, *Journal of Materials Processing Technology*, **210**, 2010, 1411-1418.

83. H. C. Chen, A. J. Pinkerton and L. Li: Fibre laser welding of dissimilar alloys of Ti-6Al-4V and Inconel 718 for aerospace applications, *International Journal of Advanced Manufacturing Technology*, **52 (9-12)**, 2011, 977-987.

84. P. Sahoo, T. DebRoy and M. J. McNallan: Surface tension of binary metal-surface active solute systems under conditions relative to welding metallurgy, *Metallurgical and Materials Transactions B*, **19**, 1988, 483-491.

85. P. Sahoo, M. M. Collur and T. DebRoy: Effects of Oxygen and Sulfur on Alloying Element Vaporization Rates during Laser Welding, *Metallurgical Transactions B*, **19**, 1988, 967-972.

86. W. Pitscheneder, T. DebRoy, K. Mundra, and R. Ebner: Role of sulphur and processing variables on the temporal evolution of weld pool geometry during multi-kilowatt laser beam welding of steels, *Welding Journal*, **75 (3)**, 1996, 71-78.

87. Y. Wang and H. L. Tsai: Effects of surface active elements on weld pool fluid flow and weld penetration in gas metal arc welding, *Metallurgical Materials Transactions B*, **32**, 2001, 501-515.

88. L. Zhao, S. Tsukamoto, G. Arakane and T. Sugino: Influence of oxygen on weld geometry in fibre laser welding. *ICALEO 2009*, 2009, 759-765.

89. K. Ramazan and K. Koray: Effect of controlled atmosphere on the mig-mag arc weldment properties, *Materials and Design*, **26 (6)**, 2005, 508-516.

90. K. Bayram, K. K. Ramazan, G. Suleyman and H. Fatih, An effect of heat input, weld atmosphere and weld cooling conditions on the resistance spot weldability of 316L austenitic stainless steel, *Journal of Materials Processing Technology*, **195**, 2008, 327-335.

91. O. Dursun: An effect of weld current and weld atmosphere on the resistance spot weldability of 304L austenitic stainless steel, *Materials and Design*, **29**, 2008, 597-603.

92. A. A. Ostsemin: Estimating the temperature of an electrode-metal drop when welding in a carbon-dioxide atmosphere, *Russian Engineering Research*, **29 (7)**, 2009, 668-670.

93. C. R. Heiple and P. Burgardt: Effects of So_2 shielding gas additions on GTA weld shape, *Welding Journal*, **64**, 1985, 159-162.

94. J. E. Ramirez, B. Han and S. Liu: Effect of welding variables and solidification substructure on weld metal porosity, *Metallurgical and Materials Transactions A*, **25**, 1994, 2285-2294.

95. P. G. Jonsson, T. W. Eagar and J. Szekely: Heat and metal transfer in gas metal arc welding using argon and helium, *Metallurgical and Materials Transactions B*, **26**, 1995, 383-395.

96. H. J. Kim, H. R. Frost and D. L. Olson: Electrochemical oxygen transfer during direct current arc welding, *Welding Journal*, 1998, 488-493.

97. M. Tanaka, T. Shimuzu, H. Terasaki, M. Ushio, F. Koshi-ishi and C. L. Yang: Effects of activating flux on arc phenomena in gas tungsten arc welding, *Science and Technology of Welding and Joining*, **5**, 2000, 397-402.

98. S. Lu, H. Fujii and K. Nogi: Marangoni Convection in Weld Pool in CO2-Ar–Shielded Gas Thermal Arc Welding, *Metallurgical and Materials Transactions A*, **35**, 2004, 2861-2867.

99. S. Lu, H. Fujii and K. Nogi: Influence of welding parameters and shielding gas composition on GTA weld shape, *ISIJ International*, **45 (1)**, 2005, 66-70.

100. X. Li, J. Xie and Y. Zhou, Effects of oxygen contamination in the argon shielding gas in laser welding of commercially pure titanium thin sheet, *Journal of Materials Science*, **40**, 2005, 3437-3443.

101. B. Y. Kang, K. D. V. Yarlagadda, M. J. Kang, H. J. Kim and I. S. Kim: The effect of alternate supply of shielding gases in austenite stainless steel GTA welding, *Journal of Materials Processing Technology*, **209**, 2009, 4722-4727.

102. S. Lu, W. Dong, D. Li, and Y. Li, Numerical study and comparisons of gas tungsten arc properties between argon and nitrogen, *Computational Materials Science*, **45**, 2009, 327-335.

103. W. C. Dong, S. P. Lu, D. Z. Li and Y. Y. Li: GTAW liquid pool convections and the weld shape variations under helium gas shielding, *International Journal of Heat and Mass Transfer*, **54**, 2011, 1420-1431.

104. A. Savas and V. Ceyhun: Finite element analysis of GTAW arc under different shielding gases, *Computational Materials Science*, **51**, 2011, 53-71.

105. P. Sathiya and M. Y. A. Jaleel: Influence of shielding gas mixtures on bead profile and microstructural characteristics of super austenitic stainless steel weldments by laser welding, *International Journal of Advanced Manufacturing Technology*, **54**, 2011, 525-535.

106. S. Yang, B. Carlson and R. Kovacevic: Laser welding of high-strength galvanized steels in a gap-free lap joint configuration under different shielding conditions, *Welding Journal*, **90**, 2011, 8-18.

107. H. Ki, J. Mazumder and P. S. Mohanty: modeling of laser keyhole welding: Part I. mathematical modeling, numerical methodology, role of recoil pressure, multiple reflections, and free surface evolution, *Metallurgical and Material Transactions A*, **33**, 2002, 1817-1830.

108. W. Dong, H. Kokawa, S. Tsukamoto, and S. S. Yutaka, "Nitrogen desorption by high-nitrogen steel weld metal during Co2 laser welding", Metall. Mater. Trans. B, **36**, 2005, 677-681.

109. I. Eriksson, J. Powell and A. F. H. Kaplan: Measurements of fluid flow on keyhole front during laser welding, *Science and Technology of Welding and Joining*, **16 (7)**, 2011, 636-641.

110. Y. Cheng, X. Jin, S. Li and L. Zeng: Fresnel absorption and inverse bremsstrahlung absorption in an actual 3D keyhole during deep penetration CO2 laser welding of aluminium 6016, *Optics & Laser Technology*, 44 (5), 2012, 1426-1436.

111. C. Meng, F. Lu, H. Cui and X. Tang: Research on formation and stability of keyhole in stationary laser welding on aluminum MMCs reinforced with particles, *International Journal of Advanced Manufacturing Technical*, **67**, 2013, 2917-2925.

112. D. Fan, R. Zhang, Y. Gu, and M. Ushio: Effect of flux on A-TIG welding of mild steel, *Transactions of JWRI*, **30**, 2001, 35–40.

113. D. D. Schwemmer, D. L. Olson and D. L. Williamson: The relationship of weld penetration to the weld flux, *Welding Journal*, **58**, 1979, 153–160.

114. C. R. Heiple and J. R. Roper: Effect of selenium on GTAW fusion zone geometry, *Welding Journal*, **60(8)**, 1981, 143-145.

115. C. R. Heiple and J. R. Roper: Mechanism for minor element effect on GTA fusion zone geometry, *Welding Journal*, **61(4)**, 1982, 97-102.

116. C. R. Heiple and J. R. Roper: Effects of minor elements on GTAW fusion zone shape, *Trends in Welding Research in the United States*, ed. S .A. David, 1982, 489-520.
117. C. R. Heiple, J. R. Roper, R. T. Stagner and R. J. Aden: Surface active element effects on the shape of GTA, laser, and electron beam welds, *Welding Journal*, **62(3)**, 1983, 72-77.
118. Y. Zhao, Y. Lei and Y. Shi: Effects of surface-active elements sulfur on flow patterns of welding pool, *Journal of Materials Science and Technology*, **21 (3)**, 2005, 408-414.
119. M. Mishra, T. J. Lienert, M. Q. Johnson and T. DebRoy: An experimental and theoretical study of gas tungsten arc welding of stainless steel plates with different sulphur concentrations, *Acta Materialia*, **56**, 2008, 2133-2146.
120. S. Lu, H. Fujji, H. Suguyama, M. Tanaka and K. Nogi: Effects of Oxygen additions to argon shielding gas on GTA weld shape, *ISIJ International*, **43**, 2003, 1590-1595.
121. S. P. Lu, W. C. Dong, D. Z. Li and Y. Y. Li: Numerical simulation for welding pool and welding arc with variable active element and welding parameters, *Science and Technology of Welding and Joining*, **14 (6)**, 2009, 509-516.
122. F. Lu, S. Yao, S. Lou and Y. Li: Modeling and finite element analysis on GTAW arc and weld pool, *Computational Materials Science*, **29**, 2004, 371-378.
123. F. Lu, X. Tang, H. Yu and S. Yao: Numerical simulation on interaction between TIG welding arc and weld pool, *Computational Materials Science*, **35**, 2006, 458-465.
124. W. C. Dong, S. P. Lu, D. Z. Li and Y. Y. Li: Modeling of the weld shape development during the autogenous welding process by coupling welding arc with weld pool, *Journal of Materials Engineering and Performance*, **19(7)**, 2010, 942-950.
125. S. Bag and A. De: Development of a three-dimensional heat transfer model for GTAW process using finite element method coupled with a genetic algorithm based identification of uncertain input parameters, *Metallurgical and Materials Transactions A*, **39(11)**, 2008, 2698–2710.
126. S. Bag, A. Trivedi and A. De: Development of a finite element based conduction mode heat transfer model for laser welding process using an adaptive volumetric heat source, *International Journal of Thermal Sciences*, **48(10)**, 2009, 1923–1931.
127. D. Clayton, F. Maurizio, A. Stephen, C. B. John and B. Joseph: Autogenous laser keyhole welding of AISI 316LTi, *Materials and Manufacturing Processes*, **25**, 2010, 1269–1277.

128. R. Rai and T. DebRoy: Tailoring weld geometry during keyhole mode laser welding using a genetic algorithm and a heat transfer model, *Journal of Physics, D: Applied Physics*, **39(6)**, 2006, 1257–1266.

129. X. Z. Jin and L. J. Li: A conduction model for deep penetration laser welding based on an actual keyhole, *Optics & Laser Technology*, **35**, 2003, 5–12.

130. X. Z. Jin, L. J. Li and Y. Zhang: A heat transfer model for deep penetration laser welding based on an actual keyhole, *International Journal of Heat and Mass Transfer*, **46**, 2003, 15–22.

131. M. Jandaghi, P. Parvin, M. J. Torkamany and J. Sabbaghzadeh: Alloying element losses in pulsed Nd:YAG laser welding of stainless steel 316, *Journal of Physics, D: Applied Physics*, **41**, 2008, 235503 (9pp).

132. R. R. Rykalin: Energy sources for welding, *Welding in the World*, **12**, 1974, 227-248.

133. N. Christensen, V. Davies and K. Gjermundsen: Distribution of temperatures in arc welding, *British Welding Journal*, **12 (12)**, 1965, 54-75.

134. T. W. Eager and N. S. Tsai, Temperature fields produced by traveling distributed heat sources, Welding Journal, 62 (12), 1983, 346-355.

135. N. T. Nguyen: Thermal analysis of welds, WIT Press, 2004.

136. E. Friedman: Analysis of weld puddle distortion and its effect on penetration, *Welding Journal Research Supplement*, **57**, 1978, 161-166.

137. G. W. Krutz and L. J. Segerlind: Finite element analysis of welded structure, *Welding Journal Research Supplement*, **57**, 1978, 211-216.

138. B. A. B. Andersson: Thermal stresses in a submerged-arc welded joint considering phase transformations, *Journal of Engineering Materials and Technology*, **100**, 1978, 356-362.

139. P. D. Hibbert and Z. Paley: Computation of temperatures in actual weld designs, *Welding Journal Research Supplement*, **54**, 1975, 385-392.

140. C. S. Wu, H. G. Wang and Y. M. Zhang: A new heat source model for keyhole plasma arc welding in FEM analysis of the temperature profile, *Welding Journal*, **85**, 2006, 284-289.

141. N. Yadaiah and S. Bag: Effect of heat source parameters in thermal and mechanical analysis of linear GTA welding process, *ISIJ International*, **52 (11)**, 2012, 2069-2075.

142. C. S. Wu, Q. X. Hu and J. Q. Gao: An adaptive heat source model for finite-element analysis of keyhole plasma arc welding, *Computational Materials Science*, **46**, 2009, 167-172.

143. Y. Luo, G. You, H. Ye and J. Liu: Simulation on welding thermal effect of AZ61 magnesium alloy based on three-dimensional modeling of vacuum electron beam welding heat source, Vacuum, **84**, 2010, 890-895.

144. P. Li and H. Lu: Hybrid heat source model designing and parameter prediction on tandem submerged arc welding, *International Journal of Advanced Manufacturing Technology*, **62**, 2012, 577-585.

145. Y. Li, Y.H. Feng, X.X. Zhang and C.S. Wu: An improved simulation of heat transfer and fluid flow in plasma arc welding with modified heat source model, *International Journal of Thermal Sciences*, **64**, 2013, 93-104.

146. O. Westby: Temperature distribution in the work piece by welding, Department of Metallurgy and Metals Working, The Technical University, Trondheim, Norway, 1968.

147. J. Mazumder and W. M. Steen: Heat transfer model for CW laser material processing, *Journal of Applied Physics*, **51 (2)**, 1980, 941-947.

148. T. Chande and J. Mazumder: Estimating effects of processing conditions and variable properties upon pool shape, cooling rates, and absorption coefficient in laser welding, *Journal of Applied Physics*, **56 (7)**, 1984, 1981-1986.

149. T. Zacharia, S. A. David, J. M. Vitek and T. DebRoy: Heat transfer during Nd:YAG pulsed laser welding and its effect on solidification structure of austenitic stainless steels, *Metallurgical and Materials Transactions A*, **20**, 1989, 957-967.

150. W. Sudnik, D. Radaj, S. Breitschwerdt and W. Erofeew: Numerical simulation of weld pool geometry in laser beam welding, *Journal of Physics D: Applied Physics*, **33**, 2000, 662-671.

151. X. Jin, L. Li and Y. Zhang: A heat transfer model for deep penetration laser welding based on an actual keyhole, *International Journal of Heat* and *Mass Transfer*, **46**, 2003, 15-22.

152. W. H. Kim and S. J. Na: Heat and fluid flow in pulsed current GTA weld pool, *International Journal of Heat* and *Mass Transfer*, **41**, 1998, 3213-3227.

153. I. S. Kim, A. Basu, A mathematical model of heat transfer and fluid flow in the gas metal arc welding process, Journal of Materials *Processing Technology*., **77**, 1998, 17-24.

154. H. G. Fan, H. L. Tsai and S. J. Na: Heat transfer and fluid flow in a partially or fully penetrated weld pool in gas tungsten arc welding, *International Journal of Heat* and *Mass Transfer*, **44**, 2001, 417-428.

155. T. Cool and H. K. D. H. Bhadesia: Austenite formation in 9Cr1Mo type power plant steels, *Science and Technology of Welding and Joining*, **2**, 1997, 36-42.

156. T. Zacharia, J. M. Vitek, J. A. Goldak, T. DebRoy, M. Rapazz, and H. K. D. M. Bhadeshia: Fundamentals phenomena in welds, *Modelling and Simulation in Materials Science and Engineering*, **3**, 1995, 265–288.

157. D. A. Schauer, W. H. Giedt and S. M. Shintaku: Electron beam welding cavity temperature distributions in pure metals and alloys, *Welding Journal*, **57**, 1978, 127–133.

158. B. Zhang, Y. M. Zhang and R. Kovaceevic: Noncontact ultrasonic sensing for seam tracking in arc welding processes, *Journal of Manufacturing Science and Engineering Transactions of The ASME*, **120 (12)**, 1998, 600-608.

159. D. B. Zhao, J. Q. Yi, S. B. Chen, L. Wu and Q. Chen: Extraction of three-dimensional parameters for weld pool surface in pulsed GTAW with wire filler, *ASME Journal of Manufacturing Science and Engineering*, **125 (8)**, 2003, 493-503.

160. A. Ancona, P. M. Lugarà, F. Ottonelli and I. M. Catalano: A sensing torch for on-line monitoring of the gas tungsten arc welding process of steel pipes, *Measurement Science and Technology*, **15**, 2004, 2412-2418.

161. M. S. Weglowski: Investigation on the electric arc light emission in TIG welding, *International Journal of Computational Materials Science and Surface Engineering*, **1(6)**, 2007, 734-749.

162. R. Kovacevic, Y. Zhang and S. Ruan: Sensing and control of weld pool geometry for automated GTA welding, *ASME Journal of Engineering for Industry*, **117**, 1995, 210-222.

163. W. Pitscheneder: Contributionsto the understanding and optimization of laser surface alloying, Ph.D. thesis, University of Leoben, 2001.

164. A. Matsunawa, N. Seto, M. Mazutani and S. Katayama: Liquid motion in keyhole laser welding, Joining and Welding Research Institute, Osaka University, ICALEO'98, Orlando, U.S.A., 16-19 November 1998, 151-160.

165. P. Dutta, Y. Joshi and C. Franche: Determination of gas tungsten arc welding efficiencies, *Experimental Thermal and Fluid Science*, **9**, 1994, 80-89.

166. W. H. Giedt, L. N. Tallerico and P. W. Fuerschbach: GTA welding efficiency: calorimetric and temperature field measurements, *Welding Journal*, **68 (1)**, 1989, 28-32.

167. A. Trivedi, S. Bag and A. De: Three Dimensional Transient Heat Conduction and Thermo Mechanical Analysis for Laser Spot Welding Using Adaptive Heat Source, *Science and Technology of Welding and Joining*, **12 (1)**, 2007, 24-31.

168. D. Deng: FEM prediction of welding residual stress and distortion in carbon steel considering phase transformation effects, *Materials and Design*, **30**, 2009, 359-366.

169. V. J. Papazoglou and K. Masubuchi: Numerical analysis of thermal stresses during welding including phase transformation effects, *Journal of Pressure Vessel Technology*, **104**, 1982, 198-203.

170. T. L. Teng and C. C. Lin: Effect of welding conditions on residual stresses due to butt welds, *International Journal of Pressure Vessels and Piping*, **75**, 1998, 857-864.

171. S. A. Tsirkas, P. Papanikos, K. Pericleous, N. Strusevich, F. F. Boitout and J. M. Bergheau: Evaluation of distortions in laser welded shipbuilding parts using local-global finite element approach, *Science and Technology of Welding and Joining*, **8 (2)**, 2003, 79-88.

172. M. Mishra, T. J. Lienert, M. Q. Johnson and T. DebRoy: An experimental and theoretical study of gas tungsten arc welding of stainless steel plates with different sulphur concentrations, *Acta Materialia*, **56**, 2008, 2133-2146.

173. T. Zacharia, S. A. David and J. M. Vitek: Effect of evaporation and temperature dependent material properties on weld pool development, Metallurgical and Materials Transactions B, 22, 1991, 233-241.

174. K. Mundra, T. DebRoy, T. Zacharia and S. A. David: Role of thermophysical properties in weld pool modeling, Welding Research Supplement, 71 (9), 1992, 313-330.

175. G. H. Little and A. G. Kamtekar: The effect of thermal properties and weld efficiency on transient temperatures during welding, Computers and Structures, 38, 1998, 157–165.

176. X. K. Zhu and Y. J. Chao: Effect of temperature-dependent material properties on welding simulation, *Computers & Structures*, **80**, 2002, 967-976.

177. E. Armentani, R. Esposito and R. Sepe: The effect of thermal properties and weld efficiency on residual stresses in welding, *Journal of Achievements in Materials and Manufacturing Engineering*, **20**, 2007, 319-322.

178. W. Liang, D. Deng and H. Murakawa: Measurement of inherent deformations in typical weld joints using inverse analysis (Part 2), *Transactions of JWRI*, 34 (1), 2005, 113-123.

179. A. Służalec: Theory of thermo-mechanical processes in welding, Springer, Netherlands, 2005.

180. Y. J. Chao: Measuring welding-induced distortion in Processes and mechanisms of welding residual stress and distortion edited by Z. Feng, Woodhead Publisher, Cambridge, England, 2005.

181. V. J. Papazoglou and K. Masubuchi: Numerical analysis of thermal stresses during welding including phase transformation effects, *Journal of Pressure Vessel Technology*, **104**, 1982, 198-203.

182. E. F. Rybicki, G. L. Nagel, R. B. Stonesifer and E. G. Miller: A semi-empirical model for transverse weld deflections of square tubular automotive beams, Welding Journal, **72 (8)**, 1993, 371-380.

183. N. Shiva Prasad and T. K. Shankaranarayanan: Estimation of residual stresses in weldment using adaptive grids, Computers and Structures, **60**, 1996, 1037-1045.

184. C. Carmignani, R. Mares and G. Toselli: Transient finite element analysis of deep penetration laser welding process in a single pass butt-welded thick steel plate, *Computer Method in Applied Mechanics and Engineering*, **179**, 1999, 197-214.

185. H. S. Bang, S. M. Joo, J. M. Kim and W.S. Chang: Mechanical Characteristics of resistance multispot welded joints, Science and Technology of Welding and Joining, 8, 2003, 369-376.

186. G. H. Jung and C. L. Tsai: Plasticity based distortion analysis for fillet welded thin plate T-joint, *Welding Journal*, **83**, 2004, 177-187.

187. D. Deng and H. Murakawa: Numerical simulation of temperature field and residual stress in multi-pass welds in stainless steel pipe and comparison with experimental measurements, *Computational Materials Science*, **37 (3)**, 2006, 269-277.

188. R. Spina, L. Tricarico, G. Basile and T. Sibillano: Thermo-mechanical modeling of laser welding of AA5083 sheets, *Journal of Materials Processing Technology*, **191**, 2007, 215-219.

189. D. Deng, H. Murakawa and D. Liang: Numerical simulation of welding distortion in large structures, *Computer Methods in Applied Mechanics and Engineering*, **196**, 2007, 4613–4627.

190. D. Deng and H. Murakawa: Prediction of welding distortion and residual stress in a Thin plate butt-welded joint, *Computational Materials Science*, **43**, 2008, 353-365.

191. N. U. Dar, E. M. Qureshi and M. M. I. Hammouda: Analysis of weld-induced residual stresses and distortions in thin-walled cylinders, *Journal of Mechanical Science and Technology*, **23**, 2009, 1118-1131.

192. A. Capriccioli and P. Frosi, Multipurpose ANSYS FE procedure for welding processes simulation, *Fusion Engineering and Design*, **84**, 2009, 546-553.

193. H. A. Ameen, K. S. Hassan and M. M. Salah: Influence of the butt joint design of TIG welding on the thermal stresses, *Engineering & Technology Journal*, **29 (14)**, 2011, 2841-2858.

194. M. Asadi, J. A. Goldak, J. Nielsen, J. Zhou, S. Tchernov and D. Downey: Analysis of predicted residual stress in a weld and comparison with experimental data using regression model, *International Journal of Mechanics and Materials in Design*, **5**, 2009, 353-364.

195. P. Lacki and K. Adamus: Numerical simulation of the electron beam welding process, *Computers and Structures*, **89**, 2011, 977–985.

196. A. De and T. DebRoy: Improving reliability of heat and fluid flow calculations during conduction model laser spot welding by multi-variable optimization, *Science and Technology of Welding and Joining*, **11(2)**, 2006, 143-153.

197. S. Bag, A. Trivedi and A. De: Use of a multivariate optimization algorithm to develop a self-consistent numerical heat transfer model for laser spot welding, *International Journal of Advanced Manufacturing Technology*, **38**, 2008, 575-585.

198. A. Trivedi, A. Suman and A. De: Integrating finite element based heat transfer analysis with multivariate optimization for efficient weld pool modeling, *ISIJ International*, **46 (2)**, 2006, 267-275.

199. M. A. Katz and B. Rubinsky: An inverse finite element technique to determine the change of phase interface location in one-dimensional melting problems, *Numerical Heat Transfer*, **7**, 1984, 269-277.

200. A. De and T. DebRoy: Probing unknown welding parameters from convective heat transfer calculation and multivariable optimization, *Journal of Physics D: Applied Physics*, **37**, 2004, 140-150.

201. I. Ono and S. Kobayashi: A real-coded genetic algorithm for function optimization using unimodal normal distribution crossover, In Black, T., editor, *Proceedings of the Seventh International Conference on Genetic Algorithms (ICGA-7)*, Morgan Kaufmann, San Francisco, California, 1997, 246−253.

202. T. Higuchi, S. Tsutsui and M. Yamamura: Theoretical analysis of simplex crossover for real-coded genetic algorithms. In Schoenauer, M. et al., editors, Parallel Problem Solving from Nature (PPSN-VI), Springer, Berlin, Germany, 2000, 365−374.

203. H. Satoh, M. Yamamura and S. Kobayashi: Minimal generation gap model for Gas considering both exploration and exploitation, T. Yamakawa and G. Matsumoto editors,

Proceedings of the IIZUKA: Methodologies for the Conception, Design, and Application of Intelligent Systems, World Scientific, Singapore, 1996, 494−497.

204. S. Mishra and T. Debroy: A heat transfer and fluid-flow-based model to obtain a specific weld geometry using various combinations of welding variables, *Journal of Applied Physics*, **98**, 2005, 044902: 1 -10.

205. S. Mishra and T. Debroy: A computational procedure for finding multiple solutions of convective heat transfer equations, *Journal of Physics D: Applied Physics*, **38**, 2005, 2977-2985.

206. S. Mishra and T. Debroy: Tailoring gas tungsten arc weld geometry using a genetic algorithm and a neural network trained with convective heat flow calculations, *Materials Science and Engineering A*, **454−455**, 2007, 477–486.

207. A. Kumar and T. DebRoy: A neural network model of heat and fluid flow in gas metal arc fillet welding based on genetic algorithm and conjugate gradient optimization, *Science and Technology of Welding and Joining*, **11(1)**, 2006, 106 – 119.

208. A. Kumar and T. DebRoy: Taloring fillet weld geometry using a genetic algorithm and a neural network trained with convective heat flow calculations, *Welding Journal*, **86 (1)**, 2007, 26- 33.

209. K. Price, R. Storn, and J. Lampinen: Differential Evolution - A Practical Approach to Global Optimization, Springer, Berlin, 2005.

210. R. Storn: Differential evolution, a simple and efficient heuristic strategy for global optimization over continuous spaces, *Journal of Global Optimization*, **11**, 1997, 341-359.

211. A.W. Iorio and X. Li: Incorporating directional information within a differential evolution algorithm for multiobjective optimization, GECCO'06, July 8-12, 2006, Seattle, Washington, USA.

212. X. Shan, C. M. Davies, T. Wangsdan, N. P. O'Dowd and K. M. Nikbin: Thermo-mechanical modelling of a single-bead-on-plate weld using the finite element method, *International Journal of Pressure Vessels and Piping*, **86**, 2009, 110-121.

213. S. Bag, A. De and T. DebRoy: A genetic algorithm assisted inverse convective heat transfer model for tailoring weld geometry, *Materials and Manufacturing Processes*, **24**, 2009, 384-397.

214. S. Bag and A. De: Probing reliability of transport phenomena based heat transfer and fluid flow analysis in autogeneous fusion welding process, *Metallurgical and Materials Transaction A*, **41 (9)**, 2010, 2337-2347.

215. http://www16.ocn.ne.jp/~akiko-y/Egg/index_egg_E.html.

216. http://www.mathematische-basteleien.de/eggcurves.htm.

217. R. Hultgren, P. D. Desai, D. T. Hawkins, M. Gleiser, K. K. Kelley and D. D. Wagman: Selected Values of the Thermodynamic Properties of the Elements (ASM International, Materials Park, OH, 1973).

218. R. E. Honig and D. A. Kramer: Physicochemical Measurements in Metal Research (Interscience Publishers, New York, 1970 -517), 505.

219. C. L. Yaws: Handbook of vapor pressure, Houston: Gulf Pub. Co., c1994.

220. C. B. Alcock, V. P. Itkin and M. K. Horrigan: Vapour Pressure Equations for the Metallic Elements: 298–2500K, Canadian Metallurgical Quarterly, 23 (3), 1984, 309-313.

221. J. N. Reddy and D. K. Gartling: The Finite Element Method in Heat Transfer and Fluid Dynamics, 2nd ed., CRC Press, Boca Raton, FL, 2000.

222. O. P. Gupta: Finite and Boundary Element Methods in Engineering, Oxford and IBH Publications, New Delhi, 2003.

223. ANSYS 14.0, User manual.

224. D. Karaboga and S. Okdem, A simple and global optimization algorithm for engineering problems: differential evolution algorithm, *Turkish Journal of Electrical Engineering & Computer Sciences*, **12(1)**, 2004, 53-60.

225. S. Kumar, S. Roy, C. P. Paul and A. K. Nath: Three-dimensional conduction heat transfer model for laser cladding process, *Numerical Heat Transfer, Part B: Fundamentals: An International Journal of Computation and Methodology*, **53 (3)**, 2008, 271-287.

226. A. Kumar, C. P. Paul, A. K. Pathak, P. Bhargava and L. M. Kukreja: A finer modeling approach for numerically predicting single track geometry in two dimensions during Laser Rapid Manufacturing, *Optics & Laser Technology*, **44 (3)**, 2012, 555-565.

227. S. Bag, D. V. Kiran, Arshad A. Syed and A. De: Efficient estimation of volumetric heat source in fusion welding process simulation, *Welding in the World*, **56(11/12)**, 2012, 88-97.

228. P. Colegrove, C. Ikeagu, A. Thistlethwaite, S. Wiiliams, T. Nagy, W. Suder, A. Steuwer and T. Pirling: The welding process impact on residual stress and distortion, *Science and Technology of Welding and Joining*, **14 (8)**, 2009, 717-725.

229. K. N. Braszczynska-Malik and M. Mroz: Gas-tungsten arc welding of AZ91 magnesium alloy, *Journal of Alloys and Compounds*, **509 (41)**, 2011, 9951-9958.

230. J. M. Sa´Nchez-Amaya, T. Delgado, L. Gonza´ Lez-Rovira and F. J. Botana: Laser welding of aluminium alloys 5083 and 6082 under conduction regime, *Applied Surface Science*, **255 (23)**, 2009, 9512-9521.

231. J. M. Sa´Nchez-Amaya, Z. Boukha, M. R. Amaya-Vazquez and J. Botana: Weldability of aluminum alloys with high-power diode laser, *Welding Journal*, **91**, 2012, 155-161.

232. S. Wu, P. C. Zhao and Y. M. Zhang: Numerical simulation of transient 3-D surface deformation of a completely penetrated GTA weld, *Welding Journal*, 2004, 330-335.

233. N. Siva Shanmugam, G. Buvanashekaran, K. Sankaranarayanasamy and K. Manonmani: Some Studies on temperature profiles in AISI 304 stainless steel sheet during laser beam welding using FE simulation, *International Journal of Advanced Manufacturing Technology*, **43 (1-2)**, 2009, 78-94.

234. L. Wang and S. Felicelli: Process modeling in laser deposition of multilayer SS410 steel, *Transactions of the ASME*, **129 (1)**, 2007, 261-270.

235. L. E. Lindgren, H. Runnemalm and M. O. Nasstrom: Simulation of multipass welding of a thick plate, *International Journal for Numerical Methods in Engineering*, **44**, 1999, 1301-1316.

236. P. Michaleris and A. DeBiccari: Prediction of welding distortion. Welding Journal, **76(4)**, 1997, 172-180.

237. CEN/TC 250/SC 9: ENV 1999-1-2. Design of aluminium structures, Part 1.2, Structural fire design 1997.

238. International Magnesium Association, 2003,http://www.intlmag.org/.

239. O. Velde, A. Techel and R. Grundmann: Suppression of the development of pores during laser-induced surface dispersion of TiC into aluminium by means of a static magnetic field, *Surface and Coatings Technology*, **150 (2-3)**, 2002, 170-178.

240. S. Bannour, K. Abderrazak, H. Mhiri and G. Le Pale: Effects of temperature-dependent material properties and shielding gas on molten pool formation during continuous laser welding of AZ91 magnesium alloy, *Optics & Laser Technology*, **44 (8)**, 2012, 2459-2468.

241. J. Goldak: Thermal Analysis of Welds, in L. Karlsson (Ed.), Modelling in Welding, Hot Powder Forming and Casting, ASM International, Materials Park, OH, 1999, 17-29.

242. A. A. Reddy, B. Guha, D. R. G. Achar and S. H. Lalam: Finite Element Analysis of Heat Affected Zone Behaviour in Pulsed GTA Weldments, in H. Cerjak (Ed.), 5th International Conference on Numerical Analysis of Weldability, graz-seggau, Austria, 1999,

243. P. Dutta, Y. Joshi and R. Janaswami: Thermal modelling of GTAW process with non-axisymmetric boundary conditions, *Numerical Heat Transfer A*, **27**, 499-518.

244. J. Jaidi and P. Dutta: Three-dimensional turbulent weld pool convection in gas metal arc welding process, *Science and Technology of Welding and Joining*, 2004, **9 (5)**, 407-414.

245. X. He, J. W. Elmer and T. DebRoy: Heat transfer and fluid flow in laser micro welding, *Journal of Applied Physics*, **97**, 2005, 084909:1-9.

246. K. J. Bathe: Finite element procedures, sixth edition, Prentice-Hall of India, New Delhi, 2002, 830-835.

247. T. J. R. Hughes: Unconditionally stable algorithm for nonlinear heat conduction, *Computer Methods in Applied Mechanics and Engineering*, **10**, 1977, 135-139.

248. S. Bag and A. De: Error analysis of forward and reverse heat conduction and convection calculations considering uncertainties in welding, *Science and Technology of Welding and Joining*, **14 (7)**, 2009, 662-668.

Bibliography

1. J. A. Goldak and M. Akhalaghi: Computational Weld Mechanics, Springer Science and Business Media, Inc. New York, First edition, 2005.

2. Ø. Grong: Metallurgical Modeling of Welding, 2nd edition, The Institute of Materials, London, 1997.

3. J. F. Lancaster: The Physics of Welding, 2nd Edition, Pergamon, Oxford, 1986.

4. K. Easterling: Introduction to the Physical Metallurgy of Welding, 2nd Edition, Butterworth-Heinemann, Oxford, 1992.

5. S. Kou: Welding Metallurgy, 2nd edition, John Wiley & Sons, Hoboken, New Jersey, 2003.

6. J. Norrish: Advanced welding processes, Woodhead publishing Ltd., Cambridge, England, 2006.

7. K. Masubuchi: Analysis of Welded Structures, Pergamon Press, Oxford, 1980.

8. J. N. Reddy and D. K. Gartling: The Finite Element Method in Heat Transfer and Fluid Dynamics, 2nd ed., CRC Press, Boca Raton, FL, 2000.

9. O. P. Gupta: Finite and Boundary Element Methods in Engineering, Oxford and IBH Publications, New Delhi, 2003.

10. K. Deb: Optimization for Engineering Design: Algorithms and Examples, Prentice Hall of India Private Limited, New Delhi, India, 2005.

List of publications

Book Chapter

1. N. Yadaiah, S. Bag, C. P. Paul and L. M. Kukreja: Fiber laser welding in a controlled inert gas atmosphere: An experimental & numerical investigation, Edited by U.S. Dixit and S.N. Joshi in ***Laser Based Manufacturing***, **Springer Publisher**, pp. 399-419, 2014.

International Journals

[*]**2. N. Yadaiah** and S. Bag: Development of egg-configuration heat source model in numerical simulation of autogenous fusion welding process, ***International Journal of Thermal Sciences***, Vol. 86, pp. 125-138, 2014.

3. S. Singh, **N. Yadaiah**, S. Bag and S. Pal: Numerical simulation of welding induced residual stress in fusion welding process using adaptive volumetric heat source, ***Proceedings of the IMechE, Part C: Journal of Mechanical Engineering Science***, Vol. 228 (16), pp. 2960-2972, 2014.

4. N. Yadaiah and S. Bag: Role of oxygen as surface active element in linear GTA welding process, ***Journal of Materials Engineering and Performance***, Vol. 22 (11), pp. 2069-2075, 2013.

5. N. Yadaiah and S. Bag: Effect of heat source parameters in thermal and mechanical analysis of linear GTA welding process, ***ISIJ International***, Vol. 52(11), pp. 2069-2075, 2012.

6. N. Yadaiah, S. Bag, C. P. Paul and L. M. Kukreja: Influence of self-protective atmosphere during fiber laser welding of austenitic stainless steel, ***International Journal of Advanced Manufacturing Technology***, 2015, **accepted.**

[**]**7. N. Yadaiah**, S. Bag, C. P. Paul and L. M. Kukreja: Efficient Finite Element Modeling of Fiber Laser Welding Process under Conduction Regime on 316 Stainless Steel Plate, ***International Journal of Current Engineering and Technology***, Special Issue 2, pp.31-36, 2014.

International Conferences

8. N. Yadaiah, S. Bag, C. P. Paul and L. M. Kukreja: an experimental investigation on fiber laser welding at controlled inert gas atmosphere, 5th International and 26th All India Manufacturing Technology, Design and Research Conference ***(AIMTDR 2014)*** at IIT Guwahati, Guwahati, India, from 12th – 14th December 2014, pp. 875-1-6.

9. N. Yadaiah, S. Bag, C. P. Paul and L. M. Kukreja: Prediction of weld induced distortions in fiber laser butt joint, ***IIW International Congress 2014*** on "Advancement In Welding, Cutting And Surfacing Technologies For Improved Economy And Sustainable Environment" at New Delhi, India, from 9th – 11th April 2014, pp. 241-246.

10. N. Yadaiah and S. Bag: Egg-configuration heat source model in simulation of diode laser welding under conduction regime, ***IIW International Congress 2014*** on "Advancement In Welding, Cutting And Surfacing Technologies For Improved Economy And Sustainable Environment" at New Delhi, India, from 9th – 11th April 2014, pp. 247-252.

11. N. Yadaiah, S. Bag, C. P. Paul and L. M. Kukreja: Fiber laser welding of austenitic stainless steel in protective atmosphere of argon, Recent Development in Welding and Joining Technologies, ***7th Asia Pacific International Institute of Welding International Congress***, 2013, Singapore, from 8th to 10th July 2013, pp. 501-506.

12. S. Bag and **N. Yadaiah**: Possible role of surface active elements in weld pool modelling of fusion welding process, ***International Conference on Computational Methods in Manufacturing*** **(ICCMM 2011)**, IIT Guwahati, India, from 15th – 16th December 2011, pp.154-162.

***Science Direct top 25** list of most downloaded articles (**Rank 8th** from July to September 2014 and **Rank 19th** from October to December 2014).

Forwarded from *International Conference on Advances in Mechanical Sciences 2014* and selected for the **BEST RESEARCH PAPER AWARD presented in *International Conference on Advances in Mechanical Sciences* held at Hyderabad, India on 9th – 11th January 2014.

Acknowledgment

Over the journey of four years at IIT Guwahati, I have been accompanied and supported by many people that helped me to accomplish the task of this magnitude possible. I would first like to express my deep appreciation and sincere gratitude to my advisor **Dr. Swarup Bag**. His untiring guidance in the form of research effort, demand for excellence and encouragement, professional expertise brought the best from all involved. As well, he has helped me with many opportunities to advance my research as well as my professional development.

I would like to acknowledge, Prof. Anoop K. Das, Head, Department of Mechanical Engineering, for providing an environs for higher learning and for his valuable advices and suggestions. I would also like to acknowledge Prof. P. S. Robi, Dr. S. Pal, Dr. P. Biswas and Dr. N. Kishore for their valuable advice and suggestions on my work while serving on my thesis committee. I am very appreciative to them for giving their time to review this thesis.

I would also like to express my thanks to Dr. C. P. Paul at Laser Material Processing Division, Raja Ramanna Centre for Advanced Technology, Indore, India for his helpful discussions on fiber laser source and Dr. Fanrong Kong affiliated with Research Center for Advanced Manufacturing, Southern Methodist University, Dallas, USA for his supportive discussions on numerical modeling. I would like to express my immense gratitude to my colleague friends for their support.

I am grateful to my parents and family members for their love and support. I am profoundly indebted to my mother, Dhanamma and my wife, Rupa; those have always been supported me with their love, encouragement, understanding and faith.

Finally, I would like to acknowledge the financial support from Science & Engineering Research Board, India, under grant number SERB/F/0797/2013-2014 and IIT Guwahati under grant number SG/ME/P/SB/1 for supporting this research work.

IIT Guwahati **N. Yadaiah**

July 2015